

# Aeolian surface erodibility Measured on the Sand Engine

*From mobile wind tunnel design towards field expeditions*

*MSc Thesis*



*Jacob Marinus (Mark) van Langeraad*

# Aeolian surface erodibility Measured on the Sand Engine

*From mobile wind tunnel design towards field expeditions*

*Jacob Marinus (Mark) van Langeraad*

Student number  
4493664

In partial fulfilment of the requirements for the degree of...

Master of Science  
in Civil Engineering

Track  
Hydraulic Engineering

Specialisation  
Coastal Engineering

...at Delft University of Technology

To be defended publicly on Tuesday, June 11<sup>th</sup>, 2024, at 03:00 PM

Supervisor	Dr. ir. S. de Vries	
Thesis committee	Dr. ir. S. de Vries, Dr. ir. B. Hofland,	Delft University of Technology Delft University of Technology

An electronic version of this thesis is available at <http://repository.tudelft.nl/>

## Preface

This report contains a study performed at Delft University of Technology that lasted roughly one year in duration. In elaboration, this report is written in partial fulfilment of the requirements for the degree of Master of Science (MSc) in Civil Engineering. The degree involves a MSc-track in Hydraulic Engineering and a specialization in Coastal Engineering.

Mobi-Gust 2 was developed and used within this research. “Mobi-Gust” is the collective name for an innovative range of mobile wind tunnel systems developed at Delft University of Technology. “Mobi-Gust” indicates the words “mobile” and “wind”, which is shorthand for [Mobile Beach Investi-Gation Unit for Sand-erosion Testing](#) (table 1). The “2” refers to the second design iteration (figure 1). The Mobi-Gust series is used to explore aeolian erosion. In turn, the gained knowledge can be used to improve Aeolis. Aeolis is an open-source, process-based, numerical model that simulates aeolian processes. Amongst others, this report offers the design of Mobi-Gust 2 to accommodate the open-source philosophy; i.e., sharing and developing knowledge together.

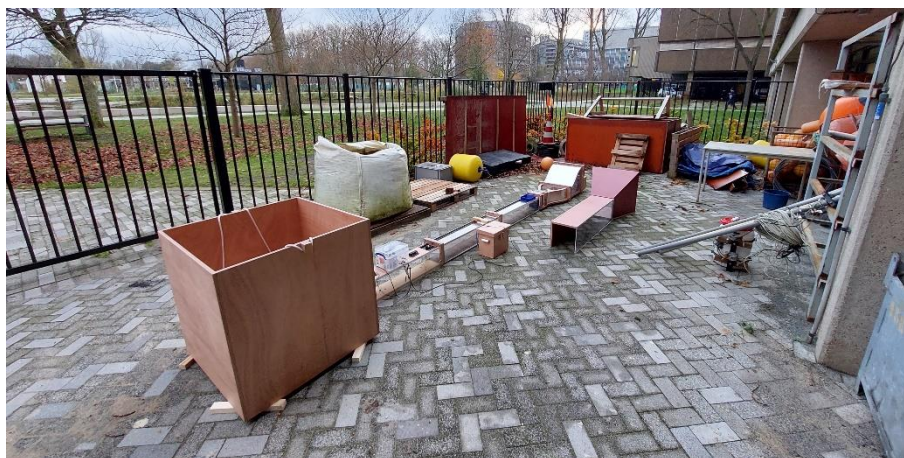
*Table 1 – Additional background on ‘Mobi-Gust’*

Mobile & Beach	Mobi-Gust is portable, allowing in-situ (beach) deployment
Investigation, Unit & Testing	Mobi-Gust 2 is a toolbox to conduct experimental research with
Sand-erosion	The research involves aeolian erosion of sand surfaces

Mobi-Gust 2 can be seen as the biggest result from this study. Mobi-Gust 2 consists of a mobile wind tunnel system and a wind gauging system. The wind tunnel system is primarily made within the Hydraulic Engineering laboratory of Delft University of Technology, with help from DEMO (‘Dienst Elektronische- en Mechanische Ontwikkeling’). Next, the Arduino community aided in shaping the wind gauging system. After realisation, Mobi-Gust 2 was tested in the already mentioned laboratory. Besides laboratory testing, Mobi-Gust 2 went on field expeditions as well. The field measurements were conducted on the Sand Engine. The Sand Engine is a mega nourishment along the Holland Coast, near The Hague (the Netherlands).

This report requires basic knowledge in aerodynamics, fluid mechanics and aeolian processes. Next, this report contains three parts. [Part 1](#) consists of a general introduction, that applies to both succeeding parts. Next, [part 2](#) provides the Proof of Concept of Mobi-Gust 2. In other words, [part 2](#) conveys the development of Mobi-Gust 2. Finally, [part 3](#) shows the applied research that was conducted with Mob-Gust 2.

*Mark van Langeraad  
Delft, June 2024*



*Figure 1 – Mobi-Gust 2 (left) next to Mobi-Gust 1 (right)*



## Acknowledgements

I want to thank all people that were involved in this MSc Thesis report. The list of people is summarized into four main groups.

First of all, I would like to thank my supervisors dr. ir. Sierd de Vries and dr. ir. Bas Hofland. Starting with acknowledging mister De Vries. Mister De Vries was my daily supervisor and also my graduation committee chair. Mister De Vries gave me this great topic. Next, he was virtually always available to help me, or to discuss matters. The conversations with mister De Vries provided me with a lot of knowledge on aeolian processes. Also, he helped me to apply this knowledge into the design and usage of Mobi-Gust 2. On top, mister De Vries made a lot of arrangements behind the scenes (e.g., finances). Secondly, I want to express my gratitude towards mister Hofland. Mister Hofland was my second supervisor and also a member of the graduation committee. The talks with mister Hofland especially helped me to design and test Mob-Gust 2 from a flow-related perspective.

Second of all, I want to thank Pieter van der Gaag. Mister Van der Gaag was my laboratory- and fieldwork supervisor. Mister Van der Gaag extensively guided me throughout my time in the Hydraulic Engineering laboratory of Delft University of Technology. Mister Van der Gaag also aided me in transforming my conceptual ideas about Mobi-Gust 2 into something constructible. Also, mister Van der Gaag helped me to prepare and execute the field expeditions using Mobi-Gust 2.

Third of all, I want to address the other employees of the Hydraulic Engineering laboratory. In particular, I would like to thank Arno Doorn and Arie van der Vlies. Mister Doorn was the head-constructor of Mobi-Gust 2. Without his fine craftsmanship there would be no mobile wind tunnel system to work with. DEMO ('Dienst Elektronische- en Mechanische Ontwikkeling') helped mister Doorn to create the complex shapes of Mobi-Gust 2. Next, both mister Doorn and mister Van der Vlies assisted me greatly while working in the laboratory. Because of this my time in the laboratory was very educational and enjoyable.

Last of all, I want to turn myself to some notable individuals from outside Delft University of Technology. I would like to express my appreciation towards my father Peter van Langeraad and partner Veerle van Moort. Without their precious help ([figure 2](#)), this report would not contain field measurements.

*Conducting research can be as unpredictable as windblown sand.*

*Mark van Langeraad  
Delft, June 2024*



*Figure 2 – My fieldwork companions standing in an aeolian transport layer*



## Summary

The Building with Nature approach helps to develop sustainable solutions for flood risk mitigation. On top, these solutions harness natural forces as much as possible. The Building with Nature approach may thus use aeolian processes to build, maintain and reinforce coastal dunes. In that case, aeolian processes are directly coupled to the (variable) flood risk of these sandy barriers. So, the Building with Nature approach is supported by accurate and robust aeolian transport predictions. In other words, the relation between wind speed and coastal sand transport is vital.

Coastal aeolian transport is usually overpredicted by traditional aeolian models. These models generally assume capacity limited transport. This type of transport implies that varying transport rates are solely caused by varying wind speeds. This approach is valid in systems where sand is abundant and available. A sandy arid environment can be seen as an example of such a capacity limited system. Yet, in systems where sand is less abundant and available, the transport capacity might be unreachable. Consequently, transport rates may not vary if wind speeds are varying. A sandy coastal environment can be seen as an example of such a supply limited system. Novel models (e.g., Aeolis) try to account for sand availability and the associated supply limitations.

Sand surface erodibility can be used to express the availability of sand. To clarify, surface erodibility describes the susceptibility of a surface to erosion. Exploring the erodibility of sand surfaces might thus improve the predictions on coastal aeolian sand exchange. To this end the idea of Mobi-Gust 2 was initiated; a specialized mobile erosion device that explores the erodibility of in-situ sand surfaces. Mobi-Gust 2 consists of a mobile wind tunnel system and a wind gauging system. A Proof Of Concept (POC) was used to check whether Mobi-Gust 2 could sustainably conduct useful, reliable and controllable erosion measurements.

The mobile wind tunnel is of the open-return geometry and is light and modular. As a result, Mobi-Gust 2 offers (aerodynamic) functionality while being mobile. The air inside the mobile wind tunnel system is pushed by a blowing fan. This fan was a constraint to the design. The created air flow is adjustable by means of a speed controller. Next, the air flow is accelerated with negligible energy losses in a short and gradually curved contraction. Next, the air flow is conditioned in two separate components. First, the air flow is straightened by a honeycomb (i.e., a cross-section divider); and the component also onsets flow development. Secondly, this flow development is continued within a transition zone. The transition zone is a closed duct that accommodates the interactions between the air flow and the boundaries. In turn, causing more generic turbulent flow properties. Next, the conditioned air flow enters an erosion zone. This erosion zone has no bottom plate so that aeolian erosion is allowed to occur. Next, a saltation hopper can be used to establish an upwind supply of sand towards the erosion zone. This upwind supply of sand enhances the erosion process. Next, the sand-laden air travels towards a sand trap. The sand trap is open to air and closed to sand; and can be manually emptied.

The wind gauging system senses the wind speed digitally. The wind speed is deduced from sensing differential pressure. The main parts involve a microcontroller, a pressure sensor and a pitot tube. This pitot tube can be installed at the up- and/or downwind end of the erosion zone. The pitot tubes are embedded in aerodynamically-shaped, height-adjustable holders. The system senses centreline wind speeds of  $9.4 \text{ [m/s]}$  and vertically averaged speeds reach  $8.6 \text{ [m/s]}$ . The wind gauging system confirms partial flow development. To clarify, the wind gauging system senses logarithmic velocity profiles up until 25 [%] of the duct, as seen from the bottom. The system also senses slightly increased relative turbulence intensities. These intensities reach 6 [%] of the mean centreline wind speed. This increased value relates to the turbulence itself; but also to the development of the flow, the pressure sensor accuracy; and interferences. Finally, the system shows a signal-to-noise ratio of 15 [–]; which triples after applying one-second moving averages.

The portable power supply of Mobi-Gust 2 provides 2 [h] measuring time, with relatively stable wind speeds. The mentioned duration is a minimum; i.e., when supplying maximum power to the fan and while using the wind gauging system.

Mobi-Gust 2 was not able to erode an in-situ sand surface in a test field expedition. Yet, wind conditions inside Mobi-Gust 2 were presumably high enough to onset erosion. It is believed that the relatively wet winter hampered the conducted tests. So, a tailored sand pit was created to explore the erodibility of the sand surface in a more focussed way; i.e., linked to moisture content.

Overall, Mobi-Gust 2 is sustainable and is reasonably capable of conducting useful, reliable and controllable aeolian erosion measurements. Most obviously the wind speed can be raised. Yet, this improvement is relatively costly and laborious. More achievable improvements involve the transition- and the erosion zone. The transition zone should be elongated to further improve the development of the flow. Next, the walls of the erosion zone should be extended and chamfered outward. To clarify, the already elongated walls are still not long enough; and may suffer from undermining. On top, driving the (blocky) walls into the sand bed causes sand displacements into the erosion zone. Next, the wind speed gauging system can be improved in three areas. Firstly, the resolution is too coarse. Improvements involve buying a higher-resolution microcontroller (e.g., an Arduino Due) or a higher-resolution pressure sensor (e.g., a Fermion LWLP5000). Secondly, the sampling frequency is still variable in time. Improving this situation implies fixing inefficient data logging. Lastly, the wind speed (accuracy) verification must be improved. To clarify, a handheld anemometer generally showed 0.5 [m/s] higher wind speeds.

Following the POC, Mobi-Gust 2 was used to investigate the following main research question.

*The aeolian erosion process on sandy beaches,  
is solely determined by wind speed and does not rely on surface erodibility.*

This main research question was explored by two tests, i.e., the erosion- and the saltation test. The erosion test is analogous to clear wind erosion, i.e., erosion with sand-clear winds. The saltation test is analogous to live bed erosion, i.e., erosion with sand-laden winds. The practical difference between the two tests thus concerns the usage of the saltation hopper. The tests explore the aeolian erosion flux related to moisture content and saltating sand grains. Both tests are conducted in the laboratory and in the field. The laboratory of interest concerns the Hydraulic Engineering laboratory of Delft University of Technology. The field location of interest concerns the Sand Engine; a mega nourishment near The Hague, along the Holland Coast (The Netherlands).

Two main comparisons tackled the main research question. The first set of observations involved two erosion tests. To clarify, an in-situ erosion test did not produce any aeolian erosion (i.e., 0 [kg/m<sup>2</sup>/s]). Yet, the same sand bed could be mobilized after excavating and drying it. In elaboration, a second laboratory erosion test showed a mean erosion flux of 0.01 [kg/m<sup>2</sup>/s]. Both tests used comparable wind conditions, exceeding the threshold of motion for dry sand. This first comparison shows that similar winds may erode a sand surface differently depending on moisture content. The second set of observations involve an erosion- and a saltation test. This time both tests were conducted in the field. The in-situ erosion test could yet again not generate any aeolian erosion (i.e., 0 [kg/m<sup>2</sup>/s]). Yet, the same sand bed (i.e., Mobi-Gust 2 was not moved) could be mobilized after the addition of an upwind supply of sand. To clarify, the saltation test showed a mean erosion flux of 0.03 [kg/m<sup>2</sup>/s]. Again, the wind conditions inside Mobi-Gust 2 were comparable and exceeded the threshold of motion for dry sand. This second comparison also demonstrates that similar winds may erode a sand surface differently; yet, now depended on whether the air flow already has sand in transport or not. Additional laboratory experiments verified the mentioned observations.

The main advice is to prioritize the use of Mobi-Gust 2 over majorly improving it. To clarify, this means only applying small upgrades and not yet improving the wind speed itself. Mobi-Gust 2 should then be deployed in more favourable circumstances. In elaboration, many successful experiments are likely possible in dryer (summer) conditions. The words 'many' and 'successful' are both important. 'Many' refers to the statistical foundation that that is still lacking in this report. 'Successful' refers to really measuring spatiotemporal variations in sand bed erodibility. These measurements are possible by applying tests that are similar to this report. Yet, the tests should include time intervals. Also, these tests should be repeated at many different beach locations. This report uses a mean erosion flux for comparison reasons. Yet, the erosion flux, steered by sand bed erodibility, is likely to be non-linear. This introduces the next big step in coastal aeolian research. What actually is this relation?

# Table of contents

Preface .....	iii
Acknowledgements .....	iv
Summary .....	v
1 General introduction .....	2
1.1 The drive to improve predictions on aeolian sand exchange .....	2
1.2 Exploring the historical context of aeolian transport.....	3
1.3 The coastal problem involving classical aeolian theory .....	3
1.4 Shifting the attention towards aeolian surface erodibility.....	6
1.5 The main research question and the report structure.....	7
2 Proof Of Concept (POC): Mobi-Gust 2.....	9
2.1 Project outline .....	9
2.2 The methodology to design and test Mobi-Gust 2.....	11
2.2.1 The design of Mobi-Gust 2 .....	11
2.2.2 The performance of Mobi-Gust 2.....	26
2.3 Analysing the performance of Mobi-Gust 2.....	34
2.3.1 Evaluating the robustness of the power supply.....	34
2.3.2 Exploring the wind (gauging system) properties .....	35
2.3.3 Evaluating the drainage rate of the saltation hopper .....	35
2.3.4 Investigating the sand tightness of Mobi-Gust 2 .....	36
2.3.5 Exploring the wind speed in the modular design of Mobi-Gust 2.....	37
2.3.6 Investigating the flow development within Mobi-Gust 2.....	38
2.3.7 Exploring the erosion performance of Mobi-Gust 2.....	39
2.4 Discussing the performance of Mobi-Gust 2 .....	40
2.4.1 Discussing the robustness of the power supply.....	40
2.4.2 Reviewing the wind (gauging system) properties .....	42
2.4.3 Discussing the drainage rate of the saltation hopper .....	44
2.4.4 Revising the sand tightness of Mobi-Gust 2.....	45
2.4.5 Reviewing the wind speed in the modular design of Mobi-Gust 2.....	46
2.4.6 Revising the flow development within Mobi-Gust 2 .....	50
2.4.7 Discussing the erosion performance of Mobi-Gust 2 .....	55
2.5 Conclusions .....	57
2.5.1 Evaluating the sustainability of Mobi-Gust 2 .....	57
2.5.2 Evaluating Mobi-Gust 2's usability .....	57
2.5.3 Judging Mobi-Gust 2's Reliability .....	58
2.5.4 Evaluating Mobi-Gust 2's controllability .....	59
2.5.5 (Dis)Mounting and configuring.....	59



2.6	Recommendations.....	60
2.6.1	Increasing the wind speed .....	60
2.6.2	Improving the development of the flow .....	61
2.6.3	Creating a tailored sand pit .....	62
2.6.4	Improving the saltation hopper.....	62
2.6.5	Never stop mitigating sand losses .....	62
2.6.6	Invest in flow visualisation .....	62
2.6.7	Remeasuring and verifying velocity profiles.....	63
2.6.8	Verification of the boundary shear stress .....	63
2.6.9	Improving the wind gauging system.....	63
2.6.10	Improving the power supply .....	64
3	The erodibility of the sand surface .....	66
3.1	Brief recap .....	66
3.2	The methodology to explore sand surface erodibility.....	67
3.2.1	The layout of the experiments .....	67
3.2.2	Using hybrid experiments to assess the main research question.....	67
3.2.3	The expected data and the additional activities .....	68
3.2.4	Transport- and time management during field expeditions .....	69
3.2.5	Safety during field expeditions.....	70
3.3	Analysing the erodibility of the sand surface .....	71
3.3.1	General remarks on the conducted field expeditions .....	71
3.3.2	The influence of moisture content on the erosion flux .....	71
3.3.3	The influence of saltation sand on the erosion flux .....	72
3.3.4	Summarizing the gathered data .....	73
3.4	Discussing the erodibility of the sand surface.....	75
3.4.1	General remarks on the acquired data.....	75
3.4.2	The influence of moisture content on the erosion flux .....	77
3.4.3	The influence of saltation sand on the erosion flux .....	79
3.5	The conclusions from the applied aeolian research .....	82
3.5.1	Aeolian erosion from a dry and wet sand surface.....	82
3.5.2	Aeolian erosion with and without an upwind supply of sand.....	83
3.5.3	Experimental verification with a viable Mobi-Gust 2.....	83
3.6	The recommendations from the applied aeolian research .....	84
3.6.1	Recommendations concerning the applied aeolian research .....	84
3.6.2	recommendations concerning Mobi-Gust 2 (POC supplement).....	84
	References.....	86
A	Sand Engine background.....	96

A.1	Building with Nature .....	96
A.2	Construction characteristics of the Sand Engine .....	97
A.3	Current characteristics of the Sand Engine.....	97
A.4	The Sand Engine is a supply limited system .....	97
A.5	Environmental conditions around the Sand Engine .....	98
B	Relevant air (flow) characteristics .....	102
B.1	Air properties for STP-conditions.....	102
B.2	Air compressibility .....	102
B.3	Mass and energy conservation.....	103
B.3.1	Continuity .....	103
B.3.2	Bernoulli.....	103
B.3.3	Applying mass- and energy conservation .....	104
C	The design Mobi-Gust 2 .....	106
C.1	Mobile wind tunnel system .....	106
C.1.1	The blowing fan .....	106
C.1.2	The speed controller .....	108
C.1.3	The horizontal- and vertical contraction .....	108
C.1.4	The honeycomb .....	111
C.1.5	The transition zone.....	113
C.1.6	The erosion zone.....	114
C.1.7	The sand trap .....	114
C.2	Wind gauging system .....	116
C.2.1	Wiring scheme of the hardware .....	116
C.2.2	Arduino sketch .....	116
C.2.3	Programming logic (summary of the Arduino sketch) .....	122
C.2.4	The adapted pitot tube formula .....	123
C.3	Power supply .....	125
D	Pipe flow analysis .....	129
E	Handling the pitot tubes.....	131
E.1.1	Levelling the pitot tube .....	131
E.1.2	Repositioning the pitot tube .....	132
E.1.3	Using a calliper .....	133
F	Anemometer .....	136
G	Fieldwork management.....	137
G.1	Preparation plan .....	137
G.1.1	Date selection .....	137
G.1.2	Packing list .....	137

G.1.3	Charging the electrical components.....	139
G.2	Measurement plan .....	139
G.2.1	Mobility .....	139
G.3	(Dis)Mount Mobi-Gust 2.....	146
G.3.1	Prepare the mobile wind tunnel .....	146
G.3.2	Prepare the wind gauge system .....	157
G.4	Experimental setup .....	158
G.4.1	Favourable conditions .....	158
G.4.2	Hampering conditions .....	161
H	Conducted field trips.....	163
H.1	Field trip 12-12-2023.....	163
H.2	Field trip 12-1-2024.....	163
H.3	Field trip 2-2-2024 .....	164
H.4	Field trip 14-2-2024.....	164
I	Results.....	165
I.1	Measuring frequency (Arduino) .....	165
I.2	Wind speed data.....	166
I.2.1	Power supply and wind gauging system.....	166
I.2.2	Wind speed vs. modular design .....	168
I.2.3	Velocity profiles.....	170
I.2.4	Wind speed data of the applied research .....	173
I.3	Erosion results.....	175
I.3.1	Field I .....	175
I.3.2	Field II .....	175
I.3.3	Field III.....	176
I.3.4	Lab I.....	179
I.3.5	Lab II.....	180
I.3.6	Lab III .....	183
I.3.7	Lab IV .....	184
I.4	Spray can calibration (used in lab III and IV).....	187
I.5	Grain Size Distribution (GSD) analysis .....	188
I.5.1	Dry sieve analysis guideline.....	188
I.5.2	An example of a sieve analysis .....	190
I.6	Moisture content.....	193
I.6.1	Field I, II and III.....	193
I.6.2	Lab III and IV .....	196





Part I  
General introduction

Part I  
General Introduction

## 1 General introduction

This chapter presents [part 1](#) of this report and regards a general introduction. In turn, the general introduction discusses the following five main topics: [§1.1](#) treats the main motivation to understand aeolian processes in coastal areas; [§1.2](#) will address the historical background on aeolian processes; [§1.3](#) discusses the coastal applicability of this fundamental theory; [§1.4](#) will clarify the research approach of this report; and finally [§1.5](#) shows the main research question and the structure of the report.

### 1.1 The drive to improve predictions on aeolian sand exchange

The Building with Nature philosophy is a sustainable approach to tackle hydraulic issues ([EcoShape, 2024](#)). In elaboration, Building with Nature concerns an interdisciplinary approach to design nature-based solutions that mitigate flood risk. On top, these solutions generally accommodate recreational services and nature development. Also, the solutions are usually context-specific, dynamic and harness natural forces as much as possible. Practical examples of Building with Nature projects concern pilots at the Houtrib Dike ([figure 3](#)), the Sand Engine ([figure 4](#)) and the Hondsbossche Dunes ([figure 5](#)). All mentioned pilots are located within The Netherlands and extensively involve coastal dunes.

Coastal dunes embody the Building with Nature approach in The Netherlands. The primary purpose of these sandy barriers is to mitigate flood risk ([Slootjes & Van der Most, 2016](#)). Yet, secondary functions may involve nature development, drinking-water resources or recreational activities ([Rijkswaterstaat, sd](#)). Coastal dunes are naturally composed of granular material and vegetation native to the area ([NIOZ, 2024](#)). The granular composition of coastal dunes also implies their dynamic shape; as well as their associated variable flood risk ([De Vries et al., 2012](#)). Coastal dunes are namely continuously (re)shaped by nature; where aeolian processes primarily control dune formation and -growth ([Bosboom & Stive, 2023](#)).

Sustainable coastal management is facilitated by accurate and robust aeolian predictions. In repetition, Building with Nature involves coastal dunes and exploits natural forces. In turn, wind driven processes might be used to build, maintain and reinforce sandy barriers ([Aarninkhof et al., 2010](#)). Consequently, aeolian processes are directly coupled to the variable flood risk of these coastal dunes. It is therefore crucial to understand the relation between wind conditions and coastal aeolian sand exchange. This report aims to better understand the mentioned relation; in order to stimulate sustainable coastal protection measures. This stimulus is particularly relevant as sustainable awareness is growing ([European Commission, N.d.](#)).



*Figure 3 – Houtrib Dike  
(EcoShape, 2024)*



*Figure 4 – Sand Engine  
(EcoShape, 2024)*



*Figure 5 – Hondsbossche Dunes  
(EcoShape, 2024)*



## 1.2 Exploring the historical context of aeolian transport

Already decades ago, [R.A. Bagnold \(1941\)](#) revolutionized the vision on windblown sand. Bagnold suggested the idea of sand particle motions as a result of wind shear. Also, he explored the effect of mobilized sand grains on the surrounding wind flow. Bagnold experimentally verified his concepts in a laboratory wind tunnel ([Bagnold, 1936](#)) & ([Bagnold, 1937](#)). On top, Bagnold conducted field experiments in the Great Sand Sea of the Libyan Desert ([Bagnold, 1941](#)). [Figure 6](#) and [figure 7](#) respectively show the whereabouts and the appearance of the mentioned site.



Figure 6 – The location of the Libyan Desert  
(Encyclopædia Britannica, N.d.)



Figure 7 – The Great Sand Sea of the Libyan Desert  
(Marsaalam tours, N.d.)

[R.A. Bagnold \(1941\)](#) found a third-power relation to describe aeolian transport rates ( $q$  [ $kg/m/s$ ]); as shown in [equation 1](#). This model depends on the density of air ( $\rho_a$  [ $kg/m^3$ ]), the gravitational acceleration ( $g$  [ $m/s^2$ ]), the median grain diameter ( $d_{50}$  [ $m$ ]), a reference grain diameter ( $D$  [ $m$ ]) of standard  $250$  [ $\mu m$ ] sand; and the shear velocity ( $u^*$  [ $m/s$ ]). The model can be fitted to data by an empirical constant ( $C_b$  [–]); which is linked to the grading of the sand in question.

1)

$$q = C_b \frac{\rho_a}{g} \sqrt{\frac{d_{50}}{D}} (u^*)^3$$

The work of R.A. Bagnold inspired many others and triggered various follow-up studies. Consequently, Bagnold's fundamental theory got validated further; while his formula ([equation 1](#)) got reformulated and extended numerous times. The extensions primarily involved tuning the empirical constant to specific circumstances. The work of [Kawamura \(1951\)](#), [Kadib \(1965\)](#) and [Sørensen \(2004\)](#) provide just a small list of the available follow-up studies. As will be explained, these studies have in common that they are applying to similar systems ([§1.3](#)).

## 1.3 The coastal problem involving classical aeolian theory

Bagnold-type models ([§1.2](#)) generally show limited applicability to coastal situations ([Sherman & Li, 2012](#)). To clarify, the third-power relations usually overpredict measured coastal transport rates. The deviations are related to the small-scaled variability in these measured rates; while the models generally use spatiotemporally invariant conditions ([Barchyn et al., 2014](#)). In elaboration, the wind speed is often the only variable ([De Vries et al., 2012](#)) and [figure 8](#) on the next page shows why this might be problematic along coasts. To clarify, it is arguable that wind conditions will not be very different across the width of this sandy beach. Yet, a notable cross-shore gradient in aeolian sand transport is visible. While the available fundamental theory ([§1.2](#)) shows limited applicability in coastal settings, it is of course not incorrect. After all, the theory is experimentally verified extensively. Actually, the theory is enclosed by a greater understanding on aeolian processes.

## Part I General introduction



Figure 8 – Considerable cross-shore sand transport differences under similar wind conditions (De Vries et al., 2022)

The limited coastal applicability of R.A. Bagnold's (1941) theory is clarified by introducing capacity- and supply limited transport. As Bagnold suggested, the wind speed greatly defines the capacity of the wind to transport granular material (equation 1; §1.2). Capacity limited transport occurs if the instantaneous transport rate approaches the transport capacity rate (De Vries et al., 2022). Consequently, a varying wind speed triggers a varying instantaneous transport rate. In contrast, supply limited transport happens if the instantaneous transport rate significantly differs from the transport capacity rate (De Vries et al., 2022). Consequently, varying wind speeds may not always produce varying instantaneous transport rates. To clarify, the transport capacity rate might be unreachable if the transport is limited by sand supply (De Vries et al., 2014). A system might be capacity- or supply limited, depending on sand availability (Hoonhout, 2017). For example, a sandy arid environment can be classified as a capacity limited system; as sand is abundant and available. In contrast, a sandy coastal environment can be seen as a supply limited system; as sand is (far) less abundant and available.

R.A. Bagnold (1941) thus actually defined a transport capacity formula by measuring in capacity limited conditions (§1.2). In turn, this clarifies why the model generally overpredicts coastal transport rates. For convenience, equation 2 repeats equation 1 (§1.2) in terms of wind speed. Equation 2 emerges after applying Prandtl's rough surface law (Bagnold, 1941). Notice also how the transport rate ( $q$  [kg/m/s]) is written as the transport capacity rate ( $q_c$  [kg/m/s]). Equation 2 uses the wind speed measured at a particular height ( $u_z$  [m/s]). Next, there is a critical velocity ( $u_c$  [m/s]) below which no transport occurs. This threshold velocity is amongst others dependent on the density of sand. Equation 2 furthermore includes a factor ( $\alpha$  [–]) that is fully written in equation 3. This factor converts the wind speed measured at a particular height ( $z$  [m]) to the near bed wind speed. This factor takes a measure for the surface roughness ( $k'$  [m]) into account.

$$2) \quad q_c = \alpha C_b \frac{\rho_a}{g} \sqrt{\frac{d_{50}}{D}} (u_z - u_c)^3$$

$$3) \quad \alpha = \left( \frac{0.174}{\log\left(\frac{z}{k'}\right)} \right)^3$$

## Part I

### General introduction

Supply limitations can arise from various sources. For example, the scale of the system may already prevent transport rates from reaching capacity conditions; as the available sand might run out. In elaboration, sandy shores are generally (much) smaller than sandy deserts. The difference in scale becomes clear from comparing [figure 3](#), [figure 4](#) and [figure 5](#) (§1.1) with [figure 7](#) (§1.2). The smaller coastal scales might pose fetch related supply limitations ([De Vries et al., 2012](#)). These limitations arise when the critical fetch exceeds the available fetch. The critical fetch involves the distance over which transport rates are developing. Just from an inertial viewpoint it is evident this development is required. On the one hand, the critical fetches rely on sediment properties and environmental conditions; which will be treated shortly. On the other hand, the available fetches may depend on beach geometry and wind angle ([Bauer & Davidson-Arnott, 2002](#)).

Supply limitations arise from sand properties. For example, sand mass ( $m [kg^1]$ ) and -size ( $d [m^1]$ ) play a role ([De Vries et al., 2012](#)); as sand density logically influences the susceptibility to movements. On top, also sand shape is important ([Rice, 1991](#)); as it both affects the susceptibility to movements, as well as particle trajectories and -impacts.

Environmental conditions may also cause supply limitations. Besides the mentioned wind conditions; other spatiotemporally variable aspects can be of importance. Moisture content can for example limit sand supply ([Davidson-Arnott et al., 2008](#)); as grains become more cohesive ([Van Rijn, 2023](#)). In turn, many aspects influence the moisture content. Examples involve humidity, precipitation, evaporation, (varying) water levels and/or beach elevation. Next, isolating layers of snow or hail, as well as frost in general, might pose supply limitations ([De Vries et al., 2022](#)). Yet, the sand surface can also be shielded by salt crusts. ([Pye, 1980](#)). These crusts form when sand surfaces dry after being wettened by saline waters. Next, (beach) armouring processes can have an impact on sand supply as well. For example, the sand surface might be armoured by shells ([McKenna Neuman et al., 2012](#)); or other non-erodible materials like pebbles ([Hoonhout & de Vries, 2019](#)). The sand surface can also armour itself through sorting processes ([Uphues et al., 2022](#)). Finally, flora and fauna may have an impact on sand supply as well. For example, the sand bed might be protected by vegetation ([Wasson & Nanninga, 1986](#)); or the sand bed is manipulated by benthos ([Winterwerp et al., 2022](#)).

Accounting for supply limitations is possible through using advection schemes. One of the novel models that uses this technique is called Aeolis ([De Vries et al., 2024](#)). Aeolis is an open-source, process-based, numerical model to simulate aeolian processes. Aeolis uses an advection scheme to model the spatiotemporal exchange of sand; from place to place and between the bed and the air. [Equation 4](#) shows such a simplified one-dimensional advection scheme ([De Vries et al., 2014](#)). The local concentration flux in the air ( $h \cdot \partial c / \partial t [kg/m^2/s]$ ) is determined from advection along a one-dimensional domain ( $\zeta u_w h \cdot \partial c / \partial x [kg/m^2/s]$ ). At the same the bed and the air may exchange sand by means of erosion ( $E [kg/m^2/s]$ ) and deposition ( $D [kg/m^2/s]$ ). [Equation 5](#) provides the relation between the sand concentration ( $c [kg/m^3]$ ) and the sand transport rate ( $q [kg/m/s]$ ). This relation depends on the wind speed ( $u_w [m/s]$ ), the height of the transport layer ( $h [m]$ ); and a factor ( $\zeta [-]$ ) that accounts for the speed difference between sand and air. Next, the model uses a Bagnold-type formulation (e.g., [equation 2](#) on the previous page) to calculate the transport capacity rate. Yet, the model also accounts for the amount of erodible material at the bed and the supply rate from the bed. Consequently, the Aeolis model is able to produce instantaneous transport rates below capacity conditions.

4)

$$h \frac{\partial c}{\partial t} + \zeta u_w h \frac{\partial c}{\partial x} = E - D$$

5)

$$q = \zeta u_w c h$$



## 1.4 Shifting the attention towards aeolian surface erodibility

Sand surface erodibility may express supply limitations. After all, the majority of the mentioned limitations originate from the bed (§1.3). The erodibility is defined as the susceptibility of a surface to erosion (Panagos et al., 2014). In simple terms, the erodibility describes the ability of the surface to supply grains to the air flow. If this ability is high, the supply to the air is probably high as well (and vice versa). As mentioned, many different aspects (§1.3) affect this ability, by altering the wind speed threshold after which erosion occurs (Van Rijn, 2023). Overall, sand surface erodibility appropriately describes supply limitations; just like novel models realize (§1.3). In turn, measuring this erodibility may improve those models.

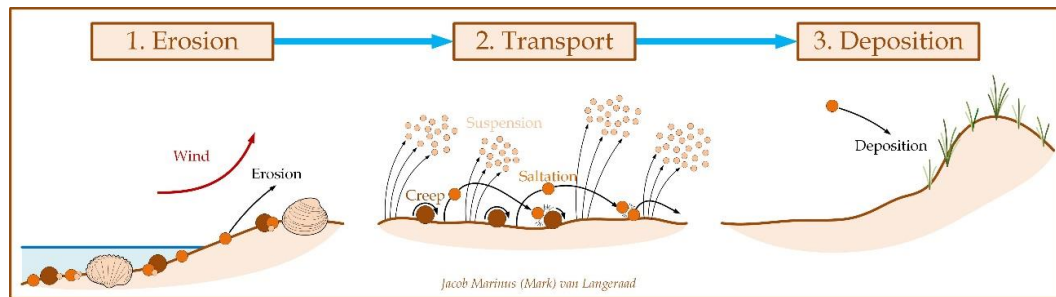


Figure 9 – Erosion, transport and deposition; figure partly taken from (Uphues et al., 2022)

Sand surface erodibility is measurable through generating erosion. The focus is thus shifted from aeolian transport to -erosion; i.e., the left part of figure 9. In order to generate erosion, a specialized aeolian erosion device will be developed and constructed. The approach is thus similar to the one of R.A. Bagnold (§1.2). Yet, this time the erosion device will be mobile as well. Consequently, enabling in-situ measurements in supply limited conditions. Ultimately, to investigate the erodibility of the sand surface (see part 3). The erodibility can for example be quantified through measuring wind speed thresholds for the initiation of motion (Sirjani et al., 2019). Such a threshold can be used in transport formulas (e.g., equation 2; §1.3). Yet, spatiotemporal variations in sand bed erodibility are also directly measurable. In clarification, sand supply dominates the exchange of sand in supply limiting conditions (§1.3). Consequently, varying wind speeds may not always cause varying erosion fluxes. Or controlled wind speeds may not always result in controlled erosion fluxes. Practically this implies that constant wind speeds can reveal temporal variations in sand bed erodibility. Performing tests at various locations also reveals the spatial dependency.

The mentioned specialized mobile erosion device will be deployed on the Sand Engine (figure 10; on the next page). The Sand Engine involves a mega nourishment along the Holland Coast, near The Hague (The Netherlands). The main reason to attend the Sand Engine involves it being a supply limited system (Hoonhout & De Vries, 2017). To clarify, measured transport rates are generally 65 [%] below the transport capacity of the wind. On top, there are three additional reasons to attend the Sand Engine. Firstly, the area of the Sand Engine is vast (Google, 2022); and its mean elevation reaches above mean sea level (AHN, 2023). Consequently, the site is majorly shaped by aeolian processes. On top, the scale of the Sand Engine implies that there will be plenty of room to conduct erosion experiments. Secondly, the distance between the Sand Engine and Delft University of Technology only concerns about 20 [km] by road (Google, 2022). This relatively short distance facilitates performing single-day expeditions; starting and ending on the university. Lastly, previous aeolian research that was initiated by Delft University of Technology focussed on the Sand Engine as well (TU Delft, 2020). Consequently, this report builds on existing knowledge. More details on the Sand Engine can be found in appendix A.

## Part I General introduction

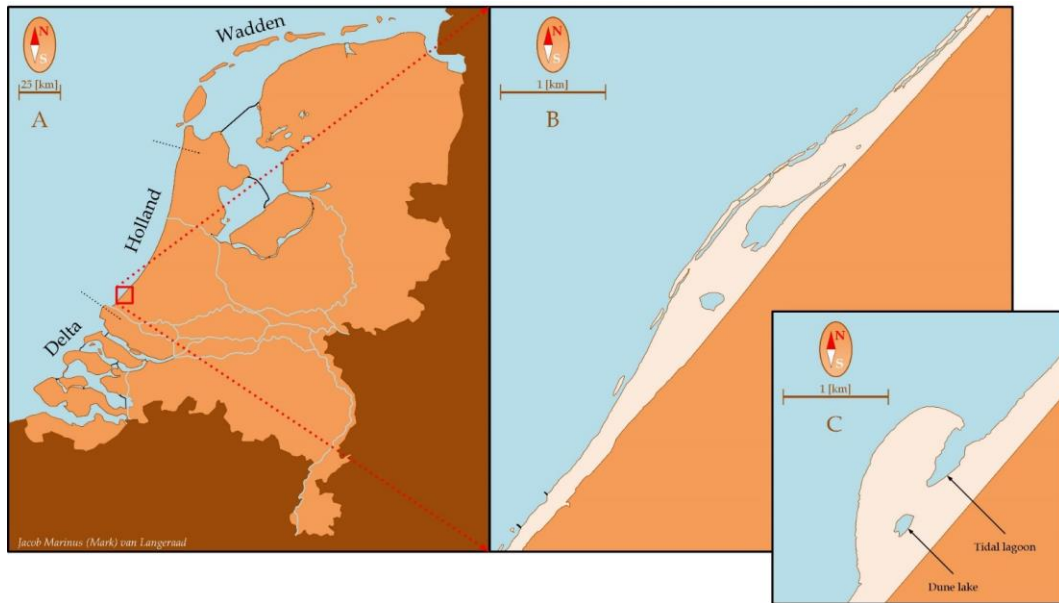


Figure 10 – Map showing The Netherlands (A), the Sand Engine in 2022 (B) and just after construction in 2011 (C)  
Adapted from (Compendium voor de Leefomgeving, 2021), (Google, 2022) and (Hoonhout & de Vries, 2017)

### 1.5 The main research question and the report structure

This report has two major stages. First, a specialized mobile aeolian erosion device will be designed and tested. Secondly, this device will be used to perform applied aeolian research. Both stages check the viability of this device. Yet, stage two also tries to learn on coastal aeolian processes. The device will namely be deployed to explore the following research question.

*The aeolian erosion process on sandy beaches,  
is solely determined by wind speed and does not rely on surface erodibility.*

Since this report concerns multiple stages, it is divided into multiple sections. The current part treats the general introduction, which applies to all coming sections. Next, [part 2](#) of this report checks the viability of the mentioned mobile aeolian erosion device. This check involves a dedicated Proof Of Concept (POC). [Part 3](#) of this report will then treat the applied research using this device.

The Proof Of Concept (POC; [Part 2](#)) has multiple subsections. [Part 2](#) starts with a project outline, which acts as a small introduction to the POC ([§2.1](#)). Amongst others, this project outline provides some background and the project criteria. Next, the methodology will be discussed ([§2.2](#)); which is split into a design section ([§2.2.1](#)) and a performance section ([§2.2.2](#)). To clarify, the performance section describes the experiments that are used to check the performance of the developed device. As the design and the performance are intertwined, they will be discussed simultaneously from the methodology onward. After the methodology there will be a results section ([§2.3](#)) and a discussion section ([§2.4](#)). [Part 2](#) is finalized by a conclusion ([§2.5](#)) and some recommendations ([§2.6](#)).

The applied research ([part 3](#)) also has multiple subsections. [Part 3](#) begins with a small recap on [parts 1](#) and [2](#) ([§3.1](#)). The purpose of this recap is to facilitate readers with little time. Next, the research approach will be discussed ([§3.2](#)). In turn, the involved results will be presented ([§3.3](#)); and discussed ([§3.4](#)). [Part 3](#) will finally end in its conclusion ([§3.5](#)) and some advices ([§3.6](#)).

# Part II

## Proof Of Concept (POC)

### Mob-Gust 2

## 2 Proof Of Concept (POC): Mobi-Gust 2

This chapter shows [part 2](#) of this report and considers the Proof Of Concept (POC) of Mobi-Gust 2. This POC is subdivided into six main topics: [§2.1](#) provides the project outline; [§2.2](#) clarifies the methodology; [§2.3](#) presents the generated results; [§2.4](#) treats the discussion; [§2.5](#) addresses the associated conclusions; and finally [§2.6](#) presents the recommendations.

### 2.1 Project outline

The project outline of this Proof of Concept (POC) starts with the project definition. The general introduction ([part 1](#)) already touched upon the following four topics: the motivation of this project ([§1.1](#)); the historical background ([§1.2](#)); the problem statement ([§1.3](#)); and finally the research approach ([§1.4](#)). In repetition, it is desired to develop a mobile aeolian erosion device. As the name suggests, the device should be able to generate (measurable) aeolian erosion. To this end, the device must set air in motion; and in turn this moving air must mobilize a sand surface. The eroded material may not leave the system and must be captured to allow measuring it. Logically, wind conditions must be quantified as well; as the erosion process is wind driven. Finally, the device must be mobile in order to explore the erodibility of in-situ sand surfaces. Overall, a mobile wind tunnel system and a wind gauging system are required ([§2.2.1](#)). The two mentioned systems are collectively called Mobi-Gust 2. Designing such an aerodynamic system requires knowing the governing air properties ([appendix B](#)). After designing and testing Mobi-Gust 2, it will be used in dedicated aeolian research ([part 3](#)).

The design of Mobi-Gust 2 builds on the design of a pre-existing prototype. The design of Mobi-Gust 2 can thus be seen as an evolution. This pre-existing prototype is called Mobi-Gust 1; and also follows from research conducted at Delft University of Technology ([De Wilde, 2020](#)). On top, Mobi-Gust 1 got deployed in a field expedition ([Bangen & Dijkstra, 2020](#)). The design and the deployment of Mobi-Gust 1 provided valuable insights for the development of Mobi-Gust 2.

The mobile wind tunnel system of Mobi-Gust 2 is greatly inspired by Mobi-Gust 1. For example, the (12-volt) blowing fan of Mobi-Gust 1 will be re-used. This choice benefits finances and mobility; while being environmentally friendly as well. To clarify, the re-usage omits purchasing a new (stronger) wind generation system, as well as large and polluting aggregators. Yet, re-using the fan also implies that the air within the system is not pulled. As air suction provides better aerodynamic properties ([Çengel & Cimbala, 2014](#)); it might also pose problems in view of trapping the eroded material. To clarify, sediment trapping requires lowering the wind speed. In turn, wind speed lowering can be achieved in several ways. The wind speed can for example be lowered by increasing the cross-sectional size as mass is conserved ([White, 2011](#)). This expanding flow further reduces its speed by additional energy losses ([Çengel & Cimbala, 2014](#)). Yet, energy dissipation can also be invoked directly through adding obstacles into the flow ([Chassagne & Van den Bremer, 2021](#)). A plenum and/or screens might be suitable to achieve these lower wind speeds; as was learned from the staff of the low-speed laboratory of Delft University of Technology. Yet, those same conversations revealed that a (12-volt) pulling fan might be too weak for the desired system. For example, the preceding research (i.e., involving Mobi-Gust 1) recommended applying a transition zone. This additional component will be explained later on ([§2.2.1.5](#)); but most importantly heightens the resistance within the aerodynamic system ([Çengel & Cimbala, 2014](#)). The fan needs sufficient pressure capacity to overcome this resistance. On top, this capacity must be high enough to generate winds that actually onset erosion; while around the fan the wind speed must again be low enough to trap the sediment. Overall, merging these conflicting interests seemed to be impossible, so that the selected fan was retained.



## Part II

### Proof Of Concept (POC): introduction

Mobi-Gust 1 involved a venturi-style wind tunnel of the open-return type. The mobile wind tunnel system of Mobi-Gust 2 will also employ the venturi effect in an open-return geometry. To clarify, the venturi-effect concerns trading pressure for velocity in a gradually shrinking cross-section (Chassagne & Van den Bremer, 2021). Next, the open-return geometry has no bends (NASA, 2021); which is beneficial in view of energy losses (Çengel & Cimbala, 2014). So, the mentioned choices facilitate the (relatively weak) blowing fan. On top, the open-return geometry confines the air flow. This confinement is important for two reasons. Firstly, confining the air flow leads to the generation of wind shear (Uijttewaal, 2022). In turn, the associated (bed) shear stresses can be used to erode the sand surface. Secondly, the confinement of the air flow also implies the confinement of the eroded material.

Besides generating and confining an air flow, it is desired to measure the wind speed. Gauging the wind speed is logically important as the erosion process is wind driven. Just like the mobile wind tunnel system, also the wind gauging system is inspired by Mobi-Gust 1. The previous study used a pitot tube to quantify the wind speed (De Wilde, 2020). Such a pitot tube measures differential pressure (White, 2011). In turn, Bernoulli's principle can be used to deduce the wind speed from this differential pressure (Çengel & Cimbala, 2014). The previous study also considered (and rejected) cup-like anemometers; as the involved contact surfaces were deemed too be too large (De Wilde, 2020). Yet, there are more arguments to retain pitot tubes. For example, pitot tubes are relatively robust; unlike techniques such as hot wire anemometry (Omega Engineering, N.d.). Also, pitot tubes are relatively inexpensive, especially when compared to acoustic- or laser doppler techniques (Uijttewaal, 2022). Overall, pitot tubes are relatively small, sturdy and cost effective. Finally, the pitot tubes will be used in a digital setup (Hrisko, 2019).

The project role of this report is primarily conceptual and exploratory. In elaboration, the staff of Delft University of Technology will take care of finances and construction works. The role of this report is to provide a conceptual design for the mobile wind tunnel system (§2.2.1); and to explore the systems performance after it got realised (§2.2.2). The mentioned conceptual design will be transformed into a constructable design by mister P. van der Gaag (i.e., laboratory- and fieldwork supervisor & laboratory- and fieldwork coordinator). Mister P. van der Gaag thus created the final design drawings that are added to this report (§2.2.1). These final design drawings are handed to mister A. Doorn (i.e., laboratory technician); and he ensures that the mobile wind tunnel system will be built. DEMO (Dutch: 'Dienst Elektronische- en Mechanische Ontwikkeling') will help mister A. Doorn in creating some of the complex (curved) shapes. All the involved financial aspects are managed by dr. ir. S. de Vries (main supervisor & associate professor Coastal Engineering). So, even the parts of the wind gauging system will be arranged. Overall, the explained role distribution clarifies why this project outline does not include key aspects of a project scope (e.g., costs).

The development of Mob-Gust 2 involves more than just one project goal. The goals can be summarized into four aspects. In elaboration, the main goals comprise of usefulness, reliability and controllability. Additionally, sustainability (i.e., financial-, societal- and environmental aspects) is of importance. The mentioned goals are unified in the following sub-research question:

*Is it possible to sustainably design a useful, reliable and controllable mobile wind tunnel system; in order to conduct aeolian erosion measurements?*

The project goals might be broad, but practical examples can easily be formulated. For example, the project goals can be linked to the project definition (i.e., explained at the beginning of this project outline). Usefulness may for example include the ability to generate measurable aeolian erosion; or the mobility of the wind tunnel system. Next, reliability may involve the aeolian erosion process itself; e.g., concerning the wind conditions or the sand tightness of the system. Yet, reliability may also include the accurateness and robustness of the wind gauging system. Next, controllability may include the wind speed and/or the erosion process. Lastly, sustainability may involve the type of power supply; or the durability of the applied materials. Of course, many more examples can be produced; yet this list functions just as an example.

## 2.2 The methodology to design and test Mobi-Gust 2

This section discusses the methodology of this Proof of Concept (POC). Both the design and the performance of Mobi-Gust 2 will determine whether the project goals will be reached or not. Design and performance can thus be seen as two stages; and this section is subdivided accordingly to explain both clearly. Firstly, the design of Mobi-Gust 2 will be clarified (§2.2.1). Secondly, the performance experiments will be outlined (§2.2.2). Beyond the methodology, the design and the performance are considered together; as the design and the performance are intertwined.

### 2.2.1 The design of Mobi-Gust 2

The first part of the methodology concerns the design of Mobi-Gust 2. Mobi-Gust 2 is a tailored toolbox that can be used to conduct aeolian research. Mobi-Gust 2 consists of a mobile wind tunnel system and wind gauging system (figure 11). The design is steered by the project criteria (i.e., usability, reliability and controllability; but also sustainability). The design is discussed through eight main topics: §2.2.1.1 provides general remarks on modularity and sturdiness; §2.2.1.2 considers the mobilisation of air; §2.2.1.3 clarifies how the air flow is accelerated; §2.2.1.4 shows how the air flow is conditioned; §2.2.1.5 describes how (enhanced) erosion is generated; §2.2.1.6 clarifies how to catch and collect the eroded material; §2.2.1.7 explains how the wind speed is measured; and lastly §2.2.1.8 concerns the power supply.

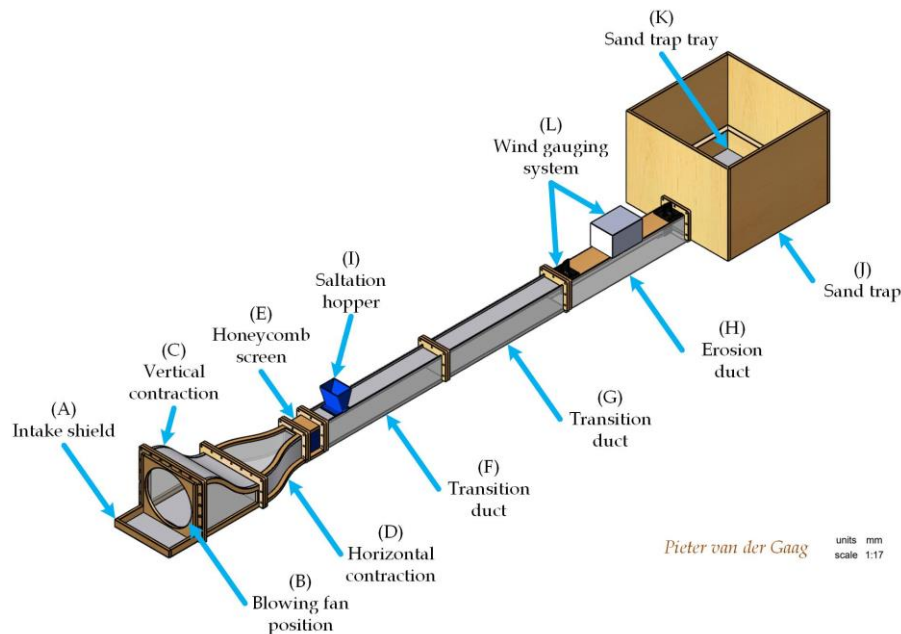


Figure 11 – Mobi-Gust 2 and its components  
(Van der Gaag, 2024)

#### 2.2.1.1 Modularity and sturdiness

Mobi-Gust 2 has a modular design. To clarify, the mobile wind tunnel system is splittable into smaller parts. This modular design preserves the portability of Mobi-Gust 2, while aerodynamic functionality can easily be added. On top, the modular design enables specialized repairs or replacements of specific parts. The main components of Mobi-Gust 2 concern: a vertical- and horizontal contraction, a honeycomb, a transition zone, an erosion zone; and a sand trap (figure 11). Unspecified components are generally inseparable; but each component will be explained in the coming sections. The connections between the components are provided by flanges and nuts, bolts and washers. All connections are similar and are operated by basic tools (e.g., spanners). Even unexperienced people are capable of correctly (dis)mounting and configuring Mobi-Gust 2, through using specialized manuals (appendix G.3).

## Part II

### Proof Of Concept (POC): methodology

The mobile wind tunnel system is created from relatively light and durable materials. The used materials involve timber, aluminium, acrylic glass; and 3d-printed plastic. Most of those materials are relatively low in density (BPS, N.d.). Even the densest material, i.e., aluminium, is still a low-density metal. The components mainly involve shells of thin plates, ensuring a lightweight construction. Experience confirmed that a single person can easily handle the separate parts. Additionally, the acrylic glass walls enable observing the processes within the mobile wind tunnel system. Next, the materials are also relatively durable, as they are strong and (made) beach resistant. To clarify, most materials have beneficial corrosion properties (Lets Talk Science, 2020). Even though aluminium is corrodible, it does not rust, as it forms a protective oxide layer (All Metals Fabrication, 2022). Even the used timber is treated for saline environments (Modinex, N.d.).

The wind gauging system involves the most fragile parts. Yet, the electrical hardware is secured and protected in a shakeable and splash-proof plastic box. Amongst others, the wind gauging system involves (pressure) sensors. Sensors are generally highly sensitive to various influences (MPS, N.d.). To this end different protective measures are put in place, which are detailed in §2.2.1.7.

#### 2.2.1.2 Mobilizing air

A blowing fan creates the air flow within Mobi-Gust 2 (B in figure 11 & figure 12). The air flow results from a pressure differential between the up- and downwind boundary of the mobile wind tunnel system (Çengel & Cimbala, 2014). To clarify, the fan pushes the air from the upwind end, towards the downwind end that is open. In other words, the fan raises pressure at the upwind end, while the downwind end approaches atmospheric pressure. The fan retains this pressure differential as it overcomes the resistance of the system (e.g., friction). Consequently, air keeps flowing from high to low pressure. Yet, the ability of the fan to overcome resistances is finite, since the fan has a certain pressure capacity. For reference, appendix C.1.1 shows the discharge-pressure relation of the fan. Other fan properties are shown in table 2. On top, the power transmission to the fan can be varied with a speed controller (figure 12). Consequently, the air flow within Mobi-Gust 2 is adjustable as well. The used fan was a constraint (§2.1); and requires measures to stabilize the air flow (§2.2.1.3). To clarify, previous research with the prototype (i.e., Mobi-Gust 1) showed that the fan produces an unnatural spiral flow (De Wilde, 2020).

Table 2 – VA18-AP70/LL-86S characteristics (Venus, 2024)

Type	Voltage [V]	Amperage [A]	Fan size [mm]	Air flow [m <sup>3</sup> ]	Weight [g]
Blowing	12.0	17.4	385.0	3,450.0	2,570.0



Figure 12 – VA18-AP70/LL-86S blowing fan (SPAL Automotive, 2024) & speed controller (RS, 2024)

Since the fan pushes air forward, air is replaced from outside. Previous research with the prototype (i.e., Mobi-Gust 1) showed that this air supply can be sand-laden (Bangen & Dijkstra, 2020). To this end, the suction of sand is mitigated through the addition of an intake shield (A in figure 11). This intake shield essentially concerns a bottom plate covering the sand-suction source. The intake shield additionally has removable walls; for further shielding.

### 2.2.1.3 Accelerating the air flow

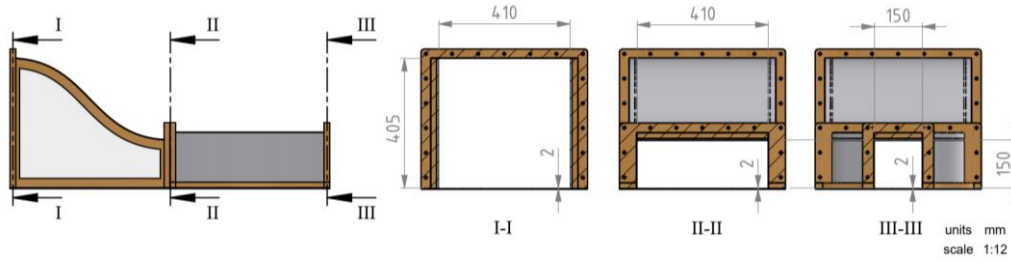


Figure 13 – The vertical- and horizontal contraction;  
Left = side view and right = cross-sections;  
(Van der Gaag, 2024)

The air flow is accelerated in a contraction (C/D in figure 11 & figure 13), by means of the venturi effect (Çengel & Cimbala, 2014). In clarification, the decreasing cross-sectional area leads to the conversion of pressure into speed. This conversion is governed by mass- and energy conservation. Mass is conserved since air only enters and leaves the contraction through the up- and downwind end. Energy is conserved as the air flow is incompressible (appendix B.2) and steady for a specific fan setting; while the contraction is short (appendix C.1.3.1) and gradually curved (appendix C.1.3.2). The acceleration of the air flow can be shown by applying Continuity (equation 6) and Bernoulli (equation 7); i.e., constant mass- and energy balances (Voorendt, 2022). The balances are evaluated between the up- (1) and downwind (2) boundary of the contraction; along a streamline of constant elevation ( $z_1 \equiv z_2$ ). The balances depend on the air speed ( $u_a$  [m/s]), the flow area ( $A_a$  [m<sup>2</sup>]), the static air pressure ( $p_a$  [N/m<sup>2</sup>]); and the density of air ( $\rho_a$  [kg/m<sup>3</sup>]). So, as the flow area decreases ( $A_{a,1} > A_{a,2}$ ), pressure is converted ( $p_{a,1} > p_{a,2}$ ) into speed ( $u_{a,1} < u_{a,2}$ ).

$$\begin{aligned} 6) \quad & u_{a,1} A_{a,1} = u_{a,2} A_{a,2} \\ 7) \quad & p_{a,2} - p_{a,1} = \frac{\rho}{2} (u_{a,1}^2 - u_{a,2}^2) \end{aligned}$$

The gradually curved contraction accelerates the air flow to the design wind speed. Natural winds of 5-12 [m/s] usually trigger coastal aeolian transport (Arens, 1996). The design wind speed (i.e., 15 [m/s]) exceeds that upper limit. As explained, mass- and energy are conserved during the acceleration. Now, imagine that the contraction is ideal and additionally the only component present in the system; while outflow losses are non-existent. In this fictitious case, the wind speed at the exit of the contraction follows from Continuity only. Equation 8 repeats the Continuity equation (i.e., equation 6); which is partly rewritten in terms of discharge ( $Q$  [m<sup>3</sup>/s]). Besides the claim that the contraction is ideal, it is certainly not the only component present in the system. For example, friction losses occur as the air traverses through other components (Çengel & Cimbala, 2014). On top, there will be an outflow loss as the air exits the system (White, 2011). These losses guarantee that the design wind speed, as calculated with equation 8, will never be reached. As a practical solution the Continuity equation (i.e., equation 8) is fitted with a loss coefficient ( $C_L$  [-]); see equation 9. This coefficient is defined as the ratio between the achieved wind speed ( $u_{a,a}$  [m/s]) and the design wind speed ( $u_{a,d}$  [m/s]); see equation 10. This coefficient accounts for losses of the entire system. Operational data of the prototype (i.e., Mobi-Gust 1) is used to provide an estimate for this factor (De Wilde, 2020). The involved calculations are shown in appendix C.1.3.3.

$$\begin{aligned} 8) \quad & u_{a,2} = \frac{Q_{a,1}}{A_{a,2}} \\ 9) \quad & u_{a,2} = C_L \frac{Q_{a,1}}{A_{a,2}} \\ 10) \quad & C_L = \frac{u_{a,a}}{u_{a,d}} < 1 \end{aligned}$$



## Part II

### Proof Of Concept (POC): methodology

Although the contractions are curved, they connect rectangular cross-sections (figure 13). The shape of the ducts is similar to the wind tunnel used by R.A. Bagnold (1936) & (1937). On top, the flat surfaces facilitate mounting equipment on them (e.g., the wind gauging system). The contraction is split into a vertical- and horizontal section to facilitate construction. To clarify, it is quite the task to create an asymmetrically curved component that shrinks along two axes.

#### 2.2.1.4 Conditioning the air flow

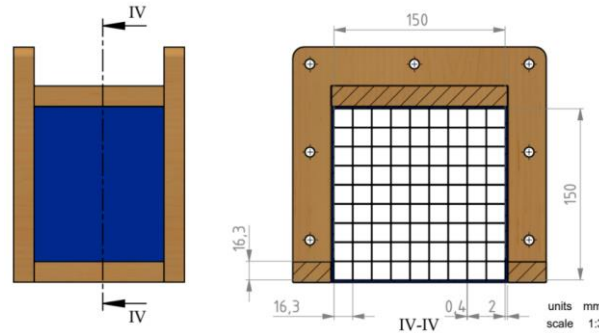


Figure 14 – The honeycomb screen;  
Left = side view and right = cross-section;  
(Van der Gaag, 2024)

The spiralling air flow (§2.2.1.2) is mitigated in a honeycomb (E in figure 11 & figure 14). A honeycomb is basically a cross-section divider (figure 14) that straightens the air flow (Scheiman & Brooks, 1981). To clarify, the openings of the honeycomb primarily reduce perpendicular velocity components. Yet, a honeycomb is only effective when it has openings within a specific range of length-to-diameter ratios; see equation 11. Obeying this optimal range results in an effective honeycomb (figure 15); regardless of the opening-shape (Kulkarni et al., 2011).

11)

$$\frac{L}{D} = 8 \text{ to } 10$$

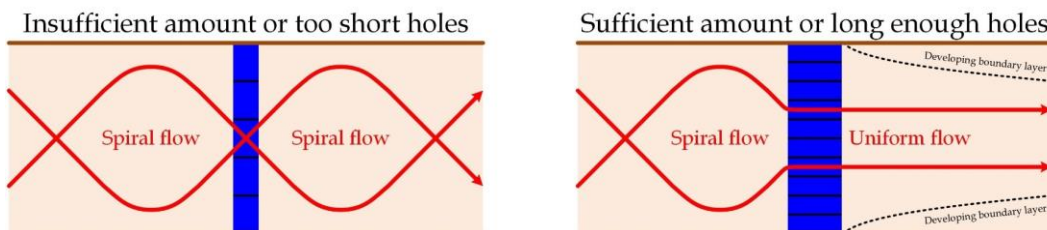


Figure 15 – Top view of an inefficient honeycomb screen (left) vs. an efficient honeycomb screen (right)

The geometry of the honeycomb is limited by abilities of the 3D-printer. Again, the honeycomb should mitigate the mentioned large scale spiral motions. As (small scaled) turbulence is not the primary target, the openings of the honeycomb can be as large as practically possible. Consequently, the honeycomb has less dividers; which minimizes flow blockage (i.e., resistance). Overall, the opening-geometry follows from selecting an optimal length-to-diameter ratio close to the mean (equation 11). Additionally, the maximum printing length of the 3D-printer, as well as the involved printing duration, defined the final design (appendix C.1.4). As design rules are obeyed, the honeycomb should effectively mitigate the spiralling flow and onset flow development.



## Part II

### Proof Of Concept (POC): methodology

The straightened air flow requires further conditioning in a transition zone (F/G in figure 11 & figure 17 on the next page). This additional conditioning is related to the development of the (turbulent) air flow (Çengel & Cimbala, 2014). To facilitate explanations, it is assumed that flow velocities are approximately uniform downwind of the honeycomb. Wall friction will impact this velocity distribution (Chassagne & Van den Bremer, 2021). The region of affected flow velocities is called the turbulent boundary layer. Just by considering inertia, it is clear that boundary layers cannot be instantly developed. The evolution of boundary layers can be summarized into three main stages (Uijtewaal, 2022). First, boundary layers emerge from all boundaries parallel to the flow, e.g., the walls, roof and bottom (i.e., where friction is maximum); secondly, the boundary layers grow into the duct by momentum transfer; and finally, the boundary layers meet along the centreline of the duct (i.e., where friction is minimum). The flow is nearly developed after the boundary layers converge. Two reasons clarify why a nearly developed flow is desirable. First of all, the boundary layers start very thin. Consequently, the velocity gradients ( $du/dz$  [1/s]) and the associated bed shear stresses ( $\tau_b$  [N/m<sup>2</sup>]) are initially very high as well (White, 2011). The formation of scour is close to unmitigable; but these relatively high bed shear stresses will dig an even bigger one (Schierreck, 2019). Second of all, a developed (turbulent) flow is associated with more generic flow properties. To clarify, a developed flow, that remains undisturbed, is characterised by a rather stable logarithmic velocity profile; equation 12 (Uijtewaal, 2022). This vertical velocity profile ( $u(z)$  [m/s]) depend on the friction velocity ( $u^*$  [m/s]), the Von Karman constant ( $\kappa \cong 0.41$  [–]), the elevation ( $z$  [m]) and an integration constant related to the roughness of the boundaries ( $z_0$  [m]). As the velocity profile remains rather stable, the velocity gradients and the associated bed shear stresses remain relatively constant as well. A developed (turbulent) flow is thus more predictable. However, the cross-section that is experienced by the air flow needs to be as homogeneous as possible. Flow disturbances namely cause a (partial) redevelopment (Çengel & Cimbala, 2014). Examples of disturbances include variations in cross-sectional shape and -size; as well as a varying boundary roughness. Figure 16 shows a 2D schematical sideview of a developing flow in a duct; between the bottom and the symmetry axis. If the upper boundary has similar roughness to the lower one; the velocity profile will be symmetric along the symmetry axis.

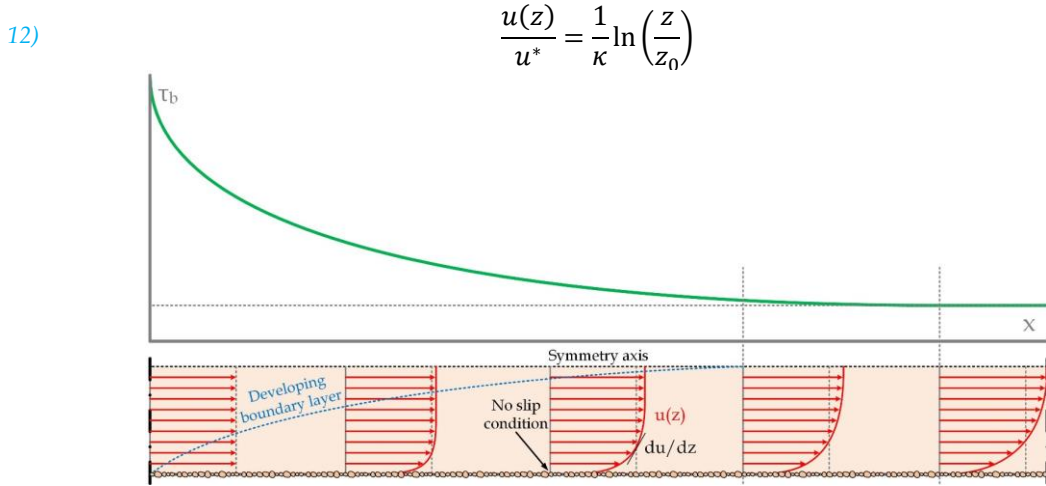


Figure 16 – Flow development between the bottom and symmetry axis of the duct (side view);  
Adapted from (Çengel & Cimbala, 2014)

The transition zone has specific properties to facilitate flow development while preventing erosion (figure 17 on the next page). The required distance for flow development can be approximated by using empirical relations. Equation 13 is just one of many (Schierreck, 2019). This relation estimates the boundary layer thickness ( $\delta$  [m]) based on the development distance ( $x$  [m]). As boundary layers emerge from all boundaries, each one has to span between the boundaries (e.g., the bottom) and the symmetry axis of the duct. Next, the ducts of the transition zone are closed off by a bottom plate; so that erosion is prevented during flow development.

## Part II

### Proof Of Concept (POC): methodology

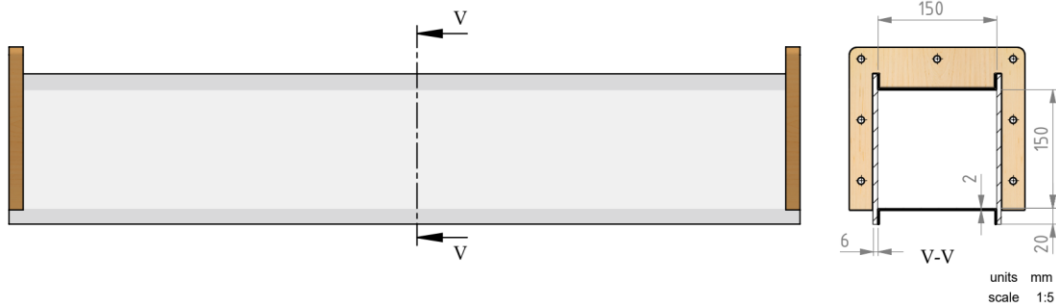


Figure 17 – The transition zone  
Left = side view and right = cross-section;  
(Van der Gaag, 2024)

13)

$$\delta(x) \approx 0.02x \text{ to } 0.03x$$

Additionally, the transition zone has specific properties to mitigate flow disturbances. The size and shape of the ducts (§2.2.1.3) are preserved throughout the entire duct system. Next, effort is made to homogenize the roughness as well. The used materials (§2.2.1.1) are also applied throughout the entire duct system. On top, the bottom plate of the transition zone contains an epoxy-glued sand bed. The used sand was deliberately scraped from the surface of the Sand Engine (figure 18), since the applied research (part 3) will also take place on this top layer. The Grain Size Distribution (GSD) of the used sand is provided in figure 19. Overall, the entire duct system (i.e., the transition- and erosion zone) will have a comparable geometry and roughness.



Figure 18 – Gathering sand grains from the top layer of the Sand Engine

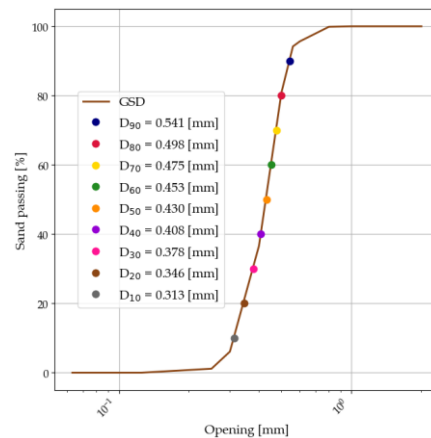


Figure 19 – The GSD of the sand that was glued on the bottom plate of the transition zone

While flow development is important it is accommodated in a realistic way. To clarify, the required development distance (equation 13) will not be fully obeyed. This choice stems from two main considerations. The first one involves the length of the mobile wind tunnel system. A shorter length namely facilitates mobility. Additionally, a shorter length means less resistance (e.g., friction); which is important as the fan has a finite pressure capacity (§2.2.1.2). The second concern involves the uncertainty around the required development distance. The distances estimated with equation 13 are exceeded easily by other estimates (appendix C.1.5). On top, the air flow will always be disturbed to some degree. Amongst other example, the bed of the transition zone is static, while the bed of the erosion zone lowers due to erosion. Overall, roughly 65 [%] of the mean distance (equation 13) is provided; spread along two separate ducts. An underdeveloped flow is thus accepted. Still, the approach mitigates the most variable and the most extreme bed shear stresses (figure 16). Besides, a logarithmic velocity profile is expected to be found in the regions nearing the boundaries; such as within the important region near the bed.

### 2.2.1.5 Generating (enhanced) erosion

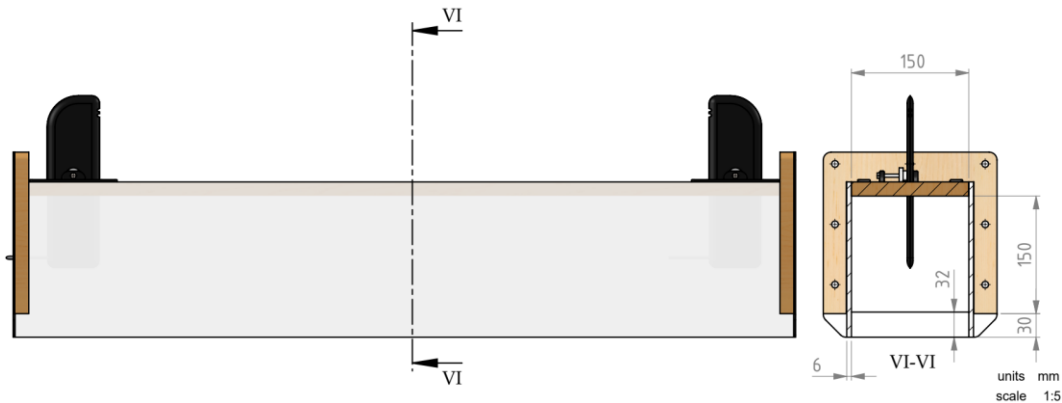


Figure 20 – The transition zone  
Left = side view and right = cross-section;  
(Van der Gaag, 2024)

The conditioned air flow might mobilize the sand surface within an erosion zone (H in figure 11 & figure 20). As mentioned, wind shear is generated in the ducts (§2.1); as the air flow interacts with the boundaries (§2.2.1.4). The erosion zone has no bottom plate, so that the generated wind shear is actually allowed to onset erosion. The sand surface is mobilized after the bed shear stress exceeds a critical value (Bosboom & Stive, 2023). Surpassing this critical value is already implicitly discussed by means of the design wind speed (§2.2.1.3). Many duct properties, such as the materials (§2.2.1.1) and the geometry (§2.2.1.3 & §2.2.1.4), are also already discussed.

Other duct properties are inspired by the prototype (i.e., Mobi-Gust 1). The length of the erosion zone (appendix C.1.6) is namely comparable to the length of Mobi-Gust 1 (De Wilde, 2020). Next, the cross-section in figure 20 appears to include a bottom plate, which is not the case. Previous research namely showed that the walls of the erosion zone are undermined easily (Bangen & Dijkstra, 2020). This undermining leads to sand exchanges with the outside world. Of course, this exchange is undesirable, as it causes unreliable erosion measurements. As a reaction, the walls are extended. These extended walls can be driven into the sand bed. The presence of extended walls clarifies the apparent bottom plate in figure 20. This apparent bottom plate is just a vertically oriented aluminium plate. These plates are installed at the up- and downwind end of the erosion zone. In this way, these plates connect the extended walls to each other providing toughness to the construction. Next, previous research also indicated the emergence of scour holes (Bangen & Dijkstra, 2020). The prototype did not include a transition zone, so the underdeveloped flow partially caused these scour holes (§2.2.1.4). Yet, another reason for scour hole development is clear wind erosion (Schierck, 2019). In elaboration, winds clear of sand traverse a granular bed, immediately onsetting erosion (i.e., when wind speeds are high enough). As no sand comes in, while it is locally leaving, a scour hole is dug. To this end, hatches (§2.2.1.7) are added to the roof of the erosion zone. These hatches give access to the interior of the erosion zone. These hatches thus enable the scour holes to be checked and measured. With (idealised) scour hole shapes one can correct the erosion volume (or -mass). Finally, the prototype also used pitot tubes, yet without a permanent suspension system. Figure 20 shows the pitot tubes and their vertically adjustable holders. These holders fit into the mentioned hatches. These pitot tubes quantify the wind speed during the erosion process (§2.2.1.7). The pitot tubes are removable, i.e., both of them do not have to be in used at the same time. When a pitot tube is removed, tailored caps seal off the resulting gaps (i.e., mitigating energy losses).

## Part II

### Proof Of Concept (POC): methodology

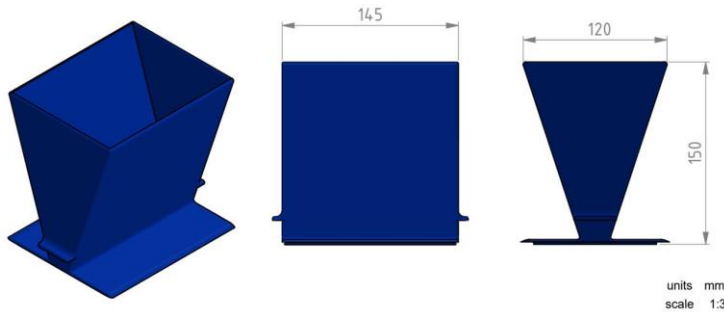


Figure 21 – The saltation hopper  
Left = 3D view, middle = front view and right = side view;  
(Van der Gaag, 2024)

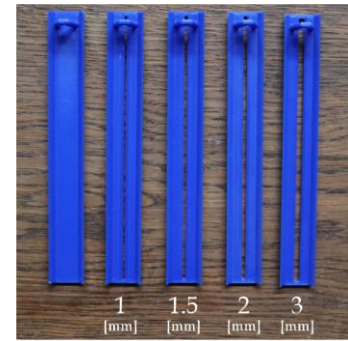


Figure 22 - Saltation hopper lids

Erosion can be enhanced by means of a saltation hopper (I in figure 11 & figure 21). This hopper is permanently fixed at the upwind end of the transition zone. This hopper is used to drain sand into duct system. Consequently, establishing an upwind supply of sand towards the erosion zone. This hopper can be fitted with lids of different gap sizes (figure 22). As a result, grains of similar sizes and shapes drain at different rates (§2.3.3). There is also a lid without gap. This gapless lid seals off the opening when the saltation hopper is not in use (i.e., mitigating energy losses). Design iterations (i.e., the old saltation hopper is visible in §2.3.7) showed that horizontally sliding parts jam in combination with sand grains. The lids are thus vertically removable.

The enhanced erosion is generated by sand particle collisions. R.A. Bagnold (1941) defined the three main transport modes of windblown sand; i.e., suspension, saltation and creep. Yet, sand particles ( $63 [\mu\text{m}]$ - $2 [\text{mm}]$ ) are usually transported in a bouncing (i.e., saltation) or rolling (i.e., creep) manner (Uphues et al., 2022). Sand is thus usually transported close to the surface, as sand is roughly 2,000 times denser than air (Bagnold, 1941). The injected sand grains will therefore collide with the sand surface within the erosion zone. These collisions ensure the generation of erosion (Rice, 1991). In other words, after subtracting the injected sand mass, from the collected sand mass (§2.2.1.6); there should be an additional (eroded) sand mass. Specialized experiments will show the generation of enhanced erosion, by adding an upwind supply of sand (part 3).

More technically speaking, the enhanced erosion results from an altered momentum distribution inside Mobi-Gust 2. To this end, momentum per unit volume (equation 14) is introduced (Chassagne & Van den Bremer, 2021). Momentum per unit volume ( $M [\text{kg}/\text{m}^2/\text{s}]$ ) describes the general combination between density ( $\rho [\text{kg}/\text{m}^3]$ ) and speed ( $u [\text{m}/\text{s}]$ ).

14)

$$M = \rho u$$

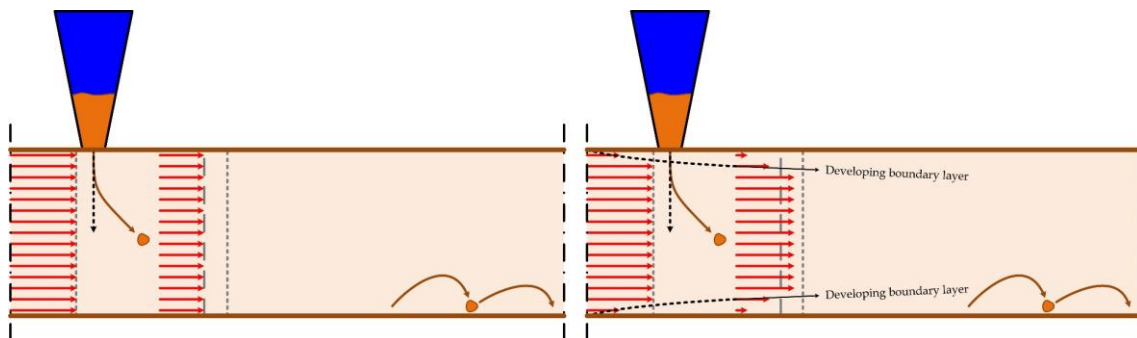


Figure 23 - Increasing, transferring and focussing momentum;  
left = without boundary friction & right = with boundary friction

## Part II

### Proof Of Concept (POC): methodology

The enhanced erosion results from increasing, transferring and focussing momentum. As explained, sand is much denser than air, causing a local increase of momentum. Simultaneously, the air flow transfers momentum to the sand grains (Van Rijn, 2023). This momentum transfer is visible as the vertically injected sand grains, will be transported horizontally. Next, all this momentum is focussed in an area close to the surface; again because of the mentioned density difference between sand and air. In the end, the injected sand grains reach the erosion zone, where they exchange momentum with the sand bed. In simple terms, collisions ensure the generation of enhanced erosion. The left part of figure 23 summarizes the explained situation, in a (very) schematic and simplified way. Of course, reality is (much) more complex. The right part of figure 23 (previous page) namely shows that friction complicates matters. On top, the flow experiences unequal friction from the roof and bottom; which is neglected in figure 23 (previous page). The bottom namely has an epoxy-glued sand bed on it (§2.2.1.4), whereas the roof does not.

#### 2.2.1.6 Collecting the eroded material

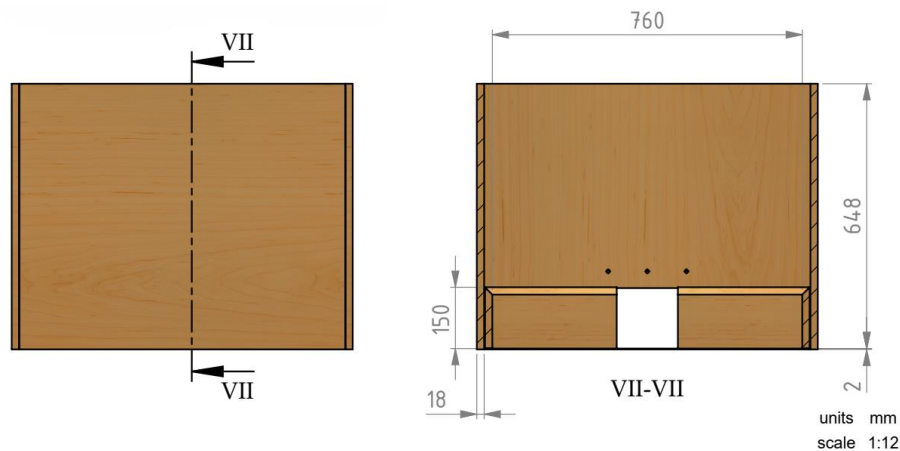


Figure 24 – The sand trap  
Left = side view and right = cross-section;  
(Van der Gaag, 2024)

The sand-laden air enters a sand trap and leaves it clear of sand (J in figure 11 & figure 24). The sand trap is a relatively large cuboid-shaped box with a vertical exit. The sand-laden air enters this box immediately, i.e., without diffusers and the like. To clarify, a diffuser is a gradually expanding cross-section (Anderson Jr., 2005). Three main principles ensure the sand-tightness of this sand trap. Firstly, the sand-laden air flow decelerates as the flow area increases while mass is conserved (White, 2011). Secondly, a decelerating flow relates to negative pressure gradients; i.e., causing flow separation and recirculation, or energy losses (Schierreck, 2019). These additional losses further decelerate the sand-laden air flow. The lower wind speeds will onset the deposition of sand (Bosboom & Stive, 2023). Finally, the sand trap has a vertical exit, so that it resembles a chimney. Consequently, sand grains must ascent in order to leave the sand trap. The gravitational pull of the Earth ensures two beneficial aspects. First of all, gravity ensures that the vertically oriented flow is further decelerated. Second of all, gravity directly acts on the sand grains. So, as sand is (much) denser than air (§2.2.1.5) gravity greatly helps the sand trap being sand tight.



## Part II

### Proof Of Concept (POC): methodology

The dimensions of the sand trap are determined in a straightforward assessment. The sand traps dimensions are chosen as such, that the cross-sectionally averaged exit velocity ( $u_{exit}$  [m/s]) exceeds the fall velocity ( $w_s$  [m/s]) of the expected range in grain sizes. The investigated grain sizes concern very fine-, fine-, medium- and coarse sand (U.S. Geological Survey, N.d.); as well as the construction material (i.e., 280 [ $\mu m$ ]) of the Sand Engine (Luijendijk et al., 2017). A grain might either settle in a laminar ( $Re_s < 0.1$  to 0.5) or in a turbulent ( $400 < Re_s < 2 \cdot 10^5$ ) manner (Bosboom & Stive, 2023); i.e., both modes are assessed (equation 15 & 16). The Reynolds number of the grain (equation 17) describes which mode is most likely to occur (Bosboom & Stive, 2023). Mind that the Reynolds number of the grains conveys information about the grains relative to the surrounding fluid. In other words, it does not provide information on the flow itself (Schierreck, 2019); as the flow is most certainly turbulent. The involved calculations are shown in appendix C.1.7. The calculations do not involve energy losses; which is a safe approach as energy losses result in an even lower cross-sectionally averaged exit velocity.

$$15) \quad w_{s,S} = \frac{1}{18} \frac{g}{\eta_a} (\rho_s - \rho_a) D_{50}^2$$

$$16) \quad w_{s,N} = \sqrt{\frac{8g}{3} \frac{(\rho_s - \rho_a)}{\rho_a} D_{50}}$$

$$17) \quad Re_s = \frac{\rho_a w_s D_{50}}{\eta_a}$$

The sand trap has a shorter height than calculated because of mobility-reasons. The height of the sand trap is based on the loading space of a Chrysler Voyager (i.e., an MPV-vehicle) and a Toyota Hilux (i.e., 4x4-vehicle). This lower height is acceptable, as the exit flow is vertically oriented.

However, some extra measures have to be taken in order to catch and collect all the sand. Outflow velocities are namely expected to be higher than predicted. The exit flow from the duct system will probably concern a jet flow (Schierreck, 2019). A jet is a barely widening (i.e., hardly decelerating) flow. A jet results from an abrupt increase in flow area. As a reaction, a (re)movable wire mesh cylinder is added to the design of the sand trap (figure 25). This wire mesh can be positioned in the path of the jet in order to break it. Breaking this jet ensures that the flow approaches the estimated cross-sectionally averaged exit velocities faster. In turn, ensuring the sand tightness of the sand trap (§2.3.4). Collecting the trapped sand can be done by means of a sand trap tray (K in figure 11). This tray is simply the bottom of the sand trap, which is manually removable through ropes.

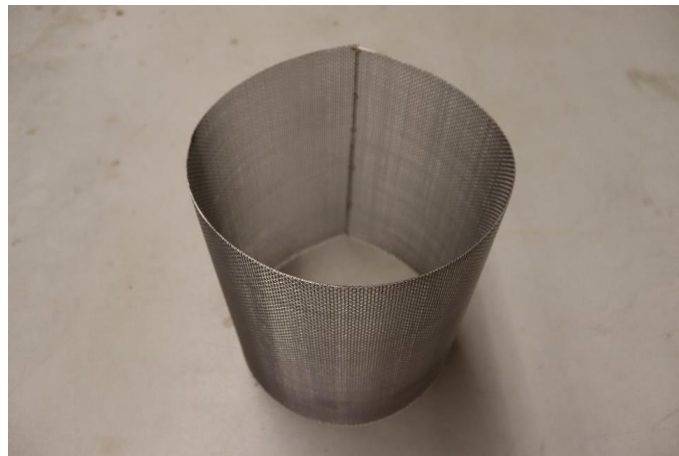


Figure 25 – Wire mesh cylinder

## Part II

### Proof Of Concept (POC): methodology

#### 2.2.1.7 Gauging the wind speed

The wind gauging system senses the wind speed inside the erosion zone (L in figure 11). Quantifying the wind speed is logically important as the erosion process is wind driven. Yet, the ability to measure velocity profiles may also be of importance; for example, to assess flow development (§2.2.1.4). As described in the project outline (§2.1), wind speeds will be measured with pitot tubes in a digital setup. The three main components of the wind gauging system are shown in figure 27. The main components involve a differential pitot tube, a differential pressure sensor and a microcontroller. On top, the pitot tubes are fixed in removable and height-adjustable holders (figure 26). These holders are 3D-printed and have an aerodynamic shape in flow direction. The holders are in turn attached in removable hatches in the roof of the erosion zone (§2.2.1.5).

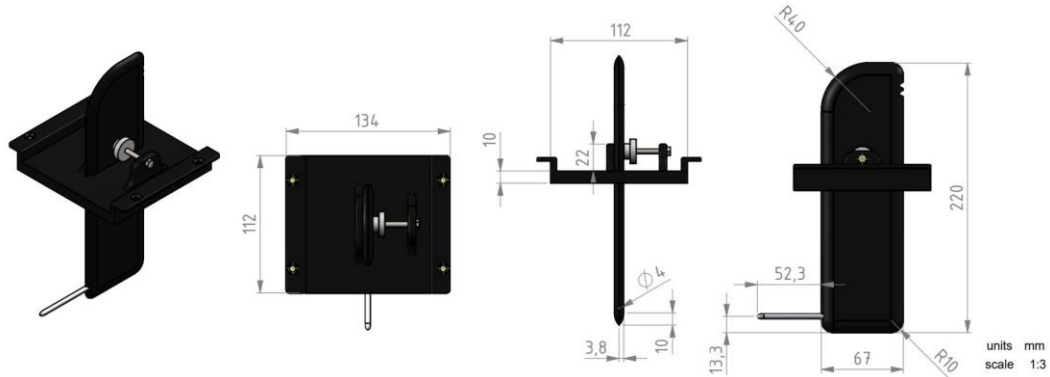


Figure 26 – The removable and height-adjustable pitot tube holders in the removable erosion zone hatches

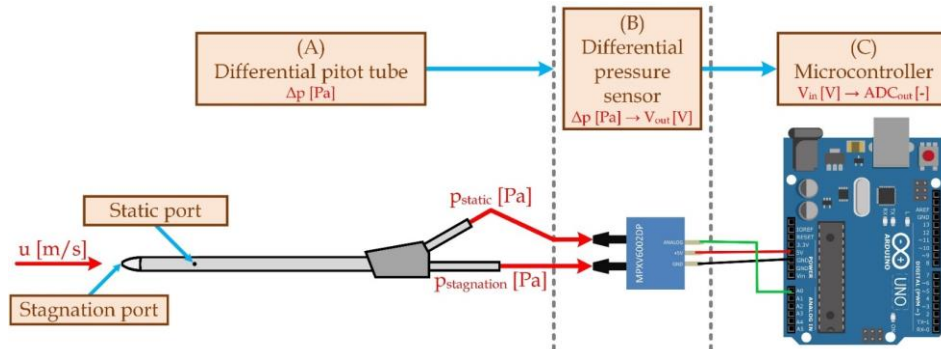


Figure 27 – The main components of the wind gauging system  
Partly taken from (Hrisko, 2019)

The pitot tube (A in figure 27) measures differential pressure. This pressure differential is measured between the stagnation- and static port of the pitot tube (NASA, 2023). To clarify, both ports sense the static air pressure, while the stagnation port also senses the dynamic air pressure (i.e., including the wind speed). The measured differential pressure ( $\Delta p$  [ $N/m^2$ ]) is used to estimate the air speed ( $u_a$  [ $m/s$ ]) using the pitot tube formula (Çengel & Cimbala, 2014); as shown in equation 18. The pitot tube formula additionally includes the density of air ( $\rho_a$  [ $kg/m^3$ ]). The pitot tube formula can be derived from Bernoulli's principle (Chassagne & Van den Bremer, 2021); the derivation is shown in appendix B.3.3. Using Bernoulli is allowed as the flow is incompressible (appendix B.2); and steady for a particular fan setting. On top, energy losses (e.g., friction) between the two ports can be neglected, as the associated distances are relatively short.

18)

$$u_a = \sqrt{\frac{2\Delta p}{\rho_a}}$$

## Part II

### Proof Of Concept (POC): methodology

The differential pressure sensor (**B in figure 27**) converts the received differential pressure into voltage output. The used MPXV7002DP pressure sensor is piezoresistive (NXP, 2021). Such a sensor includes conductive and stretchy material (Avnet, N.d.). Consequently, the electrical resistance is varied according to the pressure applied. This change of electrical resistance can be sensed and converted into voltage output; according to Ohms law. Ohms law describes the relation between voltage, current and resistance within an electrical system (Fitzgerald & Shiloh, 2015). The used sensor is calibrated by the manufacturer (NXP, 2021). The relation between the differential pressure ( $\Delta p [N/m^2]$ ) and the voltage output ( $V_{out} [V]$ ) is shown in figure 28 and equation 19 (i.e., without error range).

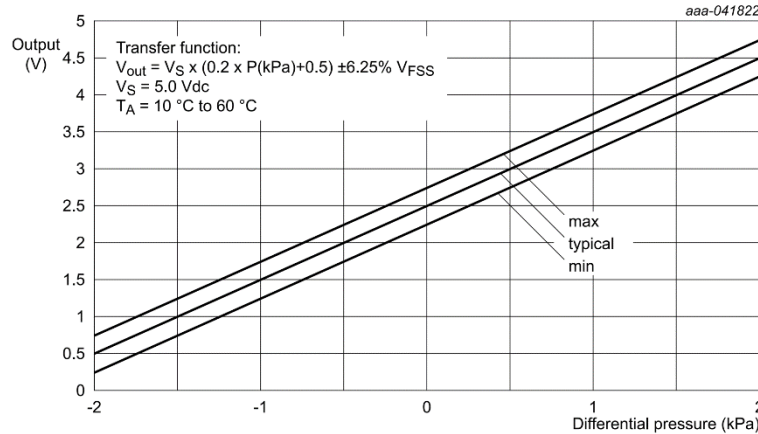


Figure 28 – Transfer relation between the differential pressure and voltage output used by the sensor (MPXV7002DP) (NXP, 2021)

$$19) \quad V_{out} = V_s \left( \frac{1}{5} \Delta p + \frac{1}{2} \right)$$

The microcontroller (**C in figure 27**) digitizes the received voltages. The used microcontroller concerns an Arduino Mega 2560 Rev3 that operates at 5 [V] (Arduino SRL, 2024). The voltage output of the pressure sensor is received as input in one of the analogue-input pins. A microcontroller cannot understand this continuous input signal. The input signal is thus discretized by an Analogue-to-Digital Converter (ADC). The used ADC has a resolution ( $n [b]$ ) of 10-bits. The output of the ADC is determined by a balance of ratios (Elektor, 2022); see equation 20. The first ratio concerns the resolution of the ADC ( $ADC_{res} [-]$ ); to the system voltage ( $V_s [V]$ ) of the microcontroller. This resolution is defined as the number of discreet values that the ADC is able to represent (equation 21). The second ratio concerns the digital output of the ADC ( $ADC_{out} [-]$ ); to the input voltage ( $V_{in} [V]$ ) that was received.

$$20) \quad \frac{ADC_{res}}{V_s} = \frac{ADC_{out}}{V_{in}}$$

$$21) \quad ADC_{res} = 2^n$$

The air speed follows from back calculating the pressure differential; and applying the pitot tube formula. The calculation is visualized in a block diagram (figure 29). The relation between the air speed ( $u_a [m/s]$ ) and the other parameters (i.e., the ADC output ( $ADC_{out} [-]$ ), the voltage output ( $V_{out} [V]$ ) or the differential pressure ( $p [N/m^2]$ ) are visualized in figure 30. The graphs are continued up until the design wind speed (i.e., 15 [m/s]). By combining equation 18, 19 and 20 into equation 22 the air speed can be estimated. Mind that the input voltage ( $V_{in} [V]$ ) of the microcontroller is equal to the output voltage ( $V_{out} [V]$ ) of the differential pressure sensor. Additionally, a factor 1,000 [-] appears in equation 22, as the pressure sensor measures in kilo-Pascals (i.e., [kPa] or [ $kN/m^2$ ]). The derivation is shown in §C.2.4.

## Part II

### Proof Of Concept (POC): methodology

22)

$$u_a = \sqrt{\frac{10,000 \left( \frac{ADC_{out}}{ADC_{res}} - \frac{1}{2} \right)}{\rho_a}}$$

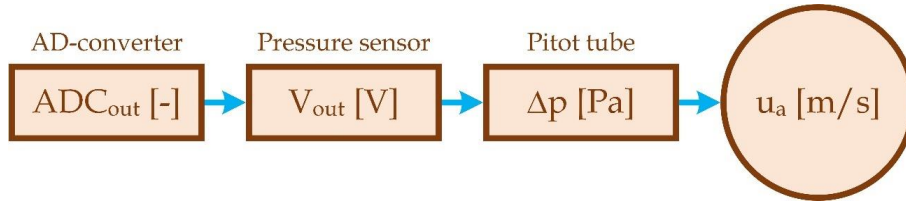


Figure 29 – Schematic representation of estimating the air speed from the ADC output

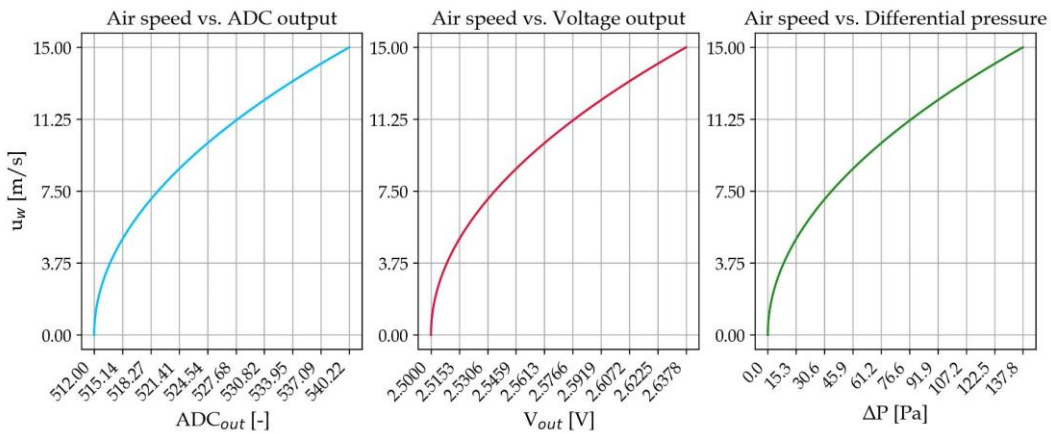


Figure 30 – The relationship between air speed and ADC output, voltage output or differential pressure

Active mitigation of zero deviations boosts accurate and robust wind speed measurements. Zero deviations concern deviations from the baseline of a (pressure) sensor (MPS, N.d.). To clarify, non-zero values are obtained; when measuring quantities that are zero (e.g., when measuring zero differential pressure in wind still conditions). The zero deviations can be subdivided into a constant zero offset and variable zero drift (SensorOne, N.d.). In elaboration, the constant offset can for example be caused by (calibration) errors, used sensor-materials; or manufacturing tolerances. This constant offset generally differs between sensors; even if they originate from the same batch. Next, the variable drift can be caused by all kinds of (variable) interferences. Examples include electromagnetic interferences, such as thermal-, shot- and flicker noise (Eastsensor, 2022); mechanical interferences, such as stresses or vibrations (SensorsONE, N.d.); or environmental interferences, such as humidity changes, dust particles or chemicals (Xidibei, 2023). Mitigating the zero deviations involves three hardware-related aspects. Firstly, the sensors are mounted outside the wind gauging box (figure 31 & figure 32); i.e., mitigating electrical interferences. Secondly, the sensors are shielded by 3D-printed caps (figure 31 & figure 32); i.e., mitigating mechanical interferences. Finally, couplers are added between the pressure sensors and the pitot tubes. These couplers ensure that the sensors can be left untouched, when disconnecting them from the pitot tubes (figure 32); i.e., mitigating mechanical interferences. Additional to the mentioned measures, the pressure sensor is temperature compensated by the manufacturer (NXP, 2021); i.e., mitigating environmental interferences. Next, zero deviations are also mitigated by a software-related aspect. To clarify, the actual measurements are preceded by zero-measurements. As explained, non-zero values are obtained when measuring quantities that is zero. The mean of multiple readings will be used to correct the actual measurements. The zero-measurements are triggered every experiment, as the zero drift has a variable nature.



## Part II

### Proof Of Concept (POC): methodology

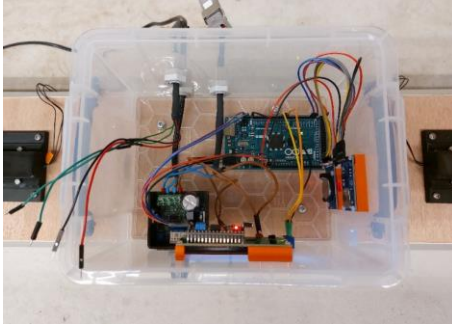


Figure 31 – The electrical hardware is secured in a splash-proof and shakeable box

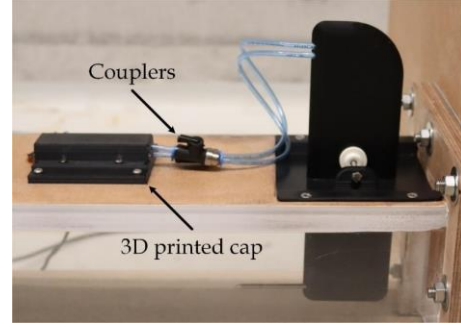


Figure 32 - The pressure sensors are shielded by 3D printed caps; and the PVC-tubing is connected through couplers

The wind gauging system is completed by some additional hardware. The other parts concern a Secure Digital (SD) module, a Liquid Crystal Display (LCD) module and Real Time Clock (RTC) module. These parts are respectively used for datalogging, data visualization and timekeeping. The mentioned parts are shown in [figure 33](#), [figure 34](#) and [figure 35](#). The entire system can be operated through a set of toggle switches. The hardware is secured in the already mentioned shakeable and splash-proof box ([figure 31](#)); by 3D-printed holders. Yet, if for some reason hardware breaks down, the components are easily replaceable. The connections between the components namely concern removable jumper wires ([figure 31](#)). On top, replacements are financially rather cheap (i.e., see the references below [figure 33](#), [figure 34](#) and [figure 35](#)).



Figure 33 – SD module  
(AZ-Delivery, N.d.)



Figure 34 – LCD module  
(AZ-Delivery, N.d.)

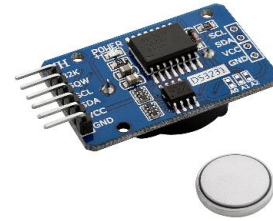


Figure 35 – RTC module  
(AZ-Delivery, N.d.)

The sampling frequency of the wind gauging system is determined from the software. In elaboration, the hardware is controlled by a program full of code, that is written in the Arduino IDE software ([Arduino SRL, N.d.](#)). The 'millis' command ([equation 23](#)) is used to record the time ( $t$  [ms]) that has passed, relative to when the microcontroller started running the program ([Arduino SRL, 2023](#)). Mind that [equation 23](#) records the time in milliseconds. A period ( $T$  [ms]) is thus obtained after subtracting two recorded times ([equation 24](#)). The sampling frequency ( $f$  [Hz]) is obtained from this period ([equation 25](#)). The analysis is shown in [appendix I.1](#).

$$\begin{aligned}
 &23) \quad t = \text{millis}( ) \\
 &24) \quad T = t_2 - t_1 \\
 &25) \quad f = \frac{1,000}{T}
 \end{aligned}$$

The Arduino sketch that is used to operate all hardware is added in [appendix C.2](#). On top, the wiring schemes and the programming logic are added as well. The programming logic is important, as it shows that the wind gauging system can be configured into three modes. In elaboration, one mode determines, visualizes and logs the wind speed; as well as the raw data (i.e., the ADC output). Another mode does exactly the same, without datalogging. And the final mode can be seen as a pause-mode; in which virtually nothing happens, except for time-visualization.



### 2.2.1.8 Supplying power

Yet, without a supply of power there is not wind flow (measurement). The fan and wind gauging system are powered by a  $\text{LiFePO}_4$  battery (Victron Energy, N.d.). These type of batteries produces a relatively stable voltage while discharging (Shepard, 2021). Next, these batteries are relatively durable if used and maintained correctly (Kassaeian, 2023); even in harsh environments. In elaboration, the longevity of the power supply can be increased by managing the (dis)charging process; which includes using a suitable charger. Next,  $\text{LiFePO}_4$  batteries are safer than other lithium-based chemistries (Relion, N.d.). The discharge duration ( $\Delta t_d [h]$ ) of this power supply, depends on the power demand ( $P_d [W]$ ) of Mobi-Gust 2; and the power capacity ( $P_c [Wh]$ ) of the battery itself. The discharging duration can be roughly estimated by using equation 26. The mentioned calculation, plus extra information on the used battery, can be found in appendix C.3.

26)

$$\Delta t_d = \frac{P_c}{P_d}$$

## 2.2.2 The performance of Mobi-Gust 2

The second part of the methodology involves checking the performance of Mobi-Gust 2. The design of Mobi-Gust 2 greatly determines its performance. Yet, correct instalment matters as well. The instalment of Mobi-Gust 2 includes mounting the mobile wind tunnel system; and configuring the wind gauging system. [Appendix G.3](#) shows elaborate manuals how to properly set Mobi-Gust 2. Verifying the performance of Mobi-Gust 2 involves seven tests: [§2.2.2.1](#) explores the durability of the power supply; [§2.2.2.2](#) investigates the properties of the wind (gauging system); [§2.2.2.3](#) explores the saltation hopper drainage; [§2.2.2.4](#) considers the sand tightness of Mobi-Gust 2; [§2.2.2.5](#) investigates the modular design, in relation to the achievable wind speeds; [§2.2.2.6](#) considers flow development; and [§2.2.2.7](#) investigates the in-situ erosion performance of Mobi-Gust 2. The experiments are mostly conducted in the Hydraulic Engineering laboratory of Delft University of Technology. However, the last test ([§2.2.2.7](#)) involves a field expedition that will visit the Sand Engine ([appendix A](#)). Safety is paramount at the Delft University of Technology. Making use of the laboratory is inherently linked to a dedicated safety plan. The same holds for conducting field work; also, that activity involved a dedicated safety plan.

### 2.2.2.1 Testing the robustness of the power supply

In-situ experiments using a portable power supply requires knowing the operational window. This operational window does not only rely on the power supply itself. Other electrical systems (i.e., the fan and the wind gauging system) of course matter as well. To test the theoretical discharge duration ([§2.2.1.8](#)) will be verified to through a test. To this end, the experimental discharge duration is introduced. This experimental discharge duration concerns the period between fully charging and fully draining the power supply. On top, wind speeds will be measured to reveal practical window of Mobi-Gust 2. As explained ([§2.2.1.8](#)), a  $\text{LiFePO}_4$  battery is rather stable. Yet, at the operational edges of the power supply (i.e., when the battery is almost fully charged or drained) electrical systems can be affected by the battery ([Vatrer, N.d.](#)).

The test involves three main tasks. Firstly, the battery is fully charged ([figure 36](#)). Secondly, the fan and wind gauging system are switched on. Thirdly, Mobi-Gust 2 is kept operational, until the power supply runs out. During the test, the fan is supplied with maximum power; i.e., the test provides a lower limit for the experimental discharge duration. On top, the pitot tube is positioned along the centreline of the duct ([appendix E](#)); i.e., measuring maximum velocities, as friction along the centreline of the duct is at its minimum ([Çengel & Cimbala, 2014](#)).

The analysis is rather straightforward. The discharging duration will reveal itself by keeping track of time ([figure 37](#)). On top, the wind speed is measured. The gathered data validates the recorded duration; and shows the explained practical window of Mobi-Gust 2.



Figure 36 – A prepared (charged)  $\text{LiFePO}_4$  battery



Figure 37 – The most nearby clock in the HE laboratory

It is stressed that this experiment should not be reconducted too often. Fully (dis)charging a  $\text{LiFePO}_4$  battery can be harmful to its performance and longevity ([Himax Electronics, 2024](#)).

### 2.2.2.2 Exploring the wind (gauging system) properties

Quantifying aeolian erosion requires knowing the governing wind (gauging system) properties. The dataset from the previous experiment (§2.2.2.1) is re-used for this analysis. The dataset will be analysed in two steps. First of all, the entire dataset is analysed. This first step thus provides information across a full discharging cycle. Second of all, specific time intervals are isolated from this full dataset. In this case, data will be isolated around the start, middle and end of the dataset. The second step thus provides specific information related to the state of the power supply (i.e., nearly charged, half-drained and nearly drained).

The data is analysed through basic statistics. To this end, means and standard deviations will be determined; see equation 27 and 28 (Dekking et al., 2005). The mean ( $\mu_u$  [m/s]) involves summing all air speed observations ( $u_i$  [m/s]); and dividing it by the number of observations ( $N$  [-]). In turn, the standard deviation ( $\sigma_u$  [m/s]) considers the deviations from the calculated mean ( $u_i - \mu_u$  [m/s]). In elaboration, the mentioned differences are squared and averaged; and then the square root of the result is taken. From a statistical point of view, it is noted that the isolated datasets are samples of the population (i.e., the entire dataset).

$$\begin{aligned} 27) \quad \mu_u &= \frac{\sum_{i=1}^N u_i}{N} \\ 28) \quad \sigma_u &= \sqrt{\frac{\sum_{i=1}^N (u_i - \mu_u)^2}{N}} \end{aligned}$$

Next, these general statistics are used to compute signal-to-noise ratios. The mentioned signal-to-noise ratio ( $RNS_u$  [-]) is approached by equation 29 (NIST, 2019). If the ratio is above one, signals prevail over noise (and vice versa). In other words, the information to be measured, exceeds random variations around this information (Smith, 1999).

$$29) \quad SNR_u = \frac{\mu_u}{\sigma_u}$$

Next, the relative turbulence intensity is determined. This dimensionless ratio provides information on the strength of fluctuations (Schierreck, 2019); see equation 30. The relative turbulence intensity ( $r_u$  [-]) considers the square root of the averaged and squared velocity fluctuations ( $\sqrt{u'^2}$  [m/s]); and compares it to the mean velocity ( $\bar{u}$  [m/s]). This intensity cannot be determined from averaging the fluctuations themselves; as these are zero by definition. The relative turbulence intensity makes use of the Reynolds decomposition (Uijttewaai, 2022); see equation 31. To clarify, an arbitrary and varying (longitudinal) velocity ( $u$  [m/s]); can be seen as the sum of a mean velocity ( $\bar{u}$  [m/s]) and a velocity fluctuation ( $u'$  [m/s]) around this mean.

$$\begin{aligned} 30) \quad r_u &= \frac{\sqrt{u'^2}}{\bar{u}} \\ 31) \quad u &= \bar{u} + u' \end{aligned}$$

The theoretical sampling frequency (§2.2.1.7) will be verified as well. This last step simply involves measured wind speed data; and counting the number of datapoints in a single second.

### 2.2.2.3 Testing the drainage rate of the saltation hopper

Testing the discharge rate of the saltation hopper is important for multiple reasons. Roughly knowing the discharge rate is valuable in view of usability. This rate can be used to estimate the amount of sand required in a single test; or it reveals the available time (i.e., for other activities) between filling and draining the hopper. Knowing the discharge rate is logically also important for other project criteria (i.e., reliability and controllability).

## Part II

### Proof Of Concept (POC): methodology

The experiment is broken down in some basic tasks. A quantity of sand will be weighted; and added in the saltation hopper. In this case, sand samples of approximately 1 [kg] will be used. Next, the duration is recorded between filling and draining the hopper. The discharge rate is then determined from a basic ratio between mass and time. In elaboration, the discharging rate ( $u_s$  [kg/s]), follows from dividing the added sand mass ( $m_s$  [kg]) by the elapsed drainage time ( $t_s$  [s]); see [equation 32](#).

$$32) \quad u_s = \frac{m_s}{t_s}$$

The discharging rate depends on the size (and shape) distribution of the used sand sample. After all, the larger the sand grain the less easy it fits through a certain gap size (and vice versa). The used sand is collected from the Sand Engine as shown in [figure 38](#). The Grain Size Distribution (GSD) of this sand is shown in [figure 39](#). Mind that this sand differs from the glued sand in the transition zone (§2.2.1.4).



Figure 38 - Retrieving sand from the Sand Engine

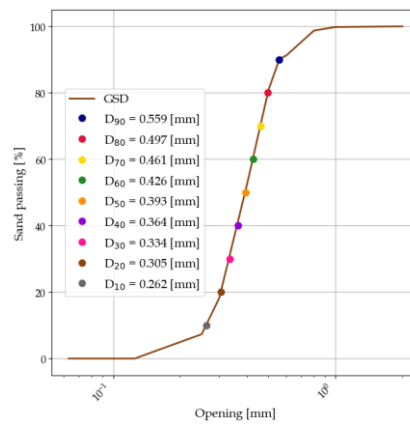


Figure 39 - The GSD of the retrieved sand

Logically also the gap size of the saltation hopper determines the drainage rate. Mobi-Gust 2 has lids of different gap sizes (§2.2.1.5). Every gap size will thus have another drainage rate, for the same granular material. [Table 3](#) shows the different gap sizes that were 3D-printed. These gap sizes were determined using a calliper ([appendix E.1.3](#)).

Table 3 - The different lids that were tested in the saltation hopper drainage test

Lid [-]	1	2	3	4	5
Size [mm]	0.97	1.01	1.52	2.03	3.01

#### 2.2.2.4 Investigating the sand tightness of Mobi-Gust 2

Measuring aeolian erosion requires checking the sand tightness of Mobi-Gust 2. After all, the measured erosion flux will be off, when Mob-Gust 2 leaks sand. Two additional measures are required to make Mobi-Gust 2 sand-tight. The first mitigation involves gap taping ([figure 40](#) & [figure 41](#)) at three distinct locations. The first location concerns the hatches of the erosion zone (i.e., where the pitot tubes are mounted). The second location concerns the transition between the erosion zone and the sand trap. The last location concerns the edges of the sand tray within the sand trap. The mentioned locations were identified from experience. The second sand loss mitigation measure involves using the wire mesh cylinder ([figure 41](#)). This repositionable wire mesh breaks the sand-laden jet flow that exits the erosion zone (§2.2.1.6).



## Part II

### Proof Of Concept (POC): methodology



Figure 40 – Gap taping



Figure 41 – Gap taping and wire mesh positioning

The experiment will be conducted by straightforwardly using the saltation hopper. Before injecting the sand, it is weighted. The weighted sand is then inserted into Mobi-Gust 2; while the fan operates at maximum power. Next, the saltation hopper must be fully drained, before emptying the sand trap. The collected sand is then weighted again. The lost sand mass ( $m_l$  [kg]) is estimated as the difference between the added sand mass ( $m_a$  [kg]) and the collected sand mass ( $m_c$  [kg]). The approach is summarized in [equation 33](#).

$$33) \quad m_l = m_a - m_c$$

The sand tightness is assessed in relation to the extra measures. In clarification, the experiments will be conducted with and without gap taping. Also, the test will be conducted with and without wire mesh cylinder. The test is thus involving a total of four configurations; see [table 4](#). The test is conducted with sand samples of 10 [kg] and using lid 4 ([§2.2.2.3](#)).

Table 4 – Configurations of the sand loss test

Configuration	1	2	3	4
Gap taping	–	–	x	x
Wire mesh cylinder	–	x	–	x

Mounting Mobi-Gust 2 on a solid surface presents some problems. The erosion zone namely has elongated walls ([§2.2.1.6](#)). In turn, the bottom of the transition- and the erosion zone are not levelled on hard surfaces. To this end, a plank is fitted within the erosion zone ([figure 42](#) & [figure 43](#)). Sand is wood-glued on this plank to mimic field conditions. The same sand was glued on the plank as on the bottom plate of the transition zone ([§2.2.1.5](#)); i.e., the roughness matches. Next, the edges of the plank are taped to the erosion zone walls. To clarify, this is done to mimic field conditions; as the erosion zone walls are normally driven into the sand. In elaboration, that means that sand and air cannot leak through the sides (i.e., excluding undermining). The adverse effect of the taping concerns that the air flow around the edges is less representative for field conditions. Yet, this situation is accepted as the interest is directed towards sand losses.



Figure 42 – Preparing the placement of the levelling plank



Figure 43 – A view from the sand trap into the erosion zone



## Part II

### Proof Of Concept (POC): methodology

#### 2.2.2.5 Exploring the wind speed in the modular design of Mobi-Gust 2

Next, the achievable wind speeds within Mobi-Gust 2 are explored. The achievable wind speed depends on the resistance (e.g., friction) of the system (Chassagne & Van den Bremer, 2021). Simultaneously, Mobi-Gust 2 has a modular design (§2.2.1.1). Consequently, the in- or exclusion of parts causes different achievable wind speeds. Mobi-Gust 2 specifically has parts that condition the air flow (§2.2.1.4). It is insightful to learn the 'costs' of these parts in terms of wind speed. Knowing this information also shapes the vision towards expanding Mobi-Gust 2 in the future.

The experiment involves three main tasks. Firstly, the components of Mobi-Gust 2 are systematically in- or excluded (table 5). Secondly, Mobi-Gust 2 is switched on; which means that the fan and wind gauging system are both in use. The fan is supplied with maximum power in each test; so that wind conditions are comparable. On top, the pitot tube is mounted along the centreline of the duct (appendix E); i.e., sensing maximum velocities, as friction is minimum along the centreline of the duct (Çengel & Cimbala, 2014). Lastly, Mobi-Gust 2 is kept operational for some period of time. The obtained wind speed data of various tests are compared afterwards.

The combinations that are tested are shown in table 5. The table does not include the fan (§2.2.1.2), the contractions (§2.2.1.3), the erosion zone (§2.2.1.5) and the sand trap (§2.2.1.6). The mentioned components are namely the bare minimum to have a functioning Mobi-Gust 2. In elaboration, Mobi-Gust 2 is a fan-powered, venturi-style wind tunnel, that generates and measures aeolian erosion. This bare minimum also approaches to the configuration of the prototype (i.e., Mobi-Gust 1). This comparison disregards differences in shape and size (figure 44 & figure 45). To close off, test 10, 11 and 12 concerns the upwind ( $x_d$ ), centred ( $x_c$ ) or downwind ( $x_u$ ) placement of the wire mesh cylinder within the sand trap.

*Table 5 – The configurations (rows) and the components in use (columns)*

Configuration	1	2	3	4	5	6	7	8	9	10	11	12	13
Intake shield walls									$x$				
Honeycomb screen	$x$	$x$	$x$	$x$					$x$	$x$	$x$	$x$	$x$
Upwind transition duct	$x$	$x$				$x$	$x$		$x$	$x$	$x$	$x$	$x$
Downwind transition duct	$x$		$x$				$x$	$x$	$x$	$x$	$x$	$x$	$x$
Wire mesh cylinder										$x_d$	$x_c$	$x_u$	$x_c$
Saltation test													$x$



Figure 44 – A minimally equipped Mobi-Gust 2



Figure 45 – Mobi-Gust 1 on a field expedition

#### 2.2.2.6 Investigating the flow development within Mobi-Gust 2

Besides pure speed, velocity distributions are important as well. As explained, Mobi-Gust 2 does not fully accommodate flow development (§2.2.1.4). Consequently, this test tries to find how far flow development actually reaches. The approach consists of measuring velocity distributions. As explained, a developing flow is associated with a developing logarithmic velocity profile (§2.2.1.4). For convenience, equation 34 repeats this logarithmic velocity profile (Uijtewaalt, 2022).

$$34) \quad \frac{u(z)}{u^*} = \frac{1}{\kappa} \ln\left(\frac{z}{z_0}\right)$$

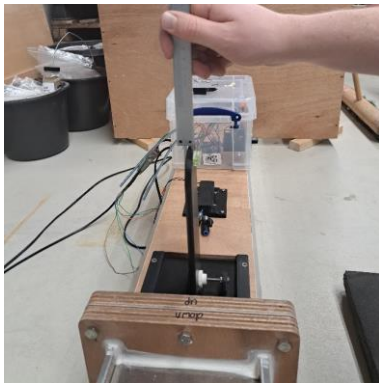
## Part II

### Proof Of Concept (POC): methodology

Obtaining velocity profiles requires some physical actions. Analogous to [equation 34](#) the velocity profiles will be measured along the vertical ([table 6](#)). The pitot tubes are namely solely adjustable in that direction ([§2.2.1.7](#)). The profiles will be measured between the centreline and bottom of the duct. This lower region is namely important, because of the erosion process. Adjusting the position of the pitot tubes involves using a calliper and mini levels. The calliper allows changing the elevation of the pitot tubes within Mobi-Gust 2 from outside ([figure 46](#)). The mini-levels help positioning the pitot tubes parallel to the flow ([figure 47](#)). The methods are explained in [appendix E](#). The earlier mentioned plank with glued sand ([§2.2.2.4](#)) was again used to match the roughness of the transition zone ([figure 48](#)). Before positioning the pitot tube to the following desired vertical position, it is shortly manoeuvred towards the roof of the duct. This manoeuvre will create spikes in the measured velocity data. The measurements namely focus below the centreline. Consequently, the pitot tube crosses the centreline of the duct, until it reaches the roof (i.e., passing maximum and minimum velocities respectively). These spikes become visible by averaging the raw measured velocity data. These spikes help identifying the different periods over which the actual averaging will take place. Recognizing periods namely gets harder while moving away from the walls, as velocity gradients become more subtle. The fan will be configured into maximum power, to provide similar wind conditions throughout the test. It is noted that the power supply will not be recharged in between measuring a full velocity profile.

*Table 6 - Elevations measured; all values are in [mm]*

$z_c$	$z_1$	$z_2$	$z_3$	$z_4$	$z_5$	$z_6$	$z_7$	$z_8$	$z_9$	$z_{10}$	$z_{11}$
75.0	5.0	7.5	10.0	12.5	15.0	17.5	20.0	25.0	30.0	35.0	50.0



*Figure 46 – Using a calliper to adjust the elevation of the pitot tube*



*Figure 47 – Using a mini-level to place the pitot tube parallel to the flow*



*Figure 48 – A view of the measurement setup*

The obtained data must be processed. [Figure 49](#) (next page) summarizes the approach. The upper panel in [figure 49](#) shows raw velocity data. The first elevation ( $z_c$  [mm]), i.e., before the strong variability starts, lies along the vertical centreline of the duct ([table 6](#)). This initial measurement showed whether the flow was steady or not. The actual measurement then continued near the bottom; and progressed upward. The middle panel in [figure 49](#) shows a one-second moving average of the same data, so that the explained spikes appear. Consequently, periods are more easily isolated and averaged per elevation. The averaging will take place over one-minute periods. The lower left panels in [figure 49](#) show how the logarithmic fits are obtained. The fitting requires three basic steps. Firstly, the elevations and velocities are plotted on a semi-log scale (lower left panel in [figure 49](#)). Secondly, the logarithmic velocity profile ([equation 34](#)) is transformed using elementary logarithmic operations ([equation 35](#)). The transformed logarithmic profile is linear on the mentioned semi-log scale. Finally, linear regression is used to fit the data. The fitting parameters ( $A$  [m/s] &  $B$  [m<sup>2</sup>/s]) are shown in [equation 36](#) and [37](#). These fitting parameters directly follow from the mentioned transformations. These fitting parameters are used to calculate the earlier mentioned flow properties ([§2.2.1.4](#)). Overall, the results are plotted on a normal linear scale (lower right panel in [figure 49](#)). After doing so, the logarithmic profiles appear (if applicable).

## Part II

### Proof Of Concept (POC): methodology

35)

$$u(z) = A \ln(z) + B$$

36)

$$A = \frac{u^*}{\kappa}$$

37)

$$B = -\frac{u^*}{\kappa} \ln(z_0)$$

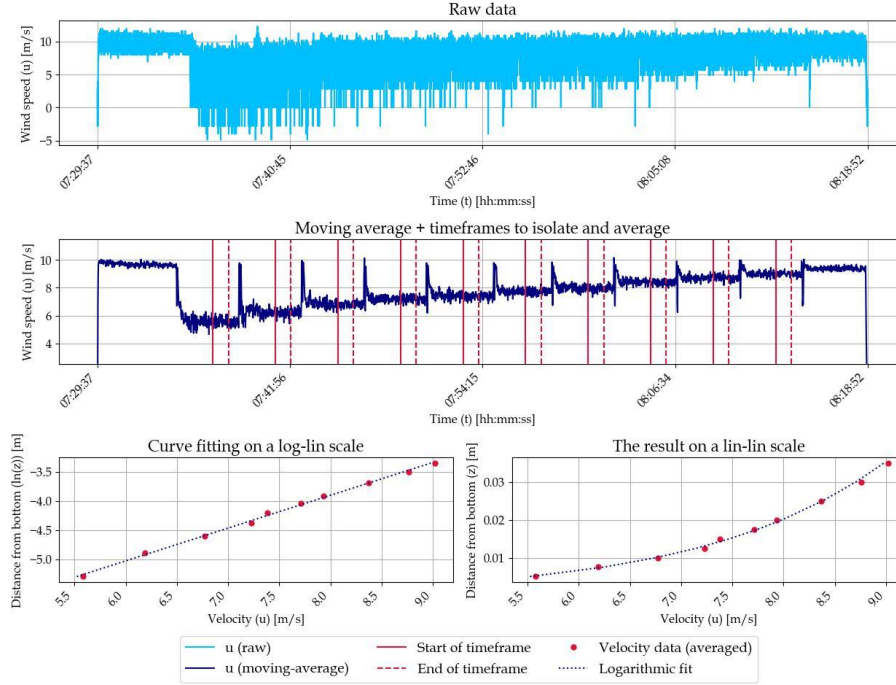


Figure 49 – The followed approach to measure velocity profiles within Mobi-Gust 2

The fitting parameters are used to estimate the bed shear stress. The bed shear stress ( $\tau_b$  [ $N/m^2$ ]) follows from the friction velocity ( $u^*$  [ $m/s$ ]) and the air density ( $\rho_a$  [ $kg/m^3$ ]); see [equation 38](#) ([Schierck, 2019](#)). The pitot tube can be mounted at the up- and downwind end of the erosion zone. Consequently, changes in the bed shear stress can be assessed along this stretch. This is shown in [figure 50](#); which for convenience simplifies the bed and the development of the flow.

38)

$$\tau_b = \rho_a (u^*)^2$$

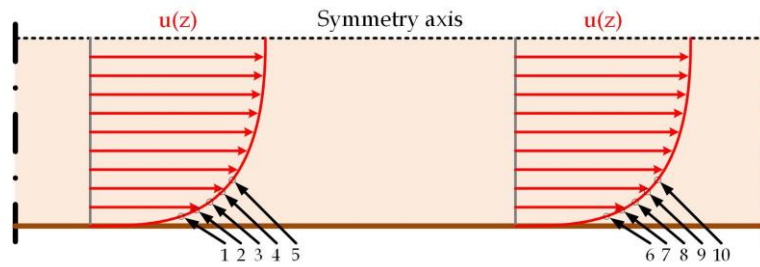


Figure 50 – Side view: measuring velocity profiles at two longitudinal locations

To close off, the Root Mean Squared Error ( $RMSE$  [ $m/s$ ]) is determined; [equation 39](#) ([Barnston, 1992](#)). This parameter is used to check the resemblance of a fit to the measured data; and considers the squared distance between the measured- ( $u_i$  [ $m/s$ ]) and the fitted ( $\hat{u}_i$  [ $m/s$ ]) velocities. The result averaged over the amount of datapoints ( $N$  [ $-$ ]); and the square root is taken.

39)

$$RMSE = \sqrt{\frac{\sum_{i=1}^N (u_i - \hat{u}_i)^2}{N}}$$

## Part II

### Proof Of Concept (POC): methodology

#### 2.2.2.7 Exploring the erosion performance of Mobi-Gust 2

The last experiment is probably the most important. The test namely uses Mobi-Gust 2 to check whether it is able to generate erosion in-situ. To this end, Mobi-Gust 2 is taken to the same location where the applied research will take place; i.e., the Sand Engine ([appendix A](#)). Additionally, the mobility of Mobi-Gust 2 is put to the test; as well as the (dis)mounting process. Mobi-Gust 2 is designed to fit in a relatively normal car ([appendix G.2.1.2.1](#)); still, that has to be tested. Next, a box wagon is converted so that Mobi-Gust 2 can be transported by foot ([appendix G.2.1.2.2](#)). The box wagon was converted for two reasons. Firstly, an available 4x4 vehicle requires supervision to be used. Yet, the staff of the Hydraulic Engineering laboratory of Delft University of Technology endure a relatively busy period. Secondly, the weather is very unpredictable; as it is wintertime in The Netherlands. Overall, in order to plan spontaneous field expeditions, the box wagon was converted to allow independent expeditions. This box wagon namely allows using private transportation, making the mentioned assistance obsolete. As mentioned before, conducting fieldwork is inherently linked to a dedicated safety plan. While assistance is not strictly required, field expeditions cannot be performed solo because of safety.



## 2.3 Analysing the performance of Mobi-Gust 2

This section regards the results and analysis of this Proof of Concept (POC). A large share of the results is occupied by the realisation of Mobi-Gust 2 itself (figure 51 & figure 52). As explained, Mobi-Gust 2 consists of a mobile wind tunnel system and a wind gauging system. The performance of Mobi-Gust 2 is largely determined by its design (§2.2.1) and its instalment (appendix G.3). Mobi-Gust 2's performance is checked through a series of experiments (§2.2.2). The experiments are subdivided in seven main tests: §2.3.1 explored the durability of the power supply; §2.3.2 studied the wind (gauging system) and its properties; §2.3.3 explored the drainage rate of the saltation hopper; §2.3.4 tested Mobi-Gust 2's sand tightness; §2.3.5 studied the achievable wind speeds within Mobi-Gust 2, in relation its modular design; §2.3.6 tested the flow development within Mobi-Gust 2; and §2.3.7 explored Mobi-Gust 2's in-situ erosion performance. These experiments are primarily conducted in the Hydraulic Engineering laboratory of Delft University of Technology. Yet, the last experiment involved a field expedition that visited the Sand Engine (appendix A).



Figure 51 – Constructing the mobile wind tunnel system

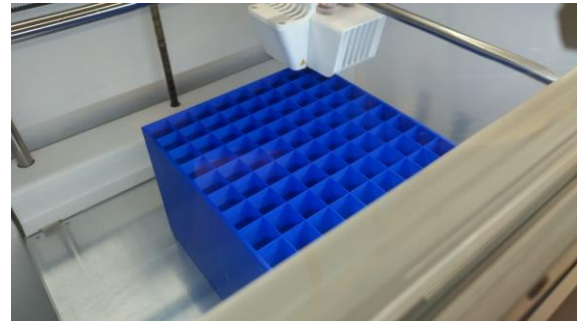


Figure 52 - 3D-printing the honeycomb screen

### 2.3.1 Evaluating the robustness of the power supply

This test considered the robustness of the power supply. Next to the power supply, other electrical systems are involved as well (i.e., the fan and the wind gauging system). The theoretical discharge duration (§2.2.1.8) is tested, as described in the approach (§2.2.2.1). The test was reconducted once, due to a compromised power supply. The problem concerned loose connections between the power supply and Mobi-Gust 2's electrical systems. The faulty result is also included, as it matters for the main research (part 3; §3.4). The duration of both tests slightly varied, as the initial test lasted 139 [min] and 29 [s]; while the follow-up test lasted 135 [min] and 55 [s]. The gathered raw wind speed data is visible in figure 53, as well as their moving averages (i.e., abbreviated to MA). The moving averages are determined over one-second intervals. The wind speed data is also visible in appendix I.2.1 (i.e., raw and processed).

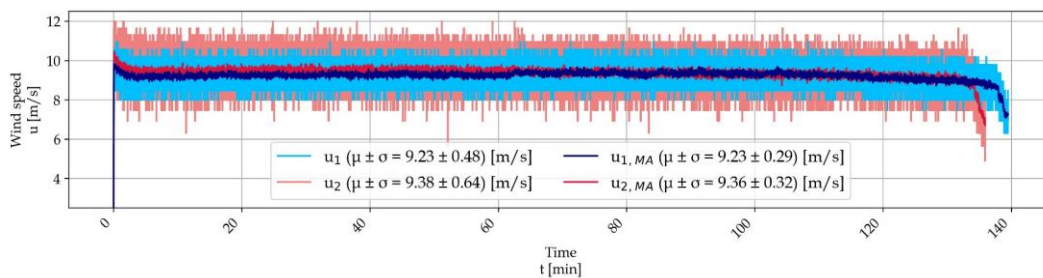


Figure 53 – The wind speed data (non-trimmed) used to assess the durability of the power supply



### 2.3.2 Exploring the wind (gauging system) properties

The second test considers the properties of the wind (gauging system). The test is conducted according to the described methodology (§2.2.2.2). As explained, this involves re-using the data from the previous experiment (§2.3.1). One of these experiments was faulty; and the valid one was of course used in this analysis. The isolated periods are visible in figure 54. Next, table 7 shows the calculated statistics (§2.2.2.2). These statistics were determined for the raw data, as well as the moving averages (i.e., abbreviated to *MA*). The moving averages are again determined for one-second periods. Unfortunately, the system revealed a variable sampling frequency. The number of measurements at the start, middle and end of the dataset respectively are 2,615 [–], 1,915 [–] and 1,547 [–]. Consequently, the mean sampling frequency at the start, middle and end of the dataset respectively concern 43.58 [Hz], 31.92 [Hz] and 25.78 [Hz] (i.e., rounded to two decimals). The wind speed data is also visible in appendix I.2.1 (i.e., raw and processed).

Table 7 – Wind gauging characteristics (SNR = Signal to Noise)

Statistics	$\mu_u$ [m/s]	$\sigma_u$ [m/s]	$SNR_u$ [–]	$r_u$ [–]	$\sigma_{u,MA}$ [m/s]	$SNR_{u,MA}$ [–]	$r_{u,MA}$ [–]
Full dataset	9.40	0.59	15.93	0.062	0.20	47.00	0.021
Begin isolated	9.90	0.60	16.50	0.060	0.17	58.24	0.017
Middle isolated	9.41	0.57	16.51	0.060	0.16	58.81	0.017
End isolated	8.80	0.52	16.92	0.059	0.15	58.67	0.017

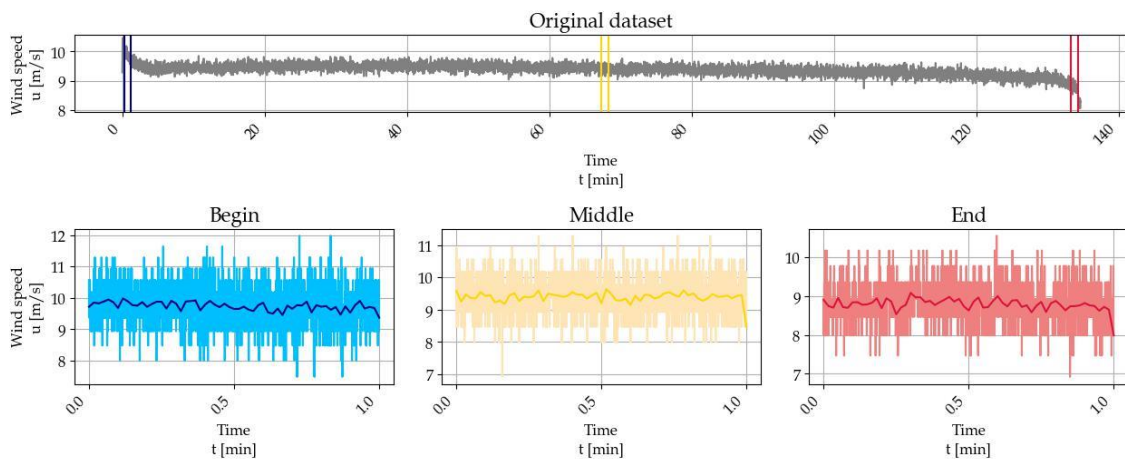


Figure 54 – The wind speed data used to find the properties of the wind gauging system;  
The upper panel shows the original data (timed and averaged), originating from the second test in figure 53;  
The upper panel additionally shows where the subsets are originating from (i.e., begin, middle and end)

### 2.3.3 Evaluating the drainage rate of the saltation hopper

The third test regarded the drainage rate of the saltation hopper. The test was conducted by following the instructions from the methodology (§2.2.2.4). A small repetition includes the following. A known mass of sand was added in the saltation hopper. After filling, the time was recorded until the hopper fully drained (figure 55). The recorded mass and time were used to establish discharge rates per gap size.

## Part II

### Proof Of Concept (POC): results and analysis



*Figure 55 – Recording the drainage period of the saltation hopper*

Table 8 shows the results of the test. Some of the lids clogged; and the tests were thus reconducted a couple of times (i.e., to rule out mistakes in the approach).

*Table 8 – Saltation hopper calibration for Sand Engine sand*

Lid [–]		1	2	3	4	5
Size [mm]		0.97	1.01	1.52	2.03	3.01
Test one	$m_s$ [g]	Clogged	Clogged	1,008	1,001	1,005
	$t_s$ [s]	Clogged	Clogged	123.25	41.56	17.65
Test two	$m_s$ [g]	Clogged	Clogged	997	1,010	1,009
	$t_s$ [s]	Clogged	Clogged	152.97	42.13	18.08
Test three	$m_s$ [g]	Clogged	Clogged	998	1,001	1,006
	$t_s$ [s]	Clogged	Clogged	139.57	37.65	17.16
Mean rate	$\mu_{u_s}$ [g/s]	Clogged	Clogged	7.28	24.88	57.12
Standard deviation rate	$\sigma_{u_s}$ [g/s]	Clogged	Clogged	0.60	1.14	1.00

### 2.3.4 Investigating the sand tightness of Mobi-Gust 2

The fourth test considers the sand tightness of Mobi-Gust 2. The test is performed according to the described approach (§2.2.2.4). Yet, a small recap includes the following. The saltation hopper was used to discharge a known mass of sand into an operational Mobi-Gust 2. After the saltation hopper fully drained, the sand trap was emptied. After weighing the collected sand, it was compared to the added sand mass. The outcomes of the experiment are shown in table 9; which also repeats the configuration of each test.

*Table 9 – Outcomes of the sand tightness test*

Gap taping	–	–	x	x
Wire mesh cylinder	–	x	–	x
Configuration	1	2	3	4
Added sand mass [g]	10,047	10,031	10,040	10,032
Collected sand mass [g]	9,840	9,966	9,879	10,017
Lost sand mass [g]	207	65	161	15
Loss [%]	2.06	0.65	1.60	0.15
Loss compared to configuration one [%]	0.00	–68.60	–22.22	–92.75

## Part II

### Proof Of Concept (POC): results and analysis



Figure 56 - Not using additional measures leads to sand losses;  
Sand is able to climb out of the sand trap without using the wire mesh



Figure 57 - Additional sand losses were spotted at transitions (this is from a few tests)

### 2.3.5 Exploring the wind speed in the modular design of Mobi-Gust 2

The fifth test explored the achievable wind speeds within the modular design of Mobi-Gust 2. The methodology clarified the approach (§2.2.2.5). In short, the wind speeds within Mobi-Gust 2 were measured; while systematically in- or excluding components. Table 10 repeats the configuration of each test. As explained, the intake (i.e., the fan and contractions), the erosion zone and the sand trap were used in all combinations. The wind speed data that belongs to table 10 is shown in figure 58 (next page). The shown wind speed data (figure 58) concerns moving averages over one-second periods. The wind speed data is also added to appendix I.2 (i.e., raw and processed).

Table 10 – The configurations (rows) and the components in use (columns) in the speed-component test

Configuration	1	2	3	4	5	6	7	8	9	10	11	12	13
Intake shield walls									x				
Honeycomb screen	x	x	x	x					x	x	x	x	x
Upwind transition duct	x	x				x	x		x	x	x	x	x
Downwind transition duct	x		x				x	x	x	x	x	x	x
Wire mesh cylinder										$x_d$	$x_c$	$x_u$	$x_c$
Saltation test													x

The tests in figure 58 (next page) are grouped. The grouping facilitates the readability and the assessment. The first group (upper left panel) considers the in- or exclusion of transition ducts; while including the honeycomb. The second group (upper centre panel) essentially does the same, while excluding the honeycomb. The third group (upper right panel) considers the influence of the intake shield walls. The fourth group (lower left panel) considers the influence of the wire mesh cylinder position. The fifth group (lower centre panel) considers the influence of using the saltation hopper. The sixth and final group (lower right panel) concerns the influence of battery drainage throughout the experiment. In elaboration, the sixth group consists of the first experiment ( $1_a$ ) that was reconducted at different instances. Reconducting the first experiment was done between experiment 8 and 9 (i.e.,  $1_b$ ), between experiment 12 and 13 (i.e.,  $1_c$ ) and after experiment 13 (i.e.,  $1_d$ ). The battery was not charged in the entire experiment. To finalize, the vertical bounds of each panel in figure 58 are constant; which enables visual comparison between the panels.

## Part II

### Proof Of Concept (POC): results and analysis

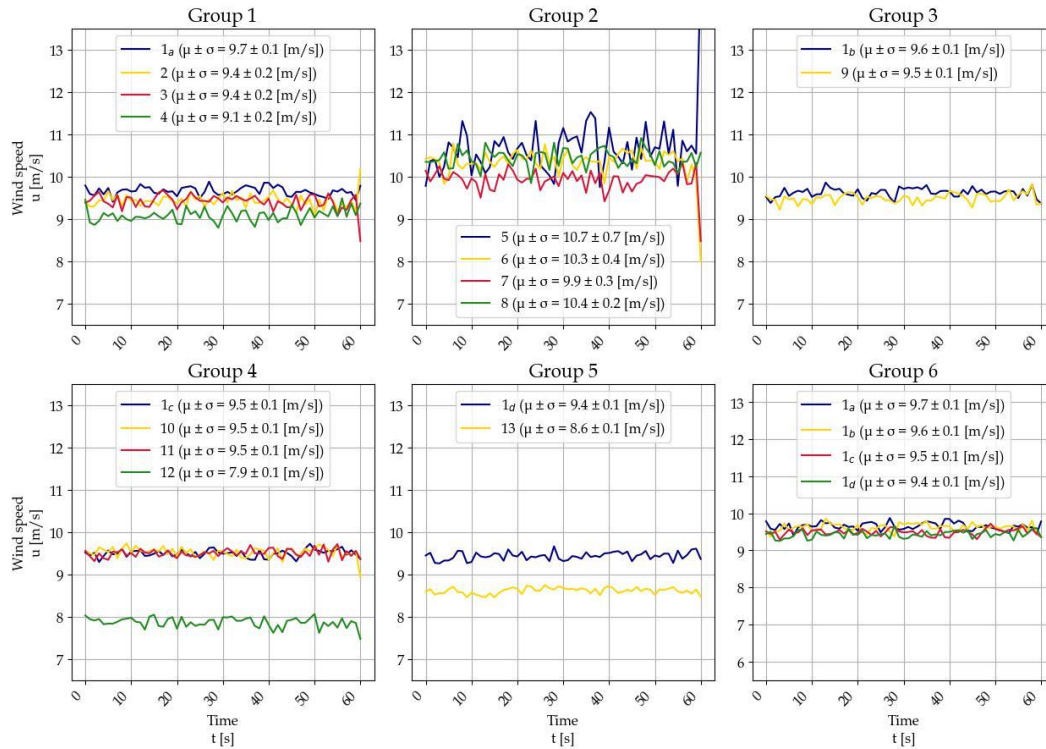


Figure 58 – Results of the speed-component test (grouped)

### 2.3.6 Investigating the flow development within Mobi-Gust 2

The sixth (and final laboratory) test explored the development of the flow within Mobi-Gust 2. The approach was detailed in the methodology (§2.2.2.6). A short recap contains the following. Vertical velocity profiles were measured, at the up- and downwind end of the erosion zone. Next, logarithmic velocity profiles were fitted to the measured data. Having those fits enables computing various flow parameters (table 11). The attained fits are compared to the measured data as well (i.e., by the Root Mean Squared Error). The data in table 11 belongs to the fits shown in figure 59. Two vertical profiles were measured per location (i.e., up- and downwind of the erosion zone). In elaboration, showing the variability between the tests, e.g., checking the employed method. The mean velocities in table 11 concern the vertically averaged velocities of the fitted profiles; between the bottom and the centreline of the duct. The raw wind speed data that was used to construct the velocity profiles are added to appendix I.2.

Table 11 – The fitting- and flow parameters originating from the fitting process

Velocity profile	Location	$A$ [ $m^1s^{-1}$ ]	$B$ [ $m^2s^{-1}$ ]	$RMSE$ [ $m^1s^{-1}$ ]	$u_m$ [m/s]	$u_*$ [ $m^1s^{-1}$ ]	$z_0$ [m]	$\tau_b$ [Pa]
A	Up	1.341	13.506	0.229	8.694	0.550	0.00004	0.0012
B	Down	1.567	13.969	0.133	8.348	0.642	0.00013	0.0039
C	Up	1.317	13.261	0.275	8.536	0.540	0.00004	0.0012
D	Down	1.609	14.199	0.156	8.425	0.660	0.00015	0.0045



## Part II

### Proof Of Concept (POC): results and analysis

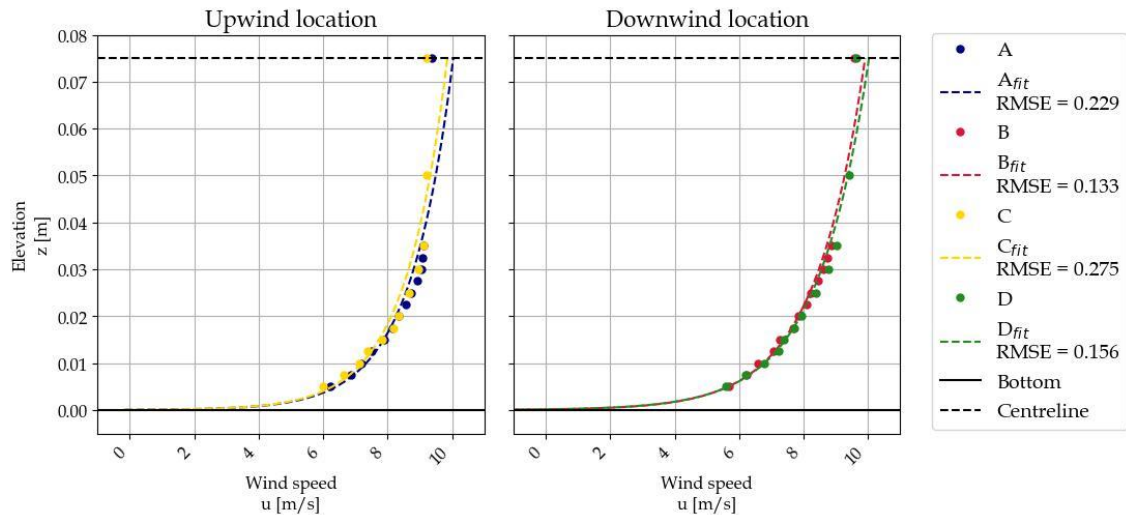


Figure 59 – The measured and fitted vertical velocity profiles that belong to table 11  
The logarithmic profiles are plotted between the bottom and centreline of the duct

### 2.3.7 Exploring the erosion performance of Mobi-Gust 2

Testing the in-situ performance of Mobi-Gust 2 caused mixed results. Mobi-Gust 2 easily fitted in the Chrysler Voyager (i.e., an MOV-vehicle); and the box wagon performed as intended (figure 60). Mounting Mobi-Gust 2 lasted about 20 [min] (i.e., with a field crew of three persons); and presented no problems. A mounted Mobi-Gust 2 is visible in figure 61. However, Mobi-Gust 2 was not able to generate aeolian erosion in-situ. Mind that figure 61 shows the old saltation hopper.



Figure 60 – Transporting Mobi-Gust 2 with the modified box wagon



Figure 61 – Mobi-Gust 2 deployed in a field expedition



## 2.4 Discussing the performance of Mobi-Gust 2

This section provides the discussion of this Proof of Concept (POC). Mobi-Gust 2's performance is checked by a series of experiments (§2.2.2). The performance of Mobi-Gust 2 is largely determined by its design (§2.2.1) and its instalment (appendix G.3). The experiments are subdivided in seven main tests: §2.4.1 explored the durability of the power supply; §2.4.2 studied the properties of the wind (gauging system); §2.4.3 explored the drainage rate of the saltation hopper; §2.4.4 tested the sand tightness of Mobi-Gust 2; §2.4.5 studied the achievable wind speeds within a modular Mobi-Gust 2; §2.4.6 tested the flow development within Mobi-Gust 2; and §2.4.7 explored Mobi-the in-situ erosion performance of Mobi-Gust 2. These experiments are mostly conducted in the Hydraulic Engineering laboratory of Delft University of Technology. Yet, the last experiment involved a field expedition that visited the Sand Engine (appendix A).

### 2.4.1 Discussing the robustness of the power supply

This test regarded the robustness of the power supply. The approach (§2.2.2.1) provided the results (§2.3.1) that are discussed in this section. Above all, the stability of the power supply seems suitable for its purpose.  $\text{LiFePO}_4$  batteries are known to exhibit minor voltage variations while discharging (PowerTech Systems, sd). The stability of  $\text{LiFePO}_4$  batteries is very different from other chemistries (figure 63). On the one hand, the linear discharging of a lead-acid battery allows to make simple estimates on the remaining lifetime (i.e., based on the remaining charge). Such estimates are handy when measuring outdoors. Yet on the other hand, the stability of the  $\text{LiFePO}_4$  battery results in rather stable winds (figure 62). This stability is crucial for the controllability and the reliability of Mobi-Gust 2. And after all, the durability test provides a total discharging duration; so that timekeeping still allows estimating the remaining lifetime of the power supply. For convenience, figure 62 repeats the moving averages of the performed tests (§2.3.1). The discharge curve of the  $\text{LiFePO}_4$  battery (figure 63) is directly visible in the timeseries (figure 62). While the wind speeds are relatively stable some variability can be spotted. This variability primarily focusses in the first and last 5 [min] of the timeseries. Outside these timespans variations are not very striking. Overall, the power supply supports aeolian research that requires stability (part 3).

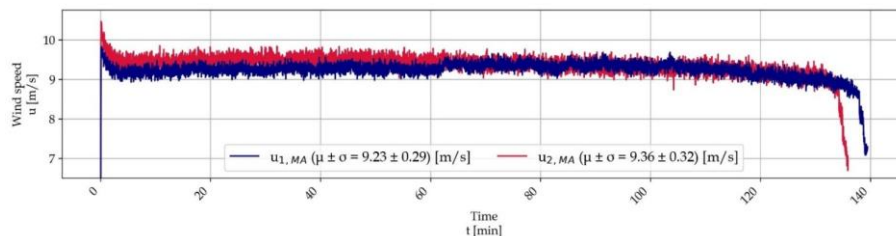


Figure 62 – The trimmed and averaged wind speed data used to assess the durability of the power supply

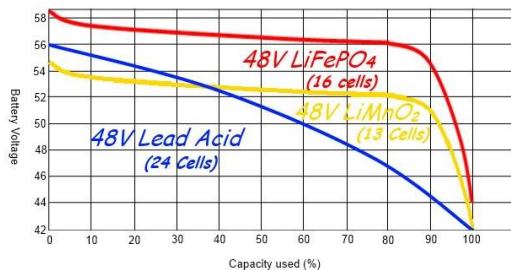


Figure 63 – Typical discharge curves for some batteries (Warren, 2016)



Figure 64 - The tailored casing of the power supply

Robustness, safety and mobility are generally safeguarded by this power supply. Safety (§2.3.1) is logically important when measuring outdoors. In elaboration, this power supply can cope with relatively harsh weather (Kassaeian, 2023). On top, the power supply is extra protected by a

## Part II

### Proof Of Concept (POC): discussion

tailored casing (figure 64; previous page). This casing amongst others shields against (saline) wetness. And as introduced, the power supply boosts the mobility of Mobi-Gust 2, as it is relatively small and light. Experience showed that the power supply is easy to handle and transport (§2.3.7).

Yet the robustness and the safety can also be compromised in some cases. As mentioned (§2.3.1), the durability test was reconducted once due to the malfunctioning of the power supply. With assistance from the laboratory staff the problem was identified. The issue concerned loose connections between the battery and other electrical components (figure 65). When these connections loosen, a reduced contact surface causes less efficient power transfer and losses into heat (Lokithor, 2022). The mentioned heat losses helped exposing the problem, as the battery connections became (very) hot. Again (§2.2.1.8), while  $\text{LiFePO}_4$  batteries are generally reliable and safe (Himax, 2024); it is clear that this release of heat might pose safety hazards.

The loose connections were discovered after roughly 65 [min] in test one. After discovery, the loose connections were immediately fastened. This fastening caused an immediate increase of the wind speed (i.e., the blue line in figure 62). This increase in wind speed confirms a restored power transmission between the power supply and the fan. In elaboration, the curve of the first test (i.e., the blue line in figure 62) roughly collapses on the second one (i.e., the red line in figure 62) following the repair. Next, the compromised test (i.e., the blue line in figure 62) lasted slightly longer (~5 [min]) than the other one (i.e., the red line in figure 62). This longer duration directly follows from the less efficient power transfer.

Multiple reasons may have caused the power supply issues. A possible cause is the charging process. Every time the battery is charged, clamps are fitted around the connections (figure 66). So, the charging may affect the connections; especially when charging takes place frequently. Next, transportation could also be the culprit. A driving car namely vibrates, which may have further impacted the situation. Yet mitigating the problem is rather straightforward. The problem is resolved by regularly checking the connections; and fastening them when necessary.



Figure 65 - The connections that may loosen

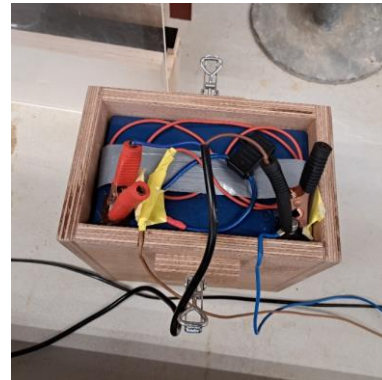


Figure 66 - Charging the battery

The second test represents conditions without issues. This test lasted about 135 [min] (i.e., the red line in figure 62). Mobi-Gust 2 thus stays operational for about 2 [h] and 15 [min]. This duration is a lower bound, as the fan was provided with maximum power (§2.2.2.1). As said, stable winds are observed after the first and before the last 5 [min] of the test. So, the power supply allows for about 2 [h] of relatively stable measurements. This duration is (far) less than the theoretical estimate of 180 [min] (appendix C.3). Amongst others, the difference is caused by neglecting various electrical components. For example, the power cables of Mobi-Gust 2 are quite long and thin. Besides having an effect on heat losses (Victron Energy, N.d.); the thinner and longer the cables, the higher the electrical resistance (Chomppff, 2021). The mentioned electrical resistance ( $R$  [ $\Omega$ ]) impacts other electrical properties, i.e., voltage ( $V$  [V]) and current ( $I$  [A]); that in turn impacts power transmission ( $P$  [W]); equation 40 and 41 (Chapman Electric Supply, Inc., 2024).

40)

$$V = IR$$

41)

$$P = VI$$

## 2.4.2 Reviewing the wind (gauging system) properties

The next experiment considered the wind (gauging system) properties. As explained, the data of the previous test was re-used for this analysis; and this data is relatively stable (§2.4.1). Wind speeds on average reach about 9.4 [m/s] (i.e., the red line in figure 62). Yet, wind speeds can be as high as 9.9 [m/s] or as low as 8.8 [m/s] (lower right panel of figure 67) at the operational edges of the power supply (i.e., when nearing fully charged, or fully drained conditions). It is stressed that these wind speeds concern maximum values; as measurements took place along the centreline of the duct (White, 2011). Vertically averaged velocities are logically lower than this maximum velocity, as treated in the flow development section (§2.4.6).

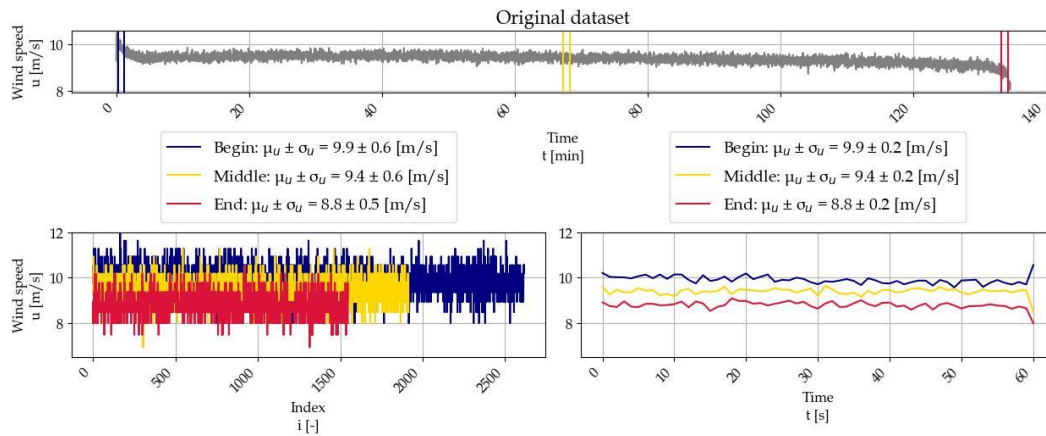


Figure 67 – The wind speed data used to find the properties of the wind gauging system; The upper panel shows the original data (timed and averaged), originating from the second test in figure 62; The upper panel additionally shows where the subsets are originating from (i.e., begin, middle and end)

The achieved wind speeds are (much) lower than the design wind speed (i.e., 15 [m/s]). The lower wind speeds follow directly from the design approach (§2.2.1.3). In repetition, empirical data from the prototype (i.e., Mobi-Gust 2) defined the cross-sectional area of Mobi-Gust 2. This approach matched with the recommendations from that research (appendix C.1.3); yet it neglects the system characteristics of Mobi-Gust 2 itself. In elaboration, the followed approach neglects the balance between the (finite) pressure capacity of the fan; and the pressure losses throughout Mobi-Gust 2. This balance can be accounted for by conducting a pipe flow analysis (appendix D). Such a method unifies mass conservation and energy losses (Çengel & Cimbala, 2014).

Next, the wind gauging system measures signals over noise. The associated signal-to-noise ratios double or triple after averaging (§2.3.2). It was expected that the system would measure signals over noise; as interferences (e.g., electromagnetic, mechanical or environmental) were actively mitigated during the design stage (§2.2.1.7). As explained, these interferences primarily target the pressure sensor. Interference-mitigation for example involved sensor shielding and regularly performing zero-measurements. Measuring signals over noise manifested itself in several observations. As mentioned, the discharging curve of the power supply (figure 63) emerges from the wind speed data (figure 62). Another large-scale motion that could be present is a spiralling flow produced by the fan (De Wilde, 2020). Yet, this spiralling motion seems to be absent in the gathered data (also see §2.4.5 and §2.4.6). Next, on the smaller scale the wind gauging system seems to be effective as well. The non-averaged data in figure 67 (lower left panel) shows all kinds of fluctuations. These fluctuations result from the mentioned interferences, the accuracy of the pressure sensor (NXP, 2021), or turbulence (Uijtewaai, 2022). The measured fluctuations are on average 0 [m/s]; which is by definition required (Schiereck, 2019). The fluctuations provide a measured relative turbulence intensities of 6 [%], with respect to the centreline wind speed (§2.3.2 & appendix I.2.1). This slightly increased relative turbulence intensity might result from the mentioned interferences. The pressure sensors are namely shielded by 3D-printed caps. Yet a conductive cap works even better against (electromagnetic) interferences (Eastsensor, 2022). For example, a grounded metal box would be a very effective shield (Elektor, 2022). On top, the

## Part II

### Proof Of Concept (POC): discussion

accuracy of the pressure sensor (NXP, 2021), as well as the less generic flow properties of an underdeveloped flow, might have been influential as well. The development of the flow will be further treated shortly (§2.4.6). Still, the observed relative turbulence intensities are also not very striking. In elaboration, the relative turbulence intensities in uniform wall flow reach between 5-10 [%] (Schiereck, 2019). In mixing layers or jets this value might even increase to 20-30 [%]. Mind, that the percentages in this case are defined with respect to the average centreline velocity. Overall, Mobi-Gust 2 seems free of large distortions (e.g., the mentioned spiral flow). Lastly it is noted that averaging the velocity results in lower relative turbulence intensity (i.e., about 2 [%] with respect to the average centreline velocity; §2.3.2 & appendix I.2.1). This decrease follows from averaging (turbulent) fluctuations.

The analysis also brought a variable sampling frequency to light. This variable sampling frequency is visualized in the lower two panels of figure 67. The figure namely shows identical data, having a duration of one minute each. As reported in the results (§2.3.2), the figure thus actually shows a decreasing sampling frequency (i.e.,  $f_{begin} > f_{middle} > f_{end}$  [Hz]). The cause is not yet fully identified; but is most likely software-related (Isra, 2017). In elaboration, inefficient datalogging (appendix C.2.2) seems to be the main suspect (Todd, 2016).

Another critical point involves the resolution of the wind gauging system. As explained (§2.2.1.7), the wind speed is measured through a set of communicating hardware. A short recap includes the following. The wind speed is estimated by means of the pitot tube formula (Çengel & Cimbala, 2014). This formula requires the differential pressure; which is measured by a pitot tube. In turn, the differential pressure is converted by a pressure sensor into an output voltage. Finally, this voltage converted by a microcontroller into digital output. The associated relations (equation 18, 19 and 20; §2.2.1.7) can be combined into one relation, as repeated in equation 42, while minding an incorporated factor of 1,000 (§2.2.1.7). The combined relation provides a direct link between digital output (i.e.,  $ADC_{out}$  [-]) and wind speeds (i.e.,  $u_a$  [m/s]). The resolution of the wind speed can be determined from this combined relation. The Analogue-to-Digital Converter (ADC) namely has a resolution of 10-bits (Arduino SRL, 2024). In other words, the ADC can represent 1,024 [-] discrete integer values. Using an implied step size of 1 [-] for the digital output, enables determining the step size of the wind speed. Figure 68 shows the result. The mentioned figure also includes the step size of the differential pressure and the voltage output. These step sizes follow from the mentioned (adapted) relations. In the case of the used measurement setup, the baseline of the ADC is 512 [-] (i.e., when measuring zero pressure differential). Moving just one digital value away from this baseline causes a wind speed change of 2.82 [m/s] (figure 68). Wind speed step sizes are however decreasing for increasing pressure differentials. To be clear, measured values are not faulty, yet between 0-2.82 [m/s] there is simply no information.

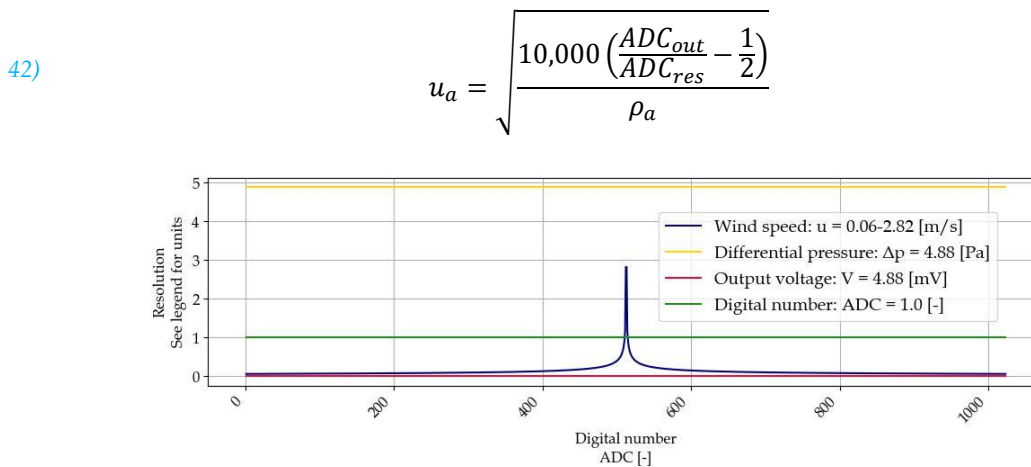


Figure 68 – Resolution of the wind speed, differential pressure, output voltage and the Analogue-to-Digital Converter



## Part II

### Proof Of Concept (POC): discussion

The coarseness of the resolution is caused by several main reasons. The pitot tube formula is quadratic and steepest around the baseline (figure 68). For convenience, the pitot tube formula (§2.2.1.7) is repeated in equation 43. Next, the resolution of the pressure sensor itself is rather coarse. To clarify, the pressure range of the sensor is  $\pm 2$  [kPa] (NXP, 2021). Yet, the measured differential pressures concern only about  $\pm 62.25$  [Pa] of this range. The calculated differential pressure originates from applying the pitot tube formula (equation 43); and substituting a wind speed representative for this research (e.g., 10 [m/s]); and an air density applicable to Standard Temperature and Pressure (STP) conditions (i.e., 1.225 [kg/m<sup>3</sup>]; appendix B). Next, the resolution of the ADC matters. As said, the ADC discretizes the mentioned pressure range into a finite number of values. A higher ADC resolution thus implies smaller step sizes. Mind that the step sizes around the baseline remain largest due to the pitot tube formula. All in all, the pressure range is too wide and discretized too coarse, causing relatively large step sizes for small wind speeds (figure 68).

43)

$$\Delta p = \frac{\rho_a u^2}{2}$$

Next the accuracy of the wind gauging system is verified. The wind speed was verified using a handheld anemometer (Amazon, N.d.); and the specifications of the device are added in appendix F. Most importantly the anemometer has an error of about 5 [%] relative to the sensed values. The anemometer senses wind speeds between 9.5-10.5 [m/s] (e.g., figure 69 and figure 70). The lowest values from the anemometer thus approach the mean values from the wind gauging system (e.g., figure 62 or figure 67). Or, the mean values from the anemometer (e.g., 10 [m/s]) deviate about 5 [%] from the mean values from wind gauging system (e.g., figure 62 or figure 67). So, the wind gauging system (just) falls within the accuracy range of the used handheld anemometer.

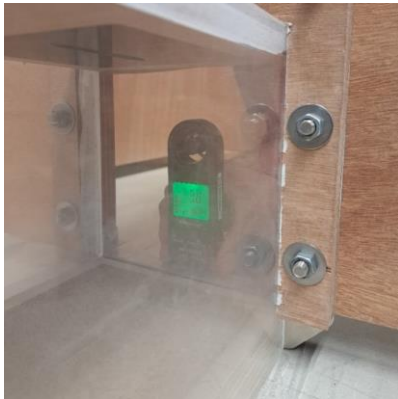


Figure 69 – Using a handheld anemometer (1)



Figure 70 – Using a handheld anemometer (2)

### 2.4.3 Discussing the drainage rate of the saltation hopper

Next, the drainage rate of the saltation hopper was considered. The methodology (§2.2.2.3) provided the results (§2.3.3) that are reviewed in this section. In repetition, this basic test involved filling the hopper with a known mass of sand. Next, the time was recorded until the hopper fully drained. The recorded mass and time provided an estimate of the drainage rate.

Not all lids performed well, given the used granular material. Some lids clogged completely (i.e., lid 1 and 2; §2.3.3). Yet, these lids are not useless; because if finer granular material is used, these might still be functional. Next, Lid 3 (§2.3.3) partly clogged (figure 71), primarily due to artefacts in the granular material (e.g., shell fragments). Next, lid 4 (§2.3.3) showcased the best results, as it did not clog; and since lid 5 (§2.3.3) drained relatively fast. To clarify, lid 5 (§2.3.3) drains 1 [kg] of sand in just 17.5 [s] (on average). Yet, in the end also lid 4 provided trouble. The drainage rate of lid 4 (i.e., 24.88 [g/s]) amounts to roughly requiring 15 [kg] of sand in a test of 10 [min]. Yet, various tests showed that less sand was needed (e.g., §3.3.4). This observation shows that also lid 4 occasionally jams; probably due to mentioned artifacts (figure 71).



## Part II

### Proof Of Concept (POC): discussion

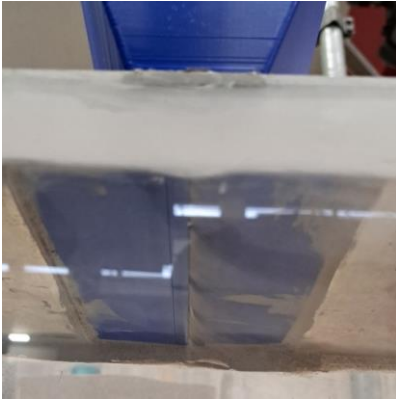


Figure 71 - Partial clogging of the saltation hopper



Figure 72 - Temporary closing lid

Some final remarks can be made. It is noted that this saltation hopper calibration is not universal. To clarify, the calibration is not valid when using sand that has another size- or shape distribution; or if new lids with other gap sizes are printed. Strictly speaking, this calibration only holds for the Sand Engine at the time the sand samples were taken. To clarify, the Sand Engine is morphodynamically active ([appendix A](#)), so the size- and shape distribution its sand grains changes over time. Next, this test and the next one showed that some residual mass remains on the lids (see [§2.3.3](#) for the picture). This residual mass is measured ([appendix I.3.5](#)) and the experiments were corrected for this discrepancy. The applied research ([part 3](#)) which involves the saltation hopper will be corrected for this as well. On top, the same granular material will be used in these tests, so that the calibration holds. As a final remark, it is noted that sand grains are ejected upward when the saltation hopper almost fully drains; i.e., because of the air pressure within Mobi-Gust 2. For the time being an acrylic plate was used to mitigate this ([figure 72](#)).

#### 2.4.4 Revising the sand tightness of Mobi-Gust 2

This test considered the sand tightness of Mobi-Gust 2. The results ([§2.3.4](#)), which followed from the approach ([§2.2.2.4](#)), are discussed in this section. Overall, the system is virtually sand tight when all available mitigation measures are used. As explained, this involves gap taping and using the wire mesh cylinder ([§2.3.4](#)). In repetition, the taping should be performed at the transition between the erosion zone and the sand trap; as well as the hatches in the roof of the erosion zone; and the inclined edges of the removable sand tray in the sand trap. On top, if the wire mesh cylinder is used correctly, it does not affect the airflow within Mobi-Gust 2 ([§2.3.5](#)). When using all these measures, only 0.15 [%] of 10 [kg] sand is lost. Most of this negligible loss is observed beneath duct connections ([§2.3.4](#)). Mobi-Gust 2 was namely elevated during the experiments ([figure 73](#)). Consequently, there is an empty space below the connections. Yet, when measuring in-situ there will be a surface beneath these connections; likely mitigating the observed losses.



Figure 73 - An elevated Mobi-Gust 2 in the Hydraulic Engineering laboratory

## Part II

### Proof Of Concept (POC): discussion

Still, there is some concern about the mentioned connections. The flanges are namely fixed to the ducts by sealant edges. Experience showed that these sealant edges fail quite easily. Some existing voids might thus grow by using Mobi-Gust 2. While sand losses are negligible at the moment; this might change in the (near) future.

Next, sand losses are only assessed by means of using the saltation hopper. This approach is justified as it provides the limiting case. If sand is added through the saltation hopper, it needs to cross the entire duct system. In other words, these sand grains encounter more transitions, with respect to sand grains that would have been eroded in the erosion zone. Consequently, the sand grains that are added in the saltation hopper has the largest opportunity to leave the system. So, if sand losses are negligible in this test, they are surely negligible in a normal erosion test without using the saltation hopper.

#### 2.4.5 Reviewing the wind speed in the modular design of Mobi-Gust 2

Next, the achievable wind speed within a modular Mobi-Gust 2 was tested. The approach (§2.2.2.5) provided the results (§2.3.5) that are discussed in this section. For convenience, the configuration per test is repeated in table 12. The outcomes are reviewed per group; and these groups were already clarified in the results section (§2.3.5). The graphs within this section show moving averages that are determined over one-second intervals. The raw data and the associated unaveraged variability can be seen in appendix I.2.2.

Table 12 – The configurations (rows) and the components in use (columns) in the speed-component test

Configuration	1	2	3	4	5	6	7	8	9	10	11	12	13
Intake shield walls									x				
Honeycomb screen	x	x	x	x					x	x	x	x	x
Upwind transition duct	x	x				x	x		x	x	x	x	x
Downwind transition duct	x		x				x	x	x	x	x	x	x
Wire mesh cylinder										$x_d$	$x_c$	$x_u$	$x_c$
Saltation test													x

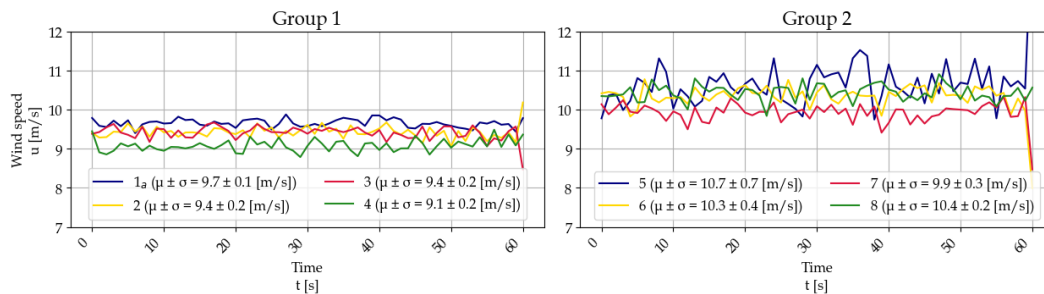


Figure 74 – The results for group 1 and 2 of the speed-component tests

Group one considers the influence of omitting (transition) ducts, while using the honeycomb. From an energy-loss perspective, velocities should increase when excluding parts from the system. To clarify, using fewer parts leads to a lower (frictional) resistance (White, 2011); and thus higher wind speeds. Yet the opposite is observed when the measured centreline velocities are checked; see the left panel of figure 74 ( $u_1 > u_2 \&_3 > u_4$  [m/s]). The observations can be explained by swapping the energy-loss perspective for a flow-development perspective. In clarification, just downwind of the honeycomb the flow is nearly uniform; except around the centreline of the duct, where (fan-) velocities are generally lower (Stevens, N.d.). From the honeycomb onward boundary layers start to develop from all boundaries (§2.2.1.4). In other words, wall friction ensures that velocities near the boundaries decrease (i.e., no-slip); while centreline velocities increase because of mass conservation (Chassagne & Van den Bremer, 2021). As mentioned, the fan produces lower centreline velocities, which increase by the explained aerodynamic effects. This further illustrates the importance of the transition zone. When this developing process is unhindered, momentum

## Part II

### Proof Of Concept (POC): discussion

transfer will finally ensure that a logarithmic velocity profile will appear (Uijttewaal, 2022). Overall, omitting parts results in less (frictional) resistance and thus higher cross-sectionally averaged velocities. Yet simultaneously, centreline velocities have increased less, as the flow is less developed. Consequently, omitting parts may lead to lower centreline velocities, even though the cross-sectionally averaged velocity has increased. And the pitot tube of course exactly measured along the centreline of the duct; which explains the behaviour. Figure 75 illustrates the explanation in a schematized way. The flow just downwind of the honeycomb screen was drawn completely uniform to ease the schematisation. On top, the observations show that the honeycomb effectively mitigates the spiral flow from the fan, as the component onsets flow development.

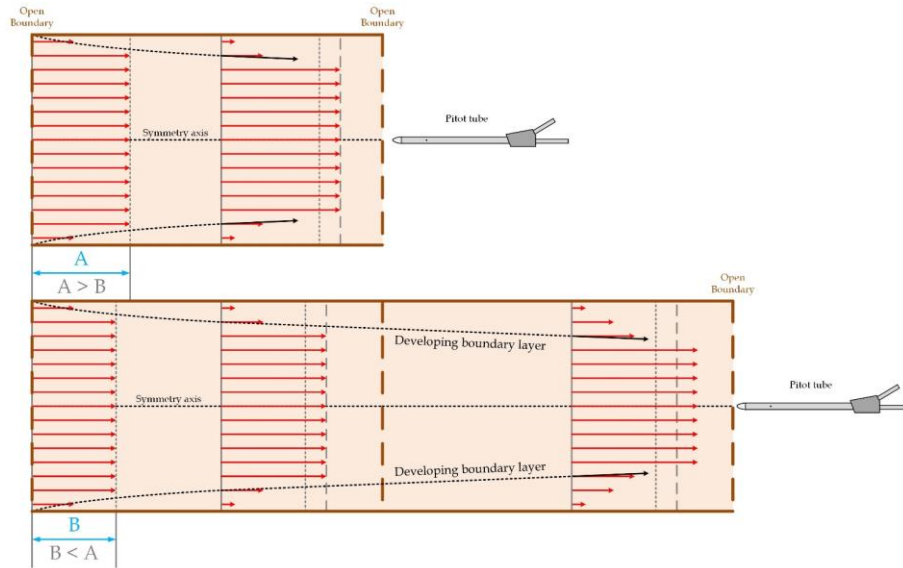


Figure 75 – Less parts means a higher cross-sectionally averaged velocity (energy-loss perspective); Yet also centreline velocities are less increased (flow-development perspective)

The second group focussed on excluding (transition) ducts, without using the honeycomb. In contrast to group one, measured centreline velocity increase if ducts are excluded from the system; see the right panel of figure 74 ( $u_5 > u_{6 \& 8} > u_7$  [m/s]). In this experiment, the energy-loss perspective seems to be more important than the flow-development perspective. This is explained by not using the honeycomb; i.e., hampering the onset of flow development. The lack of flow development is visible in the more chaotic flow behaviour. The graphs in the right panel of figure 74 namely show much more variability. On top, the variability increases when omitting ducts; which is logical as the pitot tube approaches the fan and its chaotic motions. Mind that the graphs in figure 74 are just showing moving averages. Consequently, much of the variability is averaged out. Yet, as explained appendix I.2.2 contains the unaveraged wind speed data. The unaveraged data shows much more chaos. Especially, when comparing in test setup 5-8 with test setup 1-4. Non-averaged velocities even approach 0 [m/s] occasionally. This chaotic behaviour hints at the presence of larger flow structures (e.g., the spiral flow produced by the fan). These observations support the claims about the honeycomb effectively mitigating the spiral motions from the fan. This large-scale spiralling flow could also not be observed during smoke tests (figure 76). Yet, it was hard to visually analyse the smoke-laden flow; as the smoke was advected relatively fast. Using a high-speed camera would probably improve this. Other flow-visualizing techniques may include Particle Tracking Velocimetry (PTV) or Particle Image Velocimetry (PIV) (Uijttewaal, 2022). Yet Mobi-Gust 2 can also be digitized to simulate the flow.

## Part II

### Proof Of Concept (POC): discussion

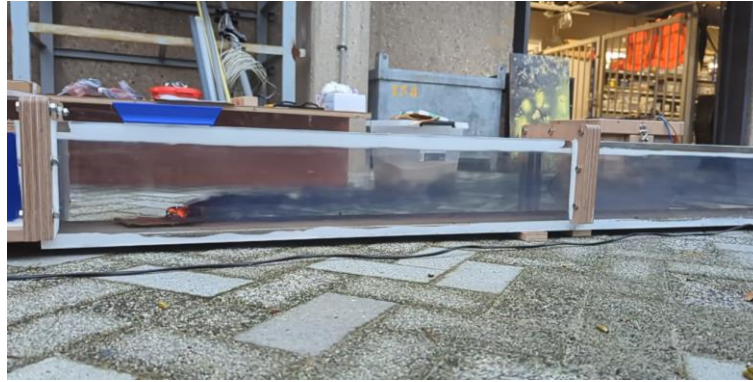


Figure 76 - Performing a smoke test (also notice the old saltation hopper)

The first two groups provided some valuable insights. As mentioned, group one and two suggest the onset of flow development; i.e., an effective honeycomb and transition zone. At the same time, the data of group two (i.e., where energy losses were dominant) suggest that extra ducts are not that 'expensive' in terms of the achievable wind speed. Adding one transition duct decreases the centreline wind speed by only 3-4 [%]; with respect to using no transition ducts at all. Adding two transition ducts causes a total decrease of only about 7-8 [%]. These observations open up the discussion to add extra transition ducts in order to accommodate flow development. It is however stressed that the fan only has a limited pressure capacity. On top, it might be wise to not base the decision on measured centreline velocities only, but also on cross-sectionally averaged velocities. Yet now that Mobi-Gust 2 is already built, extra transition ducts can easily be added and tested.

Next, some layouts in the first two groups approached the geometry of prototype; i.e., Mobi-Gust 1 (figure 44 & figure 45; §2.2.2.5). As shown in the referenced figures, Mobi-Gust 1 included a contraction, an erosion zone and a sand trap. This configuration corresponds to Mobi-Gust 2 in configuration 4 and 5 (table 12). Compared to the prototype, Mobi-Gust 2 has a longer but more streamlined contraction. Next, both design iterations make use of a honeycomb screen. On top, both mobile wind tunnels employed the exact same fan (appendix C.1.1). The sand trap appears to differ the most, yet outflow losses primarily depend on the flow speed in the ducts (Çengel & Cimbala, 2014). So, apart from the mentioned differences in shape and size both wind tunnels are relatively comparable. Without using the honeycombs, Mobi-Gust 1 and 2 respectively reach  $10.8 [m^1s^{-1}]$  (De Wilde, 2020) and  $10.7 [m^1s^{-1}]$  (right panel of figure 74). The mentioned values are indeed comparable. The wind speed variability within Mobi-Gust 1 is unknown, so that it could not be compared to Mobi-Gust 2. Next, significant differences arise when the honeycombs are in use. With the honeycombs in place, velocities within Mobi-Gust 1 and 2 respectively dropped to  $6.6 [m^1s^{-1}]$  (De Wilde, 2020) and  $9.1 [m^1s^{-1}]$  (left panel of figure 74). Wind speeds thus respectively decreased  $4.2 [m^1s^{-1}]$  ( $\downarrow 38.9 [\%]$ ) and  $1.6 [m^1s^{-1}]$  ( $\downarrow 15.0 [\%]$ ). The observations show that the honeycomb of Mobi-Gust 2 causes lower energy losses. This difference is explained by the layout of the honeycomb screens. The honeycomb of Mobi-Gust 1 consisted of straws of small diameters; cut to size by means of a saw (i.e., causing ragged edges). In contrast, the honeycomb of Mobi-Gust 2 was tailored by means of a 3D-printer. Besides the larger holes, they are also much smoother. The flow within Mobi-Gust 2 is thus obstructed less; which explains the observed improvement. As a final remark, the honeycomb of Mobi-Gust 1 lowered the wind speed to such an extent, that it was not used in the field measurements (Bangen & Dijkstra, 2020). Yet, test setup 5 (right panel of figure 74; appendix I.2.2) shows how chaotic (i.e., unreliable) the flow must have been during these field tests.



## Part II

### Proof Of Concept (POC): discussion

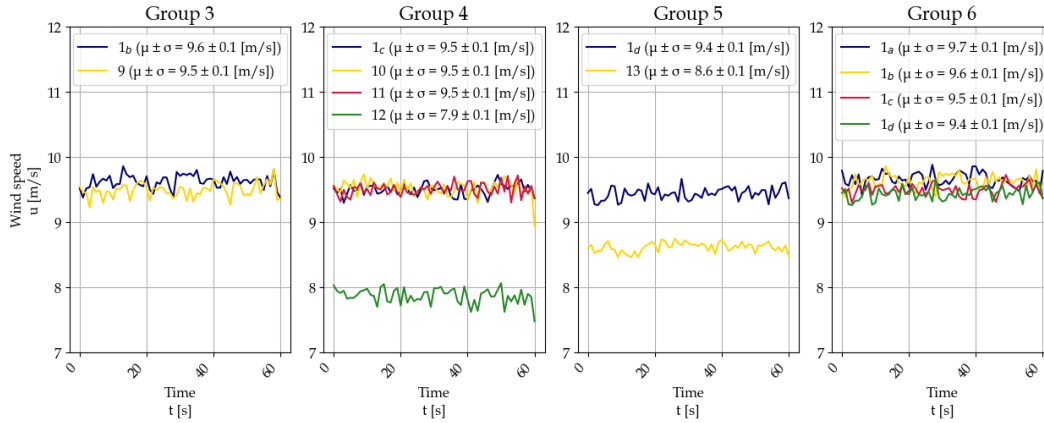


Figure 77 - The results for group 3, 4, 5 and 6 of the speed-component tests

The third group considered the influence of the removable intake shield walls. These walls might affect the flow within Mobi-Gust 2; as it partly blocks the air supply from outside. This partial blocking leads to a bended air supply from outside, which can have adverse effects on the flow within Mobi-Gust 2 (Michigan Air Products, 2017). On top, circulation patterns may arise as the air supply flows over these walls. These circulation patterns are analogues to flow over a backstep (Uijtewaald, 2022). As can be seen (left panel of figure 77), using walls only slightly lowers the wind speed ( $\downarrow 1$  [%]). Overall, the influence of these walls seems to be negligible. In turn, the mentioned component can thus be used to further shield the intake when necessary.

The fourth group considered the influence of the position of the wire mesh cylinder. The wire mesh cylinder is a standalone part and can thus be moved within the sand trap (§2.2.1.6). The measured data (middle left panel of figure 77) suggests that the majority of positions have little to no influence. To clarify, between the most downwind location until the centred location (i.e., test setup 10 and 11), the wind speed is roughly unaffected. Yet, placing the wire mesh cylinder at the upwind end of the sand trap (i.e., test setup 12) lowers the wind speed considerably; from  $9.5$  [m/s] to  $7.9$  [m/s] ( $\downarrow \sim 17$  [%]). As mentioned before, this observation is caused by air blockage. Yet, as the component is permeable, it only partly blocks the exit flow from the erosion zone. Yet, this blockage is sufficient enough to heighten the resistance of the system (Çengel & Cimbala, 2014); and the increased counterpressure makes sure the wind speeds lower.

The fifth group considered an upwind supply of sand. As explained, this upwind supply of sand follows from injecting sand through the saltation hopper (§2.2.1.5). In repetition, this upwind supply of sand alters the momentum distribution within Mobi-Gust 2 enhancing the erosion process. The obtained data shows that the injected sand extracts momentum from the wind. The wind speed namely changed from  $9.4$  [m/s] to  $8.6$  [m/s] ( $\downarrow 8.5$  [%]) after injecting the sand. It is important to note that the same fan setting was used. This momentum transfer is further assessed by adapting equation 14 (§2.2.1.5) into equation 44 (Lü & Dong, 2011). This equation calculates the momentum change (per unit volume) of the air ( $\Delta M_a$  [kg/m<sup>2</sup>/s]), as a result from a difference between the sand-clear wind speed ( $u_{a,sc}$  [m/s]) and sand-laden wind speed ( $u_{a,sl}$  [m/s]). A value applicable to Standard Temperature and Pressure (STP) conditions was used for the density of air ( $\rho_a = 1.225$  [kg/m<sup>3</sup>]; appendix B). Using the measured wind speeds (middle right panel of figure 77) results in a rounded momentum transfer of  $1$  [kg/m<sup>2</sup>/s]. This is comparable to observed values (Lü & Dong, 2011). To clarify, slightly larger sand-clear wind speeds (i.e.,  $14$  [m/s]) result in a slightly larger momentum exchange (i.e.,  $1.1$  [kg/m<sup>2</sup>/s]) at the same elevation (i.e.,  $0.075$  [m]). Next to the altered momentum distribution, the injected sand also suppresses turbulence (Zhu et al., 2019). Yet, this is not visible in the middle right panel of figure 77; as fluctuations are averaged out in these moving averages. The suppression of turbulence is however visible in the raw data (appendix I.2.2); as the standard deviation reduces considerably.

44)

$$\Delta M_a = \rho_a (u_{a,sc} - u_{a,sl})$$



## Part II

### Proof Of Concept (POC): discussion

The final group regards battery drainage during the entire experiment. The battery was namely not charged during the entire experiment. Comparisons generally involved setups that were tested close after one another. So, not charging the battery is not a big deal; also since wind speeds are rather stable (§2.4.1). Yet, configuration 1 can be seen as a base case (i.e., a fully equipped Mobi-Gust 2). Some configurations that were not tested directly after configuration 1, still required a comparison to the base case. To rule out the influence of battery drainage, the base case was reconducted at several instances. In repetition (§2.3.5), this involved extra experiments between setup 8 and 9 (i.e.,  $1_b$ ); and between setup 12 and 13 (i.e.,  $1_c$ ); as well as after setup 13 (i.e.,  $1_d$ ). From the obtained data (right panel of figure 77) it is clear that battery drainage played a minor factor role during the tests. Only at the start (i.e.,  $1_a$ ) the wind speed was a slightly increased. Yet the decreasing wind speeds within the first two groups (figure 74) cannot be explained by battery drainage alone. To clarify, the lowest value of group one (i.e., 9.1 [m/s]; left panel of figure 74); is still lower than the lowest value of the battery check (i.e., 9.4 [m/s]; figure 77); which was performed far later in time. The same holds for group two.

#### 2.4.6 Revising the flow development within Mobi-Gust 2

The next test considered velocity profiles. These profiles can be used to assess flow development. The approach (§2.2.2.6) provided the results (§2.3.6) that are discussed in this section. Most importantly, the pitot tubes were used at two locations (i.e., the up- and downwind end of the erosion zone); so the results are grouped accordingly. Next, the velocity profiles are measured along the vertical at the transverse centreline of the duct. On top, the measurements focussed solely below the vertical centreline of the duct (§2.2.2.6). From an erosion perspective this is quite logical, as the erosion process takes place over there. Yet from an aerodynamic viewpoint some valuable information is missing. The velocity profiles will namely not be symmetric along the vertical centreline of the duct; as the roughness between the bottom and the roof differs (Uijtewaal, 2022). The transition zone namely has epoxy-glued sand on its bottom (§2.2.1.4); while the roof is made of aluminium (§2.2.1.1 & §2.2.1.4). Next, the bottom of the erosion zone contains a (removable) plank with wood-glued sand on it (§2.2.2.6); while the roof is made of timber (§2.2.1.1 & §2.2.1.5).

The obtained data (table 11; §2.3.6) is repeated in table 13 for convenience. As two profiles were measured at each location, the quality of the data is checkable. When comparing the upwind locations (A & C in table 13) results seem to be in agreement to each other; as is the case for the downwind locations (B & D in table 13). The results are especially comparable in view of the approach and the associated sources for variations (§2.2.2.6). These sources for example concern height-adjustments of the pitot tubes using callipers; or aiming them using mini-levels (appendix E). These actions rely on the accuracy of the human eye (appendix E).

The data exhibits a developing flow. While the fits show sizable Root Mean Squared Errors (RMSE); they are decreasing in flow direction (A & B vs. C & D in table 13). Flow development is also expressed by the variable shear stresses and friction velocities (A & C vs. B & D in table 13). Yet fits improve considerably if they are only based on sensed velocities in the lower region of the flow (i.e., figure 83); which also shows the onset of flow development. The development also suggests the absence of spiral motions produced by the fan. These rapidly varying conditions would namely disturb and prevent flow development. The data does not reach lower than 0.005 [m] above the bed; as the pitot tubes could not be lowered further. Yet very close to the bed the viscous sublayer is found, which contains no logarithmic profile by definition (Uijtewaal, 2022).

*Table 13 – The fitting- and flow parameters originating from the fitting process*

Velocity profile	Location	A [ $m^1s^{-1}$ ]	B [ $m^2s^{-1}$ ]	RMSE [ $m^1s^{-1}$ ]	$u_m$ [m/s]	$u_*$ [ $m^1s^{-1}$ ]	$z_0$ [m]	$k_s$ [m]	$\tau_b$ [Pa]
A	Up	1.341	13.506	0.229	8.694	0.550	0.00004	0.0012	0.370
B	Down	1.567	13.969	0.133	8.348	0.642	0.00013	0.0039	0.505
C	Up	1.317	13.261	0.275	8.536	0.540	0.00004	0.0012	0.357
D	Down	1.609	14.199	0.156	8.425	0.660	0.00015	0.0045	0.533

## Part II

### Proof Of Concept (POC): discussion

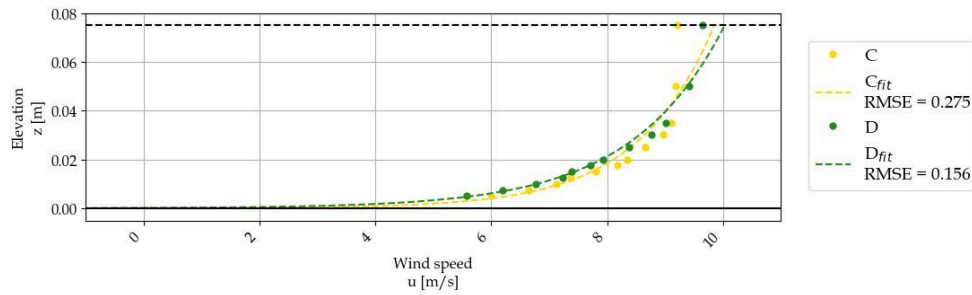


Figure 78 – A developing (turbulent) flow as visualized by profile C (upwind) and D (downwind)

The flow is still developing; which directly follows from design choices. To clarify, the required developing length was not met (§2.2.1.5). The developing flow is visible in figure 78, showing an upwind profile (i.e., C) and a downwind profile (i.e., D). The measured velocities are generally smaller near the centreline of the duct, whereas they are a bit larger near the bottom of the duct (i.e., compared to the fits). Yet, the measured velocities near the centreline of the duct deviate the most from the fits. Next, velocities near the bottom decrease in flow direction (i.e., comparing C & D in figure 78); because of wall friction (White, 2011). In contrast, centreline wind speeds increase in flow direction (i.e., comparing C & D in figure 78); due to mass conservation (Çengel & Cimbala, 2014). This process continues until the logarithmic velocity profile appears (Uijtewaal, 2022). This mechanism was already shown in several schematics throughout the report (i.e., figure 16 in §2.2.1.4; figure 23 in §2.2.1.5; or figure 75 in §2.4.5); yet it is now shown by measurements.

Next, the bed shear stresses are increasing in flow direction. The bed shear stresses at the upwind locations (A & C in table 13) are namely smaller than at the downwind locations (B & D in table 13). Yet it was expected that the bed shear stresses would decrease in flow direction because of flow development (e.g., figure 16; §2.2.1.4). Yet the sensed roughness's provide a possible explanation to the observations. The roughness's ( $z_0$  [m]) are namely increasing in flow direction as well (A & C vs. B & D in table 13). The flow thus experienced rougher conditions in the direction of the flow; which also explains the increased bed shear stresses. As the bed shear stress ( $\tau_b$  [Pa]) is proportional to the friction velocity ( $u^*$  [m/s]) squared (Bosboom & Stive, 2023); i.e.,  $\tau_b \propto (u^*)^2$ ; also the friction velocity increased in flow direction (A & C vs. B & D in table 13).

Next, the roughness length ( $z_0$  [m]) can be reviewed by the Nikuradse roughness ( $k_s$  [m]); see equation 45 (Winterwerp et al., 2022). At the upwind location (A & C in table 13) this amounts to an average Nikuradse roughness of about 0.0012 [m] (i.e., 1.2 [mm]). For the downwind location (B & D in table 13) the average Nikuradse roughness is about 0.0042 [m] (i.e., 4.2 [mm]). The calculated Nikuradse roughness's are added to table 13.

$$45) \quad k_s = 30z_0$$

The calculated Nikuradse roughness reveals issues. The bottom within the transition zone and the plank within the erosion zone contains a glued sand bed; having median diameter ( $D_{50}$  [m]) of 430 [ $\mu\text{m}$ ] (figure 19; §2.2.1.4). This sand is narrowly graded, as the ratio between the  $D_{60}$  (i.e., 453 [ $\mu\text{m}$ ]; §2.2.1.4) and the  $D_{10}$  (i.e., 313 [ $\mu\text{m}$ ]; §2.2.1.4) is smaller than 4 [–] (Geo Engineer, N.d.). For narrowly graded sand the Nikuradse roughness is about two times the median diameter (Voorendt, 2022). The Nikuradse roughness is only about 2.5-3.0 times the median diameter at the upwind location (A & C in table 13). Yet the Nikuradse roughness is considerably larger at the downwind location (B & D in table 13); i.e., 9.0-10.5 times the median diameter. The calculated Nikuradse roughness's suggest that the sand was not glued neatly at all locations. To clarify, the sand bed within the transition zone was professionally epoxy-glued by the staff of the Hydraulic Engineering laboratory. Still a slight bump is observable at the very downwind end of the transition zone (figure 79). As the upwind pitot tube sticks a bit into the transition zone, this disturbance is only sensed by the downwind pitot tube. Next, the sand bed within the erosion zone (figure 80) was a 'do-it-yourself' solution using wood glue. The differences between the upwind location and the downwind location (A & C vs. C & D in table 13) are thus further explained by the work ethics.

## Part II

### Proof Of Concept (POC): discussion



Figure 79 – A slight bump at the downwind end of the transition zone with sand epoxy-glued on it



Figure 80 – The used plank with sand wood-glued on it

Yet, some more disturbances were observed. For example, the height of the plank in the erosion zone is slightly lower than the bottom of the transition zone; i.e., creating a small backstep (figure 81). It is stressed that the shown picture originates from the sand loss test (§2.3.4); as the visible taping was forgotten during this test. Next, the roof of the transition zone and the erosion zone are not connected well (figure 82). After closer inspection, the disturbance follows from a small error in the final design drawings. Yet again, the upwind pitot tube does not measure all of these disturbances, as it sticks into the transition zone.



Figure 81 – The plank introduces a slight backstep

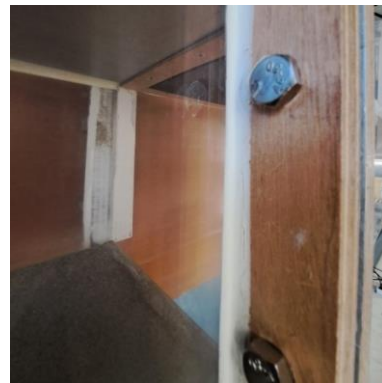


Figure 82 – The roof of the transition- and erosion zone is not completely levelled

The development of the flow can be checked further. For convenience, the empirical relation that assesses the development of the flow (§2.2.1.4) is repeated in equation 46. The flow travels 2 [m] between the honeycomb and the upwind erosion zone location (A & C in table 13). The total distance between the honeycomb and the downwind erosion zone location (B & D in table 13) is 3 [m]. The boundary layer thickness ( $\delta$  [m]) should thus roughly reach 0.04-0.06 [m] at the upwind location (A & C in table 13); and about 0.06-0.09 [m] at the downwind location (B & D in table 13).

$$46) \quad \delta(x) \approx 0.02x \text{ to } 0.03x$$

These estimated boundary layer thicknesses are compared to the sensed data. To this end, it was checked when measured velocities start to deviate considerably from the logarithmic velocity profile. In turn, this provides an estimate for the boundary layer thickness. Consequently, table 14 and figure 83 emerge. It is stressed that table 14 belongs to figure 83; and that table 11 (§2.3.6) and table 13 belong to figure 59 (§2.3.6); i.e., these cannot be mixed. In general, the measured data at the upwind location (A & C in table 14) starts to deviate considerably from about 0.030 [m] upward (figure 83). At the downwind location (B & D in table 14) considerable deviations occur from about 0.035 [m] upward (figure 83). Since there is no information between 0.035 [m] and

## Part II

### Proof Of Concept (POC): discussion

0.050 [m], the obtained value at the downwind location (B & D in table 14) could possibly be a bit higher. Overall, the boundary layers at both locations span around 25 [%] of the total duct height (i.e., as seen from the bottom). In other words, flow development reaches roughly 50 [%] of the total distance required (i.e., the distance between the bottom and the centreline of the duct). The determined boundary layer thickness corresponds to the lower bound of equation 46. As explained, equation 46 is just one of many empirical estimates (appendix C.1.5). Others for example require 150 characteristic length scales (i.e., half the cross-sectional dimension of the duct); if Reynolds stresses are considered as well (Uijttewaalt, 2022). That estimate would amount to a required development length of about 11.25 [m]. All in all, the used relation (equation 46), as well as the measured flow development at the upwind location (A & C in table 14), seem to be reasonable. However, the boundary layer is considerably less thick than expected at the downwind location (B & D in table 14). Several reasons have already been identified and explained.

Table 14 – The fitting- and flow parameters originating from the fitting process (only including reasonable points)

Velocity profile	Location	$A$ [ $m^1 s^{-1}$ ]	$B$ [ $m^2 s^{-1}$ ]	$RMSE$ [ $m^1 s^{-1}$ ]	$u_m$ [ $m/s$ ]	$u_*$ [ $m^1 s^{-1}$ ]	$z_0$ [ $m$ ]	$\tau_b$ [ $Pa$ ]
A	Up	1.599	14.617	0.051	8.881	0.655	0.00011	0.526
B	Down	1.683	14.465	0.070	8.428	0.690	0.00018	0.583
C	Up	1.684	14.888	0.062	8.845	0.691	0.00014	0.584
D	Down	1.776	14.931	0.056	8.560	0.728	0.00022	0.649

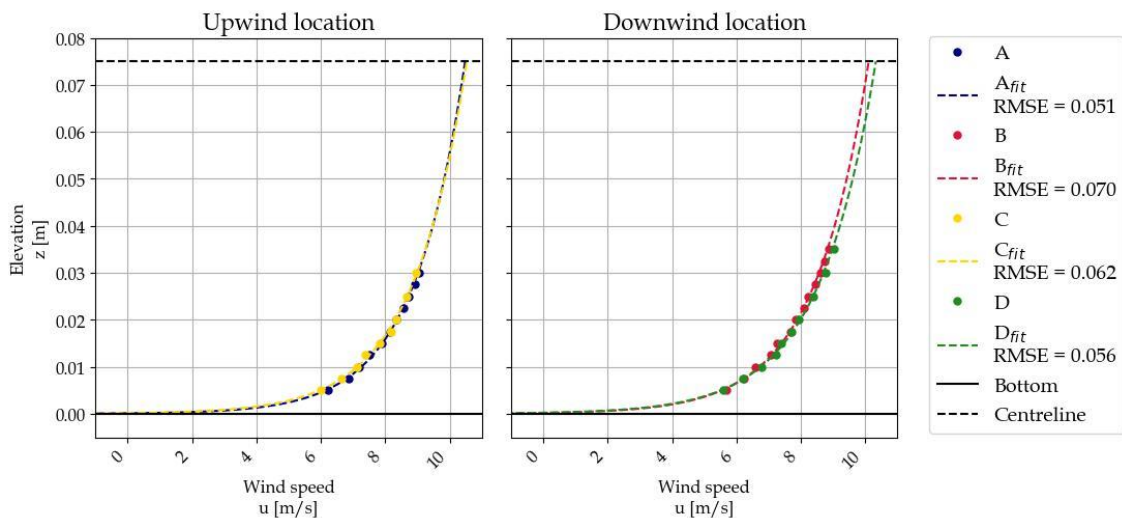


Figure 83 - The measured and fitted vertical velocity profiles that belong to table 13 (only including reasonable points)  
The logarithmic profiles are plotted between the bottom and centreline of the duct

Next, the measured velocity data also suggest that Mobi-Gust 2 was leaking during the experiment. The mean velocities are namely decreasing in flow direction (A & C vs. B & D in table 14). As explained, the walls of the erosion zone are normally embedded in the sand surface (§2.2.2.4); i.e., sand and air cannot leave the system. Yet the plank is enclosed by gaps; and leakage was possible as those were forgotten to be taped.

The wind conditions inside Mobi-Gust 2 are then compared to natural wind conditions. A normal elevation to measure natural winds is about 10 [m]. The Royal Netherlands Meteorological Institute (i.e., the KNMI) for example measures at this elevation (KNMI, N.d.). The obtained logarithmic fits are extended to this elevation as well. If all data points are used (i.e., table 13), then figure 84 emerges. If only reasonable data points are used (i.e., table 14) then figure 85 emerges. Including all data points (figure 84), a minimum wind speed of about 16.29 [m/s] is found at an elevation of 10 [m]; which corresponds to winds of about 7 [bft] (KNMI, N.d.). By only including reasonable data points (figure 85), minimum wind speed of 18.30 [m/s] are found at 10 [m] elevation; corresponds to winds of 8 [bft] (KNMI, N.d.). Next, the dynamics within Mobi-



## Part II

### Proof Of Concept (POC): discussion

Gust 2 in relation to nature is of interest as well. The dynamics relate to turbulent length- and timescales (Uijttewaai, 2022). The strength of a turbulent Eddy is proportional to the available space (Schierck, 2019). For example, the wind speeds were projected at an elevation of 10 [m]. A turbulent Eddy can be thus 10 [m] in size between the bottom and this elevation. Yet, turbulent Eddies within Mobi-Gust 2 are restricted to the cross-sectional size of the duct, i.e., 0.15 [m] (§2.2.1.5). The turbulent Eddies within Mobi-Gust 2 are thus (much) smaller and (much) weaker compared to nature. If the cross-sectional size of Mobi-Gust 2 is increased, then dynamics might be 'won'; while achievable wind speeds might be 'lost' (i.e., for the same wind generating system).

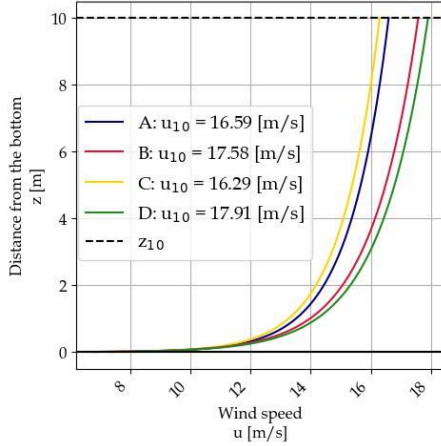


Figure 84 – Employing the logarithmic fits that are based on all data points

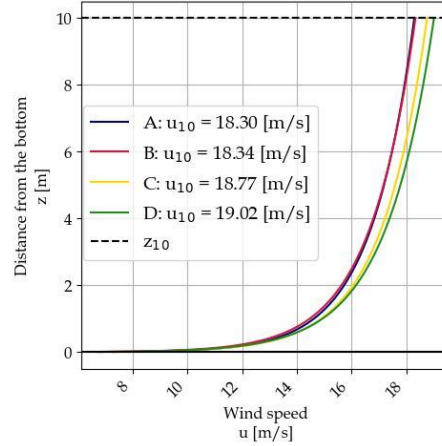


Figure 85 – Employing the fits that are based on the most reasonable data points only

Two verification steps are still missing. First of all, velocity profiles can be verified. To do so, three velocity profiles must be measured, for three unique cross-sectionally averaged flow velocities. These velocity profiles intersect on a semi-log scale in (nearly) developed conditions (Bagnold, 1941). Second of all, the bed shear stresses can be verified. In elaboration, stationary duct flow is maintained by a pressure gradient (Schierck, 2019); equation 47. This pressure gradient balances the (Reynolds) shear stress at the boundaries (Uijttewaai, 2022); equation 48. The bed shear stress can thus be determined from measuring pressure gradients. Measuring pressure gradients is possible through applying a longitudinal array of pressure sensors. The approach thus requires at least two pressure sensors, to establish one pressure gradient; equation 49. The associated bed shear stress can then be compared to the bed shear stress that was determined from the velocity profiles (i.e., implicitly verifying them as well).

$$\begin{aligned}
 47) \quad & \tau = \frac{dP}{dX} (y - h) \\
 48) \quad & \tau_0 = \frac{dP}{dX} h \\
 49) \quad & \tau_0 = \frac{p_2 - p_1}{x_2 - x_1} h
 \end{aligned}$$

As a final remark, in- or excluding data points changes the calculated flow properties. In- or excluding data points namely causes velocity gradients to change. Velocity gradients are directly coupled to the determined flow properties, i.e., friction velocities and bed shear stresses (Uijttewaai, 2022). The data in table 13 (as well as table 11 and figure 59; §2.3.6) therefore differs from the data in table 14 (and figure 83).



### 2.4.7 Discussing the erosion performance of Mobi-Gust 2

Mobi-Gust 2 was not able to mobilize an in-situ sand surface. In contrast, the prototype (i.e., Mobi-Gust 1) could produce aeolian erosion (De Wilde, 2020) & (Bangen & Dijkstra, 2020). That is an unexpected observation, as Mobi-Gust 2 generates higher wind speeds compared to this prototype (§2.4.7). On top, the achieved wind speeds within Mobi-Gust 2 were likely suitable enough to onset aeolian erosion. To clarify, the achieved centreline wind speed within Mobi-Gust 2 reaches about 9.5 [m/s] (e.g., §2.4.1 or §2.4.2). Projected at an elevation of 10 [m], wind speeds even reach at least 15 [m/s] (§2.4.6); which is equal to the design wind speed. The velocity gradients within Mobi-Gust 2 are thus comparable to these projected wind speeds. In capacity limited situations already 6 [m/s] might be enough to onset aeolian erosion (Fryberger, 1979). Yet, in supply limited situations the required wind speed can be higher. In elaboration, moderate winds of roughly 5-12 [m/s] typically onset aeolian erosion; whereas above 15 [m/s] aeolian erosion is often completely ceased; as more extreme conditions often coincide with rain (Arens, 1996). As mentioned, natural winds are often measured at an elevation of 10 [m] (KNMI, N.d.). Mobi-Gust 2 reaches all the mentioned values at this projected height. In other words, Mobi-Gust 2 must have been hypothetically able to onset aeolian erosion in many cases. The strength of Mobi-Gust 2 is expressed in other characteristics as well. For example, several tests were conducted using the saltation hopper (§2.2.2.3 and §2.2.2.4). Virtually all injected (dry) sand ended up in the sand trap, if Mobi-Gust 2 was fully equipped. Yet, it must be noted that a transporting velocity might not be able to erode that same material. This is simply true because of Newton's first law (NASA, 2023).

It is believed that the experiments were hampered by moisture content. The field expedition was namely conducted in the Dutch winter. Normally this is the wettest period of the year. To clarify, precipitation generally lasts longer (KNMI, 2023), while evaporation is usually lower (KNMI, N.d.). On top, the year 2023 was the wettest year ever recorded by the Royal Netherlands Meteorological Institute (KNMI, 2023). This wet period even continued into 2024 (KNMI, 2024). The preceding days before the field expedition were also quite rainy. This is illustrated by figure 86; as it shows a wet sand surface and wet knees from crouching. As said, aeolian erosion is normally hampered during extreme conditions as it coincides with rain. Already 2 [%] moisture content might be enough to cease aeolian transport (Hallin et al., 2023). Checking previous studies provides additional insights. The prototype (i.e., Mobi-Gust 1) was namely employed in (dry) summer conditions (Bangen & Dijkstra, 2020). Yet the prototype could also not mobilize the wet sand surface within the intertidal zone. Overall, it is believed that Mobi-Gust 2 could not generate aeolian erosion because of the wet conditions. Yet also the fan has to be mentioned (appendix C.1.1), as a stronger fan might have been able to mobilize this wet sand surface. The proposed causes, related to moisture content, changed the direction of this research.



Figure 86 - Wet conditions on the Sand Engine

## Part II

### Proof Of Concept (POC): discussion

As said, the focus of this research is redirected towards moisture content. Investigating other supply limiting factors (§1.3) is expected to be difficult in this (wet) time of year. The main research question of the applied research (part 3) was however retained. Answering it will now involve a moisture content perspective. To this end, the old measurement plan is discarded (appendix G.4.1); and a new one was adopted (part 3). The new measurement plan involves a tailored sand pit (figure 87). This sand pit allows for erosion testing in the laboratory. In short, the sand pit can be filled with (dried) in-situ sand to investigate the moisture content. The dimensions of the sand pit logically define how much sand fits in it. The sand pit has a length ( $L$  [m]) of 1 [m], a width ( $B$  [m]) of 0.30 [m]; and height ( $H$  [m]) of 0.10 [m]. Equation 50 allows to estimate the volume of sand that is required to be excavated. Mind that this approach is very simplistic, as it does not account for the porosity of the sand. This is acceptable, as the in-situ sand probably has a higher porosity after retrieval it (i.e., because of the excavation process).

50)

$$V = LBH$$

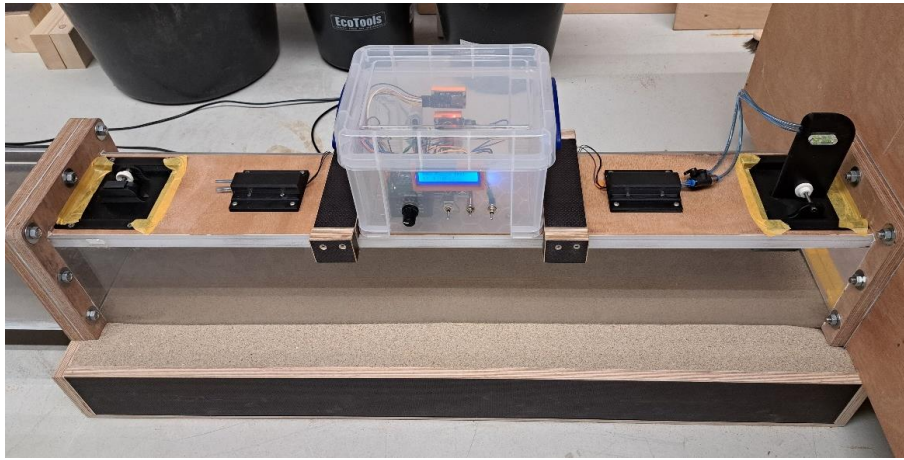


Figure 87 – The erosion duct and its tailored sand pit

## 2.5 Conclusions

The project criteria of Mobi-Gust 2 are used to assess the design and the performance of Mobi-Gust 2 (§2.1). The project criteria are summarized in a sub-research question that is repeated below for convenience. This research question will be considered in four steps: §2.5.1 considers the sustainability of Mobi-Gust 2; §2.5.2 regards the usability of Mobi-Gust 2; §2.5.3 considers the reliability of Mobi-Gust 2; and finally §2.5.4 considers the controllability of Mobi-Gust 2.

*Is it possible to sustainably design a useful, reliable and controllable mobile wind tunnel system; in order to conduct aeolian erosion measurements?*

### 2.5.1 Evaluating the sustainability of Mobi-Gust 2

The design of Mobi-Gust 2 is reasonably sustainable. To clarify, the used materials are durable and beach resistant (§2.2.1.1). Consequently, the materials are likely to last. On top, the design is modular (§2.2.1.1), which allows for specialized repairs or replacements. To clarify, only a local fix is required if one of the sturdy components breaks down. Yet, it is noted that the components of the wind gauging system are the most fragile (§2.2.1.1). Still, mitigation measures have been put in place to protect the hardware (§2.2.1.7). The mitigation measures amongst others involve 3D-printed caps for the pressure sensors; and a splash-proof and shakeable box for the other hardware. On top, the design of the wind gauging system is also modular, as connections are governed by jumper wires. Consequently, the relatively cheap components are also easily repairable or replaceable. Finally, re-using the 12-volt fan considerably boosts the sustainability of Mobi-Gust 2 (§2.1). To clarify, re-usage was financially attractive, as well as being environmentally friendly. To clarify, re-usage omits the purchase of a new fan, as well as (possible) polluting aggregators.

### 2.5.2 Evaluating Mobi-Gust 2's usability

Mobi-Gust 2 fails to meet its main purpose; which is still within reach. To clarify, Mobi-Gust 2 did not generate aeolian erosion in-situ (§2.3.7). However, it is hypothesised that moisture content caused this (§2.4.7). Mobi-Gust 2 namely reaches wind speeds which should onset aeolian erosion in most cases. To clarify, Mobi-Gust 2 reaches centreline wind speeds of 9.4 [m/s] averaged over an entire discharging cycle (§2.3.2). Yet, centreline wind speeds can be as high 9.9 [m/s] or as slow as 8.8 [m/s]; respectively measured at the start and end of each discharge cycle. Mind that the mentioned centreline wind speeds are the maximum wind speeds within Mobi-Gust 2. Next, vertically averaged velocities reach 8.6 [m/s] and 8.4 [m/s]; respectively measured at the up- and downwind end of the erosion zone (§2.3.6). The vertically averaged wind speed at the upwind location is however most representative. To clarify, the erosion zone was subjected to leakage during the test (§2.4.6). As said, these measured wind speeds should be high enough to onset aeolian erosion in most cases (§2.4.7). Velocity thresholds (i.e., the velocity from which erosion occurs) lies usually between 5-12 [m/s]; and above 15 [m/s] natural aeolian erosion is often ceases (§2.4.7). These extreme conditions namely often involve rain; and research shows that 2 [%] moisture content might be enough to completely hamper natural aeolian erosion (§2.4.7). Fits to measured velocity profiles are used to compare the mentioned values to the wind conditions within Mobi-Gust 2 (§2.4.6). A height of 10 [m] is often used for wind speed measurements; i.e., the mentioned fits can be extended to that elevation. These projected wind speeds reach a minimum of 16.3 [m/s] (§2.4.6); i.e., far above the required upper limit (i.e., 12 [m/s]). The velocity gradients and the bed shear stresses within Mobi-Gust 2 must have been similar to conditions that onset natural aeolian erosion. Together with some other arguments (§2.4.7), it is believed that Mobi-Gust 2 is able to erode a dry sand surface. In order to substantiate the statements, as well as ensuring the continuation of the main research (part 3), a tailored sand pit was created. This tailored sand pit enables erosion tests within the laboratory; and to explore the influence of moisture content (see part 3). Also, Mobi-Gust 2 has a saltation hopper (§2.2.1.5). The purpose of this hopper is to enhance aeolian erosion, which will be verified in the main research as well (part 3). While erosion was not yet generated, acrylic walls enable to visualize it (§2.2.1.1).

## Part II

### Proof Of Concept (POC): conclusions

The erosion process must be measurable in order to have a useful Mobi-Gust 2. Wind conditions are measurable; both at single elevations (§2.3.2), or via vertical profiles (§2.3.6). Next, the erosion process itself is also measurable. To clarify, while in-situ erosion could not yet be generated, tests show that Mobi-Gust 2 is sand tight (§2.3.4). The erosion process is thus measurable, as the sand trap can be manually emptied; so that the eroded material can be collected and measured (§2.2.1.6).

The mobility of Mobi-Gust 2 is the following important characteristic. The design of Mobi-Gust 2 is modular (§2.2.1.1). Consequently, Mobi-Gust 2 fits in an MPV car (e.g., a Chrysler Voyager) and can be transported via box wagons (§2.3.7). On top, the modularity of Mobi-Gust 2 preserved its mobility, even if more aerodynamic functionality is added. Aerodynamic functionality may include developing the flow to get more reliable wind conditions (§2.5.3). Next, the setup is easy (dis)mountable with (very) basic tools and little to no experience (appendix G.3). Next, components are light as well (§2.2.1.1). Experience showed that the parts are indeed easy to handle. Next, the power supply is portable, so that Mobi-Gust 2 is able to measure independently. Mobi-Gust 2 is minimally able to measure for 2 [h] straight with stable wind speeds (§2.4.1). Next, the entire sustainability section (§2.5.1) already substantiates the usability of Mobi-Gust 2. Without the explained level of robustness Mobi-Gust 2 could not conduct field measurements at all.

### 2.5.3 Judging Mobi-Gust 2's Reliability

In general, Mobi-Gust 2 is reasonably reliable. For example, the design of Mobi-Gust 2 is available (§2.2.1); which greatly boosts the reproducibility of this research. As explained, Mobi-Gust 2 is sand tight (§2.3.4). Next, real-time wind speeds are visible in the field, via a Liquid Crystal Display (LCD) module. These real-time velocities concerns valuable information. For example, these real-time velocities can be used to check the wind speed after the experiment. Besides, these real-time velocities directly indicates whether the wind gauging system is operates correctly (e.g., observing wind speeds nearing 40 [m/s] might indicate an error).

Mobi-Gust 2 has aerodynamic functionality enhancing its reliability. The honeycomb (§2.2.1.4) for example is effective in two ways. Firstly, the honeycomb mitigates the spiral motions that are produced by the fan; and secondly it onsets flow development (e.g., §2.4.2, §2.4.5 or §2.4.6). Yet flow conditions are still underdeveloped (as expected). In elaboration, logarithmic velocity profiles span approximately 50 [%] of the total required length (§2.4.6). In turn, this effectively means that boundary layers approximately span 25 [%] into the duct. On top, similar vertical velocity profiles have been measured repetitively (§2.4.6); especially when considering the sources for variations present in the approach (§2.2.2.6). Next, the intake shield walls might further mitigate sand suction, without affecting the wind speeds within Mobi-Gust 2 (§2.4.5).

The wind gauging system however requires some development still. First some positives. The wind gauging system is namely designed to be reliable. To clarify, interferences are actively mitigated (§2.2.1.7); e.g., by shielding the hardware and regularly performing zero-measurements. Consequently, the wind gauging system measures signals over noise (§2.2.2.2). For example, the discharging curve of the power supply can be deduced from wind speed data (§2.4.1). On top, measured relative turbulent fluctuations are only slightly increased; and are near values from uniform wall flow (§2.4.2). Measuring signals over noise is additionally demonstrated by two other tests. Firstly, the wind gauging system is able to capture wind speed adjustments as a result of changing system characteristics (§2.4.5). Secondly and in repetition, vertical velocity profiles are measurable by the wind gauging system (§2.4.6). Yet as introduced there are also some concerns on the reliability of the wind gauging system. The concerns are threefold. First of all, the resolution of the system is still rather coarse (§2.4.2). Second of all, the wind speed accuracy is still ambiguous (§2.4.2). And finally, the sampling frequency of the system is still variable in time (§2.4.2).

Next, the reliability of the saltation hopper is not up to standards. To clarify, artifacts (e.g., shell fragments) in the used natural sand samples partly clog the hopper (§2.4.3).

Next, the power supply is relatively reliable. The power supply generates a stable voltage (§2.2.1.8); allowing stable wind speed measurements (§2.4.2). Next, the power supply is durable and is able to cope with relatively harsh weather (§2.2.1.8). On top, the power supply is also



## Part II

### Proof Of Concept (POC): conclusions

relatively safe; i.e., far safer than other lithium-based chemistries (§2.2.1.8). Yet a negative aspect on the power supply can be provided as well. The connections between the power supply and the electrical systems of Mobi-Gust 2 namely easily loosen (§2.4.1). In elaboration, the loose connections impact the wind conditions within Mobi-Gust 2.

#### 2.5.4 Evaluating Mobi-Gust 2's controllability

Mobi-Gust 2 is relatively controllable. For example, wind speeds can be adjusted (§2.2.1.2). In turn, a controllable wind speed implies a controllable erosion process (i.e., provided the wind speed determines the erosion flux). Next, the saltation hopper is controllable as well. To clarify, the hopper has lids of different gap sizes (§2.2.1.5). These lids ensure different discharging rates, for the same granular material used (§2.3.3). Next as mentioned implicitly, the pitot tubes are height adjustable. On top, these pitot tubes can also be installed either at the up- or downwind end of the erosion zone. It is stressed that both pitot tubes do not have to be used at the same time (§2.2.1.7). Finally, the wind gauging system is configurable into different modes (§2.2.1.7).

#### 2.5.5 (Dis)Mounting and configuring

Especially the usability and the reliability of Mobi-Gust 2 also depends on its instalment. To this end appendix G.3 shows manuals on (dis)mounting and configuring Mobi-Gust 2.



## 2.6 Recommendations

The conclusions showed that Mobi-Gust 2 can be improved. The improvements involve multiple sections: i.e., the wind speed (§2.6.1); the development of the flow (§2.6.2); the tailored sand pit (§2.6.3); the saltation hopper (§2.6.4); the visualisation of the flow (§2.6.6); velocity profiles (§2.6.7); shear stresses (§2.6.8); the wind gauging system (§2.6.9); and the power supply (§2.6.10). A supplement of recommendations is provided in §3.6.2. The mentioned supplement could only be created after successfully generating aeolian erosion with Mobi-Gust 2; i.e., explaining it is not added within this section.

### 2.6.1 Increasing the wind speed

Most obviously the wind speed can be improved. Yet, improving the wind speed can be laborious and expensive. The wind speed improvements are summarized into five main options

The first option involves changing the position of the honeycomb. To clarify, the honeycomb can be moved in upwind direction. In that direction, cross-sectional areas become larger. In other words, flow velocities are smaller. As energy losses scale by the velocity squared (appendix D); moving the honeycomb in upwind direction, has a quadratic effect on the associated energy losses. As the vertical contraction is asymmetric; the best location might be between the vertical- and horizontal contraction.

The second option involves the cross-sectional shape around the fan. The fan is namely enclosed by a squared cross-section (§2.2.1.3). At the corners of this squared cross-section flow separation and recirculation will occur. In other words, energy is lost right after generating the air flow. By enclosing the fan in a circular cross-section the situation improves. Yet, in this way the contraction also becomes much more complex.

The third option involves purchasing an additional fan. A fan can be applied in series (i.e., doubling the pressure) or in parallel (i.e., doubling the discharge); see appendix D. The air flow that is produced by the current fan is high enough in view of Mobi-Gust 2's cross-sectional size. In other words, the fan does not produce high enough pressures to overcome all resistances (e.g., friction). Consequently, the fan has to be applied in series. However, buying a second fan also involves some negative side effects. Having a second identical fan doubles the total amperage required (i.e., 17.4 [A] → 34.8 [A]). However, the used speed controller cannot cope with this (appendix C.1.1). Next, the power supply only has a finite power capacity (appendix C.3). Buying an extra identical fan thus means that the power supply will be draining at least a factor 2 faster. This factor might be larger as other electrical parts (e.g., wiring) have effects as well. Overall, buying a second fan might also result in replacing the speed controller and power supply.

The fourth option involves a more powerful wind generation system. Yet this solution may involve similar electrical problems as described in the previous paragraph. On top, if this new wind generation system is considerably more powerful; then it may also require a large and polluting power aggregator. In terms of finances, mobility and sustainability that would provide issues; while re-using the fan of the prototype (i.e., Mobi-Gust 1) actively mitigated these adverse effects (§2.1). It is also noted that the air can be pulled instead of being pushed; if another wind generating system is applied. As said (§2.1), pulling the air causes better aerodynamic properties.

The fifth option involves a complete redesign of Mobi-Gust 2 based on energy losses. In other words, Mobi-Gust 2 should be overhauled based on a pipe flow analysis (appendix D). For convenience, the of minor- and major loss terms are shown below (equation 51 and 52). These losses reveals design options; i.e., including adjusting boundary roughness, changing length scales or altering cross-sectional sizes of components.

$$\begin{aligned} 51) \quad \Delta p_{minor} &= -K_l \frac{\rho u^2}{2} \\ 52) \quad \Delta p_{major} &= -f \frac{L}{D_h} \frac{\rho_a u^2}{2} \end{aligned}$$

## Part II

### Proof Of Concept (POC): recommendations

The mentioned options based on a pipe flow analysis ([appendix D](#)) seem to be laborious and unviable in general. First of all, decreasing the boundary roughness is difficult; as most surfaces already are quite smooth ([§2.2.1.1](#)); i.e., aluminium and acrylic glass. The only rough surfaces concern the ones of the transition- and erosion zone. These surfaces are intentionally rough; for example since the roughness of the transition zone matches the one of the erosion zone ([§2.2.1.4](#)). Second of all, decreasing the length scales of parts implies losing aerodynamic functionality. For example, omitting transition ducts results in even less developed flow conditions in the erosion zone ([§2.2.1.4](#)). Third of all, the cross-sectional area of the ducts can be increased. The increased cross-sectional size allows for stronger dynamics within Mobi-Gust 2. The analysis to be conducted involves finding the sweet spot between mass conservation and energy losses ([appendix D](#)).

#### 2.6.2 Improving the development of the flow

A design choice resulted in not obeying the required development length ([§2.2.1.4](#)). Yet tests with Mobi-Gust 2 showed that the situation can be improved relatively easily. The speed-component test ([§2.4.5](#)) namely revealed that the addition of one transition duct decreases the wind speed by only 3-4 [%]. On top, adding two transition ducts results in a wind speed loss of 7-8 [%]. Both reductions are relative to using no transition ducts at all. Adding more transition ducts thus seems viable; so that flow development is facilitated further ([§2.2.1.4](#)). Extra ducts can easily be created and evaluated now that Mobi-Gust 2 is realised. Assessing the additional ducts requires measuring the achievable wind speeds; and checking whether this is still sufficient enough to onset aeolian erosion. Yet to check the feasibility upfront, a pipe flow analysis ([appendix D](#)) can be performed as well. As boundary layers currently span approximately 50 [%] of the total length required ([§2.4.6](#)); it is advised to add two or three extra transition ducts; i.e., each of them having a length of 1 [m]. It is stressed that the roughness of the transition zone is important. To clarify, a sand bed was glued on the bottom plate of the transition zone ([§2.2.1.4](#)); and the used sand must be similar in all duct sections. Consequently, the entire transition zone should be re-glued (i.e., 1  $D_{50}$  [m] thick). On top, re-glueing the sand bed would fix the imperfections related to the bottom; which are treated shortly. Besides, experience showed that the flanges of the ducts fail relatively easily ([§2.4.4](#)). If new ducts are created, the flanges can be attached more firmly to the ducts. This strengthens the design and improves the sand tightness of Mobi-Gust 2.

Next are the mentioned imperfections within Mobi-Gust 2. While the flow is underdeveloped because of design choices, the imperfections further hamper flow development. These imperfections cause more variable and increased variable velocity gradients and (bed) shear stresses ([§2.2.1.4](#)). These imperfections thus need to be smoothened out. For example, the sand-glueing can be improved. In elaboration, at the downwind end of the transition zone a sill has formed ([§2.4.6](#)). The sill needs to be sanded and reglued. Even better would be to sand and reglue the entire transition zone to get a uniform result. Next, the roof of the duct system includes a protruding edge of about 2 [mm] ([§2.4.6](#)); caused by a minor flaw in the design drawings. It is advised to chamfer off this ridge by an angle less than 15-30 [°]. The chamfering effectively creates a gradual contraction, which is associated negligible energy losses ([appendix C.1.3](#)). Additionally, the cross-sectional shape between the erosion zone and the sand trap is not entirely squared; which can be smoothened as well. Next, the removable plank with wood-glued sand presented issues ([§2.4.6](#)). This plank must not be used anymore in aerodynamic tests. This plank was namely a source for disturbances ([§2.4.6](#)); for example due to the presence of a small back step, or leakage around the edges. A solution includes creating a new removable bottom plate. This plate must be manufactured similarly to the transition zone. In elaboration, the plate must be created from similar materials; and should contain the same epoxy-glued sand bed. Instead of a removable plate, one can also use the sand pit. To clarify, Mobi-Gust 2 could not mobilize a wet sand surface. In turn, by spraying the sand surface soaking wet really mimics field conditions and replaces the need for a tailored plate. On top, the erosion zone walls can be driven into that wet sand bed; i.e., simultaneously sealing the edges.

## Part II

### Proof Of Concept (POC): recommendations

Next, the performed experiments used a static bed (§2.2.2). It might be interesting to re-do some of the experiments using a dynamic bed (e.g., §2.4.5 or §2.4.6). A dynamic bed mimics field conditions even more. Again, the sand pit can be used for this. However, directly measuring in the field is also a possibility. To clarify, the laboratory tests can be re-done in the field quite easily; provided the weather and the preparation are adequate (appendix G).

It is finally stressed that flow development must not become an obsession as well. At first glance, it seems wise to keep investing in improved flow properties. After all, this benefits the reliability of the experiments. Yet there are multiple side aspects to consider. For example, the pressure capacity of the wind generation system (e.g., a fan or pump) is important. To clarify, the ducts cannot be extended infinitely, as the added resistance can become too large for the system to manage. It is additionally important to realise, that even if the flow at the downwind end of the transition zone is near perfect; it still gets disturbed when entering the erosion zone. This disturbance is caused by the very process that is explored in this research. To clarify, the bottom of the transition zone is static, while the one of the erosion zone is lowering. In other words, a backstep-like feature will be formed. The widening cross-section is associated with negative pressure gradients; i.e., impacting flow performance. A (very) futuristic solution would include an automatically lowering bottom in the transition zone, mimicking the lowering of the bed within the erosion zone. Besides the formation of a backstep-like feature, beaches are generally characterised by a variety of roughness elements (e.g., bed forms, shells or litter). All these roughness elements lead to additional disturbances.

#### 2.6.3 Creating a tailored sand pit

The test field expedition was unsuccessful. The failure likely followed from the relatively wet conditions (§2.4.7). To this end, a tailored sand pit was designed. Consequently, the focus of the research is shifted. Instead of considering supply limitations in general, the influence of moisture content and saltating sand are explored. It is namely believed that Mobi-Gust 2 is able to transport dry granular material (§2.4.7). It is therefore also suggested that Mobi-Gust 2 is fit to conduct experiments in dryer (summer) conditions.

#### 2.6.4 Improving the saltation hopper

The saltation hopper (partly) clogs if natural sand is used. Partial clogging is also an issue, as tests are not repeatable anymore. As explained (§2.4.3), natural sand contains all kinds of artifacts (e.g., shells, pebbles or litter). Mitigation involves filtering the sand before usage. Using filtered sand also implies that the saltation hopper calibration should be redone (§2.4.3). The discharging rate namely changes if sand of another size- and shape distribution is used; or when other gap sizes are applied.

Next, some sand mass remains on the lids when using the saltation hopper (e.g., §2.3.3 or §2.3.4). Experiments need to be corrected for this. Yet, a permanent fix would be re-designing the lids. V-shaped lids (i.e., descending towards the gap) likely ensures all sand will be drained.

#### 2.6.5 Never stop mitigating sand losses

It is stressed to never forget the gap taping and using the wire mesh cylinder. Mobi-Gust 2 is only sand tight if all these mitigation measures are used (§2.4.4). The best position for the wire mesh cylinder is in the centre of the sand trap (§2.4.5). Any closer to the exit of the ducts might hamper the flow within Mobi-Gust 2.

#### 2.6.6 Invest in flow visualisation

An attempt was made to visualize the flow within Mobi-Gust 2 using smoke. In turn, to better understand the aerodynamic functioning of Mobi-Gust 2. For example, the empirical data suggests the effectiveness of the honeycomb (e.g., §2.4.2, §2.4.5 or §2.4.6). Flow visualisation might however be helpful to check whether the spiral motions from the fan are actually mitigated or not. The smoke was however advected so fast that the analysis was complicated (§2.4.5). Of course,

## Part II

### Proof Of Concept (POC): recommendations

flow visualisation can be re-attempted. The smoke tests can for example be supplemented by high-performance cameras. Other techniques possible techniques might include Particle Tracking Velocimetry (PTV) or Particle Image Velocimetry (PIV) (§2.4.5). Yet, Mobi-Gust 2 can also be digitized. This enables flow analysis through simulations (e.g., Reynolds-average modelling or Large Eddy Simulations). As an additional benefit, the digitizing enables testing newly created or improved components, before actually constructing them.

#### 2.6.7 Remeasuring and verifying velocity profiles

The velocity profiles need to be remeasured. Especially, the velocity profiles measured at the downwind end of the transition zone are of inadequate quality (§2.4.6). As explained (§2.6.2), the poor-quality results from the underperforming plank in the erosion zone; or the imperfections within the duct system itself. However, upwind velocity profiles need to be remeasured as well; after improving the development of the flow (§2.6.2). On top, velocity profiles also need to be measured above the vertical centreline of the duct (§2.4.6). To clarify, velocity profiles are not symmetric along this vertical centreline, as the roof and bottom have different roughness's.

Next, the velocity profiles must also be verified. The verification can be performed after applying the improvements on flow development (§2.6.2). Then one should measure three velocity profiles, for three unique cross-sectionally averaged flow speeds (i.e., three different fan-settings). These velocity profiles intersect on a semi-log scale if the flow is (nearly) developed (§2.4.6).

#### 2.6.8 Verification of the boundary shear stress

Shear stresses can also be verified. Again, flow development improvements must be applied first (§2.6.2); and then velocity profiles should be remeasured and verified (§2.6.3). The re-established flow parameters can then be verified using additional techniques. An example of an additional verification technique concerns a longitudinal array of pressure sensors (§2.4.6). At least two pressure sensors can measure one pressure gradient. In stationary duct flow, such a pressure gradient is proportional to the boundary shear stress. To this end one can verify the bed shear stress, as calculated with the velocity profiles (§2.4.6). On top, this for example helps verifying flow development (§2.4.6); and the working of the wind gauging system (§2.4.2).

#### 2.6.9 Improving the wind gauging system

The sampling frequency of the wind gauging system is variable. Sampling frequencies are namely decreasing in time (§2.4.2). Presumably, this is caused by inefficient datalogging. A possible solution concerns buffering; i.e., a distinct way of datalogging involving set time intervals. The buffering additionally triggers higher sampling frequencies. However, when the wind gauging system malfunctions, one can lose buffered data that was not yet logged. So, a careful investigation is required, as to what the problem is. Another possible cause for the variable sampling frequency might namely be insufficient computing power of the microcontroller.

Next, the resolution of the wind gauging system is relatively coarse. Improving the coarse resolution involves two viable option. The first option involves a purchasing a higher resolution pressure sensor. The pressure range and the operating voltage of the pressure sensor are important aspects. As explained (§2.4.2), wind speeds of about 10 [m/s] involves a pressure differential of 61.25 [Pa]. If wind speeds increase to 20 [m/s] the pressure differential increases to 245 [Pa]. So, a pressure range of 0-500 [Pa] seems suitable. On top, the pressure sensor must operate at the same voltage as the microcontroller (§2.2.1.7); i.e., 3.3-5 [V]. If the operating voltage of the pressure sensor is not suitable, measures like voltage dividers could be required. An example of an appropriate pressure sensor involves the Fermion LWLP5000 (DFRobot, 2024). The second option involves investing in a more powerful microcontroller. To clarify, the used microcontroller divides the mentioned pressure range into 1,024 [-] discreet values. Yet, a 12-bit microcontroller divides this pressure range into 4,096 [-] discreet values. For example, the new generation Arduino Uno (i.e., 14-bit) or the Arduino Giga (i.e., 16-bit) are suitable options (Arduino S.R.L., N.d.).



## Part II

### Proof Of Concept (POC): recommendations

Then, the accuracy of the wind gauging system has to be regarded in a more detailed fashion. The accuracy of the wind gauging system was verified with a handheld anemometer (§2.4.2). However, the error range of the wind gauging system is still ambiguous. The verification of the wind gauging system involved checking the wind speed. However, it is also possible to directly verify the pressure sensor itself. For example, pressures of known magnitude can be measured in order to check whether the pressure sensor returns the same.

Next, interferences can be mitigated more effectively. Electromagnetic interferences are best shielded by conductive caps; i.e., a grounded metal box (§2.4.2).

Then, the Real Time Clock (RTC) module requires an upgrade. The used RTC-module has a resolution equal to one second. However, the wind gauging system samples above 1 [Hz]; i.e., multiple measurements receive the same timestamp. This complicates creating timeseries and might be solved by purchasing a higher resolution RTC-module.

#### 2.6.10 Improving the power supply

Finally the power supply can be improved. Theoretically the power supply should last about 3 [h] (appendix C.3). The experimented discharging duration reaches only 2.25 [h] (§2.4.1). These discrepancies are mainly caused by the electrical resistance of various electrical components. For example, improvements can be made by applying shorter and thicker wires between the battery and the electrical systems of Mobi-Gust 2.

Next, battery management is important. Battery management involves three main aspects. First of all, the connections between the battery and the electrical systems of Mobi-Gust 2 should be regularly checked (§2.4.1). Experience showed that these connections loosen easily (e.g., by charging or transporting). Besides the associated and undesired safety hazards; the loose connections directly impact the performance of the fan. Permanently fastening these connections however provides the best solution. Second of all, the first and last 5-10 [min] of each power cycle should be excluded from measurements (§2.4.1). Most variability was namely measured within these timespans. This explains the claim that only 2 [h] of the total measured discharge duration (i.e., 2.25 [h]) is practically useful (§2.4.1). Within the mentioned timespan winds are relatively stable. Third of all, the power supply should not be overcharged or fully drained too often (§2.4.1). Avoiding this improves the overall performance of the power supply; and extends its lifetime. For example, the battery-durability test should not be redone too often (§2.2.2.1).

# Part III

## The erodibility of the sand surface

### 3 The erodibility of the sand surface

This chapter presents [part 3](#) of this report and regards the aeolian erodibility of sand surfaces. To this end, Mobi-Gust 2 is employed in applied aeolian research. [Part 3](#) will start off by providing a short recap on [part 1](#) and [2](#) ([§3.1](#)). Amongst others, this recap facilitates readers with little time. Next, the methodology of the mentioned applied research is clarified ([§3.2](#)). This approach leads to the results ([§3.3](#)); which are discussed ([§3.4](#)) thereafter. [Part 3](#) then ends by providing the conclusions ([§3.5](#)) and the associated recommendations ([§3.6](#)).

#### 3.1 Brief recap

[Part 1](#) of this report regarded the general introduction of this research. In short, this introduction considered five main topics. Firstly, the main motivation of this research was clarified ([§1.1](#)). Secondly, the historical background on aeolian research was regarded ([§1.2](#)). Thirdly, the limited coastal applicability of this fundamental theory was treated ([§1.3](#)). Fourthly, the general approach of this research was explained ([§1.4](#)); which additionally introduced [part 2](#) of this report. Finally, the main research question was introduced ([§1.5](#)); which is repeated below for convenience.

*The aeolian erosion process on sandy beaches,  
is solely determined by wind speed and does not rely on surface erodibility.*

[Part 2](#) of this report provided the Proof Of Concept (POC). This POC explored whether a specialized mobile erosion device could be realised. This tailored device is called Mobi-Gust 2; and consists of a mobile wind tunnel system and a wind gauging system. The POC started off by clarifying the project outline ([§2.1](#)); which amongst others described the project criteria. Besides sustainability, these project criteria involve the usability, reliability and controllability of Mobi-Gust 2. Next, the approach to develop Mobi-Gust 2 was clarified ([§2.2](#)). This methodology was split into a design section ([§2.2.1](#)) and a performance section ([§2.2.2](#)). In summary, Mobi-Gust 2 has a sturdy and modular design ([§2.2.1.1](#)) that consists of the following main components: a fan (i.e., propelling the air; [§2.2.1.2](#)); a contraction (i.e., accelerating the air flow; [§2.2.1.3](#)); a honeycomb and a transition zone (i.e., conditioning the air flow; [§2.2.1.4](#)); an erosion zone and a saltation hopper (i.e., allowing and enhancing the erosion process; [§2.2.1.5](#)); a sand trap (i.e., catching the eroded granular material; [§2.2.1.6](#)); a wind gauging system (i.e., measuring the wind speed; [§2.2.1.7](#)); and a power supply (i.e., powering the electrical systems; [§2.2.1.8](#)). After completing the design, the performance of Mobi-Gust 2 was checked through a series of experiments. The experiments covered the following main topics: the durability of the electrical systems ([§2.2.2.1](#)); the wind (gauging system) properties ([§2.2.2.2](#)); the drainage rate of the saltation hopper ([§2.2.2.3](#)); the sand-tightness of the mobile wind tunnel system ([§2.2.2.4](#)); the achievable wind speeds in relation to the modular design of the mobile wind tunnel system ([§2.2.2.5](#)); the development of the flow within the mobile wind tunnel system ([§2.2.2.6](#)); and finally the in-situ erosion performance of Mobi-Gust 2 ([§2.2.2.7](#)). The separation between the design and the performance was not applied anymore from the methodology onward. To clarify, the design and the performance of Mobi-Gust 2 were discussed simultaneously, as they are closely related. Next, the results of the methodology were provided ([§2.3](#)) and discussed thereafter ([§2.4](#)). The results and the discussion allowed the formulation of a conclusion regarding the project criteria ([§2.5](#)). Overall, Mobi-Gust 2 partially meets the project criteria. However, Mobi-Gust 2 is still suitable to explore the main research question of this applied research (e.g., [§2.4.7](#) or [§2.5.2](#)). As the project criteria were only partially fulfilled, recommendations could be formulated ([§2.6](#)). The recommendations for the mobile wind tunnel system mainly target flow development. On top, it is advised to not yet improve the achievable wind speeds within the mobile wind tunnel system; as this is relatively laborious and costly. The recommendations for the wind gauging system mainly target the variable sampling frequency, as well as improving its resolution and accuracy.

## 3.2 The methodology to explore sand surface erodibility

This section clarifies the approach of the applied aeolian research using Mobi-Gust 2. In general, the methodology describes how the main research question is confronted. On top, the methodology highlights how the field expeditions are conducted. This section is subdivided in five subsections. Firstly, the general outline of the experiments are clarified (§3.2.1). Secondly, it is discussed how these experiments are used (§3.2.2). Thirdly, the data to be gathered will be discussed (§3.3.3). Fourthly, transport- and time management are treated (§3.2.4). Finally, remarks are provided on the safety during field expeditions (§3.2.5).

### 3.2.1 The layout of the experiments

The applied research employs two types of experiments. These experiments are called the erosion test (§3.2.1.1) and the saltation test (§3.2.1.2). Both tests will be explained in outline.

#### 3.2.1.1 The outline of the erosion test

The erosion test is analogous to clear wind erosion (Schiereck, 2019). To clarify, the erosion test involves generating aeolian erosion, without an upwind supply of sand. Practically this means that the saltation hopper (§2.2.1.5) is not used during the test. The erosion test can be compared to natural erosion, caused by winds that attack the beach from the ocean. To clarify, these landward directed winds are also clear of sand (i.e., as the ocean surface does not contain erodible material).

The experiment can be summarized in three main steps. Step one concerns mounting and configuring Mobi-Gust 2 according to the manuals (appendix G.3). To be clear, this includes correctly setting the mobile wind tunnel system, as well as the wind gauging system. Step two concerns switching on the fan. Consequently, an enclosed and adjustable wind flow is generated within Mobi-Gust 2 (§2.2.1.2 & §2.2.1.3). In turn, the associated wind shear (§2.2.1.4) can be used to generate aeolian erosion (§2.2.1.5). Step three concerns manually emptying the sand trap (§2.2.1.6). Emptying the sand trap is done after specified intervals and/or after a full experiment.

#### 3.2.1.2 The outline of the saltation test

The saltation test is analogous to live bed erosion (Schiereck, 2019). To clarify, the saltation test involves an upwind supply of sand during the aeolian erosion process. Practically this means that the saltation hopper (§2.2.1.5) is used during the test. Likewise to the erosion test, the saltation test is representative for natural processes. In elaboration, the experiment describes the generation of aeolian erosion at one location (e.g., the supratidal beach); while being influenced by a supply of sand from another location (e.g., the intertidal beach).

The experiment can be summarized in four main steps. All steps are similar to the erosion test (§3.2.1.1); yet between step two and three the saltation hopper must be used. This hopper injects sand into Mobi-Gust 2 with a specific rate (§2.3.3). As explained, the resulting upwind supply of sand causes enhances the aeolian erosion process within the erosion zone (§2.2.1.5). The enhanced erosion process will be experimentally demonstrated.

### 3.2.2 Using hybrid experiments to assess the main research question

The Proof Of Concept (POC) showed issues concerning the erosion performance of Mobi-Gust 2 (§2.4.7). In repetition, the finite pressure capacity of the fan and the (wet) time of year were likely influential. To this end, it is expected to be difficult to explore the aeolian erodibility of sand surfaces through field expeditions only. Consequently, an alternative measurement strategy is adopted. The original strategy is however provided in appendix G.4.1 for reference. The mentioned alternative uses a series of hybrid tests. The new strategy employs the erosion- and the saltation test as explained (§3.2.1). However, both tests are embedded in overarching hybrid experiments. In this case, the hybrid tests refer to two experimental combinations. The first combination of tests explores the influence of the moisture content on the erosion flux. The second combination investigates the influence of an upwind supply of sand on the erosion flux.



## Part III

### The erodibility of the sand surface: introduction

The first hybrid experiment involves conducting two erosion tests. Six main steps summarize the total approach of this overarching experiment. Step one involves performing an erosion test (§3.2.1.1) in the field (i.e., on the Sand Engine; appendix A). Step two involves excavating the experimented sand bed. Step three concerns transporting the excavated sand to Delft University of Technology. Step four involves drying the sand sample. Step five involves filling the tailored sand pit with the dried sand (§2.4.7). The last step concerns reconducting an erosion test (§3.2.1.1) in the laboratory. This first hybrid test can be used to assess the main research question; as both tests are conducted with the same (dried) granular material. To clarify, if both tests exhibit a unique erosion flux, while wind conditions were similar, the main research question must be incorrect. This hypothetical result namely demonstrates that similar winds might erode a sand surface differently, depending on moisture content variations.

The second hybrid experiment involves performing an erosion test and a saltation test. Two main steps summarize the total approach of this overarching test. Step one again involves performing an erosion test (§3.2.1.1) in the field (i.e., on the Sand Engine; §1.4). In contrast, step two involves conducting a saltation test (§3.2.1.2) at that exact same location. To be clear, this means that Mobi-Gust 2 will not be relocated in between the experiments. In preparation the quantity of sand required is estimated for a single saltation test. This estimate is based on the mentioned discharge rate of the saltation hopper (§2.3.3). The same granular material will be used, with which this discharge rate was established. This hybrid test can again be used to assess the main research question; since both tests will be conducted on the same in-situ sand surface. To clarify, if the tests show different erosion fluxes, while wind conditions were similar, the main research question must again be incorrect. This hypothetical result namely shows that similar winds might erode a sand surface differently, depending on already having sand in transport or not.

Both hybrid experiments will be verified in the laboratory. After all, Mobi-Gust 2 has a tailored sand pit (§2.4.7), while an in-situ sand bed will be sampled. Besides verifying the results of the hybrid experiments, these laboratory tests add robustness to the applied research. To clarify, the second hybrid experiment only involves field tests. As explained, in-situ erosion experiments might present difficulties (§2.4.7). Consequently, an erosion test (§3.2.1.1) and a saltation test (§3.2.1.2) will be reconducted in the laboratory. Field conditions are mimicked by occasionally wetting the sand surface. This artificial wetting is done systematically (appendix I.4).

Overall, a variety of experiments will be conducted. Table 15 includes the hybrid experiments. To clarify, Field I and Lab I form the first hybrid experiment. The second hybrid experiment concerns Field II and Field III. As explained, Field II and Field III are conducted on the same in-situ sand surface. Field II thus reconducts Field I, as the bed of Field I is already excavated. Table 15 also includes the verification tests. The first hybrid experiment can be verified by comparing Lab I and Lab III. The second hybrid experiment can either be verified by comparing Lab I and Lab II; or by comparing Lab III and Lab IV.

*Table 15 – The experiments (rows) and their characteristics (columns)*

	Field I	Field II	Field III	Lab I	Lab II	Lab III	Lab IV
Erosion test	<i>x</i>	<i>x</i>		<i>x</i>		<i>x</i>	
Saltation test			<i>x</i>		<i>x</i>		<i>x</i>
Wet surface	<i>x</i>	<i>x</i>	<i>x</i>			<i>x</i> *	<i>x</i> *
Excavation	<i>x</i>						

### 3.2.3 The expected data and the additional activities

Different tests must be compared. To this end, erosion fluxes are estimated (De Vries et al., 2014); see equation 53. The erosion flux ( $E$  [ $kg/m^2/s$ ]) regards the eroded sand mass ( $m_e$  [ $kg$ ]) averaged over the surface area where the erosion took place ( $A_e$  [ $m^2$ ]) and the duration involved ( $t_e$  [ $s$ ]).

$$53) \quad E = \frac{m_e}{A_e t_e}$$

### Part III

#### The erodibility of the sand surface: introduction

Conducting the experiments provides all necessary parameters. To clarify, a timekeeping device, such as a stopwatch, reveals the elapsed time ( $t_e [s]$ ). The eroded sand mass ( $m_e [kg]$ ) follows from collecting and weighing the content of the sand trap. However, the saltation test requires an additional step to determine the eroded sand mass. To clarify, sand will also be injected into Mobi-Gust 2 using the saltation hopper (§2.2.1.5). So, to find the erosion mass ( $m_e [kg]$ ), the collected sand mass ( $m_c [kg]$ ) should be corrected for the added sand mass ( $m_a [kg]$ ). This is summarized in equation 54. Next, the surface area ( $A_e [m^2]$ ) of the erosion process is already known. The surface of the erosion zone is namely 1 [m] by 0.15 [m] (§2.2.1.5).

$$54) \quad m_e = m_c - m_a$$

The wind speeds within Mobi-Gust 2 will be measured during the experiments. Specifically, the wind gauging system senses pressure differentials; and uses this data to calculate and visualize wind speeds in real-time (§2.2.1.7). Simultaneously, the calculated wind speeds are logged. Also the raw data will be logged, in order to add robustness to the approach. The raw data concerns a digitized version of the measured pressure differentials. The approach thus allows to recalculate and check the measured wind speeds; for example using programming tools.

Additional activities are performed as well. One of the activities concerns mapping the field location, using the Global Navigation Satellite System (GNSS). Sand properties are explored using a Grain Size Distribution (GSD) analyses. Next, environmental conditions are regarded by conducting Moisture Content (MC) analyses. The sand bed will be photographed as well (e.g., showing shells, bed forms or vegetation). These actions involve specific rules to enhance the reproducibility; see for example appendix I.5 or I.6.

#### 3.2.4 Transport- and time management during field expeditions

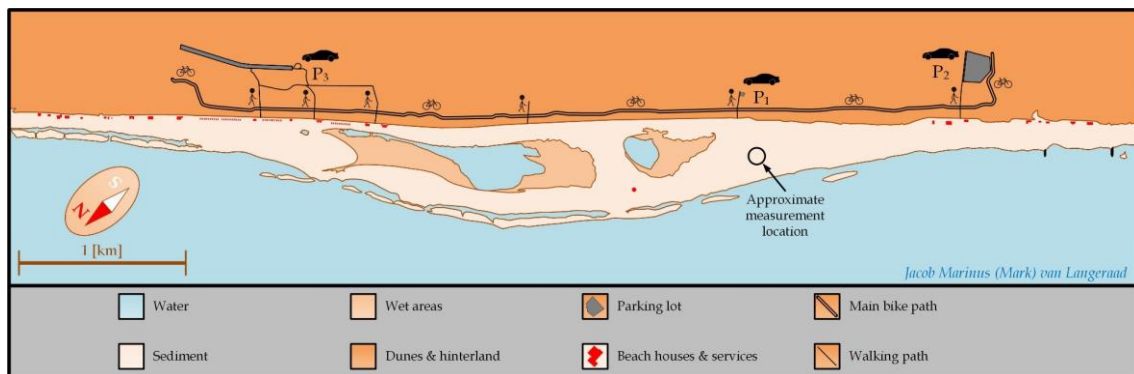


Figure 88 - The Sand Engine and its accessibility; see also appendix A

The Sand Engine (appendix A) is relatively accessible (Google, 2022). The mega nourishment is located relatively near Delft University of Technology; and is surrounded by major highways (appendix G.2). Around the Sand Engine there are three parking lots are available (figure 88). The distances and transit times between the university and these parking lots are relatively similar. On average the journey involves a distance of about 20 [km] in a duration of roughly 30 [min]. However, the involved duration might be different depending on traffic. In elaboration, the rush hours around 5PM tend to be busiest. More information is listed in appendix G.2. A performed test expedition (§2.3.7) roughly confirmed mentioned transit times. As introduced (§1.4), the close proximity of the Sand Engine enables short-lasting field expeditions. In this case, the field expeditions will last just one day; and are launched from and ended on the university.

Independent transportation will be used to transport Mobi-Gust 2. The used vehicle concerns a general MPV car (i.e., a Chrysler Voyager). Mobi-Gust 2 easily fits in such a car (figure 89), which also demonstrated in appendix G.2.1.2. Parking will primarily take place closest to the measurement location (figure 88); i.e., parking P1. This parking is normally solely available for bikes, yet specialized access is granted from the authorities. The parking is expected to be available

### Part III

#### The erodibility of the sand surface: introduction

always, as the parking is normally restricted for cars. Next, the measurement location ([figure 88](#)) is reached by means of a converted box wagon. Mobi-Gust 2 fits completely on this box wagon ([figure 90](#)), which is also demonstrated in [appendix G.2.1.2](#). A test expedition (§2.2.2.7) revealed that loading the car takes roughly 30 [min]. However, if the equipment is prepared the day before, this duration shortens a bit. Next, it takes about 30 [min] to simultaneously unload the car and pack the box wagon. With the fully packed box wagon it roughly takes an additional 30 [min] to reach the measurement location. Yet the mentioned durations can be a bit different, depending on the number of people within the field crew. On the one hand, this way of transporting involves long durations and is rather laborious. On the other hand, this way of transporting provides robustness and flexibility to the applied research. Using a private car, as well as the upgraded box wagon, omits the need for assistance from Delft University of Technology.



Figure 89 - Fitting Mobi-Gust 2 in an MPV



Figure 90 - Moving Mobi-Gust 2 by means of a box wagon

The field expeditions are conducted within normal working hours. In elaboration, that means that field expeditions generally focus between 9AM and 5PM. The (un)loading and the cleaning of equipment might fall outside the mentioned timespans. Next, it is possible to conduct multiple experiments during one field expedition. The number of achievable experiments per day depends on multiple aspects, of which six are listed. Firstly, the duration of individual experiments matters. Secondly, the power supply is of importance, as it has a finite power capacity (§2.4.1). Thirdly, an available solar panel can provide extra power (i.e., 100 [W]) on sunny days. Fourthly, the size of the field crew is of importance; i.e., having more or less assistance. Fifthly, the distance between subsequent measurement locations is of importance as it takes time to reposition Mobi-Gust 2. Finally, the available daylight is of importance as well. To clarify, the field expeditions are conducted in wintertime, in which the sun may set as soon as 5PM ([Weeronline, 2023](#)). The available daylight is of course important in view of safety. In most cases it is expected that the number of experiments per day is restricted by the power supply. If the presence of the solar cell is neglected, it is for example possible to conduct four experiments of half an hour each.

#### 3.2.5 Safety during field expeditions

Safety is a major concern during field expeditions. As mentioned, assistance from Delft University of Technology is not required. However, that does not mean that field expeditions are allowed to be conducted individually. From a safety perspective, at least one extra person is required to be present during the expedition. However, this person does not have to be tied to Delft University of Technology. As explained (§2.2.2), a dedicated safety plan was made for the field measurements. Amongst others, this safety plan includes general safety hazards. These safety hazards are for example related to the flora and fauna to be encountered; as well as environmental conditions (e.g., weather, water levels or winds). On top, research hazards are regarded as well. These research hazards for example concerns the used equipment and how these are protected during field expeditions. Finally, the safety plan considers mitigation measures to the mentioned risks.

### 3.3 Analysing the erodibility of the sand surface

This section displays the results of the applied aeolian research. Mobi-Gust 2 was used to gather the erosion- and wind speed data; and additional activities were conducted as well (§3.2.3). The gathered data is exhibited in four subsections. Firstly, general remarks are provided on the attempted field expeditions (§3.3.1). Secondly, the results from the first hybrid experiments are shown (§3.3.2). Thirdly, the results from the second hybrid experiments are shown (§3.3.3). Lastly, the results from all experiments, i.e., including the verification tests, are provided (§3.3.4).

#### 3.3.1 General remarks on the conducted field expeditions

Mobi-Gust 2 was employed in field expeditions. The unsuccessful expeditions still contributed to the insights of this research. In short, the experiments were hampered by rainfall, frost and intense winds. Small reports of the field expeditions are added in [appendix H](#).

As explained (§3.2.2), hybrid tests were used to assess the main research question. In elaboration, a series of erosion tests (§3.2.1.1) and saltation tests (§3.2.1.2) were employed. These tests explore the aeolian erosion process; related the erosive ability of the wind, opposed to the supplying ability of the sand surface. [Figure 91](#) shows the location of the successful measurements.

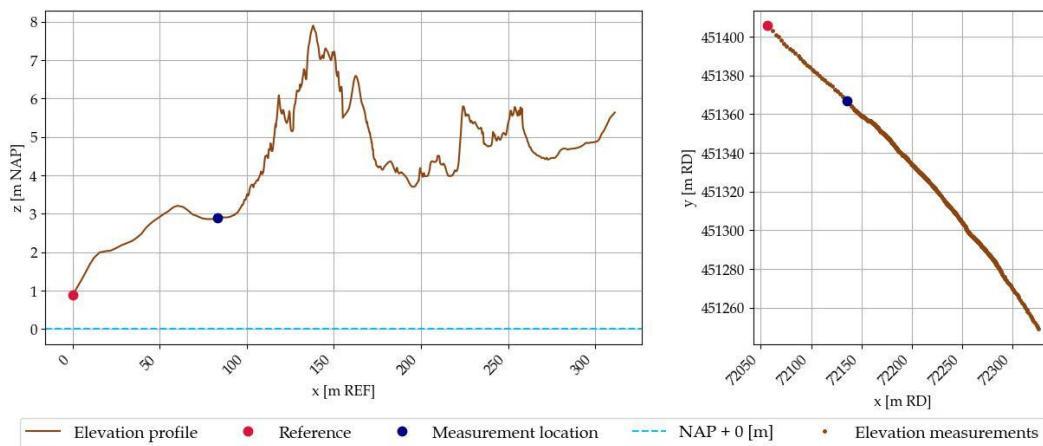


Figure 91 – The measurement location on the Sand Engine; see also [Figure 88](#)

#### 3.3.2 The influence of moisture content on the erosion flux

The first hybrid experiment explored the influence of moisture content on the erosion flux. To this end, an erosion test (§3.2.1.1) was conducted in the field ([figure 92](#)); i.e., Field I. The experimented sand surface was relatively 'clean' ([figure 93](#)); e.g., relatively free of shells, vegetation or litter. Moisture contents reached roughly 5 [%]; see [appendix I.6](#). Yet, the moisture content samples were taken relatively deep; and are therefore not representative for the surface layer ([appendix I.6](#)). Field I did not produce any measurable erosion (i.e.,  $0.00 [kg/m^2/s]$ ). The average centreline wind speed within Mobi-Gust 2 was  $9.05 [m/s]$ . On top, the centreline wind speed had a standard deviation of  $0.61 [m/s]$ . After Field I, the sand bed was excavated ([figure 94](#)). This excavated sand volume was similar to the volume of the sand pit (§2.4.7); and was sampled right below the erosion zone. The excavated sand bed was then taken to the laboratory, where it was dried ([figure 95](#)). Next, a Grain Size Distribution (GSD) analysis was conducted ([figure 96](#)). Eventually, the erosion test (§3.2.1.1) was reconducted in the laboratory ([figure 97](#)) using the tailored sand pit (§2.4.7); i.e., Lab I. Lab I showed an erosion flux of  $0.01 [kg/m^2/s]$ . The average centreline wind speed within Mobi-Gust 2 was  $9.38 [m/s]$  (i.e., + 3.65 [%] with respect to Field I). On top, the centreline wind speed exhibited a standard deviation of  $0.65 [m/s]$  (i.e., + 6.56 [%] with respect to Field I). All mentioned data is also shown in §3.3.4.



## Part III

### The erodibility of the sand surface: results and analysis



Figure 92 – A prepared Mobi-Gust 1 just before conducting Field I on the Sand Engine

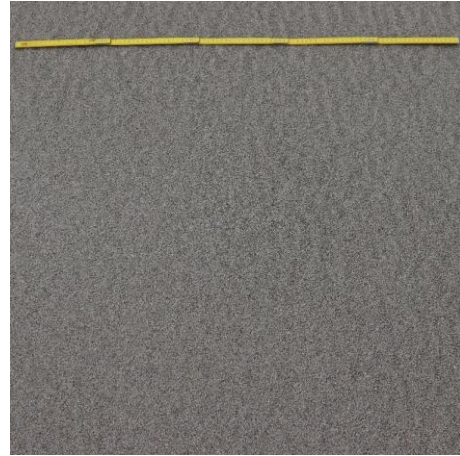


Figure 93 – A close up of the tested bed of Field I; the picture includes a 1 [m] folding ruler for reference



Figure 94 – Excavating the sand bed following Field I



Figure 95 – Drying the excavated sand bed

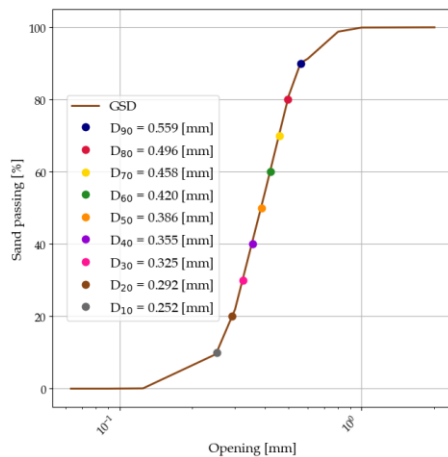


Figure 96 – The GSD of the excavated material

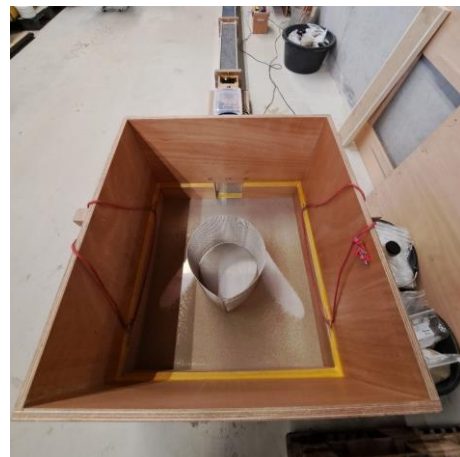


Figure 97 – Conducting Lab I

### 3.3.3 The influence of saltation sand on the erosion flux

The second hybrid test explored the effects of an upwind supply of sand on the erosion flux. To this end an erosion test (§3.2.1.1) was performed in the field (figure 98); i.e., Field II. The explored sand surface again appeared relatively 'clean' (figure 99); and was very similar to the previous one (i.e., Field I). As both tests are conducted close to each other (e.g., see figure 98) this is logical. The moisture content remained virtually unchanged; and roughly reached roughly 5 [%]; see appendix 1.6. It is stressed that this moisture content is not representative for the surface layer.

### Part III

#### The erodibility of the sand surface: results and analysis

Field II did again not produce any measurable erosion (i.e.,  $0.00 \text{ [kg/m}^2\text{/s]}$ ). The average centreline wind speed within Mobi-Gust 2 was  $9.00 \text{ [m/s]}$ . On top, the centreline wind speed had a standard deviation of  $0.54 \text{ [m/s]}$ . Next, a saltation test (§3.2.1.2) was conducted at the exact same spot (figure 100); i.e., Field III. Notice the presence of pre-packed sand samples of known mass. The total amount of sand required was estimated using the drainage rate of the saltation hopper (§2.3.3). Field III produced an erosion flux of  $0.03 \text{ [kg/m}^2\text{/s]}$  (figure 101). The average centreline wind speed within Mobi-Gust 2 was  $8.43 \text{ [m/s]}$  (i.e.,  $-6.33 \text{ [%]}$  with respect to Field II). On top, the wind speed exhibited a standard deviation of  $0.36 \text{ [m/s]}$  (i.e.,  $-33.33 \text{ [%]}$  with respect to Field II). The mentioned data is visualized in §3.3.4.



Figure 98 - Conducting Field II;  
Notice the excavation hole from Field I behind Mobi-Gust 2

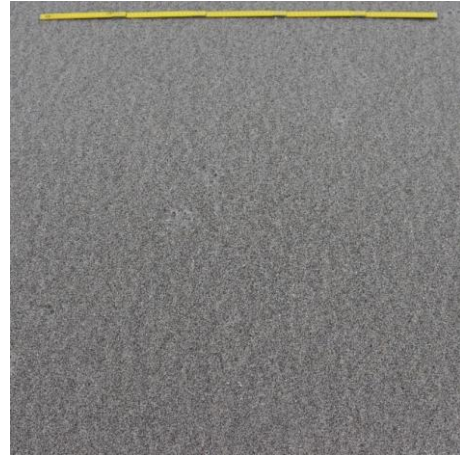


Figure 99 - A close up of the tested bed of Field II;  
the picture includes a 1 [m] folding ruler for reference



Figure 100 - Conducting Field III on the Sand Engine

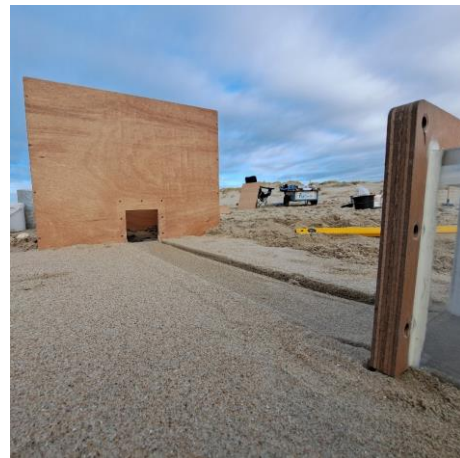


Figure 101 - The eroded bed after conducting Field III

#### 3.3.4 Summarizing the gathered data

Table 16 (on the next page) shows the gathered data from all tests (§3.2.2). The mentioned table thus includes the hybrid tests (i.e., Field I, II and III; and Lab I); as well as the additional laboratory tests (i.e., Lab II, III and IV). For convenience, table 16 repeats the setup of each test. It is stressed that all laboratory tests used the excavated sand bed from Field I (figure 96). Amongst others, table 16 shows: the duration ( $t_e \text{ [s]}$ ) of each test; the eroded sand mass ( $m_e \text{ [kg]}$ ); and the surface area ( $A_e \text{ [m}^2\text{]}$ ) over which the erosion took place. The stated parameters are used to establish the erosion fluxes ( $E \text{ [kg/m}^2\text{/s]}$ ); see equation 53 (§3.2.2). If applicable, table 16 also includes the added sand mass ( $m_a \text{ [kg]}$ ) and the collected sand mass ( $m_c \text{ [kg]}$ ); see equation 54 (§3.2.2). Table 16 finally shows the statistics of the non-averaged wind speed data, i.e., the means ( $\mu_u \text{ [m/s]}$ ) and standard deviations ( $\sigma_u \text{ [m/s]}$ ). The eroded mass is corrected for a mass of roughly  $10 \text{ [g]}$  (see §2.4.3, §2.4.4 & appendix I.3.5). Appendix I.3 shows pictures of the sand mass determination.

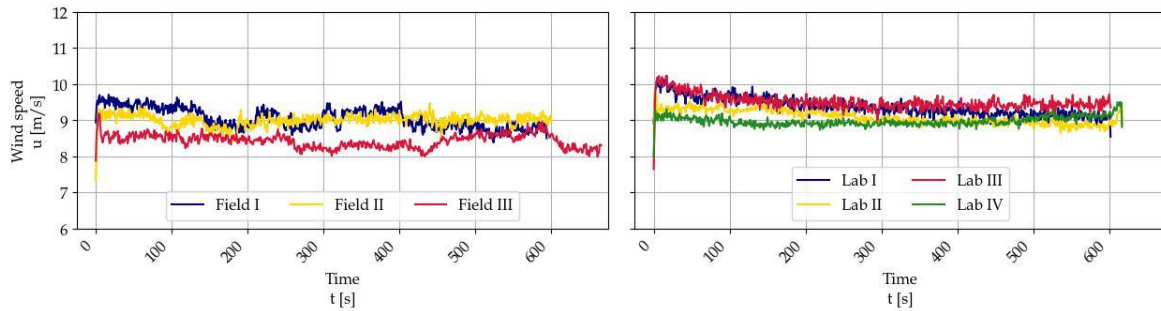
### Part III

#### The erodibility of the sand surface: results and analysis

*Table 16 – All results of the conducted experimental research (\*the saltation hopper)*

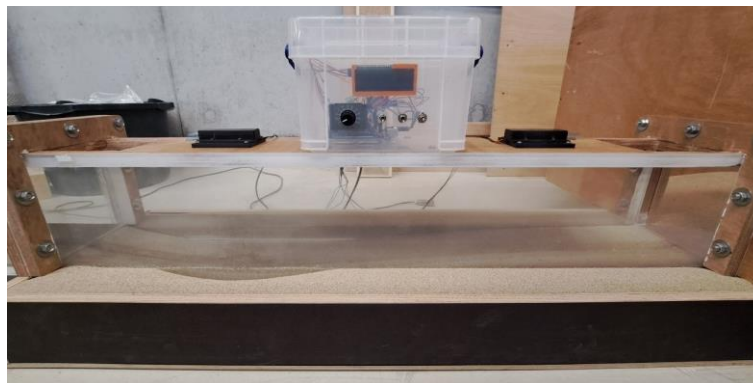
Test setup	Experiment	Field I	Field II	Field III	Lab I	Lab II	Lab III	Lab IV
	Erosion test	$x$	$x$	—	$x$	—	$x$	—
	Saltation test	—	—	$x$	—	$x$	—	$x$
	Wet surface	$x$	$x$	$x$	—	—	$x^*$	$x^*$
	Excavation	$x$	—	—	—	—	—	—
Test duration	$t_e$ [s]	594	600	666	602	618	602	617
Sand masses	$m_a$ [kg]	—	—	12.05	—	12.52	—	13.32
	$m_c$ [kg]	0	0	15.22	1.07	18.24	0	15.10
	$m_e$ [kg]	0	0	3.17	1.07	5.72	0	1.78
Surface area	$A_e$ [m <sup>2</sup> ]	0.15	0.15	0.15	0.15	0.15	0.15	0.15
Erosion flux	$E$ [kg/m <sup>2</sup> /s]	0	0	0.03	0.01	0.06	0	0.02
Wind conditions	$\mu_u$ [m/s]	9.05	9.00	8.43	9.38	9.08	9.51	8.97
	$\sigma_u$ [m/s]	0.61	0.54	0.36	0.65	0.35	0.61	0.31

For reference, [figure 102](#) provides the wind speed data. Mind that these graphs show moving averages evaluated over one-second intervals. Using moving averages namely improves the clarity of the graphs. [Appendix I.2.4](#) contains the raw wind speed data.



*Figure 102 – Wind speed data (one-second moving averages);  
Left = field data & right = laboratory data*

Finally, the erosion zone walls were undermined in experiment Lab II ([figure 103](#)).



*Figure 103 - Lab II showing undermining of the erosion zone walls*



## 3.4 Discussing the erodibility of the sand surface

This section discusses the results of the applied aeolian research using Mobi-Gust 2. This discussion is divided into three subsections. To start off, general remarks are provided on the acquired field data and the associated difficulties (§3.4.1). Next, the measured erosion data is discussed, in relation to the moisture content (§3.4.2). Finally, the measured erosion data is discussed, but then in relation to an upwind supply of sand (§3.4.3).

### 3.4.1 General remarks on the acquired data

General variations exist between the performed tests. These differences are tackled first to facilitate the comparisons later on. To this end, the gathered data (§3.3.4) is partly visualized in figure 104. The surface area of the erosion is not added but concerns a constant value of  $0.15 [m^2]$ .

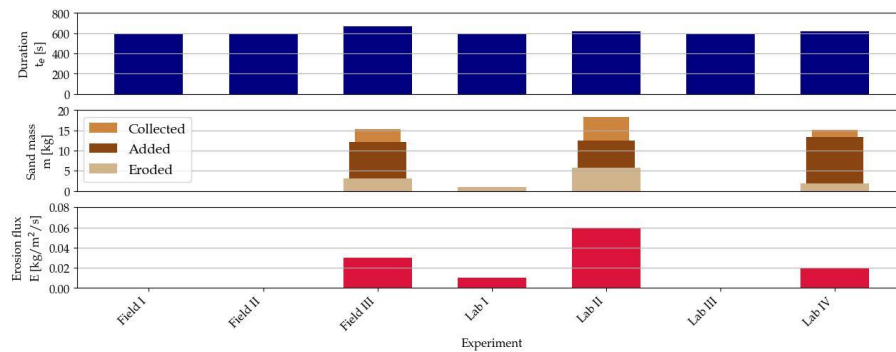


Figure 104 – Visualization of the data in table 16

The first variation source concerns the duration of the tests (figure 104 & §3.3.4). Most variability is present in the saltation tests (§3.2.1.2); i.e., Field III, Lab II and Lab IV. These variations are primarily caused by the drainage of the saltation hopper. After filling, the hopper must fully drain, as the sand samples are weighted upfront. This drainage is more manageable in the laboratory. In the laboratory the sand can namely be weighted while carrying out the tests. In that case, the hopper must still fully drain after filling, yet sand samples are more easily varied in size. Weighing the sand samples in the field is not reliable without shielding the weighing scale. The surrounding wind namely exerts pressure on the weighing plate. Pre-packed sand samples were used to mitigate this situation; which also reduced the workload during Field III. Yet, the sample bags were filled quite well (i.e., about  $1 [kg]$  each). Overall, this explains why Field III is the most off. The differences in the other tests are not very striking. The erosion tests (§3.2.1.1) almost show no variability at all; i.e., Field I, Field II, Lab I and Lab III. This is logical as the tests can be stopped when necessary. Only Field I was stopped a bit too early, due to an undefined error. By defining an erosion flux the differences are however smoothened out. While, the fluxes are based on a bit shorter or longer duration, the tests are still comparable.

Another source of variation concerns the undermining of the erosion zone walls in Lab II (§3.3.4). The undermining does not compromise this research. This can be summarized in three main arguments. Firstly, no other test has exhibited this undermining. Secondly, Lab II is not part of the main comparisons, but concerns a verification test. Thirdly, the nature of this research still enables using this compromised result; yet in a quantitative manner. To clarify, this study primarily produced absolute differences, rather than exposing spatiotemporal variations. So, the erosion flux itself may not be very useful. Yet, a binary observations (i.e., observing or not observing erosion) might still be valuable. After all, the undermining results from relatively severe aeolian erosion; while other tests could not even produce aeolian erosion.

Another source of variation concerns the wind speed within Mobi-Gust 2. While the wind speed statistics (§3.3.4; table 16) might be comparable, there is still some variation present. Figure 105 visually shows this by comparing the main experiments (§3.2.2). Again, these graphs show one-second moving averages for clarity purposes. Appendix I.2.4 shows the raw wind speed data.



### Part III

#### The erodibility of the sand surface: discussion

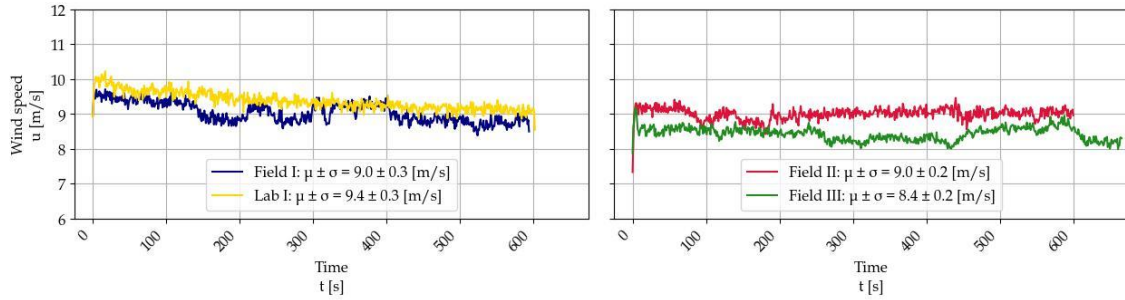


Figure 105 – Wind speed data (one-second moving averages);  
Left = Field I vs. Lab I & right = Field II vs. Field III

Starting off with the statistics of the measured wind speeds. Especially, the means and standard deviations of the saltation tests (i.e., Field III, Lab II and Lab IV) are lower than the ones of the erosion tests (i.e., Field I, Field II, Lab I and Lab III). Yet, maximum power was provided to the fan in all the tests. These discrepancies are caused by the added upwind supply of sand in the saltation tests (§3.2.1.2). As explained (§2.4.5), the injected sand extracts momentum from the wind flow (Lü & Dong, 2011); and it also suppresses turbulence levels (Zhu et al., 2019). In turn, clarifying the observed differences. Equation 44 (§2.4.5) is re-used on the data in figure 105 to learn how much momentum was extracted; see table 17. The Proof of Concept (POC) also used this analysis, so that value is repeated in table 17 as well. The calculations used an air density applicable to Standard Temperature and Pressure (STP); i.e.,  $1.225 \text{ [kg/m}^3\text{]}$  (appendix B). The value of the POC mostly agrees with observed data (Lü & Dong, 2011). While being a bit lower, field II/III and Lab III/IV resemble each other the most. Field II/III and Lab III/IV included a dynamic bed, i.e., the changing flow area influenced the velocities as well (White, 2011). The value that is most off concerns Lab I/II. Yet, this group includes Lab II, which suffered from undermining.

Table 17 - Comparison momentum extraction from the centreline wind speed

	POC	Field II & III	Lab I & II	Lab III & IV
Sand-clear speed ( $u_c \text{ [m/s]}$ )	9.43	9.00	9.38	9.51
Sand-laden speed ( $u_l \text{ [m/s]}$ )	8.61	8.43	9.08	8.97
Momentum extraction ( $\Delta M \text{ [kg/m}^2\text{/s]}$ )	1.00	0.70	0.37	0.66

Additionally, the field data shows more large-scale variations. These oscillations are caused by two effects. Firstly, the power supply was compromised during the field expeditions. The POC (§2.4.1) already demonstrated this; however, the problem was not recognized in time. In repetition, loose battery connections causes more variability in the generated wind speeds, as the fan receives a varying power. Secondly, the oscillations are also caused by pressure fluctuations of the surrounding wind (Voorendt, 2022). To clarify, if surrounding winds were constant and collided with the entrance of Mobi-Gust 2, pressure is locally raised. This increased pressure travels through Mobi-Gust 2. As surrounding winds are variable, it is clear why the field data shows more variability.

The initiation of motion for dry sand is assessed, to mitigate the impact of the stated wind variability. R.A. Bagnold (1941) specified an experimentally verified (capacity limited) threshold equation (equation 55). This threshold friction velocity ( $u_c^* \text{ [m/s]}$ ) depends on: the median grain diameter ( $D_{50} \text{ [m]}$ ); the gravitational acceleration ( $g \text{ [m/s}^2\text{]}$ ); the density of sand ( $\rho_s \text{ [kg/m}^3\text{]}$ ); the density of air ( $\rho_a \text{ [kg/m}^3\text{]}$ ); and an empirical coefficient (i.e., equal to 0.1 [-] in air). Substituting equation 55 into general expressions for the bed shear stress (Bosboom & Stive, 2023); provides a critical bed shear stress ( $\tau_{b,c} \text{ [N/m}^2\text{]}$ ) for the initiation of motion for dry sand (equation 56).

$$55) \quad u_c^* = A \sqrt{D_{50} g \left( \frac{\rho_s - \rho_a}{\rho_a} \right)}$$

$$56) \quad \tau_{b,c} = \rho_a (u_c^*)^2$$

## Part III

### The erodibility of the sand surface: discussion

Analysis reveals that dry granular material could have been moved by Mobi-Gust 2. Measured flow properties within Mobi-Gust 2 namely exceed the critical values as calculated with [equation 55](#) and [56](#). To clarify, the critical values are determined for the median grain sizes that were encountered within this research. These grain sizes concern 430 [ $\mu\text{m}$ ] ([figure 19](#) in [§2.2.1.4](#)), 393 [ $\mu\text{m}$ ] ([figure 39](#) in [§2.2.2.3](#)) and 386 [ $\mu\text{m}$ ] ([figure 96](#) in [§3.3.2](#)). The coarsest grains will result in the highest critical values; which provides a safe approach. On top, the coarsest grains (i.e., 430 [ $\mu\text{m}$ ]) were also scraped from the sand surface, while the others (i.e., 393 and 386 [ $\mu\text{m}$ ]) were excavated. Overall, the coarsest grains are most representative for the sand surface in the applied research. As explained, standard values are used for the other parameters (i.e.,  $A = 0.1$  [–];  $g = 9.81$  [ $\text{m/s}^2$ ];  $\rho_s = 2,650$  [ $\text{kg/m}^3$ ];  $\rho_a = 1.225$  [ $\text{kg/m}^3$ ]). The outcomes for the critical friction velocity ( $u_c^*$  [ $\text{m/s}$ ]) and the critical bed shear stress ( $\tau_{b,c}$  [ $\text{N/m}^2$ ]) respectively become 0.302 [ $\text{m/s}$ ] and 0.112 [ $\text{N/m}^2$ ]. These outcomes are compared to the measured data within Mobi-Gust 2 ([§2.4.6](#)). The lowest measured friction velocity ( $u^*$  [ $\text{m/s}$ ]) and the lowest measured bed shear stress ( $\tau_b$  [ $\text{N/m}^2$ ]), respectively concern 0.540 [ $\text{m/s}$ ] and 0.357 [ $\text{N/m}^2$ ] ([§2.4.6](#)). These measured values exceed the critical friction velocity and the critical bed shear stress by roughly 80 [%] and 220 [%] (i.e., these percentages are rounded to increments of 10 [%]). If even coarser grain sizes are used (e.g.,  $D_{90}$  [ $\mu\text{m}$ ]), the critical values are still exceeded considerably. Mobi-Gust 2 was thus able to move the sand grains if they were dry. As a critical remark, the measured friction velocity and the measured bed shear stress are established in the laboratory. Yet, those values are representative for field conditions as well. To clarify, the measured values originate from the pitot tube mounted at the upwind end of the erosion zone. This pitot tube measures the conditions leaving the transition zone. These flow conditions thus also enter the erosion zone in field experiments. The pitot tube even sticks a bit into the transition zone.

A final remark is provided on the erosion zone walls. These walls are quite blocky; and driving them into the sand bed, tends to displace sand into the erosion zone. While this effect was minor, it still disturbed the sand bed. These disturbances can however not explain the observed differences. To clarify, these disturbances affected all experiment, yet there are tests that showed no aeolian erosion, while others did.

#### 3.4.2 The influence of moisture content on the erosion flux

The conducted tests show that the moisture content may impact the erodibility of the sand surface (i.e., Field I vs. Lab I). The measured variations in the erosion flux ([figure 104](#) or [table 16](#) in [§3.3.4](#)) are namely not explained from variations in wind conditions alone. The wind speed statistics were namely of a comparable order of magnitude ([figure 105](#)). On top, while wind speed variations exist, Mobi-Gust 2 should have been able to move a dry sand surface ([§3.4.1](#)). The winds within Mobi-Gust 2 were namely already strong enough at the upwind end of the erosion zone. Yet on the one hand, a wet in-situ sand surface could not be moved ( $E_{field I} = 0.00$  [ $\text{kg/m}^2/\text{s}$ ]; [table 16](#) in [§3.3.4](#)). While on the other hand, that same dried sand surface could be moved in the laboratory ( $E_{lab I} = 0.01$  [ $\text{kg/m}^2/\text{s}$ ]; [table 16](#) in [§3.3.4](#)); just as predicted with [equation 55](#) and [56](#). Overall, the results show that the erodibility of the sand surface varies, depending on moisture content.

A verification test backs the observations from the main comparison (i.e., Field I vs. Lab I). The moisture content was likely not perfectly isolated within this main comparison. The approach (i.e., excavating, transporting and drying the sand bed) may have also loosened and mixed, a possibly compacted and armoured sand surface. These factors may also influence the erodibility of the sand surface ([Van Rijn, 2023](#)). Luckily, all laboratory tests used the same loosened and mixed sand surface. Consequently, moisture content concerns the only variation within the laboratory test. [Figure 104](#) shows that an erosion tests ([§3.2.1.1](#)) performed on a dry or a wet surface (i.e., Lab I vs Lab III) supports the main comparison (i.e., Field I vs. Lab I). The sand surface in Lab I could namely be mobilized ( $E_{lab I} = 0.01$  [ $\text{kg/m}^2/\text{s}$ ]; [table 16](#) in [§3.3.4](#)). But after artificially wetting the sand surface in Lab III erosion could be stopped ( $E_{lab III} = 0.00$  [ $\text{kg/m}^2/\text{s}$ ]; [table 16](#) in [§3.3.4](#)). The wind conditions in Lab I and Lab III were even more comparable ([figure 106](#)) than in the main comparison (i.e., Field I vs. Lab I). Yet as mentioned, possible differences should not matter, as the threshold of motion for dry sand was exceeded ([§3.4.1](#)).

### Part III

#### The erodibility of the sand surface: discussion

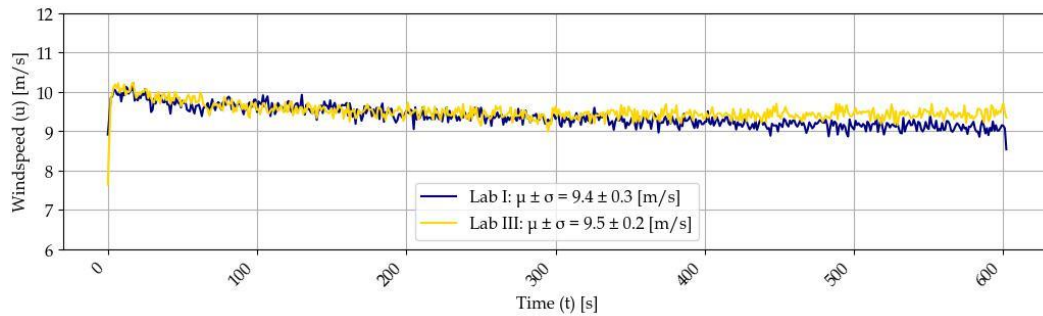


Figure 106 – Wind conditions during the laboratory experiments Lab I and Lab III

Other comparisons seem possible at first glance but are less usable. For example, Lab II and Lab IV maybe also show different erosion fluxes (figure 104), between a wet and a dry sand surface. Yet, both tests involve the saltation hopper; and saltation hopper issues (§2.6.4) caused differences in amount of sand added (figure 104). On top, Lab II was affected by undermining (§3.4.1). Next, Field II and Lab I also seem comparable at first glance. Yet strictly speaking these tests did not use the same sand surface. As explained, the laboratory tests used the excavated sand bed from Field I. Due to the mentioned reasons, also Field III and Lab II are hard to compare.

The first hybrid experiment can be linked to seasonal variations in sand surface erodibility. While the amount of rain is rather equally distribution across the year; rain in the Dutch winter is generally weaker and lasts longer (KNMI, 2023). On top, the evaporation in winter is generally much weaker (KNMI, N.d.). Overall, winter conditions tend to be wetter, causing moisture contents to be higher. As mentioned before, a moisture content of 2 [%] might be enough to completely halt aeolian transport (Hallin et al., 2023). That explains why natural aeolian transport tends to coincide with moderate wind conditions, as more extreme conditions often involve rain (Arens, 1996). Dune growth patterns along the Dutch coast tend to depend on precipitation patterns as well. In elaboration, beaches tend to be narrower during wet periods (Van Straaten, 1961). In general, dune growth tends to focus within calmer periods of moderate weather; while extreme periods of stormy weather generally involve to dune erosion (Bosboom & Stive, 2023). The mentioned conditions are representative for the winter. Counterintuitively, the winds in the Netherlands are generally strongest in winter (Janssen, 2021); because of (strong) westerlies and seasonal effects (Bosboom & Stive, 2023). While stronger winds should have higher drift potentials (Hoonhout, 2017). It is however noted that stronger winds may also winnow erodible material (Huisman et al., 2021). The described seasonality in weather- and dune growth patterns, illustrate the importance of sand surface erodibility along the Dutch coast. This seasonality is also implicitly shown through figure 107 and figure 108. These two pictures are taken within different seasonal periods, roughly at the same location (i.e., notice the tower in the back). Already visually, it appears as if the sand surface is more erodible when summer is closing in. The tests conducted with Mobi-Gust 2 demonstrated this seasonality. On the one hand, the bed of figure 107 (next page) can be compared to the sand surface in Lab I. In contrast, the figure 108 (next page) can be compared to the sand surface in Field I. The contrasting observations of the mentioned tests are steered by differences in moisture content, compaction and armouring. As a final remark it is noted that rain may also generate aeolian transport. Yet, this is related to rain-drop impact, rather than the investigated moisture content (Van Rijn, 2023). On top, the associated transport is generally only 10 [%] compared to similar winds without rain.

## Part III

### The erodibility of the sand surface: discussion



Figure 107 – The Sand Engine in May, 2023



Figure 108 – The Sand Engine in January, 2024

#### 3.4.3 The influence of saltation sand on the erosion flux

The conducted experiments also shows that an upwind supply of sand may impact the erodibility of the sand surface (i.e., Field II vs. Field III). Variations in the wind conditions only, cannot explain the observed differences in the erosion flux (figure 104 or table 16 in §3.3.4). Again, the wind speed statistics were of a comparable order of magnitude (figure 105). On top, despite the variations in the wind conditions, comparisons can still be made because of two main reasons. First of all, the wind did not lose momentum, but transferred it to the injected sand grains (§2.2.1.5, §2.4.5 or §3.4.1). As mentioned, the sand grains focus the extracted momentum in a region close to the sand surface. The momentum redistribution is also actually the process studied in these tests. Second of all and as mentioned, Mobi-Gust 2 should have been able to mobilize dry granular material (§3.4.1). Yet on the one hand, Mobi-Gust 2 was not able to mobilize a wet in-situ sand surface ( $E_{field II} = 0.00 [kg/m^2/s]$ ; table 16 in §3.3.4). But on the other hand, Mobi-Gust 2 was able to mobilize that same sand surface, after the introduction of an upwind supply of sand ( $E_{field III} = 0.03 [kg/m^2/s]$ ; table 16 in §3.3.4). Overall, the tests demonstrate that the erodibility of the sand surface changes, depending on whether the wind already transports sand or not.

A remark is made on the formation of scour holes. Field III namely showed scour development at the upwind end of the erosion zone (figure 109). This was expected, as the flow is underdeveloped (§2.2.1.4). But scour holes have not been clearly observed in the other tests (i.e., except for Lab II; the test that suffered from undermining). Scour holes appear to emerge in tests involving relatively strong erosion; or when an upwind supply of sand is involved; or both, since the upwind supply of sand triggers relatively strong erosion. However, the erosion flux was not corrected for the presence of these scour holes. The approach seems justifiable in view of this research. As explained, binary observations are still meaningful (i.e., observing, or not observing erosion). On top, the erosion process took place across the entire erosion zone (figure 109). In other words, scour holes did not solely cause the observed differences.



Figure 109 – The appearance of the explored sand surface just after conducting Field III



### Part III

#### The erodibility of the sand surface: discussion

Laboratory tests verified the observations. Lab III and Lab IV are performed on the same sand surface, that was artificially wettened ([appendix I.4](#)). The tests were performed shortly after one another, in order to minimize the effect of sand surface drying in between the tests. On top, the sand surface was also not altered in between the tests (e.g., by re-spraying it or something else). All this to ensure that the conditions were as equal as possible. In Lab III the artificially wettened sand surface could not be moved ( $E_{lab\ III} = 0.00 \text{ [kg/m}^2\text{/s]}$ ; [table 16](#) in [§3.3.4](#)). In contrast, after introducing an upwind supply of sand (i.e., Lab IV) the sand surface could be moved ( $E_{lab\ IV} = 0.02 \text{ [kg/m}^2\text{/s]}$ ; [table 16](#) in [§3.3.4](#)). Again, winds in the Lab IV were less strong and less variable ([figure 110](#)) due to the redistribution of momentum. On top, the wind conditions within Mobi-Gust 2 exceeded the threshold of motion for dry sand.

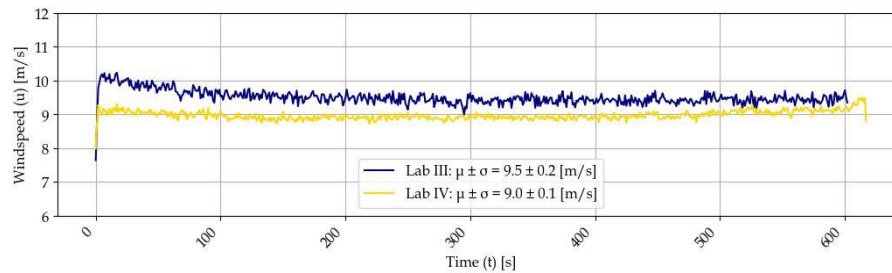


Figure 110 – Wind conditions during the laboratory experiments Lab I and Lab III

Other comparisons seem possible but are again less usable. For example, Lab I vs. Lab IV or Lab II vs. Lab III, also involve comparisons between an erosion test and a saltation test. Yet these also include variations in moisture content (dry vs. wet). Next, Field III can also not be compared freely to any of the laboratory tests, as the laboratory tests used the excavated sand bed of Field I. It is also hard to compare Field I to Lab IV, as moisture contents did not match ([appendix I.6](#)).

The second hybrid experiment can be linked to the non-linearity in sand surface erodibility. For example, consider two locations; one situated upwind of the other. On top, this upwind location is higher elevated than the downwind location (e.g., it is a berm). After precipitation, the upwind location probably dries and drains faster than the downwind location; as it is more exposed and higher elevated. Velocity thresholds at the upwind location are thus also lowering faster than at the downwind location; as moisture contents are dropping faster ([Arens, 1996](#)). The upwind location will thus suffer from erosion earlier than the downwind location. While the sand surface at the downwind location is still too wet for erosion to occur; it all of a sudden receives a supply of sand from the upwind location. As explained, this upwind supply of sand focusses in an area close to the sand surface ([§2.2.1.5](#)). These saltating (i.e., bouncing) and creeping (i.e., rolling) sand grains transfer momentum (i.e., collide) to the sand surface of the downwind location. As a result, the downwind location might be eroded, even before it has dried enough for sand-clear winds to actually erode it. In that case, the erodibility of the downwind location depends on the erodibility of the upwind location. The erodibility of the sand surface thus exhibits non-linear behaviour as it depends on itself. The mentioned example is observed in the field ([Hallin et al., 2023](#)).

This non-linear behaviour is also present along the vertical axis. To clarify, a simplified two-dimensional and layered sand bed is considered ([figure 111](#)). A shielded sand layer (A) can only be eroded, after the grains on top are eroded (B). This top layer (B) might also be more or less erodible at one place or another. The erodibility of the sand surface is for example impacted by differences in grain sizes (C), interlocking processes (D), the presence of shells (E), or many other examples (e.g., [§1.3](#)). The moisture content is also of importance ([figure 111](#)), which is influenced by the examples given. Overall, the erodibility of the sand surface concerns a non-linear interplay between sand characteristics and environmental conditions.

### Part III

#### The erodibility of the sand surface: discussion

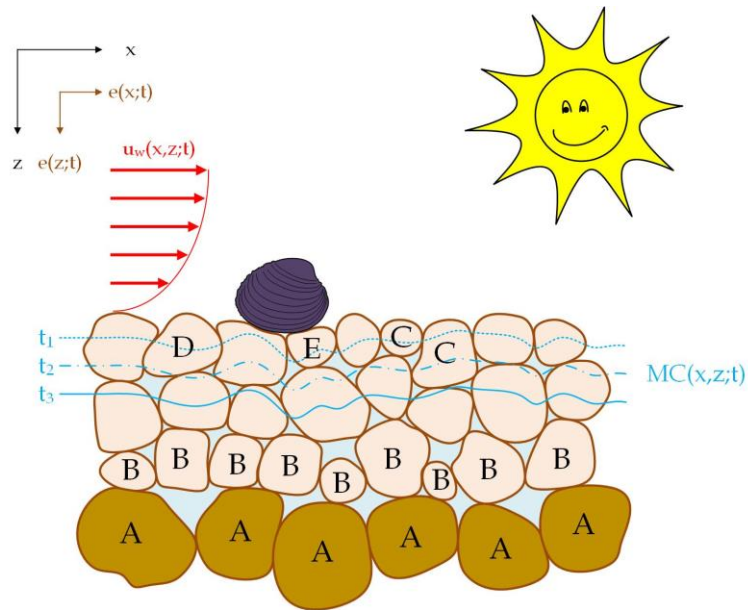


Figure 111 - Non-linearities in sand bed erodibility

The discussed non-linearity has consequences for the results in this research. Erosion fluxes are namely used to compare the results (e.g., [figure 104](#), or [table 16](#) in [§3.3.4](#)). These erosion fluxes are computed for entire experiments, i.e., without using intervals. In other words, the computed erosion fluxes assume a linear erosion process throughout the experiment. In view of the provided explanations within this section, that assumption cannot be accurate. Actually, this concerns the next big step in coastal aeolian research. What actually is this relation?

### 3.5 The conclusions from the applied aeolian research

The research question of the applied research with Mobi-Gust 2 is assessed within this chapter. This research question follows from the desire to better understand coastal aeolian sand exchange (see [part 1](#) of this report). To answer the research question, a novel and specialized mobile erosion device was developed and tested (see [part 2](#) of this report). In clarification, the mentioned device is called Mobi-Gust 2; and consists of a mobile wind tunnel system and wind gauging system. Subsequently, Mobi-Gust 2 was deployed in the laboratory and in field expeditions (see [part 3](#) of this report). For convenience, the research question to be answered is repeated below.

*The aeolian erosion process on sandy beaches,  
is solely determined by wind speed and does not rely on surface erodibility.*

The conclusions on this research question are divided into two stages. The research was namely conducted using two sets of experiments. The first set of experiments provides a conclusion related to moisture content ([§3.5.1](#)). The second set of experiments substantiates this conclusion, but then related to an upwind supply of sand ([§3.5.2](#)). To finalize, remarks are provided on the position of these conclusions within the academic field of coastal aeolian research ([§3.5.3](#)).

#### 3.5.1 Aeolian erosion from a dry and wet sand surface

The experiments studied aeolian erosion from sand surfaces of different wetness ([§3.2.2](#)). In short, these experiments involved laboratory- and field tests. Mobi-Gust 2 was first used in a field expedition that attended the Sand Engine (see [appendix A](#) for more information). Here it was tried to generate aeolian erosion from a wet in-situ sand surface with sand-clear winds ([§3.2.2](#)); i.e., analogues to clear wind erosion ([§3.2.1.1](#)). Following this in-situ test, the sand bed was excavated. Next, the sand sample was dried within the Hydraulic Engineering laboratory of Delft University of Technology. The same experiment was then repeated in a tailored sand pit ([§3.3.2](#)).

Coastal aeolian erosion is not solely controlled by the wind speed. In contrast, coastal aeolian erosion also relies on sand surface erodibility. This conclusion follows from comparing experiments Field I and Lab I ([§3.3.2](#) & [§3.4.2](#)). The wet in-situ sand surface could namely not be eroded (i.e.,  $E_{field I} = 0.00 [kg/m^2/s]$ ). However, that same dried sand surface could be eroded (i.e.,  $E_{lab I} = 0.01 [kg/m^2/s]$ ). Besides comparable wind conditions within Mobi-Gust 2 ([§3.4.2](#)); both tests involved wind conditions above the threshold of motion for dry sand ([§3.4.1](#)). As a result, the wind conditions cannot explain the observed differences. Verification tests (i.e., Lab I vs. Lab III) exhibited similar outcomes ([§3.3.2](#) & [§3.4.2](#)). Verification was important as the approach (e.g., excavation) likely also loosened and mixed the explored sand bed. However, the verification tests involved the same loosened and mixed granular material. In one of the verification tests the sand surface was artificially wettened ([appendix I.4](#)). Consequently, the verification tests isolated moisture content even better. Overall, the erodibility of the sand surface varies, depending on differences in the moisture content.

A final remark is made on the seasonality of aeolian processes; as a result of seasonal variations in sand surface erodibility. Aeolian processes govern dune growth ([§1.1](#)). Both aeolian processes and dune growth are stronger in moderate conditions; while being weaker in more extreme conditions ([§3.4.2](#)). To clarify, extreme (stormy) conditions often coincide with rain; and moisture content hampers aeolian erosion. Moderate conditions can be representative for (dry) summer conditions, while extreme conditions can be representative for (wet) winter conditions. In that same manner, Lab I can be representative for (dry) summer conditions; while Field I can be representative for (wet) winter conditions. These tests thus implicitly demonstrate seasonal variations in sand surface erodibility ([§3.4.2](#)).

### 3.5.2 Aeolian erosion with and without an upwind supply of sand

The experiments investigated aeolian erosion from a wet in-situ sand surface with and without an upwind supply of sand (§3.2.2). In short, these experiments concerned field experiments on the already mentioned Sand Engine (see appendix A for more information). Two different experiments were conducted during the field measurements. The first experiment tried to generate aeolian erosion from a wet in-situ sand surface with sand-clear winds (§3.2.2); i.e., analogues to clear wind erosion (§3.2.1.1). In contrast, the second test tried to generate aeolian erosion from that same wet in-situ sand surface with sand-laden winds (§3.2.2); i.e., analogues to live bed erosion (§3.2.1.2). Simulating sand-clear or -laden winds can be done by means of a saltation hopper (§2.2.1.5). In short, this hopper injects sand grains into Mobi-Gust 2 upwind of the erosion zone.

Again, coastal aeolian erosion is not solely governed by the wind speed. In contrast, coastal aeolian erosion also depends on the erodibility of the sand surface. This conclusion stems from comparing experiments Field II and Field III (§3.3.3 & §3.4.3). The wet in-situ sand surface could not be eroded with sand-clear winds (i.e.,  $E_{field II} = 0.00 [kg/m^2/s]$ ). Yet after adding an upwind supply of sand, that exact same sand surface could be eroded (i.e.,  $E_{field I} = 0.03 [kg/m^2/s]$ ). On the one hand, wind conditions within Mobi-Gust 2 exhibited variations (§3.4.3). On the other hand, the wind conditions can still not explain the observed differences due to two main reasons. First of all, one of the test did not suffer from momentum losses, but merely suffered from momentum redistribution (§3.4.3). On top, it was intended to explore exactly that redistribution effect. Second of all, the wind conditions in both tests were above the threshold of motion for dry sand (§3.4.1). In other words, wind conditions alone cannot explain the observed differences. Verification tests (i.e., Lab III vs. Lab IV) provided similar outcomes (§3.3.3 & §3.4.3). Overall, the sand surface erodibility varies, depending on whether the wind already transports sand or not.

A final remark is made on the non-linear behaviour of sand surface erodibility. Sand-laden winds may erode a sand surface, which was unerodable for sand-clear winds (§3.3.3 & §3.4.3). This discrepancy means that the erodibility at one place, might depend on the erodibility at another place. By example, two hypothetical beach locations are considered; one upwind of the other. The upwind location is higher elevated and more exposed (e.g., a berm) than the downwind location. Compared to the downwind location, the upwind location thus dries and drains faster after being wettened (e.g., by precipitation). When the erodibility of the upwind location becomes sufficient enough, an upwind supply of sand is generated towards the downwind location. This upwind supply of sand may then cause aeolian erosion at the downwind location (i.e., Field III); even before sand-clear are able to erode that surface (i.e., Field II).

### 3.5.3 Experimental verification with a viable Mobi-Gust 2

The development of Mobi-Gust 2 (part 2) changed the direction the applied research (part 3). The initial focus concerned aeolian erosion in a more general context; just as the tone of the main research question suggests. Yet, the Proof Of Concept (POC) of Mobi-Gust 2 (part 2) demonstrated that a shift of focus was necessary (e.g., §2.4.7). To this end, the applied research concentrated on aeolian erosion; but then in relation to moisture content (e.g., §3.4.2) and an upwind supply of sand (e.g., §3.4.3). Consequently, the research question could be retained and solved in relation to the mentioned perspectives. As multiple sources within this report already suggested, the answer to the main research question might have been (partly) known already. Amongst others, this report can thus be regarded as experimental verification of known literature. However, this report also demonstrated the viability of Mobi-Gust 2 in conducting applied aeolian research. Consequently, Mobi-Gust 2 can be employed to fill in knowledge gaps surrounding coastal aeolian processes. For example, Mobi-Gust 2 might be used to find the mentioned (non-linear) erodibility relations (§3.4.3). Ultimately, to improve predictive models, such as Aeolis (§1.3).



### 3.6 The recommendations from the applied aeolian research

The performed applied research with Mobi-Gust 2 resulted in a set of recommendations. These recommendations are subdivided into two sections. The first set of recommendations focusses on the aeolian research itself (§3.6.1). The second set of recommendations however concerns Mobi-Gust 2, in relation to the applied aeolian research (§3.6.2). To clarify, extra remarks arose on the performance of Mobi-Gust 2; which could only be made after conducting the applied aeolian research (part 3). The second set of recommendations can thus be regarded as a supplement to the Proof Of Concept (POC; part 2) of Mobi-Gust 2.

#### 3.6.1 Recommendations concerning the applied aeolian research

The main recommendation involves using Mobi-Gust 2 before improving it extensively. To clarify, the Proof Of Concept (POC; part 2) already showed that Mobi-Gust 2 is reasonably capable of conducting useful, reliable and controllable measurements. The applied research (part 3) verified that Mobi-Gust 2 is indeed capable of performing applied aeolian research. As a result, the main recommendations involves two steps. Firstly, it is advised to only perform minor improvements, regarding the performance of Mobi-Gust 2 (§2.6). It is stressed, that these minor improvements do not include a major overhaul related to improving the wind speed. Secondly, Mobi-Gust 2 should be employed in more applied aeolian research as soon as possible. Both the POC (part 2) and the applied research (part 3) demonstrated the viability of Mobi-Gust 2. Especially, when Mobi-Gust 2 gets deployed in more favourable (summer) conditions. Deploying Mobi-Gust 2 allows exploring other supply limiting factors; i.e., other than moisture content and an upwind supply of sand. After conducting more applied research, it might be considered to improve achievable wind speeds within Mobi-Gust 2; so that Mobi-Gust 2 might cope with more adverse (winter) conditions.

When using Mobi-Gust 2 in more applied aeolian research, it can be employed to quantify the aeolian erodibility of the sand surface. As explained, there are multiple ways to achieve this (§1.4). To clarify, velocity thresholds for the initiation of motion can be found. However, Mobi-Gust 2 can also be used in supply limited conditions; in order to directly measure spatiotemporal variations in sand bed erodibility. In short, the approach involves generating aeolian erosion by using controlled wind speeds (§1.4). Adding time intervals to the experiments, might reveal temporal variations in sand surface erodibility. Next, the spatial dependency is found by conducting experiments at different beach locations. For example, Mobi-Gust 2 can be used to explore spatial differences between the intertidal- and supratidal beach. Or experiments may for example focus on shell pavements, vegetated areas or sloping surfaces. There are of course other (supply limiting) factors that can be explored (§1.3). It is stressed that this report assumed a linear erosion process, by establishing mean erosion fluxes (§3.3.4). Yet, the erodibility of the sand surface is most likely (far) from linear.

Creating aeolian erosion by means of sand-laden winds can be further explored. To clarify, the saltation hopper of Mobi-Gust 2 is used to create an upwind supply of sand towards the erosion zone (§2.2.1.5). This sand supply enhances the erosion process (§3.3.3 & §3.4.3). Yet for example, if the amount of injected sand is doubled, does that cause a doubled erosion quantity as well?

Finally, a statistical foundation must be added to this report. In other words, if the weather allows Mobi-Gust 2 should be deployed in as many experiments as possible. After doing so, statistical quantities can be derived and compared. The original measurement plan of this report contained some statistical analysis; and is added in appendix G.4.1 for reference.

#### 3.6.2 recommendations concerning Mobi-Gust 2 (POC supplement)

Finally, some recommendations could be formulated concerning the performance of Mobi-Gust 2; i.e., related to the Proof of Concept (POC) of Mobi-Gust 2 (part 2).

The erosion zone walls must be improved in two departments. Firstly, a dry sand surface and/or an upwind supply of sand, causes undermining due to relatively strong erosion (i.e., Lab II; §3.4.1). This undermining leads to exchanges of sand and air with the outside world. The erosion zone walls were already elongated in the design stage (§2.2.1.5). Yet, this extension was not sufficient enough. Secondly, driving the (blocky) erosion zone walls into the sand bed causes issues.

### Part III

#### The erodibility of the sand surface: recommendations

The issue concerns sand displacements into the erosion zone (§3.4.1). As the erosion zone walls already need to be extended, they easily be chamfered outward. This chamfering will ensure that sand displacements are directed out of the erosion zone.

Next, scour holes should be accounted for. The mentioned undermining primarily occurred at the upwind end of the erosion zone (i.e., Lab II; §3.4.1); as a result from scour development. On top, one of the saltation tests in the field (i.e., Field III; §3.4.3) also showed some minor scour development. In view of this research the formation of scour was less of an issue. To clarify, conclusions could still be drawn from observing or not observing aeolian erosion. On top, erosion took place in the entire erosion zone (i.e., not just at the scour holes). However, if spatiotemporal variations in sand bed erodibility are measured one might want to account for these scour holes. To this end, hatches were added to the roof erosion zone (see §2.2.1.5 or §2.2.1.7). These hatches give access to the interior of Mobi-Gust 2. To this end, the dimensions of emerging scour holes can be measured. By means of idealised scour hole shapes, the eroded sand volume (or mass) can be corrected for the scour volume (or mass).

Surrounding winds in the field impact the wind conditions within Mobi-Gust 2 (§3.4.1). Consequently, measured wind speeds exhibit more variability in the field than in the laboratory (i.e., as the laboratory generally contains no surrounding wind). It might therefore be sensible to determine the properties of the wind gauging system in field conditions as well. This means redoing some assessments from the Proof Of Concept (POC; §2.4.2) using field data. However, the increased variability in the field can also be mitigated to some extent. The situation can namely be improved by actively minding the orientation of Mobi-Gust 2. The entrance of Mobi-Gust 2 should not be oriented directly into the surrounding wind; as pressure fluctuations from the surrounding wind will propagate into Mobi-Gust 2. The situation is for example mitigated by orienting the entrance of Mobi-Gust 2 parallel to the surrounding winds. When active repositioning is not enough, the removable intake shield walls can be used to further (partially) shield the entrance. While these walls cause a bended air supply, the Proof Of Concept (POC; §2.4.5) demonstrated that these walls have a negligible effect on the achievable wind speeds within Mobi-Gust 2. These walls may not only (partially) block winds but surrounding aeolian transport as well. However, it is questionable whether environmental conditions are appropriate enough to use Mobi-Gust 2 when ambient aeolian transport is occurring (appendix H). It is namely advised to only measure in moderate conditions and stop when these are exceeded. When conditions worsen ( $> 5 [bft]$ ) experiments might become impossible from a physical, practical and safety point of view. First of all, the influx of sand into Mobi-Gust 2, from surrounding aeolian transport, becomes close to unmitigable. Secondly, the eyesight might be reduced by painful sand grains, from the mentioned surrounding aeolian transport. Thirdly, wielding equipment becomes practically difficult and unsafe. This was all learned from experience (appendix H).

Measuring in wet conditions benefits from longer experiments. To clarify, when the sand surface is wet, Mobi-Gust 2 must be kept operational for as long as possible, in order to dry the surface. This practically means performing one test of 1 [h] instead of four of 15 [min] each.

The success rate of field experiments also depends on preparation and strategy. To this end, appendix G includes a preparation- and a measurement plan. These manuals are a supplement to the already mentioned (dis)mounting and configuration manuals (POC; §2.5.5).

Two aspects from the Proof Of Concept (POC; §2.4.2) are stressed once again. These aspects namely also affected the field measurements in the applied research (part 3). The first aspect concerns the saltation hopper. The use of natural sand hampered the discharging ability of this hopper (§3.4.1). As the POC (part 2) indicated, mitigation involves using filtered sand. Additionally, pre-weighted sand samples were prepared for the field expeditions (§3.4.1). In itself, that is a good preparational move. However, it is advised to also prepare a few smaller sand samples. These smaller samples can be used when the experiment almost ends. Consequently, to not overshoot in time, as the hopper needs to be fully drained. The second aspect concerns the power supply. These connections easily loosen, affecting the wind conditions within Mobi-Gust 2 (§3.4.1). These connections should be checked regularly and fastened if applicable. However, permanently fixing the issue might be most robust.

## References

- Aarninkhof, S., Dalfsen, J. v., & Rijks, D. (2010). Sustainable development of nourished shorelines: Innovations in project design and realisation. *Proceedings of: PIANC MMX Congress*. Liverpool, UK: PIANC.
- AHN. (2023). *Ahnviewer*. Retrieved 04 2023, 10, from Ahn.arcgisonline: <https://ahn.arcgisonline.nl/ahnviewer/>
- Airconco. (2024). *VA18-AP70-LL-86A-S.pdf*. Retrieved 05 21, 2024, from shop.airconcoparts.co: <https://shop.airconcoparts.co.uk/WebRoot/epagesUK/Shops/es117975/58A5/8E19/2209/56DD/B24A/0A0F/111B/5D13/VA18-AP70-LL-86A-S.pdf>
- All Metals Fabrication. (2022). *Does aluminium rust?* Retrieved 05 21, 2024, from Allmetalsfab: <https://www.allmetalsfab.com/does-aluminum-rust/>
- Amazon. (N.d.). *Wind Gauges*. Retrieved 06 01, 2024, from Amazon: [https://www.amazon.nl/dp/B087P2642C?smid=A1WB7OYT373PVV&ref\\_=chk\\_typ\\_imgToDp&th=1](https://www.amazon.nl/dp/B087P2642C?smid=A1WB7OYT373PVV&ref_=chk_typ_imgToDp&th=1)
- Anderson Jr., J. D. (2005). *Introduction to flight (8th edition)*. New York: McGraw-Hill Education.
- Arduino S.R.L. (N.d.). *analogRead()*. Retrieved 06 04, 2024, from Arduino: <https://www.arduino.cc/reference/en/language/functions/analog-io/analogread/>
- Arduino SRL. (2023). *Millis()*. Retrieved 05 26, 2024, from Arduino: <https://www.arduino.cc/reference/en/language/functions/time/millis/>
- Arduino SRL. (2024). *A000067-datasheet.pdf*. Retrieved 05 25, 2024, from Docs.Arduino: <https://docs.arduino.cc/resources/datasheets/A000067-datasheet.pdf>
- Arduino SRL. (N.d.). *Software*. Retrieved 05 26, 2024, from Arduino: <https://www.arduino.cc/en/software>
- Arens, S. M. (1996). Rates of aeolian transport on a beach in a temperate humid climate. *Geomorphology*, 17 (1-3), pp. 3-18.
- Avnet. (N.d.). *Piezoresistive pressure sensors*. Retrieved 05 25, 2024, from Avnet: <https://my.avnet.com/abacus/solutions/technologies/sensors/pressure-sensors/core-technologies/piezoresistive-strain-gauge/>
- AZ-Delivery. (N.d.). *Copy of spi reader micro speicherkartenmodul fur arduino*. Retrieved 06 03, 2024, from AZ-Delivery: <https://www.az-delivery.de/nl/products/copy-of-spi-reader-micro-speicherkartenmodul-fur-arduino>
- AZ-Delivery. (N.d.). *ds3231 real time clock*. Retrieved 06 03, 2024, from AZ-Delivery: <https://www.az-delivery.de/nl/products/ds3231-real-time-clock>
- AZ-Delivery. (N.d.). *Lcd display 16x2 mit blauem hintergrund und i2c converter bundle*. Retrieved 06 03, 2024, from AZ-Delivery: <https://www.az-delivery.de/nl/products/lcd-display-16x2-mit-blauem-hintergrund-und-i2c-converter-bundle>
- Bagnold, R. A. (1936). The movement of desert sand. *Proceedings of the Royal Society of London. Series A-Mathematical and Physical Sciences*, 157(892), pp. 594-620.
- Bagnold, R. A. (1937). The transport of sand by wind. *The Geographical Journal*, 89(5), pp. 409-438.

- Bagnold, R. A. (1941). *The Physics of Blown Sand and Desert Dunes*. London: Methuen Publications.
- Bangen, P., & Dijkstra, S. (2020). *MOAWIT - MOBILE Aeolian WIND Tunnel*. Delft: TU Delft.
- Barchyn, T. E., Martin, R. L., Kok, J. F., & Hugenholtz, C. H. (2014). Fundamental mismatches between measurements and models in aeolian sediment transport prediction: The role of small-scale variability. *Aeolian Research*, pp. 245-251.
- Barnston, A. G. (1992). Correspondence among the Correlation, RMSE, and Heidke Forecast Verification Measures; Refinement of the Heidke Score. *Weather and Forecasting*, pp. 699-709. [https://doi.org/10.1175/1520-0434\(1992\)007<0699:CATCRA>2.0.CO;2](https://doi.org/10.1175/1520-0434(1992)007<0699:CATCRA>2.0.CO;2)
- Bauer, B. O., & Davidson-Arnott, R. G. (2002). A general framework for modeling sediment supply to coastal dunes including wind angle, beach geometry, and fetch effects. *Geomorphology*, pp. 89-108.
- Bosboom, J., & Stive, M. J. (2023). *Coastal Dynamics*. Delft: TU Delft Open.
- BPS. (N.d.). *Bulk material density guide*. Retrieved 05 21, 2024, from bpsvibes: <https://www.bpsvibes.com/bulk-material-density-guide/>
- Çengel, Y. A., & Cimbala, J. M. (2014). *Fluid Mechanics, fundamentals and applications (third edition)*. New York: McGraw-Hill.
- Chapman Electric Supply, Inc. (2024, 04 24). *Electrical Calculation Formulas*. Retrieved from Chapmanelectric: <https://shop.chapmanelectric.com/resources/electrical-calculation-formulas>
- Chassagne, C., & Van den Bremer, T. (2021). *Fluid Mechanics (lecture notes)*. Delft: TU Delft.
- Chomppff, L. (2021, 01 18). *Proper Power Cable Usage Prevents Poor Performance*. Retrieved 04 24, 2024, from AnDcable: <https://andcable.com/cable-management/proper-power-cable-usage/#Cable-Length-Matters>
- Compendium voor de Leefomgeving. (2021, 06 21). *Oppervlaktewater in Nederland*. Retrieved 05 16, 2024, from CLO: <https://www.clo.nl/indicatoren/nl140101-oppervlaktewater-in-nederland>
- Davidson-Arnott, R. G., Yang, Y., Ollerhead, J., Hesp, P. A., & Walker, I. J. (2008). The effects of surface moisture on aeolian sediment transport threshold and mass flux on a beach. *Earth Surface Processes and Landforms*, 33, pp. 55-74.
- De Vries, S., Arens, S., De Schipper, M., & Ranasinghe, R. (2014). Aeolian sediment transport on a beach with a varying sediment supply. *Aeolian research*, pp. 235-244.
- De Vries, S., Hoonhout, B., Van Westen, B., Cohn, N., Van IJzendoorn, C., Hallin, C., . . . Meijer, L. (2024). *Aeolis 2.1.1*. Retrieved 04 14, 2024, from PyPi: <https://pypi.org/project/aeolis/>
- De Vries, S., Southgate, H. N., Kanning, W., & Ranasinghe, R. (2012). Dune behavior and aeolian transport on decadal timescales. *Coastal Engineering*, 67, pp. 41-53.
- De Vries, S., Van Thiel de Vries, J., Van Rijn, L., Arens, S., & Ranasinghe, R. (2014). Aeolian sediment transport in supply limited situations. *Aeolian Research*, pp. 75-85.



- De Vries, S., Van Westen, B., Van IJzendoorn, C., Hallin, C., Pak, T., & Hesp, P. (2022). Aeolian processes and the development of dunes due to natural and antropogenic drivers (lecture slides). Delft.
- De Wilde, H. (2020). *Wind Tunnel tests of wind-blown sediment transport*. Delft: TU Delft.
- De Zandmotor. (N.d.). *Over de Zandmotor*. Retrieved 05 05, 2023, from De Zandmotor: <https://dezandmotor.nl/over-de-zandmotor/>
- Dekking, F., Kraaikamp, C., Lopuhaä, H., & Meester, L. (2005). *A Modern Introduction To Probability and Statistics; Understanding Why and How*. Springer Science & Business Media.
- Delft University of Technology. (2013). Dictaat CTB2120. Delft.
- Deltares. (N.d.). *Sand Motor*. Retrieved 09 30, 2023, from Deltares: <https://www.deltares.nl/en/expertise/projects/sand-motor>
- DFRobot. (2024). *Fermion: LWLP5000 Differential Pressure Sensor -  $\pm 500\text{pa}$  (Breakout)*. Retrieved 04 09, 2024, from DFRobot: <https://www.dfrobot.com/product-2096.html>
- Dillingh, D. (2013). *Kenmerkende waarden Kustwateren en Grote Rivieren*. Deltares.
- Duursma. (N.d.). *Analoge schuifmaat aflezen*. Retrieved 06 04, 2024, from Duursma: <https://duursma.nl/blog/analoge-schuifmaat-aflezen>
- Eastsensor. (2022, 12 14). *Pressure Sensor Noise and EMI*. Retrieved 04 25, 2024, from Eastsensor: <https://www.eastsensor.com/blog/pressure-sensor-noise-and-emi/#:~:text=Electrical%20noise%2C%20including%20electromagnetic%20interference,signal%20loss%2C%20and%20induce%20crosstalk.>
- EcoShape. (2024). *Houtrib Dike Pilot Project*. Retrieved 05 14, 2024, from EcoShape: <https://www.ecoshape.org/en/cases/houtrib-dike-pilot-project-3/>
- EcoShape. (2024). *Sand Motor – Delfland*. Retrieved 05 14, 2024, from EcoShape: <https://www.ecoshape.org/en/cases/sand-nourishment-sand-engine-delfland-north-sea-nl/>
- EcoShape. (2024). *Sand nourishment – Hondsbossche Dunes*. Retrieved 05 14, 2024, from EcoShape: <https://www.ecoshape.org/en/cases/sand-nourishment-hondsbossche-dunes-nl/>
- EcoShape. (2024). *The building with nature philosophy*. Retrieved 04 13, 2024, from EcoShape: <https://www.ecoshape.org/en/the-building-with-nature-philosophy/>
- Elektor. (2022). *Take Accurate Voltage Measurements with Arduino*. Retrieved 05 25, 2024, from Elektormagazine: <https://www.elektormagazine.com/news/ad-converter-how-to-take-accurate-voltage-measurements-arduino>
- Elger, D. F., Williams, B. C., Crowe, C. T., & Roberson, J. A. (2012). *Engineering Fluid Mechanics, 10th edition*. United States: Wiley.
- Encyclopædia Britannica. (N.d.). *Libyan Desert*. Retrieved 05 14, 2024, from Encyclopædia Britannica: <https://www.britannica.com/place/Libyan-Desert>
- Engineers Edge. (2024). *moody\_chart*. Retrieved 06 04, 2024, from Engineers Edge: [https://www.engineersedge.com/fluid\\_flow/pressure\\_drop/moody\\_chart.htm](https://www.engineersedge.com/fluid_flow/pressure_drop/moody_chart.htm)

European Commission. (N.d.). *Green transition*. Retrieved 10 04, 2023, from Reform Support: [https://reform-support.ec.europa.eu/what-we-do/green-transition\\_en](https://reform-support.ec.europa.eu/what-we-do/green-transition_en)

Fitzgerald, S., & Shiloh, M. (2015). *Arduino Projects Book*. Arduino SA.

Fryberger, S. G. (1979). Dune forms and wind regime. In E. D. McKee, *A Study of Global Sand Seas* (pp. 137-170). Washington, D.C., Verenigde Staten: US Government Printing Office.

Geo Engineer. (N.d.). *Step-by-Step Guide for Grain Size Analysis*. Retrieved 06 02, 2024, from Geoengineer: <https://www.geoengineer.org/education/laboratory-testing/step-by-step-guide-for-grain-size-analysis>

Google. (2022). Google Earth Pro (7.3.6.9345) [software]. Mountain View, California, United States of America.

Google. (2023). *Maps*. Retrieved 05 09, 2023, from Google: [https://www.google.com/maps/dir/TU+Delft+Faculteit+Civiele+Techniek+en+Geowetenschappen,+Faculteit+Civiele+Techniek+en+Geowetenschappen+\(CITG\),+Stevinweg,+Delft/52.0430254,4.1847265/@52.017139,4.2052611,19759m/data=!3m2!1e3!4b1!4m9!4m8!1m5!1m1!1s0x47c5b58](https://www.google.com/maps/dir/TU+Delft+Faculteit+Civiele+Techniek+en+Geowetenschappen,+Faculteit+Civiele+Techniek+en+Geowetenschappen+(CITG),+Stevinweg,+Delft/52.0430254,4.1847265/@52.017139,4.2052611,19759m/data=!3m2!1e3!4b1!4m9!4m8!1m5!1m1!1s0x47c5b58)

Google. (2023). *Maps*. Retrieved 05 09, 2023, from Google: [https://www.google.com/maps/dir/TU+Delft+Faculteit+Civiele+Techniek+en+Geowetenschappen,+Faculteit+Civiele+Techniek+en+Geowetenschappen+\(CITG\),+Stevinweg,+Delft/52.0334429,4.1731494/@52.019022,4.2184893,15484m/data=!3m1!1e3!4m9!4m8!1m5!1m1!1s0x47c5b58dd7f](https://www.google.com/maps/dir/TU+Delft+Faculteit+Civiele+Techniek+en+Geowetenschappen,+Faculteit+Civiele+Techniek+en+Geowetenschappen+(CITG),+Stevinweg,+Delft/52.0334429,4.1731494/@52.019022,4.2184893,15484m/data=!3m1!1e3!4m9!4m8!1m5!1m1!1s0x47c5b58dd7f)

Google. (2023). *Maps*. Retrieved 05 09, 2023, from Google: [https://www.google.com/maps/dir/TU+Delft+Faculteit+Civiele+Techniek+en+Geowetenschappen,+Faculteit+Civiele+Techniek+en+Geowetenschappen+\(CITG\),+Stevinweg,+Delft/52.0623122,4.2145643/@52.0353946,4.2398672,15611m/data=!3m1!1e3!4m9!4m8!1m5!1m1!1s0x47c5b58dd7f](https://www.google.com/maps/dir/TU+Delft+Faculteit+Civiele+Techniek+en+Geowetenschappen,+Faculteit+Civiele+Techniek+en+Geowetenschappen+(CITG),+Stevinweg,+Delft/52.0623122,4.2145643/@52.0353946,4.2398672,15611m/data=!3m1!1e3!4m9!4m8!1m5!1m1!1s0x47c5b58dd7f)

Hallin, C., Van IJzendoorn, C., Homberger, J.-M., & De Vries, S. (2023). Simulating surface soil moisture on sandy beaches. *Coastal Engineering*, 185, 104376.

Himax. (2024, 02 24). *Understanding the Cycle Life and Charge/Discharge Performance of LiFePO4 Batteries*. Retrieved 04 25, 2024, from Himaxelectronics: <https://himaxelectronics.com/understanding-the-cycle-life-and-charge-discharge-performance-of-lifepo4-batteries/>

Himax Electronics. (2024). *Understanding the Cycle Life and Charge/Discharge Performance of LiFePO4 Batteries*. Retrieved 05 26, 2024, from Himax Electronics: <https://himaxelectronics.com/understanding-the-cycle-life-and-charge-discharge-performance-of-lifepo4-batteries/>

Hoonhout, B. (2017). *Aeolian Sediment Availability and Transport*. Delft University of Technology. <https://doi.org/https://doi.org/10.4233/uuid:e84894d6-87d2-4006-a8c2-d9fbfacabddc>

Hoonhout, B., & De Vries, S. (2017). Aeolian sediment supply at a mega nourishment. *Coastal Engineering*, pp. 11-20.

Hoonhout, B., & de Vries, S. (2017). Field measurements on spatial variations in aeolian sediment availability at the Sand Motor mega nourishment. *Aeolian Research*, 24, pp. 93-104.

Hoonhout, B., & de Vries, S. (2019). Simulating spatiotemporal aeolian sediment supply at a mega nourishment. *Coastal Engineering*, 145, pp. 21-35.

- Hrisko, J. (2019, February). *Arduino Pitot Tube Wind Speed and Airspeed Indicator - Theory and Experiments*. Retrieved 04 002, 2023, from Makersportal: <https://makersportal.com/blog/2019/02/06/arduino-pitot-tube-wind-speed-theory-and-experiment>
- Huisman, B., De Schipper, M., & Ruessink, B. (2016). Sediment sorting at the Sand Motor at storm and annual time scales. *Marine Geology*, pp. 209-226.
- Huisman, B., Sirks, E., Van der Valk, L., & Walstra, D. (2014). Time and spatial variability of sediment grading in the surfzone of a large scale nourishment. *Journal of Coastal Research*, 70(sp1), pp. 127-132.
- Huisman, B., Wijsman, J., Arens, S., Vertegaal, C., Van der Valk, L., Van Donk, S., . . . Taal, M. (2021). *Evaluatie van 10 jaar Zandmotor: Bevindingen uit het Monitoring- en Evaluatie Programma (MEP) voor de periode 2011 tot 2021*. Delft: Deltares.
- Isra. (2017, 04 13). *Getting a fixed sampling rate*. Retrieved 04 24, 2024, from Arduino.stackexchange: <https://arduino.stackexchange.com/questions/34125/getting-a-fixed-sampling-rate>
- Janssen, W. (2021, 01 20). *Wind in Nederland*. Retrieved from Weerplaza: [https://www.weerplaza.nl/weerinhethetnieuws/klimaat/wind-in-nederland/6820/#:~:text=In%20het%20winterseizoen%20ligt%20de,5%20Bft\)%20langs%20de%20kust.](https://www.weerplaza.nl/weerinhethetnieuws/klimaat/wind-in-nederland/6820/#:~:text=In%20het%20winterseizoen%20ligt%20de,5%20Bft)%20langs%20de%20kust.)
- Kadib, A. A. (1965). *A function for sand movement by wind, HEL 2-12*. Berkely: University of California.
- Kassaeian, T. (2023). *LiFePO4 Batteries: Installation & Maintenance Best Practices*. Retrieved 05 25, 2024, from Volts: <https://volts.ca/blogs/educational/lifepo4-battery-installation-maintenance-best-practices#:~:text=Avoid%20Overcharging%2FOver-Discharging%3A,prevent%20damage%20and%20maintain%20safety.>
- Kawamura, R. (1951). *Study on sand movement by wind, 5(3)*. Tokyo: University of Tokyo.
- KNMI. (2023). *2023: natste en warmste jaar sinds het begin van de metingen*. Retrieved 06 03, 2024, from KNMI: <https://www.knmi.nl/over-het-knmi/nieuws/weeroverzicht-2023#:~:text=Dit%20jaar%20was%20het%20natste,automatische%20KNMI-weerstations%20op%20land.>
- KNMI. (2023). *Zomer bijna net zo nat als winter*. Retrieved 05 30, 2024, from KNMI: <https://www.knmi.nl/over-het-knmi/nieuws/zomer-bijna-net-zo-nat-als-winter>
- KNMI. (2024). *Natste 12 maanden aaneen ooit gemeten*. Retrieved 06 03, 2024, from KNMI: <https://www.knmi.nl/over-het-knmi/nieuws/de-natte-lente-van-2024>
- KNMI. (N.d.). *Achtergrond Verdamping in Nederland*. Retrieved 05 30, 2024, from KNMI: <https://www.knmi.nl/kennis-en-datacentrum/achtergrond/verdamping-in-nederland>
- KNMI. (N.d.). *Daggegevens*. Retrieved 05 18, 2024, from KNMI: <https://www.knmi.nl/nederland-nu/klimatologie/daggegevens>
- KNMI. (N.d.). *Wind*. Retrieved 06 02, 2024, from KNMI: [https://www.knmi.nl/kennis-en-datacentrum/uitleg/wind#:~:text=Wind%20is%20er%20vrijwel%20altijd,74%20km%2Fuur\)%20ligt.](https://www.knmi.nl/kennis-en-datacentrum/uitleg/wind#:~:text=Wind%20is%20er%20vrijwel%20altijd,74%20km%2Fuur)%20ligt.)

- KNMI. (N.d.). *Windschaal van Beaufort*. Retrieved 06 02, 2024, from KNMI:  
<https://www.knmi.nl/kennis-en-datacentrum/uitleg/windschaal-van-beaufort>
- Kulkarni, V., Sahoo, N., & Chavan, S. D. (2011). Simulation of honeycomb–screen combinations for turbulence management in a subsonic wind tunnel. *Journal of wind engineering and industrial aerodynamics*, pp. 37-45.
- Lets Talk Science. (2020). *Types of Materials*. Retrieved 05 21, 2024, from Letstalkscience:  
<https://letstalkscience.ca/educational-resources/backgrounders/types-materials>
- Lokithor. (2022, 03 24). *What Are the Symptoms of a Battery Cable Coming Loose?* Retrieved 04 24, 2024, from Lokithorshop: <https://www.lokithorshop.com/blogs/car-news/what-are-the-symptoms-of-a-battery-cable-coming-loose>
- Lü, P., & Dong, Z. (2011). Horizontal momentum and kinetic energy loss of airflow near the surface of sandy beds. *Sedimentary Geology (234)*, pp. 116-119.  
<https://doi.org/10.1016/j.sedgeo.2010.12.007>
- Luijendijk, A. P., Ranasinghe, R., De Schipper, M. A., Huisman, B. A., Swinkels, C. M., Walstra, D. J., & Stive, M. J. (2017). The initial morphological response of the Sand Engine: A process-based modelling study. *Coastal Engineering*, pp. 1-14.
- Luijendijk, A., & Van Oudenhoven, A. (2019). *The Sand Motor: A Nature-Based Response to Climate; Findings and Reflections of the Interdisciplinary Research Program NatureCoast*. Delft University Publishers.
- Marsaalam tours. (N.d.). *Great Sand Sea*. Retrieved 05 14, 2024, from Marsaalamtours:  
<https://www.marsaalamtours.org/en/great-sand-sea>
- McKenna Neuman, C., Li, B., & Nash, D. (2012). Micro-topographic analysis of shell pavements formed by aeolian transport in a wind tunnel simulation. *Journal of Geophysical Research*, 117(F04003).
- Michigan Air Products. (2017). *Understanding fan system effects*. Retrieved 06 02, 2024, from michiganair: <https://www.michiganair.com/blog/understanding-fan-system-effects/>
- Modinex. (N.d.). *Does Saltwater Affect Timber?* Retrieved 02 21, 2024, from Modinex:  
<https://www.modinex.com.au/does-saltwater-affect-timber/>
- MPS. (N.d.). *General Properties and Characteristics of Sensors*. Retrieved 05 21, 2024, from Monolithicpower: <https://www.monolithicpower.com/en/sensors-course/intro-to-sensors/general-properties-characteristics#:~:text=The%20following%20variables%20may%20affect,humidity%2C%20or%20other%20environmental%20factors.>
- NASA. (2021). *Mach Number*. Retrieved 04 16, 2023, from Grc.Nasa.Gov:  
<https://www.grc.nasa.gov/www/k-12/airplane/mach.html>
- NASA. (2021, 05 13). *Mach Number: role in compressible flows*. Retrieved from grc.nasa.gov:  
<https://www.grc.nasa.gov/www/k-12/airplane/machrole.html>
- NASA. (2021). *Types of Wind Tunnels*. Retrieved 06 03, 2024, from NASA:  
<https://www.grc.nasa.gov/www/k-12/airplane/tuntype.html>
- NASA. (2023). *Pitot – Static Tube – Speedometer*. Retrieved 05 25, 2024, from NASA:  
<https://www1.grc.nasa.gov/beginners-guide-to-aeronautics/pitot-static-tube-speedometer/>



- NASA. (2023, 09 04). *Solar System Temperature*. Retrieved 04 14, 2024, from Science.nasa.gov: <https://science.nasa.gov/resource/solar-system-temperatures/>
- NASA. (2023, 08 07). *What are Newton's Laws of Motion?* Retrieved 04 26, 2024, from Nasa: <https://www1.grc.nasa.gov/beginners-guide-to-aeronautics/newtons-laws-of-motion/>
- Navionics. (N.d.). *#boating@6&key=gyd%7CHwnIT*. Retrieved 05 18, 2024, from Webapp Navionics: <https://webapp.navionics.com/#boating@6&key=gyd%7CHwnIT>
- NIOZ. (2024, 03 22). *Sound couch makes low dunes, marram grass builds height*. Retrieved 05 04, 2024, from Nioz: <https://www.nioz.nl/en/news/sound-couch-makes-low-dunes-marram-grass-builds-height>
- NIST. (2019). *Singal to noise ratio*. Retrieved 05 26, 2024, from NIST: <https://www.itl.nist.gov/div898/software/dataplot/refman2/auxillar/snr.htm>
- Noctua. (N.d.). *Axial fans in series or parallel operation*. Retrieved 05 21, 2024, from Noctua: <https://noctua.at/en/axial-fans-in-series-or-parallel-operation>
- NXP. (2021, 05 05). *MPXV7002*. Retrieved 04 25, 2024, from nxp: <https://www.nxp.com/docs/en/data-sheet/MPXV7002.pdf>
- Omega Engineering. (N.d.). *Anemometer*. Retrieved 06 03, 2024, from Omega: <https://www.omega.nl/prodinfo/anemometers.html>
- Panagos, P., Meusburger, K., Ballabio, C., Borrelli, P., & Alewell, C. (2014). Soil erodibility in Europe: A high-resolution dataset based on LUCAS. *Science of the Total Environment (479-480)*, pp. 189-200.
- PowerTech Systems. (n.d.). *Lithium-Ion State of Charge (SoC) measurement*. Retrieved 04 25, 2024, from PowerTechSystems: <https://www.powertechsystems.eu/home/tech-corner/lithium-ion-state-of-charge-soc-measurement/>
- Pye, K. (1980). Beach salcrete and eolian sand transport: Evidence from North Queensland. *Journal of Sedimentary Research 50(1)*, pp. 257-261.
- Relion. (N.d.). *How are LiFePO4 batteries safer than other lithium batteries?* Retrieved 05 25, 2024, from Relion battery: <https://www.relionbattery.com/knowledge/how-are-lifepo4-batteries-safer-than-other-lithium-batteries>
- Rice, M. A. (1991). Grain shape effects on aeolian sediment transport. *Aeolian Grain Transport 1* (pp. 159-166). Springer-Verlag.
- Rijkswaterstaat. (n.d.). *Kustonderhoud*. Retrieved 05 04, 2024, from Rijkswaterstaat: <https://www.rijkswaterstaat.nl/water/waterbeheer/bescherming-tegen-het-water/maatregelen-om-overstromingen-te-voorkomen/kustonderhoud>
- Rijkswaterstaat. (N.d.). *Publiek*. Retrieved 05 18, 2024, from Rijkswaterstaat: <https://waterinfo.rws.nl/#/nav/publiek>
- Rijkswaterstaat. (N.d.). *Rijkswaterstaat*. Retrieved 05 17, 2024, from Normaal Amsterdams Peil: <https://www.rijkswaterstaat.nl/zakelijk/open-data/normaal-amsterdams-peil>
- Rijkswaterstaat. (N.d.). *Zandmotor*. Retrieved from Rijkswaterstaat: <https://www.rijkswaterstaat.nl/water/waterbeheer/bescherming-tegen-het-water/maatregelen-om-overstromingen-te-voorkomen/zandmotor>

- Rotron. (N.d.). *Series and Parallel Operations*. Retrieved 05 21, 2024, from Rotrn: <https://www.rottron.com/tech-corn/series-and-parallel>
- RS. (2024). 7736838. Retrieved 04 17, 2024, from nl.rs-online: <https://nl.rs-online.com/web/p/motor-controllers/7736838>
- Scheiman, J., & Brooks, J. (1981). Comparison of experimental and theoretical turbulence reduction characteristics for screens, honeycomb, and honeycomb-screen combinations. *Journal of Aircraft*, 18(8), pp. 638-643.
- Schiereck, G. J. (2019). *Introduction to bed, bank and shore protection*. Delft: VSSD (Delft Academic Press).
- SensorOne. (N.d.). *What is the difference between zero offset and zero drift?* Retrieved 05 25, 2024, from SensorOne: <https://www.sensorsone.com/zero-offset-drift-difference/#:~:text=Zero%20Offset%20relates%20to%20the,change%20in%20zero%20over%20time.>
- SensorsONE. (N.d.). *Symptoms and Causes of Damage to Pressure Transducer Diaphragms*. Retrieved 04 25, 2024, from SensorsONE: <https://www.sensorsone.com/symptoms-and-causes-of-damage-to-pressure-transducer-diaphragms/>
- Shepard, J. (2021). *How to read battery discharge curves*. Retrieved 05 25, 2024, from Battery power tips: <https://www.batterypowertips.com/how-to-read-battery-discharge-curves-faq/>
- Sherman, D. J., & Li, B. (2012, Januari). Predicting aeolian sand transport rates: A reevaluation of models. *Aeolian Research*, 3(4), pp. 371-387.
- Sirjani, E., Sameni, A., Moosavi, A., Mahmoodabadi, M., & Laurent, B. (2019). Portable wind tunnel experiments to study soil erosion by wind and its link to soil properties in the Fars province, Iran. *Geoderma* (333), pp. 69-80.
- Slootjes, N., & Van der Most, H. (2016). *Achtergronden bij de normering van de primaire waterkeringen in Nederland*. Ministry of Infrastructure and the Environment, DG Space and Water, Directorate General.
- Smith, S. W. (1999). *The Scientist and Engineer's Guide to Digital Signal Processing*. California Technical Publishing.
- Sørensen, M. (2004). On the rate of aeolian sand transport. *Geomorphology*, 59(1-4), pp. 53-62.
- SPAL Automotive. (2024). *Axial fans*. Retrieved 05 22, 2024, from spalautomotive: <https://www.spalautomotive.it/axial-fans>
- Stevens, M. (N.d.). *Fan Performance*. Retrieved 06 02, 2024, from Wanderlodgegurus: <http://www.wanderlodgegurus.com/database/Theory/Fan%20Performance%20Static%20Pressure.pdf>
- Stive, M. J., De Schipper, M. A., Luijendijk, A. P., Aarninkhof, S. G., Van Gelder-Maas, C., Van Thiel De Vries, J. S., . . . Ranasinghe, R. (2013). A New Alternative to Saving Our Beaches from Sea-Level Rise: The Sand Engine. *Journal of Coastal Research*, 29(5), pp. 1001-1008.
- Todd, C. (2016, 12). *Datalogging, changing sampling frequency*. Retrieved 04 25, 2024, from Forum.arduino: <https://forum.arduino.cc/t/datalogging-changing-sampling-frequency/424703/3>

- TU Delft. (2020, September). *Stories of Science*. Retrieved 03 29, 2023, from TU Delft: <https://www.tudelft.nl/citg/onderzoek/stories-of-science/zandkorrels-tellen-om-duinen-te-doorgronden>
- U.S. Geological Survey. (N.d.). *chart.gif*. Retrieved 06 04, 2024, from pubs.usgs: <https://pubs.usgs.gov/of/2006/1195/html/docs/images/chart.gif>
- Uijttewaai, W. (2022). Turbulence in Hydraulics CIE5312 (lecture notes). Delft, Zuid-Holland, Nederland.
- Uphues, C. F., Van IJzendoorn, C. O., Hallin, C., Pearson, S. G., Van Prooijen, B. C., & Miot da Silva, G. (2022). Coastal aeolian sediment transport in an active bed surface: layer: Tracer study and conceptual model. *Earth Surface Processes and Landforms* 47(13), pp. 3147-3162.
- Van der Gaag, P. (2024). *Design drawings Mobi-Gust 2*. Delft University of Technology, Delft.
- Van Oord. (N.d.). *magazine.vanoord*. Retrieved 05 17, 2024, from The Sand Motor: Still running strong: <https://magazine.vanoord.com/about-marine-ingenuity-11/the-sand-motor-still-running-strong>
- Van Rijn, L. (2023). *Leovanrijn-sediment*. Retrieved 05 27, 2024, from Aeolian sand transport processes, Part 1: model formulation and calibration: <https://www.leovanrijn-sediment.com/papers/Aeoliansandtransport2018.pdf>
- Van Straaten, L. (1961). Directional effects of winds, waves and currents. *Geologie en Mijnbouw* (40), p. 363.
- Vatrer. (N.d.). *LiFePO4 Voltage Chart: A Comprehensive Guide*. Retrieved 05 25, 2024, from Vatrer power: <https://www.vatrerpower.com/en-de/blogs/news/lifepo4-voltage-chart-a-comprehensive-guide>
- Venus. (2024). *1609019*. Retrieved 04 17, 2024, from Venus: <https://www.venus.nl/spal/datasheet/1609019.htm>
- Victron Energy. (N.d.). *Lithium SuperPack 12,8V & 25,6V*. Retrieved 05 25, 2024, from Victron Energy: <https://www.victronenergy.com/batteries/12,8v-lithium-superpack#certificates>
- Victron Energy. (N.d.). *Wiring Unlimited*. Retrieved 06 10, 2024, from Victron Energy: [https://www.victronenergy.com/media/pg/The\\_Wiring\\_Unlimited\\_book/en/theory.html#:~:text=These%20are%20the%20length%20and,cable%20of%20the%20same%20thickness.](https://www.victronenergy.com/media/pg/The_Wiring_Unlimited_book/en/theory.html#:~:text=These%20are%20the%20length%20and,cable%20of%20the%20same%20thickness.)
- Voorendt, M. (2022). *Manual Hydraulic Structures*. Delft: Delft University of Technology.
- Warren, C. (2016, 03 12). *What You Need To Know About LiFePO4 Batteries*. Retrieved from Offgridham: <https://offgridham.com/2016/03/about-lifepo4-batteries/>
- Wasson, R. J., & Nanninga, P. M. (1986). Estimating wind transport of sand on vegetated surfaces. *Earth surface processes and landforms* 11(5), pp. 505-514.
- Weeronline. (2023). *Dit moet je weten over de donkerste periode van het jaar*. Retrieved 05 29, 2024, from Weeronline: <https://www.weeronline.nl/nieuws/dit-moet-je-weten-over-de-donkerste-periode-van-het-jaar>
- White, F. M. (2011). *Fluid Mechanics (7th edition)*. McGraw-Hill.

- Winterwerp, J. C., van Kessel, T., van Maren, D. S., & van Prooijen, B. C. (2022). *Fine Sediments in Open Water*. Singapore: World Scientific Publishing Co. Pte. Ltd.
- Xidibei. (2023, 04 12). *Causes Of Zero Point Drift In Pressure Sensors*. Retrieved 04 25, 2024, from Xidibei: <https://www.xidibei.com/en-nl/blogs/news/causes-of-zero-point-drift-in-pressure-sensors>
- Zhu, H.-Y., Pan, C., Wang, J.-J., Liang, Y.-R., & Ji, X.-C. (2019). Sand-turbulence interaction in a high-Reynolds-number turbulent boundary layer under net sedimentation conditions. *International Journal of Multiphase Flow* (119), pp. 56-71.  
<https://doi.org/https://doi.org/10.1016/j.ijmultiphaseflow.2019.07.001>



## A Sand Engine background

The field measurements are performed on the Sand Engine; or the Sand Motor. The Sand Engine concerns a mega nourishment near The Hague, along the Holland-Coast (The Netherlands). The location and the appearance of the Sand Engine are visible in [figure 112](#).

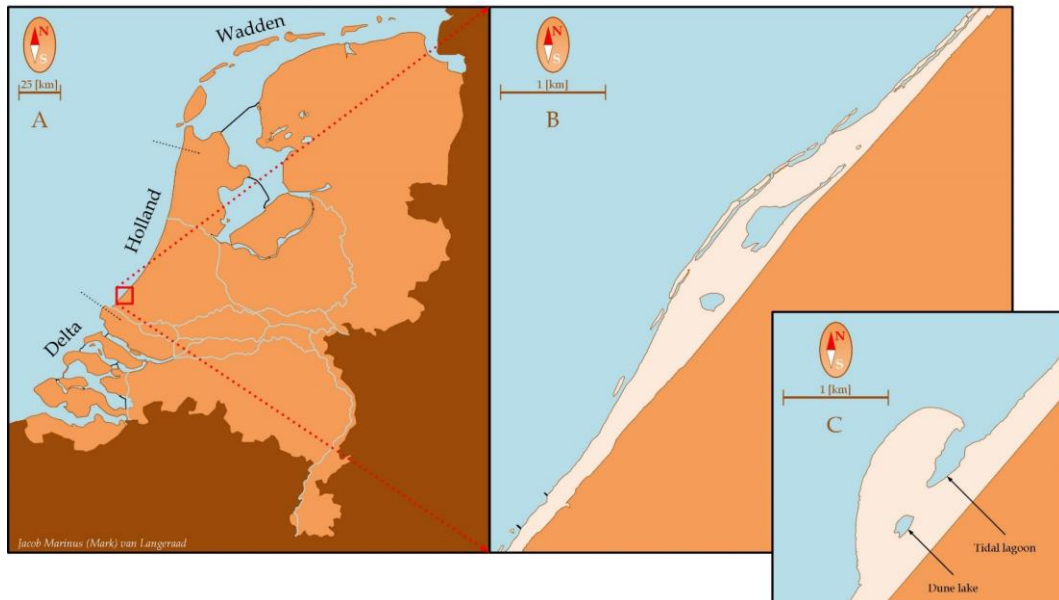


Figure 112 – Map showing The Netherlands (A), the Sand Engine in 2022 (B) and just after construction in 2011 (C)  
Adapted from (Compendium voor de Leefomgeving, 2021), (Google, 2022) and (Hoonhout & de Vries, 2017)

### A.1 Building with Nature

The Sand Engine concerns a Building with Nature pilot ([EcoShape, 2024](#)). This innovative mega nourishment mitigates structural erosion caused by sea level rise ([Stive et al., 2013](#)). Yet, the Sand Engine is not just a local measure; as it naturally feeds the adjacent coastline with sediments. The mega nourishment namely diffuses along the Holland Coast; through the combined action of (tidal) currents, winds and waves ([De Zandmotor, N.d.](#)). The Sand Engine pilot facilitates nature recovery; as it reduces the need for (more frequently required) traditional nourishing ([Huisman et al., 2021](#)). To clarify, the area of influence is expected to be free of maintenance, up to about 20 years after construction ([EcoShape, 2024](#)). The Sand Engine primarily mitigates flood risk, but other functions include recreational activities, drinking water resources and nature development ([Luijendijk & Van Oudenhoven, 2019](#)). [Figure 113](#) provides some functions at the smaller scale; which includes the available parking lots (i.e.,  $P_1$ ,  $P_2$  and  $P_3$ ).

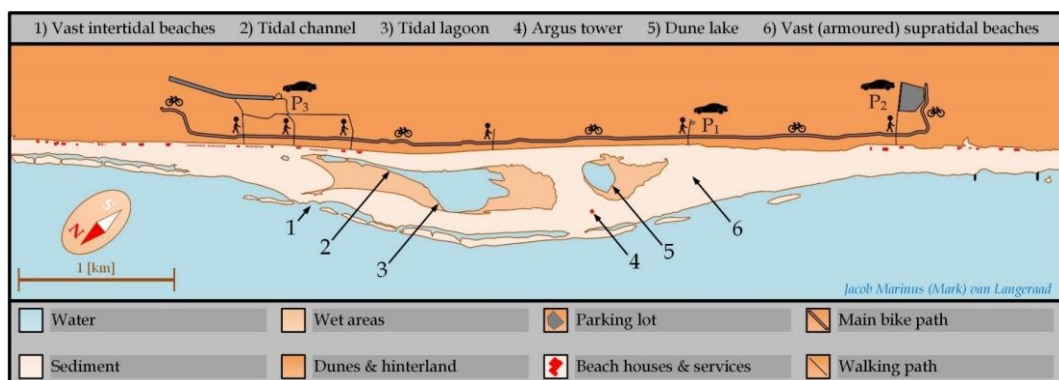


Figure 113 - Functional analysis of the Sand Engine  
(Google, 2022)

## A.2 Construction characteristics of the Sand Engine

The Sand Engine was constructed in 2011 along a formerly alongshore uniform coastline (Hoonhout & de Vries, 2019). The nourishment consisted of roughly 21.5 million [ $m^3$ ] sand (Rijkswaterstaat, N.d.); with a median grain diameter of about 280 [ $\mu m$ ] (Luijendijk et al., 2017). The sand was borrowed from the North Sea; and included shells, pebbles and other non-erodible materials (Hoonhout & de Vries, 2017). Next, the Sand Engine had a hooked-shaped appearance and initially occupied about 128 [ha] (Van Oord, N.d.). This area included a dune lake and a tidal lagoon (panel C in figure 112). In this state, the Sand Engine protruded about 1 [km] into the sea; and spanned about 2 [km] in alongshore direction (Deltares, N.d.). In vertical direction the Sand Engine reached on average about 5 [m] + MSL (Hoonhout & De Vries, 2017); which is well above common surge levels (§A.5). Consequently, the dry beach is significantly influenced by aeolian processes.

## A.3 Current characteristics of the Sand Engine

Morphodynamic activity changed the appearance of the Sand Engine over time. The Sand Engine now reaches about 0.4 [km] less far into the sea; and significantly widened (panel B in figure 112). The hook-shaped silhouette changed into a Gaussian shape. Next, the average elevation of the Sand Engine also reduced. Beach elevations still reach about 5 [m] + MSL locally; but substantial portions lowered to about 1-2 [m] + MSL (AHN, 2023). Consequently, these portions are now below common surge levels (§A.5). Two beach elevation profiles are shown in figure 114 for reference. Next, the tidal lagoon was almost closed off by the morphodynamic activity. Yet a tidal channel still connects the lagoon to the sea. Also the dune lake is still present. The volume of the Sand Engine has logically also decreased (Huisman et al., 2021). The mentioned properties show the diffusive character of the Sand Engine. In contrast to all declining trends, median grain sizes on the dry beach have been coarsening over time (Huisman et al., 2014); to about 300-350 [ $\mu m$ ]; but even larger median grain sizes are encountered in this report. On top, the dry beach remained relatively stable; and dune growth was less than expected (Hoonhout & de Vries, 2019).

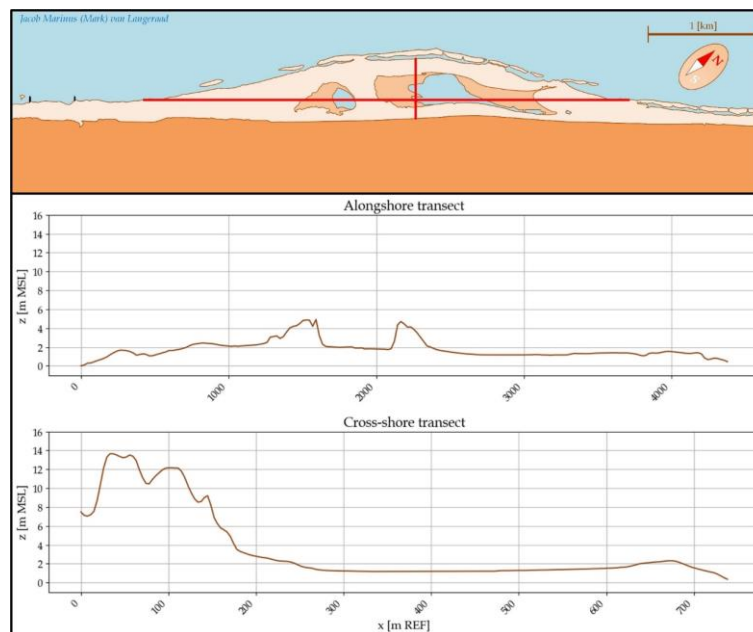


Figure 114 – Beach elevation profiles on the Sand Engine (AHN, 2023)

## A.4 The Sand Engine is a supply limited system

The relative stability of the dry beach, as well as the lower dune growth rates, are explained by supply limitations in aeolian sand transport. Measured transport rates on the Sand Engine are namely roughly 65 [%] below the transport capacity of the wind (Hoonhout & De Vries, 2017). The Sand Engine can thus be classified as a supply limited system.

The main report (§1.3) lists several reasons for supply limitations, yet the main mechanism that is limiting supply at the Sand Engine, will be explained here. To begin with, the supratidal zone is contributing less to in the supply of sand to the wind. This is caused by various beach armouring processes. To clarify, the construction sand was coarser than sandy material of the adjacent beaches and dunes (Huisman et al., 2016). On top, the construction sand contained a lot of shells, pebbles and other non-erodible materials (§A.2). Shell pavements may armour the already relatively coarse bed (McKenna Neuman et al., 2012). Additionally, the supratidal beach has been coarsening over time as well (§A.3). The coarsening occurs as the wind prefers to pick up the finer granular material first (Huisman et al., 2021). Overall, the beach armouring processes ensure that the dry beach contributes less and less in supplying sand to the wind (Hoonhout & de Vries, 2017). In contrast to the supratidal beach, the intertidal zone is continuously stirred and mixed by waves (Huisman et al., 2021). As a result, fine granular material remains available; provided the sand bed has sufficiently dried during low waters. However, morphological feedback and roughness processes ensure that the intertidal zone continuously contributes to supplying sand to the wind (Hoonhout & de Vries, 2017); even during high waters. Combining all effects largely explains the observed supply limitations; i.e., a reduced supply zone, that is dominated by the periodically flooded intertidal area. Additionally, much of the supplied sand might be trapped in the wet areas on the Sand Engine (Huisman et al., 2021); further limiting supply towards the coastal dunes.

Aeolian transport models cannot yet reproduce these supply limited transport rates fully (Sherman & Li, 2012). Yet, effort is made to improve predictions by for example using the Sand Engine as a learning case (Hoonhout, 2017). This knowledge is for example used to improve Aeolis; a process-based, numerical model; to simulate aeolian processes (De Vries et al., 2024). This model can account for sand availability, consequently it is able to limit sand supply.

## A.5 Environmental conditions around the Sand Engine

The dominant wind direction in the area of the Sand Engine is south to southwest (figure 115). On top, storms tend to attack from either the south- or northwest. Consequently, aeolian sand transport potentials show similarities to these orientations (Hoonhout & de Vries, 2017). The wind rose in figure 115 shows measured data at Hoek van Holland; which lies about 9 [km] away from the Sand Engine (Google, 2022). The data spans from the construction year of the Sand Engine (i.e., 2011) up to and including 2023.

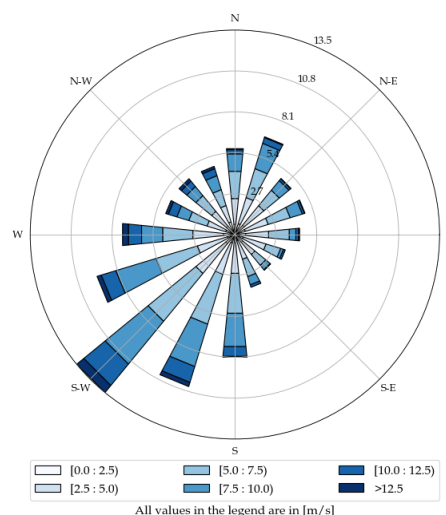


Figure 115 – Wind speed data measured at Hoek van Holland between 2011-2023;  
The used data can be downloaded online (KNMI, N.d.)

Storms might be accompanied by storm surges. Storm surges are generally most severe during north-westerly storms, because of the funnel-shaped North Sea (Bosboom & Stive, 2023). At Hoek van Holland, common storm surge levels (1-year return period) are about 2.5 [m] + NAP (table 18). Extreme storm surges (10,000-year return period) may reach about 5.1 [m] + NAP (table 18). The values in table 18 are relative to NAP (Dutch: Normaal Amsterdams Peil), which is roughly equal to the mean sea level on the North Sea (Rijkswaterstaat, N.d.). NAP only differs about 0.1 [m] from MSL (Bosboom & Stive, 2023). To get an idea of the actual water levels figure 116 shows measured data at Hoek van Holland. The graph roughly confirms the occurrence of normal surge levels. This measured water level is primarily the sum of the mean water level, the astronomical tide and the storm surges. To clarify, the tidal levels added in figure 116 are taken from figure 117.

Table 18 – Water levels at Hoek van Holland per return period determined from data between 1900-2010;  
Values rounded to increments of 0.1 [m]  
(Dillingh, 2013)

Return period [y]	1	10	100	1,000	10,000
Water level [m + NAP]	2.5	3.0	3.6	4.3	5.1

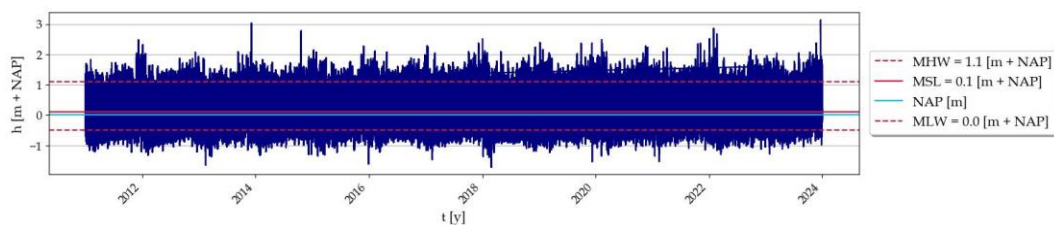


Figure 116 - Water level data measured at Hoek van Holland between 2011-2023;  
The data is online available (Rijkswaterstaat, N.d.)

As introduced, the water level also periodically varies due to the astronomical tide. Tides in the Netherlands are semi-diurnal (Bosboom & Stive, 2023); i.e., showing two high- and two low waters per day. At Hoek van Holland, Mean High Waters (MHW) occupies roughly 1.1 [m] of the mentioned storm surge levels (figure 117). Yet, average MHW during spring- and neap tidal cycles may roughly occupy 1.3 [m] and 0.9 [m] of these storm surge levels (Dillingh, 2013). Mind that figure 117 only shows data from 2023.

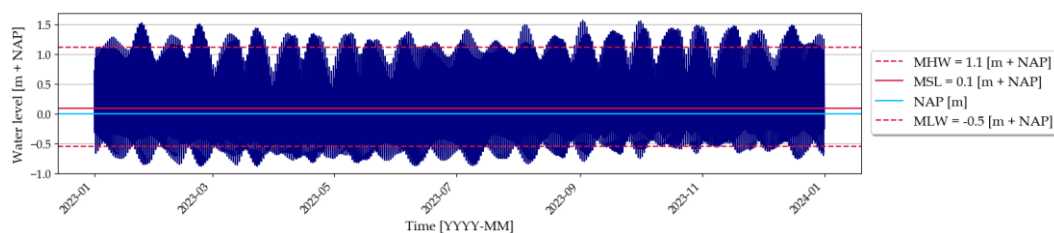


Figure 117 – Astronomical water levels measured at Hoek van Holland (2023);  
MHW and MLW are respectively calculated as the average of all high- and low waters in the timeseries;  
Values are rounded to increments of 0.1 [m];  
The data is online available (Rijkswaterstaat, N.d.)

Waves are generally largest in winter; as The Netherlands is characterised by a storm climate (Bosboom & Stive, 2023). Offshore waves tend to attack from the south- or northwest (figure 118 & figure 119). The lowest waves ( $H_s \leq 0.6$  [m]) tend to attack from the northwest (figure 118). Average waves ( $0.6$  [m]  $< H_s < 1.5$  [m]) tend to attack from the south- or northwest (figure 118). The largest waves ( $H_s \geq 1.5$  [m]) tend to attack from the south- and northwest; while the latter direction dominates (figure 118). The wave heights are classified according to their wave energy (Bosboom & Stive, 2023). The wave roses in figure 118 and figure 119 are measured at the Euro Platform. This platform is located beyond the 20 [m] depth contour (Navionics, N.d.); which is generally considered deep water relative to the waves on the North Sea (Bosboom & Stive, 2023). The Euro Platform lies approximately 55 [km] away from the Sand Engine (Google, 2022).



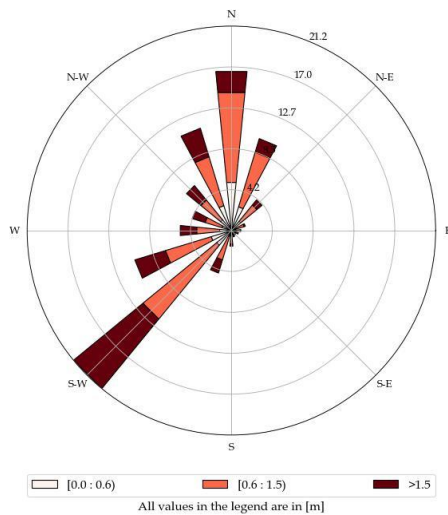


Figure 118 – Wave height and -direction data;  
Measured at Euro platform between 2011-2023;  
The data is online available (Rijkswaterstaat, N.d.)

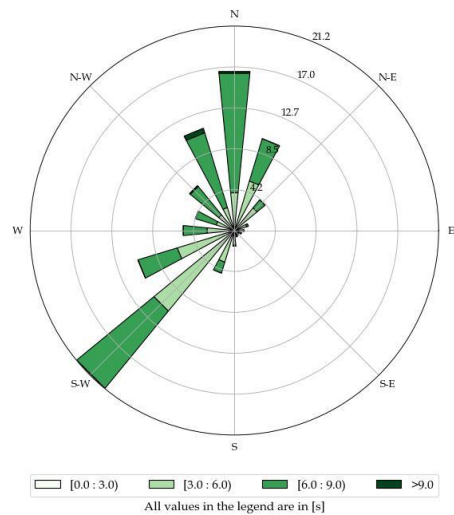


Figure 119 – Wave period and -direction data;  
measured at Euro platform between 2011-2023;  
The data is online available (Rijkswaterstaat, N.d.)

The wave properties shown in figure 118 & figure 119 are also provided as timeseries in figure 120 for further reference.

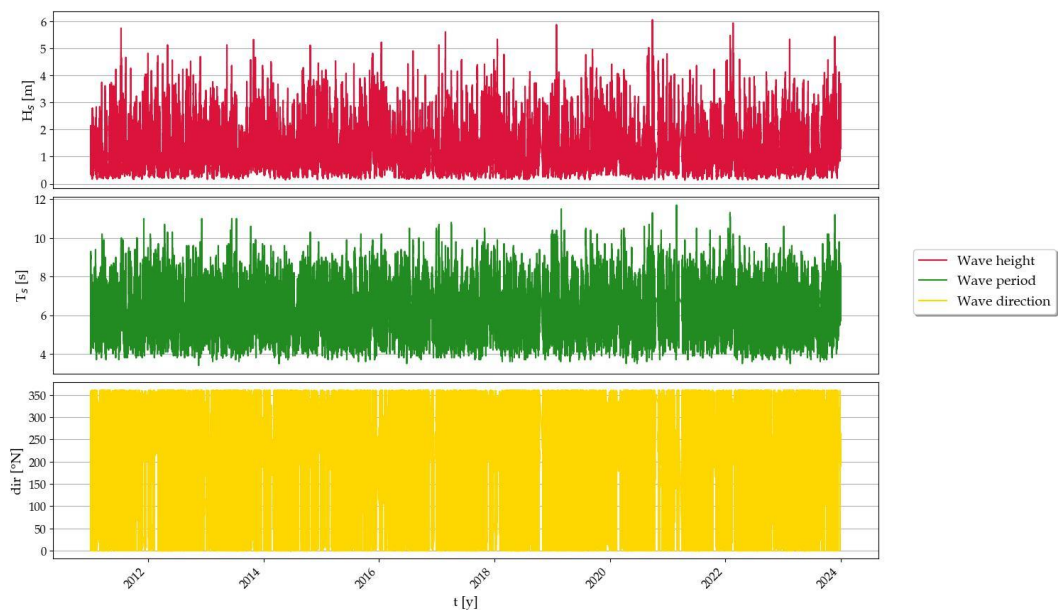


Figure 120 – The data of figure 118 & figure 119 as timeseries

Weather conditions around the Sand Engine are provided in figure 121 (next page). Again, the data is measured at Hoek van Holland and spans the year 2023.

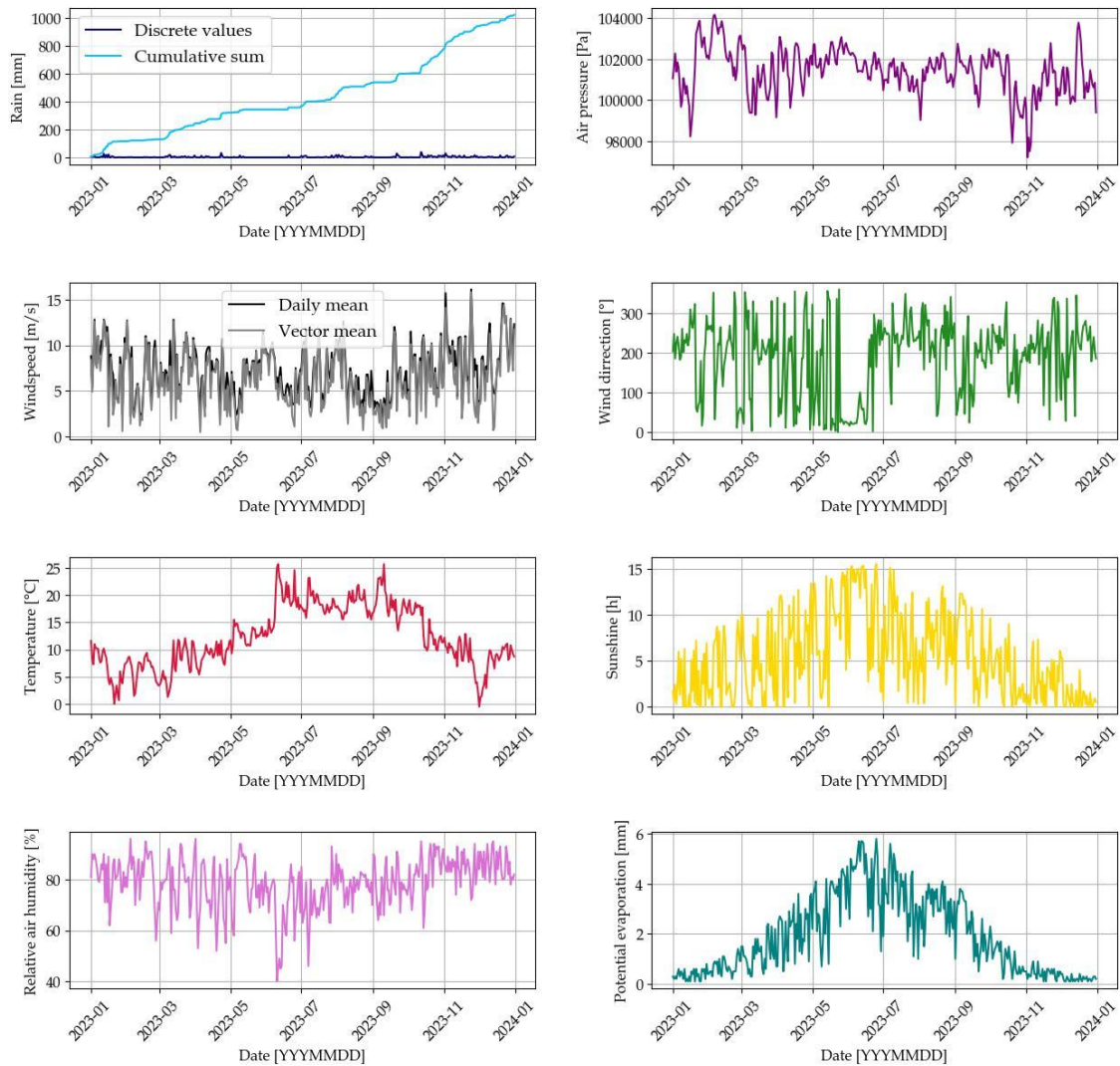


Figure 121 - Weather parameters measured at Hoek van Holland (2023)

## B Relevant air (flow) characteristics

### B.1 Air properties for STP-conditions

This report assumes Standard Temperature and Pressure (STP) conditions. Depending on the background (e.g., engineering or chemistry) STP-conditions differ a bit. Yet, the values have in common that they are representative for the surface of the Earth. Most books involving fluid- or aerodynamics use a standard temperature of 15 [°C] (White, 2011), (Çengel & Cimbala, 2014) & (Anderson Jr., 2005). The same books report a standard pressure of 1 [atm] = 101,325 [Pa]; a second valid assumption can be 1 [bar] = 100,000 [Pa]. The mentioned values concerns the air pressure at sea level; and mean surface temperature of the Earth (NASA, 2023).

$$T_{a,STP} = 15 \text{ [°C]} \text{ \& } p_{a,STP} = 101,325 \text{ [Pa]}$$

Following the STP-assumption generic air properties can be listed (White, 2011), (Çengel & Cimbala, 2014) & (Anderson Jr., 2005); see. table 19. These values are used throughout the report.

Table 19 – Air properties applicable to STP-conditions

Property	Symbol	Value	Unit
Temperature	$T_a$	15.0	[°C]
Pressure	$p_a$	101,325.0	[N/m]
Speed of sound	$u_a$	340.3	[m/s]
Density	$\rho_a$	1.225	[kg/m <sup>3</sup> ]
Dynamic viscosity	$\eta_a$	$1.789 \cdot 10^{-5}$	[kg/m/s]

### B.2 Air compressibility

In contrast to water, air is compressible. The air density changes when temperatures, pressures or humidity changes (Anderson Jr., 2005). This complicates matters. For example Bernoulli's principle is only valid along streamlines, in steady conditions, without friction; and most importantly for an incompressible fluid (Chassagne & Van den Bremer, 2021).

However, air can still be assumed incompressible in some cases, i.e., when the air density variations are relatively little. The Mach number can be used to assess the compressibility of air (NASA, 2021). The Mach number ( $M$  [–]) is a dimensionless number, which compares the speed ( $u$  [m/s]) of an object (or flow); to the speed of sound ( $c_s$  [m/s]) through a medium. In this case the speed of air is compared to the speed of sound through air. The Mach number is shown in equation 57 (Çengel & Cimbala, 2014). When the threshold of Mach 0.3 [–] is exceeded, air must be considered compressible; as air density variations are larger than 5 [%] (Elger et al., 2012).

57)

$$M = \frac{u}{c_s}$$

The Mach number sheds light on how information is travelling through a medium (e.g., air). In this case the information concerns sound (or pressure) waves. The most obvious example why the Mach number can be used to assess the compressibility of air, is a jet plane in a sonic boom. While travelling, an airplane namely sends out pressure (or sound) waves in all directions (Anderson Jr., 2005). When the plane increases its speed the pressure (or sound) waves in front of the plane are compressed. When the airplane exceeds the speed of sound of the medium (i.e., air), it catches up on its own pressure (or sound) waves. This results in a shock wave of compressed air, traveling at the speed of sound. This shock wave, or sonic boom, occurs at Mach one (NASA, 2021).

The speed of sound ( $c_s$  [m/s]) of table 19 is used. Mobi-Gust 1 is designed to reach wind speeds ( $u$  [m/s]) of 15 [m/s]. This results in a Mach ( $M$  [–]) number as calculated on the next page. This outcome is (far) lower than the limit of Mach 0.3 [–]. It is thus safe to assume that the air is incompressible, for the conditions within this report (STP-conditions).

Table 20 – Calculation box

$M = \frac{u}{u_a}$
$M = \frac{15}{340.3} = 0.044 \dots \approx 0.04 [-]$

The compressibility limit can also be assessed in another way. For example, one may calculate from which wind speed onward the air becomes compressible in STP-conditions. To this end [equation 57](#) is set equal to Mach 0.3 [-]. The associated outcome is (far) above the design wind speed of Mobi-Gust 2 (i.e., 15 [m/s]).

Table 21 – Calculation box

$M = \frac{u}{u_a} = 0.3 [-]$
$u = 0.3 \cdot 340.3 = 102.09 \left[ \frac{m}{s} \right]$

As the air is incompressible the air flow within Mobi-Gust 2 can be regarded as a hydraulic flow. In turn, equations like Continuity and Bernoulli can be used without modifications.

## B.3 Mass and energy conservation

### B.3.1 Continuity

The cross-sectionally averaged flow velocity reads as follows ([Voorendt, 2022](#)).

$$58) \quad \underbrace{Q}_{\text{Discharge}} = \underbrace{u}_{\text{Flow velocity}} \cdot \underbrace{A}_{\text{Cross-sectional area}}$$

The continuity equation (i.e., conservation of mass) reads as follows ([Voorendt, 2022](#)).

$$59) \quad Q_1 = Q_2$$

Location 1 can be upwind and location 2 can be downwind.

### B.3.2 Bernoulli

The Bernoulli equation (i.e., conservation of energy) in terms of head appears like the following ([Chassagne & Van den Bremer, 2021](#)).

$$60) \quad \underbrace{H}_{\text{Energy head}} = \overbrace{\underbrace{z}_{\text{Elevation head}} + \underbrace{\frac{p}{\rho g}}_{\text{Pressure head}}}^{\text{Piezometric head}} + \underbrace{\frac{u^2}{2g}}_{\text{Velocity head}} = \text{constant}$$

$$61) \quad \underbrace{H}_{\text{Energy head}} = \underbrace{h}_{\text{Piezometric head}} + \underbrace{\frac{u^2}{2g}}_{\text{Velocity head}} = \text{constant}$$

Assumptions ([Chassagne & Van den Bremer, 2021](#)):

- Valid along a streamline (i.e., valid for a contraction or a pitot tube; i.e.,  $z_1 = z_2$ ).
- Flow is incompressible (i.e., valid for this report; i.e., STP-conditions and low wind speeds).
- Steady flow (i.e., valid for a particular fan setting).
- Without friction (i.e., valid for a contraction or pitot tube; i.e., a short pipe,  $\frac{L}{D} < 20$ ).



The Bernoulli equation can also be written in terms of pressures (i.e., handy for designing a mobile wind tunnel system); by multiplying the Bernoulli equation (in terms of head), by the density of the fluid ( $\rho$  [ $kg/m^3$ ]) and the gravitational acceleration ( $g$  [ $m/s^2$ ]).

$$62) \quad P = z\rho g + p + \frac{\rho u^2}{2} = \text{constant}$$

### B.3.3 Applying mass- and energy conservation

The pitot tube formula can be derived from Bernoulli's equation as follows.

$$63) \quad \text{Bernoulli} \quad H_1 = H_2$$

$$64) \quad z_1 + \frac{p_1}{\rho g} + \frac{u_1^2}{2g} = z_2 + \frac{p_2}{\rho g} + \frac{u_2^2}{2g}$$

The pitot tube lies along a streamline ( $z_1 = z_2$ )

$$65) \quad \frac{p_1}{\rho g} + \frac{u_1^2}{2g} = \frac{p_2}{\rho g} + \frac{u_2^2}{2g}$$

The stagnation port measures velocity, while the static port does not ( $u_2 = 0$ )

$$66) \quad \frac{p_1}{\rho g} + \frac{u_1^2}{2g} = \frac{p_2}{\rho g}$$

Rearranging provides the pitot tube formula

$$67) \quad u_2 = \sqrt{\frac{2(p_1 - p_2)}{\rho_a}}$$

$$68) \quad u = \sqrt{\frac{2\Delta p}{\rho_a}}$$

The tables below shows the venturi effect; i.e., mass- and energy conservation over a contraction.

Table 22 - Demonstrating the Venturi effect (Çengel & Cimbala, 2014)

Derivation: Continuity (Mass conservation)	
Manipulation	Equation
1 = upwind of the contraction 2 = downwind of the contraction	$Q_1 = Q_2$
$Q = uA$	$u_1 A_1 = u_2 A_2$
Assessment	
Comparing $u_1$ to $u_2$	Comparing $u_2$ to $u_1$
$A_2 < A_1$ & $u_1 = \frac{A_2}{A_1} u_2$	$A_2 < A_1$ & $u_2 = \frac{A_1}{A_2} u_1$
$\frac{A_2}{A_1} < 1$ & $u_1 = \frac{A_2}{A_1} u_2$	$1 < \frac{A_1}{A_2}$ & $u_2 = \frac{A_1}{A_2} u_1$
$\frac{A_2}{A_1} < 1$ & $u_1 < u_2$	$\frac{A_1}{A_2} > 1$ & $u_2 > u_1$
Derivation: Contraction relation (Bernoulli's equation)	
Manipulation	Equation
1 = upwind of the contraction 2 = downwind of the contraction	$\left(\rho g z + p + \frac{\rho u^2}{2}\right)_1 = \left(\rho g z + p + \frac{\rho u^2}{2}\right)_2$
$z_{up} = z_{down}$	$\rho g z_1 + p_1 + \frac{\rho u_1^2}{2} = \rho g z_2 + p_2 + \frac{\rho u_2^2}{2}$
Rearranging	$p_1 + \frac{\rho u_1^2}{2} = p_2 + \frac{\rho u_2^2}{2}$
Rearranging	$\frac{\rho u_1^2}{2} - \frac{\rho u_2^2}{2} = p_2 - p_1$
Rearranging	$\frac{\rho}{2} (u_1^2 - u_2^2) = p_2 - p_1$
Rearranging	$p_2 - p_1 = \frac{\rho}{2} (u_1^2 - u_2^2)$
Assessment	
Comparing $p_1$ to $p_2$	Comparing $p_2$ to $p_1$
$u_2 > u_1$ & $p_1 = p_2 - \frac{\rho}{2} (u_1^2 - u_2^2)$	$u_2 > u_1$ & $p_2 = \frac{\rho}{2} (u_1^2 - u_2^2) + p_1$
$u_2 - u_1 > 0$ & $p_1 = p_2 - \frac{\rho}{2} (u_1^2 - u_2^2)$	$u_2 - u_1 > 0$ & $p_2 = \frac{\rho}{2} (u_1^2 - u_2^2) + p_1$
$0 > u_1 - u_2$ & $p_1 = p_2 - \frac{\rho}{2} (u_1^2 - u_2^2)$	$0 > u_1 - u_2$ & $p_2 = \frac{\rho}{2} (u_1^2 - u_2^2) + p_1$
$u_1 - u_2 < 0$ & $p_1 = p_2 - \frac{\rho}{2} (u_1^2 - u_2^2)$	$u_1 - u_2 < 0$ & $p_2 = \frac{\rho}{2} (u_1^2 - u_2^2) + p_1$
$u_1 - u_2 < 0$ & $p_1 > p_2$	$u_1 - u_2 < 0$ & $p_2 < p_1$

Table 23 - Demonstrating the Venturi effect (short)

Bernoulli	$p_2 - p_1 = \frac{\rho}{2} (u_1^2 - u_2^2)$
Continuity	$u_1 A_1 = u_2 A_2$
$A_2 < A_1$	$u_2 > u_1$
$u_2 > u_1$	$p_2 < p_1$







The outcomes are implying around the fan immediately some energy will be lost. This is because the fan is not enclosed by a circular cross-section; i.e., the flow immediately expands. The choice was however made to retain a squared cross-section, to facilitate the construction process. The squared cross-section was however made as small as possible; to minimize these energy losses.

## C.1.2 The speed controller

### EM-285 DC-MOTOR SPEED REGULATOR 12 / 24V 20A



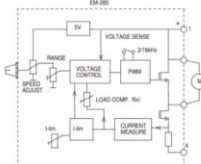
#### FEATURES

- Speed cont. to 1-direction
- Panel mountable
- Small size
- Motor size 30-200W
- Good speed regulation
- Load comp. adjustable Rxl
- Adjustable current limit
- Overheating protection
- EMC tested.

EM-285 is a PWM-based DC-motor driver. The materials and features meet the industrial standards. Motor voltage is regulated against supply voltage changes, and there is also a load compensation adjustment (Rxl), which enables steady speed during motor loading. Because of these features EM-285 can offer a good DC-motor speed regulation. In the power line of EM-285 there is an overvoltage limit, which trips the power stage in case the voltage would try to rise too high. This is possible in deceleration situation (emf voltage generation in braking). If potentiometer is turned on zero-position, the driver will make a shorting on motor wires for 5s. This creates a powerful braking (dynamic brake) which can be used to stop or lower the motor speed fast. The current limit and potentiometer range can be adjusted with on-board trimmer potentiometer. The device is EMC measured and meets industrial requirements in typical installation. EM-285 is easy to mount to a D10mm hole in the assembly panel. The power stage is not short circuit protected, so it is recommended to use an external fuse in application supply wiring.

#### TECHNICAL DATA

Supply voltage 10-35Vdc  
Overvoltage shut down 38V  
Undervoltage shut down 10V  
Start up voltage 11V  
Idle current typ. 20mA  
Motor current cont. max 20A (Ta<50°C)  
Motor current peak max 30A (10s.)  
Power losses 5W (at 20A and 16kHz)  
Power losses 4W (at 20A and 2kHz)  
Current limit adj. 1-30A  
PWM frequency 2kHz or 16kHz  
Temperature limit 90°C  
Motor and supply connectors 2.5mm  
EMC EN 50061-2 & EN 50082-2  
Weight 85g  
Operating temp (Ta) -20...60°C



### EM-285 WIRING and INSTALLATION

Recommended supply voltage 12-32Vdc filtered DC  
Ripple should be less than 20% at max. power.  
At high power use the supply wires should be as short as possible. The use of external fuse is recommended.  
ATT: Wrong supply polarity can damage device.  
ATT: Driver has no inbuilt fuse.

Select operation frequency. At 2kHz there are lower power losses and lower EMC emission level, but some cases there can occur audible noise.

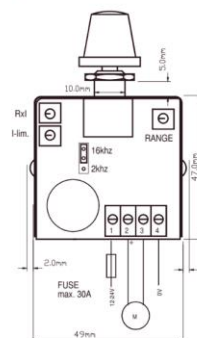
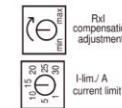
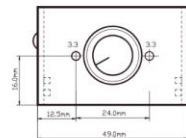
Range trim is used to scale the usable speed adjust range. See diagram below.

Current limit (I-lim) limits the motor current, in other words the motor torque. This adjustment should be used to set the limit to suitable level according to the application.

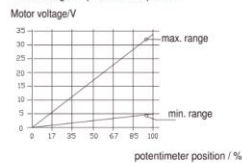
This device can be installed using one 10mm diameter hole. If the environment has high vibration level, the fastening can be secured with two external 3mm screws.

The body of this device can warm up, specially when continuous current is higher than 15A. Take this account when installing device in to plastic enclosure. In high power application the metal box is recommended. Metal box also offers a better EMC properties and cooling. The body temperature rise from ambient at 20A current is 45°C at pwm-freq. of 16kHz and 35°C at pwm-freq of 2kHz.

Load compensation (Rxl) should be set to minimum in beginning. Next set the a motor rpm 20-30%, and slowly increase compensation and simultaneously try loading the motor. If motor rpm is not affected by loading the compensation adjustment is in optimum. But if motor starts to twitch or running turns nervous the adjustment is overcompensating.



#### Motor voltage vs. potentiometer position



Range is adjustable with inbuilt range trim  
0% = potentiometer full counter clockwise  
100% = potentiometer full clockwise

Figure 125 – Page 1 of the speed controller datasheet (RS, 2024)

Figure 126 – Page 2 of the speed controller datasheet (RS, 2024)

## C.1.3 The horizontal- and vertical contraction

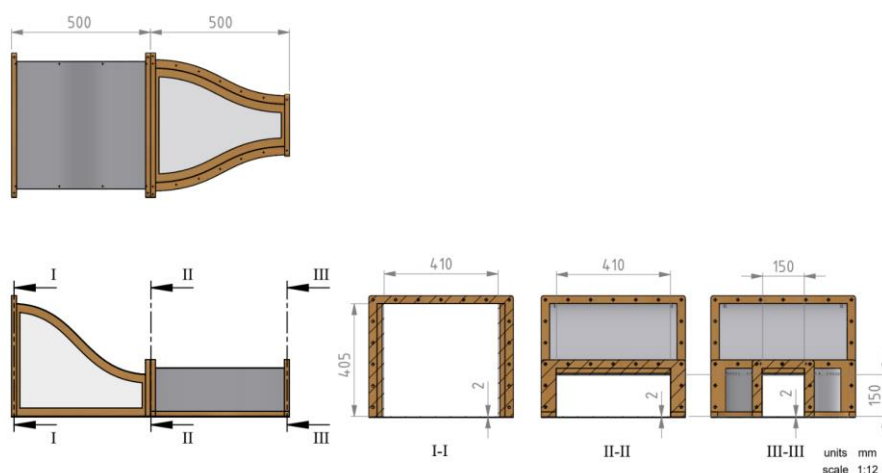


Figure 127 – The vertical- and horizontal contraction;  
Upper = top view, left = side view and right = cross-sections;  
(Van der Gaag, 2024)

### C.1.3.1 Short contractions

To minimize energy losses the contraction must be short. In elaboration, a duct is long when its length-to-diameter ( $L/D$ ) ratio is larger than 500 [–]; and a duct is short when this ratio is below 20 [–] (Delft University of Technology, 2013). Deceleration losses are negligible in long ducts, as friction losses dominate (i.e., the other way around for short pipes). The hydraulic diameter of a rectangular cross-section can be calculated according equation 73 (Çengel & Cimbala, 2014). For a squared cross-section equation 73 simplifies to the cross-sectional dimension ( $D_h = h = b$  [m]).

$$73) \quad D_h = \frac{4bh}{2(b+h)}$$

There are three cross-sections to assess. The cross-section is rectangular at the upwind end of the entire contraction ( $b_{up} = 0.410$  [m];  $h_{up} = 0.405$  [m]). The cross-section is rectangular between the vertical- and horizontal contraction ( $b_{middle} = 0.410$  [m];  $h_{middle} = 0.150$  [m]). The cross-section is however squared at the downwind end of the entire contraction ( $b_{down} = 0.150$  [m];  $h_{down} = 0.150$  [m]). See figure 127 for the selected dimensions.

Table 26 – Calculation box

$D_h = \frac{4bh}{2(b+h)}$
$D_{h,up} = \frac{4b_{up}h_{up}}{2(b_{up}+h_{up})} = \frac{4 \cdot 0.405 \cdot 0.410}{2(0.405 + 0.410)} = 0.407 \dots \approx 0.41$ [m]
$D_{h,middle} = \frac{4b_{middle}h_{middle}}{2(b_{middle}+h_{middle})} = \frac{4 \cdot 0.150 \cdot 0.410}{2(0.150 + 0.410)} = 0.219 \dots \approx 0.22$ [m]
$D_{h,down} = \frac{4b_{down}h_{down}}{2(b_{down}+h_{down})} = \frac{4 \cdot 0.150 \cdot 0.150}{2(0.150 + 0.150)} = 0.15$ [m]

The mean hydraulic diameter is calculated for the entire contraction as this provides the highest length-to-diameter ratio.

Table 27 – Calculation box

$D_{h,tot,mean} = \frac{D_{h,up} + D_{h,middle} + D_{h,down}}{3}$
$D_{h,tot,mean} = \frac{0.407 \dots + 0.219 \dots + 0.150}{3} = 0.259 \dots \approx 0.26$ [m]

The vertical- and horizontal contraction have a total length of 1 [m].

Table 28 – Calculation box

ratio = $\frac{L}{D}$
ratio <sub>tot</sub> = $\frac{L}{D} = \frac{1}{0.259 \dots} = 3.860 \dots \approx 3.86$ [–]

The contraction can thus be seen as a short duct, as the calculated length-to-diameter ratio is smaller than 20 [–]. This means that friction losses can be neglected.

### C.1.3.2 Gradually curved contractions

Next to the length of the contraction also its slope is important. Sudden- and gradual contractions exist (Çengel & Cimbala, 2014). Energy losses in gradual contractions are often neglected. Still, a (very) minor loss can be present, related to the slope of the contraction. This is summarized in figure 128. As figure 122 shows, the vertical- and horizontal contractions have maximum slopes of 45 [°] and 27 [°]. The associated losses are thus at maximum about 2-4 [%] (figure 128).

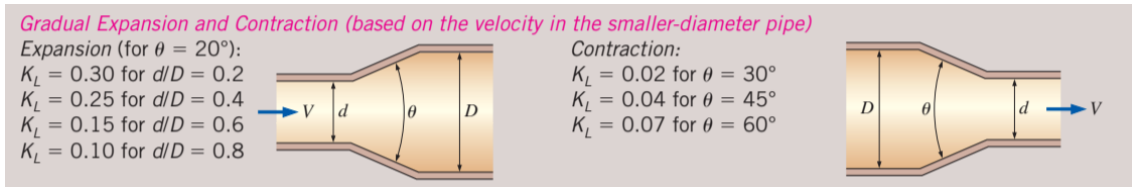


Figure 128 – Loss coefficient for gradual expansions and contractions (Çengel & Cimbala, 2014)

To minimize energy losses the contraction is also curved to guide the flow. To clarify, the slope of the entrances are nearly zero; while the curvature of the exits are nearly zero as well. These design choices resulted from conversations with the staff of the [low-speed laboratory of Delft University of Technology](#). To clarify, zero slopes at entrances mitigate flow blockage; and zero curvatures at exits mitigate flow separation. These important sources for energy losses are thus mitigated.

### C.1.3.3 Wind speeds

Likewise to the prototype (i.e., Mobi-Gust 1), Mobi-Gust 2 is desired to reach  $15 \text{ [m/s]}$ . The required cross-sectional area is based on the continuity equation and a loss coefficient ([equation 74](#) and [75](#)). Continuity is evaluated between the up- (1) and downwind (2) end of the contractions. Continuity states that the air speed ( $u_a \text{ [m/s]}$ ) depends on the discharge ( $Q_a \text{ [m}^3/\text{s]}$ ) and the flow area ( $A_a \text{ [m}^2]$ ). The loss coefficient ( $C_L$ ) depends on the achieved air speed ( $u_{a,a}$ ) and the designed air speed ( $u_{a,d}$ ). Energy losses make sure the loss-coefficient is smaller than 1 [–].

$$74) \quad u_{a,2} = C_L \frac{Q_{a,1}}{A_{a,2}}$$

$$75) \quad C_L = \frac{u_{a,a}}{u_{a,d}} < 1$$

The loss coefficient is based on operational data of the prototype (i.e., Mobi-Gust 1). The prototype was designed to achieve  $15 \text{ [m/s]}$ ; but only got to  $10.58 \text{ [m/s]}$  without honeycomb and  $6.56 \text{ [m/s]}$  with honeycomb ([De Wilde, 2020](#)).  $6.56 \text{ [m/s]}$  is used as Mobi-Gust 2 also contains a honeycomb.

Table 29 – Calculation box

$C_L = \frac{u_{a,a}}{u_{a,d}}$
$C_L = \frac{u_{a,a}}{u_{a,d}} = \frac{6.56}{15} = 0.437 \dots \approx 0.44 \text{ [–]}$

Next, [equation 74](#) and [75](#) are used to define the required cross-sectional area; in order to reach a wind speed ( $u_{a,2} \text{ [m/s]}$ ) of  $15 \text{ [m/s]}$  downwind of the contraction. The air flow ( $Q_{a,1} \text{ [m}^3/\text{s]}$ ) upwind of the contraction is still equal to  $3,450 \text{ [m}^3/\text{h]}$ .

Table 30 – Calculation box

$u_{a,2} = C_L \frac{Q_{a,1}}{A_{a,2}}$
$A_{a,2} = C_L \frac{Q_{a,1}}{u_{a,2}} = 0.44 \frac{3,450 \cdot \left(\frac{1}{3,600}\right)}{15} = 0.027 \dots \approx 0.03 \text{ [m}^2]$

The cross-sectional shape of the ducts will be squared. Amongst others, this shape facilitates mounting equipment on it. By square-rooting the calculated cross-sectional area ( $A_{a,2} \text{ [m}^2]$ ) the width ( $b_{a,2} \text{ [m]}$ ) and the height ( $h_{a,2} \text{ [m]}$ ) of the cross-section are revealed; i.e., [equation 76](#).

$$76) \quad b_{a,2} = h_{a,2} = \sqrt{A_{a,2}}$$

Table 31 – Calculation box

$b_{a,2} = h_{a,2} = \sqrt{A_{a,2}}$
$\sqrt{A_{a,2}} = \sqrt{0.027 \dots} = 0.167 \dots \approx 0.17 \text{ [m]}$

The cross-sectional dimension is rounded to 0.15 [m] because of two reasons. First of all, to facilitate the construction process. Second of all, previous research with the prototype (i.e., Mobi-Gust 1) recommended raising the design wind speed by a factor of 3 [-] (De Wilde, 2020). This recommendation amounts to a similar value as calculated above. This is shown by re-using equation 69 (C.1.1) and equation 76. As recommended, a factor 3 [-] is added to equation 69.

Table 32 – Calculation box

$3u_{a,2} = \frac{Q_{a,1}}{A_{a,2}}$	$b_{a,2} = h_{a,2} = \sqrt{A_{a,2}}$
$\sqrt{A_{a,2}} = \sqrt{\frac{Q_{a,1}}{3u_{a,2}}} = \sqrt{\frac{3,450 \cdot \left(\frac{1}{3,600}\right)}{3 \cdot 15}} = 0.145 \dots \approx 0.15 \text{ [m]}$	

The width ( $b_{a,2}$  [m]) and the height ( $h_{a,2}$  [m]) downwind of the contraction are thus chosen to be 0.15 [m]. To see the effect of energy losses, these dimensions are used to calculate the wind speed; based on continuity only. Again, equation 69 (C.1.1) is re-used, just as equation 72 (C.1.1).

Table 33 – Calculation box

$u_{a,2} = \frac{Q_{a,1}}{A_{a,2}}$	$A_{a,2} = b_{a,2}h_{a,2}$
$u_{a,2} = \frac{Q_{a,1}}{b_{a,2}h_{a,2}} = \frac{3,450 \cdot \left(\frac{1}{3,600}\right)}{0.15 \cdot 0.15} = 42.592 \dots \approx 42.59 \left[\frac{\text{m}}{\text{s}}\right]$	

Comparing this values (i.e., 42.59 [m/s]) to the design wind speed (i.e., 15 [m/s]) reveals that about 27.59 [m/s] will be lost due to the resistance within the aerodynamic system.

### C.1.4 The honeycomb

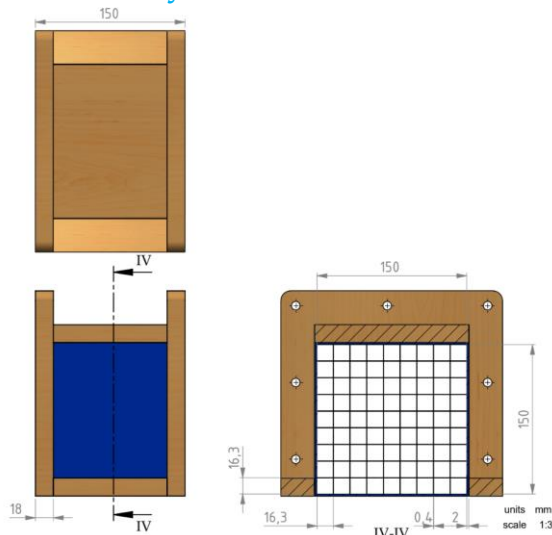


Figure 129 - The honeycomb screen;  
Upper = top view, left = side view and right = cross-section;  
(Van der Gaag, 2024)

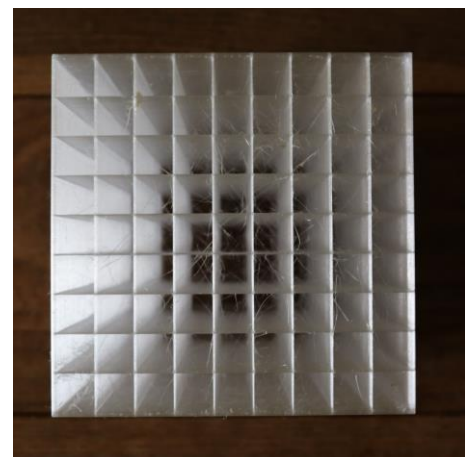


Figure 130 - Failed 3D-print of a honeycomb

The main considerations to design the honeycomb are twofold. The first consideration concerned an optimal range of length-to-diameter ratio (equation 77). When this optimal ratio is obeyed, the honeycomb is effective, irrespective of the opening-shape (Kulkarni et al., 2011). A value close to the mean ratio was chosen.

$$77) \quad \frac{L}{D} = 8 \text{ to } 10$$

The second consideration concerns the abilities of the 3D-printer. To clarify, the large-scale spiral motion (i.e., produced by the fan) must be reduced; and the (smaller scaled) turbulence is not so much the target. The openings are thus chosen to be as large as practically possible. Consequently, the honeycomb contains fewer separating walls; which minimizes flow blockage (i.e., resistance). The 3D-printer has a maximum printing length of 300 [mm]; which defines the size of the holes.

Table 34 – Calculation box

$\frac{L}{D} = 8 \text{ to } 10$
$D = \frac{300}{9} = 33\frac{1}{3} \text{ [mm]}$

Yet, selecting this value leads to multi-day printing durations. A faulty test-print (figure 130), sparked the decision to shorten the length of the honeycomb to 150 [mm]. This implies that the honeycomb is 150 [mm] long in all dimensions (i.e., it is a cube).

As can be seen in figure 129 the final length-to-diameter ratio is not exactly equal to the mean ratio (equation 77). This discrepancy results from finding the correct geometry. To clarify, one must find a squared opening-size (i.e., 16.3 [mm]), which obeys the mentioned range of optimal ratios. On top, the available cross-section is limited (i.e., 150 · 150 [mm<sup>2</sup>]); and the openings are enclosed by boundaries of a certain thickness (i.e., 2 [mm]).

Table 35 – Calculation box

$\frac{L}{D} = \text{ratio}$
$\text{ratio} = \frac{150}{16.3} = 9.202 \dots \approx 9.2 [-]$

The ratio is thus a bit higher than the mean length-to-diameter ratio. That is accepted, as too short holes might result in the spiral flow escaping the honeycomb without being reduced (figure 131).

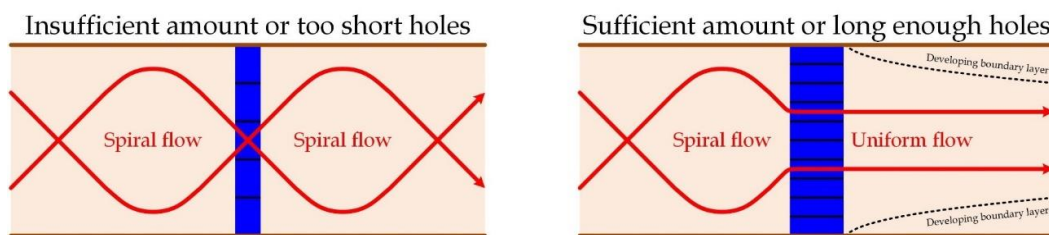


Figure 131 - An inefficient honeycomb (left) vs. an efficient honeycomb (right)



## C.1.5 The transition zone

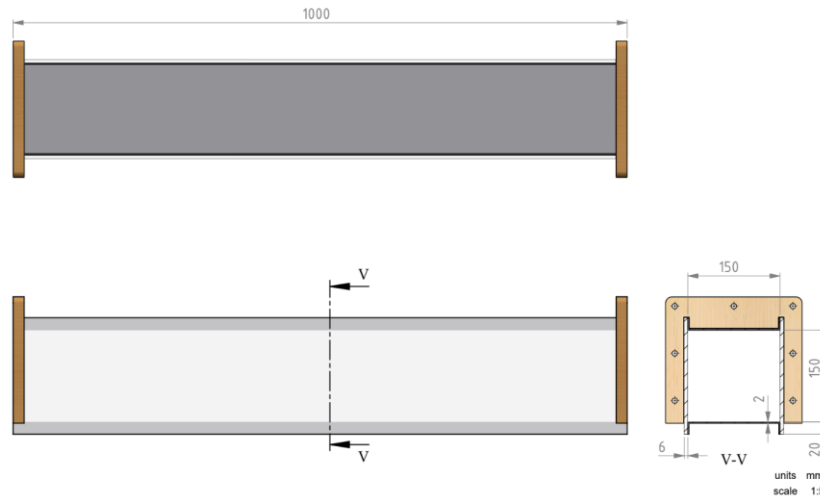


Figure 132 - The transition zone;  
Upper = top view, left = side view and right = cross-section;  
(Van der Gaag, 2024)

The transition zone develops the (turbulent) air flow. Virtually all natural flows are turbulent; except for porous flow in soils, or the flow in blood veins (Uijttewaai, 2022). The flow within Mobi-Gust 2 will also be turbulent (i.e., easily verifiable through the Reynolds number). The table below includes several empirical estimates; in order to calculate required length for flow development. The used hydraulic diameter ( $D_h$  [m]) is 0.15 [m]; which was calculated in appendix C.1.3.

Table 36 – Empirical estimates for the required development lengths

Development length	Purpose	Source	Outcome
$10D_h$	First major stresses	(Çengel & Cimbala, 2014)	1.50 [m]
$20D_h$	Lower bound development	(Uijttewaai, 2022)	3.00 [m]
$25D_h$	Upper bound development	(Uijttewaai, 2022)	3.75 [m]
$75D_h$	Homogeneous conditions	(Uijttewaai, 2022)	11.25 [m]

These empirical estimates are based on the development of the (turbulent) boundary layer. Another empirical equation is shown below (Schierreck, 2019). Inversely, this empirical relation estimates the thickness of the boundary layer ( $\delta(x)$  [m]), based on the development length ( $x$  [m]).

$$78) \quad \delta(x) \approx 0.02x \text{ to } 0.03x$$

The equation above was eventually used to dimension the transition zone. Boundary layers develop from all boundaries (i.e., no-slip). Next, they grow into the ducts because of momentum exchange. The flow is nearly developed when the boundary layers meet along the centreline of the duct. That means that the thickness of the boundary layer ( $\delta(x)$  [m]) must span half the hydraulic diameter (i.e.,  $\frac{1}{2}D_h$  [m]).

Table 37 – Calculation box

$\delta(x) \approx 0.02x \text{ to } 0.03x$	$\delta(x) = \frac{1}{2}D_h$
$x_{required} \approx \frac{D_h}{0.04} \text{ to } \frac{D_h}{0.06}$	
$x_{required} \approx \frac{0.15}{0.06} \text{ to } \frac{0.15}{0.04} = 2.5 \text{ to } 3.75 \text{ [m]}$	

## C.1.6 The erosion zone

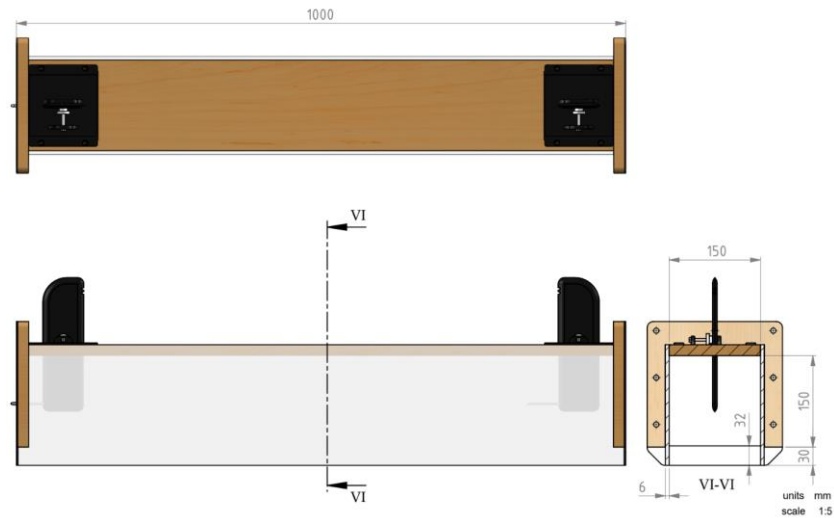


Figure 133 – The erosion zone;  
Upper = top view, left = side view and right = cross-section;  
(Van der Gaag, 2024)

The erosion zone is shown above; the involved calculations are already treated in [appendix C.1.3](#).

## C.1.7 The sand trap

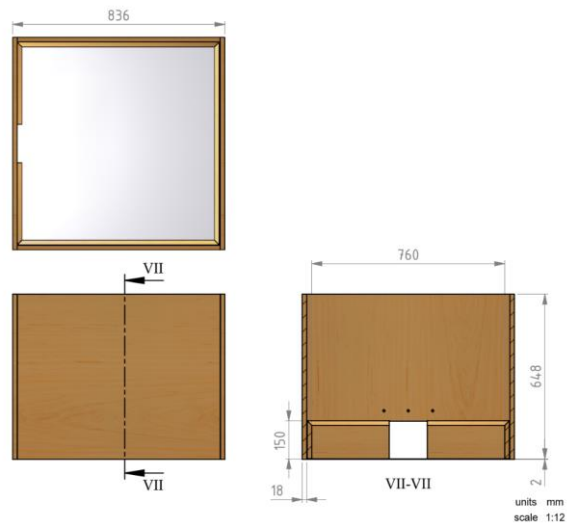


Figure 134 The sand trap;  
Upper = top view, left = side view and right = cross-section;  
(Van der Gaag, 2024)

The design of the sand trap is based on the fall velocity of sand ([Bosboom & Stive, 2023](#)). These fall velocities are considered within the Stokes ( $Re_s [-] < 0.1$  to  $0.5$ ) and within the Newton range ( $400 < Re_s [-] < 2 \cdot 10^5$ ).

79)

$$w_{s,Stokes} = \frac{1}{18} \frac{g}{\eta_a} (\rho_s - \rho_a) D^2$$

80)

$$w_{s,Newton} = \sqrt{\frac{8g}{3} \frac{(\rho_s - \rho_a)}{\rho_a} D}$$

The air properties of [appendix B](#) are used (i.e.,  $\rho_a = 1.225 \text{ [kg/m}^3\text{]}$ ;  $\eta_a = 1.7894 \cdot 10^{-5} \text{ [kg/m/s]}$ ). On top, normal values are used for the sand density (i.e.,  $\rho_s = 2,650 \text{ [kg}^1\text{m}^{-3}\text{]}$ ) ([Bosboom & Stive, 2023](#)); and the gravitational acceleration (i.e.,  $g = 9.81 \text{ [m}^1\text{s}^{-2}\text{]}$ ). The fan discharge results from [appendix C.1.1](#) (i.e.,  $Q = 3,450 \text{ [m}^3\text{s}^{-1}\text{]}$ ). The Wentworth classification was used to define the sand sizes to assess ([U.S. Geological Survey, N.d.](#)); and the construction sand has a median diameter of roughly  $280 \text{ [}\mu\text{m}]$  ([Luijendijk et al., 2017](#)). That means that the next grain sizes are assessed.

- $D_{50,coarse} = 500 \text{ [}\mu\text{m]} (= 0.500 \text{ [mm]});$
- $D_{50,construction} = 280 \text{ [}\mu\text{m]} (= 0.280 \text{ [mm]});$
- $D_{50,medium} = 250 \text{ [}\mu\text{m]} (= 0.250 \text{ [mm]});$
- $D_{50,fine} = 125 \text{ [}\mu\text{m]} (= 0.125 \text{ [mm]});$
- $D_{50,very\ fine} = 63 \text{ [}\mu\text{m]} (= 0.063 \text{ [mm]}).$

Lastly, the cross-sectional shape of the sand trap will be squared; as shown below.

$$\begin{aligned} 81) \quad & A = \frac{Q}{u} \\ 82) \quad & b = h = \sqrt{A} \end{aligned}$$

Finally, the grain Reynolds number is assessed ([Bosboom & Stive, 2023](#)); as shown below.

$$83) \quad Re_s = \frac{\rho U L}{\nu} = \frac{\rho_a w_s D_{50}}{\eta_a}$$

The next two tables emerge by using all relations and parameters described. The first table concerns the Stokes range and the second one the Newton range (i.e., rounded to two decimals).

*Table 38 – Outcomes in the Stokes regime*

Grain size ( $D_{50}$ ) [ $\mu\text{m}$ ]	500	280	250	125	63
Fall velocity (Stokes) ( $w_{s,Stokes}$ ) [ $\text{m/s}$ ]	20.17	6.32	5.04	1.26	0.32
Cross-sectional dimension ( $b = h = \sqrt{A}$ ) [ $\text{m}$ ]	0.22	0.39	0.44	0.87	1.73
Grain Reynolds number ( $Re_s$ ) [–]	690.36	121.24	86.29	10.79	1.38

*Table 39 – Outcomes in the Newton regime*

Grain size ( $D_{50}$ ) [ $\mu\text{m}$ ]	500	280	250	125	63
Fall velocity (Newton) ( $w_{s,Newton}$ ) [ $\text{m/s}$ ]	5.32	3.98	3.76	2.66	1.89
Cross-sectional dimension ( $b = h = \sqrt{A}$ ) [ $\text{m}$ ]	0.42	0.49	0.50	0.60	0.71
Grain Reynolds number ( $Re_s$ ) [–]	182.04	76.28	64.36	22.75	8.14

In all cases the grain Reynolds number is above 0.5 [–] (exceeding the upper limit of the Stokes range); but not reaching 400 [–] (i.e., the lower bound of the Newton range); so it must be somewhere in between. Overall, the dimensions are chosen to be as follows.

$$84) \quad b = h = 0.8 \text{ [m]}$$

The chosen dimension is larger than most calculated sand sizes; except for ‘fine-’ and ‘very fine’ sand (i.e., in the Stokes regime). On top, the chosen dimension is still constructable and transportable. This choice means that possibly some fine sand and/or very fine sand might be lost; if they really settle in the Stokes regime. Since the Stokes regime is only approached for very fine sand, the situation is accepted. If test experiments show that too much sand is escaping, then the sand trap will be upgraded with a cloth/mesh/filter; which is associated with extra energy losses.

## C.2 Wind gauging system

### C.2.1 Wiring scheme of the hardware

The figure below summarizes the wiring scheme of the wind gauging system.

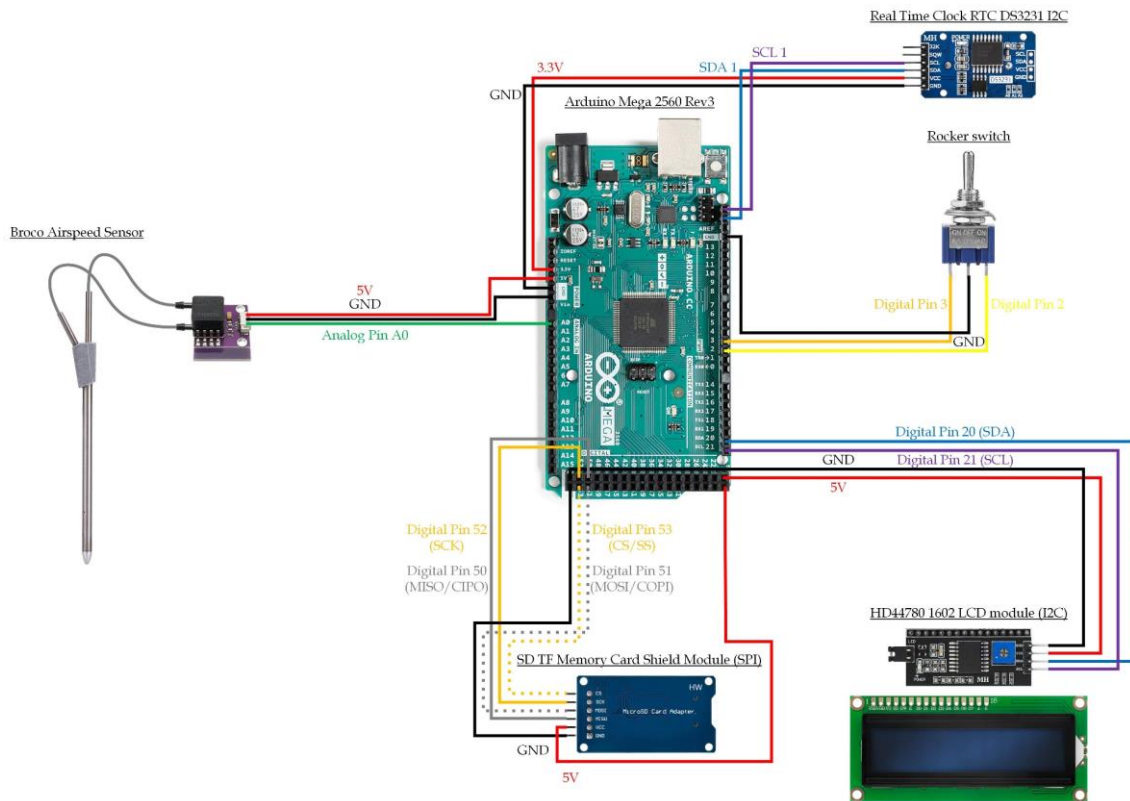


Figure 135 - Wiring scheme of the Arduino

### C.2.2 Arduino sketch

This section shows the Arduino sketch in order to program the Arduino. Consequently, the Arduino will gauge the wind speed, together with the additional hardware.

During the coding process an issue arose concerning the Real-Time-Clock (RTC) module. The issue involves the compile time; i.e., the time at which the sketch is compiled; just before it is uploaded to the Arduino. The compile time is namely used to configure the RTC-module. That means that every time the Arduino is reset, the RTC-module is configured towards this compile time. In other words, the RTC-module will be off, as the compile time is constant. The workaround is to first upload the sketch provided below, which amongst others configures the RTC-module. In that case, the RTC-module receives the compile time from the connected computer. After this, the Arduino must not be reset anymore (!); and the uploaded sketch must be overwritten by an alternative sketch. The alternative sketch ensures the RTC-module is not re-configured anymore. The alternative sketch is obtained by removing a few lines in the provided sketch below. The lines that need to be removed in the second script are the following: 108; 312 until 321; and 454 until 465. These lines are also highlighted in the sketch with the following urgent messages: "REMOVE THIS FUNCTION IN THE SECOND SCRIPT!!!" and "REMOVE THIS LINE IN THE SECOND SCRIPT!!!".

Then there was another problem concerning the RTC-module. The RTC-module is namely offline during compiling process; which produces a time delay. To this end, a drift time was added to the sketch. This drift time is dependent on the compile time, i.e., the length of the sketch. Consequently, if the sketch below is altered a new drift time has to be found by trial and error.

```

1  /*
2  This sketch contains the routine for calculating airspeed.
3
4  The list below presents the main components used to enable this routine.
5  - Broco airspeed sensor (pitot tube).
6  - MPX7002DP differential pressure sensor.
7  - Arduino Mega 2560 Rev3 circuit board.
8
9  The Broco airspeed sensor (pitot tube) measures both stagnation- and static pressure;
10 and therefore, the differential pressure between those two.
11 The Broco airspeed sensor (pitot tube) is connected to the MPX7002DP differential
12 pressure sensor, which receives this differential pressure and subsequently converts
13 it into an electrical signal.
14 The MPX7002DP differential pressure sensor sends this electrical signal to one of the
15 analogue pins of the Arduino Mega 2560 Rev3 circuit board.
16 The 10-bit Analog to Digital Converter (ADC) on the Arduino Mega 2560 Rev3 converts
17 this received electrical signal into a digital value.
18
19 The airspeed can be calculated using 3 building blocks:
20 1) The Pitot tube formula (e.g., see
21    https://www.grc.nasa.gov/www/k-12/BSF/pitot.html); derived from the Bernoulli
22    equation.
23 2) The relationship between the measured differential pressure and the output
24    voltage of the MPX7002DP differential pressure sensor
25    (https://www.mxp.com/docs/en/data-sheet/MPXV7002.pdf).
26 3) The ADC conversion, i.e., the conversion from an analogue value into a digital
27    value (e.g., https://learn.sparkfun.com/tutorials/analog-to-digital-conversion/all).
28
29 The secondary components that are used, are summarized in the list below.
30 - AD-delivery HD44780 1602 LCD 2x16 characters display (I2C).
31 - AD-delivery Real Time Clock (RTC) DS3231 (I2C).
32 - AD-delivery SPI Reader Micro Memory SD TF Card Shield Module.
33 - Sandisk 128GB Extreme MicroSDXC card (FAT32 formatted).
34 - Fafacy mini rocker switch (SPDT) with 3 pins/positions (6 mm; 6A; 125V; AC).
35
36 The airspeed is calculated in realtime and displayed on the AD-delivery HD44780 1602
37 LCD 2x16 characters display (I2C).
38 Time is being tracked by the AD-delivery Real Time Clock (RTC) DS3231 (I2C) and that
39 same module also measures temperature.
40 The data is then stored on the Sandisk 128GB Extreme MicroSDXC card (FAT32 formatted).
41 That is plugged into the AD-delivery SPI Reader Micro Memory SD TF Card Shield Module.
42 This data consists of a timestamp, the temperature, the raw data (i.e., the digital
43 representation of the differential pressure received on the Arduino Mega 2560 Rev3).
44
45 Lastly, the configuration of the Fafacy mini rocker switch (SPDT) enables usage of
46 the following 3 modes.
47 1) Test mode = airspeed measurements/calculations; airspeed display on the LCD
48    screen.
49 2) Standby mode = nothing happens (this mode can for example be used to collect the
50    needed sediment).
51 3) Experiment mode = SD card initialization; airspeed measurements/calculations;
52    airspeed display on the LCD screen; datalogging on the SD card (timestamp,
53    temperature, digital differential pressure and airspeed)
54
55 This sketch is created by Mark van Langeraad on 27-06-2023, with contributions from
56 the people listed below.
57 - Joshua Risko (pitot tube);
58   https://makersportal.com/blog/2019/02/06/arduino-pitot-tube-wind-speed-theory-and-ex-
59   periment) on 09-02-2019.
60 - Tom Igwe (datalogging; File > Examples > SD > Datalogger) on 09-06-2012.
61 - Pieter van der Gaag (rocker switch; from conversations) on 28-06-2023.
62
63 */
64 //
65
66 // start of global setup for the airspeed calculation (i.e., define analogue pin,
67 // parameters, variables)
68 //
69 // define constant: integer value of the analogue pin connected to the pressure sensor
70 const int pressureSensor = A0;
71
72 // [analogue pin]

```

Figure 136

```

80 // start of global setup for the LCD screen
81 //
82 // include library: LCD screen
83 #include <LiquidCrystal_I2C.h>
84
85 // define object: LCD I2C 0x27 address for a 16 columns (chars) and 2 lines display
86 LiquidCrystal_I2C lcd = LiquidCrystal_I2C(0x27, 16, 2);
87
88 // for a 20x04 screen change "16, 2" to "20, 4"
89
90 // define constant: the minimum interval which should be surpassed in order to
91 // send/print new info. to the LCD screen
92 const int minPrintInterval_lcd = 3000;
93
94 // [ms]
95
96 // define variable: unsigned long value (positive with no decimals) to store the
97 // millis() relative to the last time sending/printing info. to the LCD screen
98 unsigned long previousMillis_lcd = 0;
99
100 // [ms]
101
102 // end of global setup for the LCD screen
103 //
104
105 // start of global setup for the RTC module
106 //
107 // include library: communicate with RTC (Real Time Clock) devices; compatible with
108 // DS1307, DS3231, PCF8523, PCF8563 on multiple architectures
109 #include <RTClib.h>
110
111 // define RTC (Real Time Clock) object
112 RTC_DS3231 rtc;
113
114 // define variable: char-array for storing a timestamp of 8 characters ("00:00:00",
115 // "00:00:01", "00:00:02", etc.), = 1 character for the null-terminator ('\0')
116 char timestamp_rtc[9];
117
118 // [hh:mm:ss]
119
120 // define constant: integer value for the RTC module compile time drift
121 // (inaccurately determined using a stopwatch; but "driftTime" can only be an integer
122 // anyway)
123 const int driftTime = 12;
124
125 // [s]; REMOVE THIS LINE IN THE SECOND SCRIPT!!!
126
127 // end of global setup for the RTC module
128 //
129
130 // start of global setup for the SD card module
131 //
132 // include library: communicate with SPI devices using the Arduino circuit board as
133 // the controller device
134 #include <SPI.h>
135
136 // include library: reading and writing on SD cards
137 #include <SD.h>
138
139 // define object: logFile
140 File logFile;
141
142 // define constant: char-array to store the current File ('logFile') used on the SD
143 // card
144 const char* currentFile;
145
146 // define constant: integer value for the Chip-/Slave Select (CS/SS) pin (SPI

```

Figure 138

```

46 // define constants: to execute the airspeed calculation
47 const float rho_a = 1.225;
48
49 // [kg/m³]; air density
50 const float ADC_baseline = 311.5;
51
52 // [bit]; 10-bit ADC baseline: outcome of 0.5 * (2¹⁰ - 1) =
53 1023/2
54 const int ADC_offset_average_size = 20;
55
56 // [-]; number of samples: reading the average digital pressure sensor
57 offset
58 const int ADC_average_size = 20;
59
60 // [-]; number of samples: reading the average digital
61 differential pressure
62 const int u_average_size = ADC_average_size;
63
64 // [-]; number of samples: calculating the average airspeed
65 const int zero_span = 4;
66
67 // [bit]; span (or range) around the ADC baseline
68 regarded as a 0 reading
69
70 // define variable: floating point (digital) value for the offset of the pressure
71 // sensor
72 float ADC_offset_average = 0.0;
73
74 // [bit]; float; digital pressure sensor offset parameter
75
76 // end of global setup for the airspeed calculation (i.e., define analogue pin,
77 // parameters, variables)
78 //
79
80 // end of global setup for the rocker switch
81 //
82 // define constants: integer values of the digital pins that are connected to the
83 // rocker switch
84 const int switchPin_2 = 2;
85
86 // [digital pin]
87 const int switchPin_3 = 3;
88
89 // [digital pin]
90
91 // define variables: booleans tracking if the code has been executed in 'Test-',
92 // 'Standby-', or 'Experiment' mode
93 bool experimentExecuted = false;
94
95 // boolean variable for tracking 'Experiment' mode
96 bool standbyExecuted = false;
97
98 // boolean variable for tracking 'Standby' mode
99 bool testExecuted = false;
100
101 // boolean variable for tracking 'Test' mode
102
103 // end of global setup for the rocker switch
104 //
105
106 // start of global setup for I2C/TWI communication
107 //
108 // include library: communication with I2C/TWI devices
109 #include <Wire.h>
110
111 // end of global setup for I2C communication
112 //

```

Figure 137

```

127 communication)
128 const int csPin = 53;
129
130 // [digital pin]; Arduino Mega 2560 Rev3 circuit
131 board
132
133 // end of global setup for the SD card module
134 //
135
136 //
137 // The functions below are required for both the 'test-' and 'experiment' mode
138 //
139 //
140
141 // start of the readAverageOffset function: retrieve 'size' (i.e.,
142 // 'ADC_offset_average_size') samples from the pressure sensor and return an average ADC
143 // offset reading (i.e., 'ADC_offset_average')
144 float readAverageOffset(int sensor, int baseline, int size) {
145 // create temporary variable 'sum' for storing samples received from the pressure
146 // sensor; to calculate an average ADC offset
147 float sum = 0;
148
149 // start of for-loop: read the analog pin of the pressure sensor 'size' times (in
150 // this case 'ADC_offset_average_size' times), then subtract the ADC-baseline and add
151 // to the 'sum' parameter
152 for (int ii = 0; ii < size; ii++) {
153 sum += analogRead(sensor) - baseline;
154 }
155 // end of for-loop
156
157 // return sum = sum / size, i.e., divide 'sum' by 'size' samples resulting in an
158 // average 'sum' ('sum' and 'size' represent 'ADC_offset_average' and
159 // 'ADC_offset_average_size' respectively)
160 return sum / size;
161 }
162
163 // end of the readAverageOffset function
164 //
165
166 // start of the printAverageOffset_lcd function: send/print to the LCD screen:
167 // average pressure sensor 'offset' ('ADC_offset_average') over 'size'
168 // ('ADC_offset_average_size') samples; calculated with readAverageADCOffset()
169 void printAverageOffset_lcd(float offset) {
170 // define temporary variable: integer version of 'offset' (i.e.,
171 // 'ADC_offset_average')
172 int offset_lcd = 0;
173
174 // [bit]
175
176 // round float 'result_ADCOffset' (i.e., 'ADC_offset_average') towards closest
177 // whole number and store in temporary integer variable 'result_ADCOffset_lcd'
178 offset_lcd = round(offset);
179
180 // [bit]
181
182 // send/print text + result 'result_ADCOffset_lcd' (i.e., rounded version of
183 // 'ADC_offset_average') to LCD screen
184 lcd.print(offset_lcd);
185
186 // [bit]; send/print
187
188 lcd.print(" ");
189
190 // send/print; added extra spaces to whipe LCD
191 screen.clear();
192 }
193 // end of the printAverageOffset_lcd function
194 //

```

Figure 139



```

165 // start of the readAverageADC function: retrieve 'size' (i.e., 'u_reading_size')
166 // samples from the pressure sensor and return an average ADC reading (i.e.,
167 // 'ADC_average')
168 float readAverageADC(int sensor, int baseline, int size, float offset) {
169 // create temporary variable 'sum' to store samples received from the pressure
170 // sensor, to calculate an average ADC reading
171 float sum = 0;
172 // start of for-loop: read the pressure sensor 'size' (in this case
173 // 'ADC_average_size') times; subtract the average ADC offset calculated in void
174 // setup(); add to 'sum' parameter
175 for (int ii = 0; ii < size; ii++){
176 sum += analogRead(sensor) - offset;
177 }
178 // end of for-loop
179 // return sum = sum / size; divide 'sum' by 'size' samples resulting in an average
180 // 'sum' ('sum' and 'size' represent 'ADC_average' and 'ADC_average_size' respectively)
181 return sum / size;
182 }
183 // end of the readAverageADC function
184
185 -----
186 // start of the calculateAverageAirspeed function: calculate average airspeed using
187 // 'reading' (i.e., 'ADC_average') and the manipulated pitot tube formula (i.e., using
188 // the ADC and pressure sensor relation)
189 float calculateAverageAirspeed(float reading, float baseline, int span, float rho) {
190 // start of if-statement: if 'reading' is between 'baseline' + 'span' then
191 // 'reading' is regarded as 0 ('reading', 'baseline' and 'span' represent
192 // 'ADC_average', 'ADC_baseline' and 'zero_span')
193 if ((reading > baseline + span) and (reading < baseline - span)) {
194 return 0;
195 }
196 // code works the same // [m/s]; remove 'return 0' and the
197 // end of if-statement
198 // start of else-statement: else (if 'reading' is not between 'baseline' + 'span')
199 // then the airspeed is calculated from 'reading', 'baseline' and 'span'
200 // represent 'ADC_average', 'ADC_baseline' and 'zero_span'
201 else {
202 // start of if-statement: calculate a negative airspeed if 'reading' (i.e.,
203 // 'ADC_average') is below 'baseline' (i.e., 'ADC_baseline')
204 if (reading < baseline) {
205 return -sqrt((-10000.0 * ((reading / 1023.0) - 0.5)) / rho);
206 }
207 // [m/s]; the minus 10000 is necessary, otherwise the square root is negative
208 // end of if-statement
209 // start of else-statement: calculate a positive airspeed if 'reading' (i.e.,
210 // 'ADC_average') is above 'baseline' (i.e., 'ADC_baseline')
211 else {
212 return sqrt(10000.0 * ((reading / 1023.0) - 0.5)) / rho;
213 }
214 // [m/s]
215 }
216 // end of else-statement
217 // end of else-statement
218 }
219 // end of the calculateAverageAirspeed function
220
221 -----

```

Figure 140

```

251 //
252 // start of the checkSwitchPosition function: checks if the switch is in the Standby
253 // position initially, i.e., within void setup()
254 void checkSwitchPosition() {
255 // send/print text to LCD screen: rocket switch position check
256 lcd.setCursor(0, 0);
257 lcd.print("Check Switch "); // go to start (left) of first line (upward)
258 // send/print: added extra spaces to whipe LCD screen
259 clean; omits lcd.clear() // send/print: added extra spaces to whipe LCD screen
260 // start-delay of the switch check
261 delay(1000);
262 // 1000 [ms] or 1 [s]
263 // start of if-statement: check if you are in standby mode (i.e., in order to note
264 // the offset)
265 if ((digitalRead(switchPin_2) == 1) && digitalRead(switchPin_3) == 1) {
266 // send/print text to LCD screen
267 lcd.setCursor(0, 1);
268 // go to start (left) of second line (downward)
269 lcd.print("Flip to Standby!");
270 // send/print: no extra spaces needed to whipe LCD screen
271 clean
272 // start of while-loop: if the rocket switch is put into the Standby position,
273 // then you may leave the while loop
274 while (1) {
275 // start of if-statement: if the rocket switch is put into the Standby
276 // position, then you may leave the while loop
277 if ((digitalRead(switchPin_2) == 1) && (digitalRead(switchPin_3) == 1)) {
278 // send/print text to LCD screen
279 lcd.setCursor(0, 1);
280 // go to start (left) of second line
281 (downward)
282 lcd.print("Proceed "); // send/print: added extra spaces to whipe LCD screen
283 clean; omits lcd.clear() // send/print: added extra spaces to whipe LCD screen
284 // end-delay of the switch check
285 delay(1000);
286 // 1000 [ms] or 1 [s]
287 // break (free) from the loop and continue
288 break;
289 // break;
290 }
291 // end of the if-statement
292 }
293 // end of the while-loop
294 }
295 // end of the if-statement
296 // if rocket switch is in the 'Standby' position send/print text to LCD screen
297 lcd.setCursor(0, 0);
298 // go to start (left) of first line (upward)
299 lcd.print("Switch Set "); // send/print: added extra spaces to whipe LCD screen
300 clean; omits lcd.clear() // send/print: added extra spaces to whipe LCD screen

```

Figure 142

```

207 // start of the formatForLCD function: print the airspeed on the LCD screen in a 5
208 // characters format, to avoid staggered characters (improving readability and the use
209 // of lcd.clear())
210 char* formatForLCD(float result_u) {
211 // create a char-array of 6 characters (enables showing -99.99 until 999.99 [m/s])
212 // + null-terminator ('\0') to temporary store formatted speed
213 static char result_u_formatted[7];
214 // convert float 'speed' to char 'formattedSpeed' with 5 digits, 2 decimal places
215 dtostrf(result_u, 6, 2, result_u_formatted);
216 // return the measured speed ('result_u') in the format to be used for the LCD
217 screen
218 return result_u_formatted;
219 }
220 // end of the formatForLCD function
221
222 -----
223 // start of the checkRTC function: checks and prints whether the RTC module is ready
224 // or not
225 void checkRTC() {
226 // send/print text to LCD screen: RTC module communication check
227 lcd.setCursor(0, 0);
228 lcd.print("Check RTC "); // go to start (left) of first line (upward)
229 clean; omits lcd.clear() // send/print: added extra spaces to whipe LCD screen
230 // start-delay of the RTC check;
231 delay(1000);
232 // 1000 [ms] or 1 [s]
233 // start of if-statement: see if the RTC is present and can be initialized
234 if (rtc.begin()) {
235 // send/print text to LCD screen
236 lcd.setCursor(0, 1);
237 // go to start (left) of second line (downward)
238 lcd.print("RTC Fail! "); // send/print: added extra spaces to whipe LCD screen
239 clean; omits lcd.clear() // send/print: added extra spaces to whipe LCD screen
240 // start of while-loop
241 while (1) {
242 // trap code inside while-loop if RTC communication fails
243 }
244 // end of while-loop
245 // end of if-statement
246 // if RTC module communication is checked send/print text to LCD screen
247 lcd.setCursor(0, 0);
248 // go to start (left) of first line (upward)
249 lcd.print("RTC Set! "); // send/print: added extra spaces to whipe LCD screen
250 clean; omits lcd.clear() // send/print: added extra spaces to whipe LCD screen
251 // end-delay of the RTC check
252 delay(1000);
253 // 1000 [ms] or 1 [s]
254 }
255 // end of the checkRTC function

```

Figure 141

```

290 lcd.setCursor(0, 1);
291 lcd.print(" "); // go to start (left) of second line (downward)
292 clean; omits lcd.clear() // send/print: added extra spaces to whipe LCD screen
293 // end-delay of the switch check
294 delay(1000);
295 // 1000 [ms] or 1 [s]
296 // end of the checkSwitchPosition function
297
298 -----
299 // start of updateSwitchBooleans function: change the boolean variables, that keep
300 // track in which mode you are in, to either true or false
301 void updateSwitchBooleans(bool boolExperiment, bool boolStandby, bool boolTest) {
302 // change the boolean variables, that keep track in which mode you are in, to
303 // either true or false
304 experimentExecuted = boolExperiment;
305 // 'Experiment' mode
306 standbyExecuted = boolStandby;
307 // 'Standby' mode
308 testExecuted = boolTest;
309 // 'Test' mode
310 }
311 // end of updateSwitchBooleans function
312
313 -----
314 /*
315 The function below is only required to be present in the sketch that is used to set
316 the correct time on the RTC module.
317 This function can be deleted in the second sketch and that sketch will be the program
318 on the Arduino Mega 2560 Rev3 (after setting the time with sketch 1)
319 */
320
321 -----
322 // start of adjustRTC function: retrieve the compile time and add a drift to
323 // compensate for compiling + uploading + MCU start; REMOVE THIS FUNCTION IN THE SECOND
324 // SCRIPT!!!
325 void adjustRTC(int drift) {
326 // update the date and time on the RTC (setting it equal to the compile time, i.e.,
327 // at the start of compiling)
328 rtc.adjust(DateTime(__DATE__, __TIME__));
329 // add a drift compensation to compensate for compiling + uploading + MCU start;
330 // the magnitude of the drift depends on the characteristics of the sketch
331 DateTime correctTime = DateTime(rtc.now().unixtime() + drift);
332 // get
333 current time from RTC module and add time drift
334 rtc.adjust(correctTime);
335 // update time on RTC module
336 }
337 // end of adjustRTC function
338
339 -----
340 /*
341 The functions below are only required for the 'experiment' mode

```

Figure 143

```

325 */
326 //
-----
327 // start of the csvFileMaker function: checks (and prints) if the SD card module is
ready or not
328 const char* csvFileMaker() {
329 // Create a new file with 10 characters for the filename ("EXP000.CSV",
"EXP001.CSV", "EXP002.CSV", etc.), + 1 for null-terminator ('\0')
330 static char filename[] = "R000.CSV";
331
332 // start of for-loop: search through the files (% 10 is the modulus operator and
calculates the remainder after division by 10)
333 for (uint16_t i = 0; i < 1000; i++) {
334 filename[i] = i / 100 + '0';
335
336 (ASCII-offset)
filename[i] = (i / 10) % 10 + '0';
337
338 // dozens: 317 / 10 % 10 = 31.7 % 10 = 1.7 (i.e., 1); + '0'
filename[i] = i % 10 + '0';
339
340 // integers: 317 % 10 = 7; + '0' (ASCII-offset)
// start of the if-statement: if the next file does not exist... then create it
and leave the for-loop
341 if (!SD.exists(filename)) {
342 // continue loop until filename does not exist
logfile = SD.open(filename, FILE_WRITE);
343 // open a new file when it doesn't exist
break;
344
345 // leave the for-loop when the
next filename is opened/created
346 }
347 // end of if-statement
348 }
349 // end of for-loop
350 // start of if-statement: check if the requested file is opened/created successfully
for writing
351 if (!logfile) {
352 // send/print text to LCD screen
lcd.setCursor(0, 1);
353
354 lcd.print("File Write Fail!"); // go to start (left) of second line (downward)
355
356 // send/print; no extra spaces needed to whipe LCD screen
clean
357 // start of the while-loop: trap code inside while-loop if logfile
opening/creation fails
358 while (!) {
359 }
360 // end of while-loop
361 }
362 // end of if-statement
363 // close the file immediately if it is not used in this function
logfile.close();
364 // return the newly created file name (the filename array itself), so that we can
use it later
365 return filename;
366 }
367 // End of the csvFileMaker function

```

Figure 144

```

406 logfile.print("Temperature");
407 logfile.print(","); // write in file + line ending; header
408 logfile.print("ADC"); // write in file + line ending; separator
409 logfile.print(","); // write in file + line ending; header
410 logfile.println("Windspeed"); // write in file + line ending; separator
411 // write in file + line ending; header
412 // close the file after writing to it
logfile.close();
413 // end of the writeOffsetToFile function
414 //
-----
415 // start of the writeResultsToFile function: search for the last file on SD card and
write results to it
416 void writeResultsToFile(char time[], float temperature, float result_ADC, float
result_u, const char* filename) {
417 // open the file which was made in the csvFileMaker function
logfile = SD.open(filename, FILE_WRITE);
418
419 // start of if-statement: check if the requested file is opened/created successful
for writing
420 if (!logfile) {
421 // send/print text to LCD screen
lcd.setCursor(0, 1);
422
423 lcd.print("File Write Fail!"); // go to start (left) of second line (downward)
424
425 // send/print; no extra spaces needed to whipe LCD screen
clean
426 // start of the while-loop: trap code inside while-loop if logfile
opening/creation fails
427 while (!) {
428 }
429 // end of while-loop
430 }
431 // end of if-statement
432 // write 'time' (i.e., 'timestamp') to SD card
logfile.print(time);
433 // [hh:mm:ss]; send/print variable
('timestamp_rtc')
logfile.print(",");
434 // send/print (delimiter)
435 // write 'temperature' (i.e., T_rtc) to SD card ('temperature' originates from a
sensor on the RTC module)
logfile.print(temperature);
436 // [C]; send/print variable ('T_rtc')
437 logfile.print(","); // send/print (delimiter)
438 // write 'result_ADC' and 'result_u' (i.e., 'ADC_average' and 'u_average') to the
SD card
439 logfile.print(result_ADC);

```

Figure 146

```

368 //
-----
369 // start of the writeOffsetToFile function: search for the last file on SD card and
write results to it
370 void writeOffsetToFile(float result_ADCoffset, const char* filename) {
371 // open the file which was made with the csvFileMaker function
logfile = SD.open(filename, FILE_WRITE);
372
373 // start of if-statement: check if the requested file is opened/created successful
for writing
374 if (!logfile) {
375 // send/print text to LCD screen
lcd.setCursor(0, 1);
376
377 lcd.print("File Write Fail!"); // go to start (left) of second line (downward)
378
379 // send/print; no extra spaces needed to whipe LCD screen
clean
380 // start of the while-loop: trap code inside while-loop if logfile
opening/creation fails
381 while (!) {
382 }
383 // end of while-loop
384 }
385 // end of if-statement
386 // write 'result_ADCoffset' (i.e., 'ADC_offset_average') to SD card (send/print +
line ending)
logfile.print("Offset");
387 logfile.print(",");
388 // write 'result_ADCoffset' (i.e., 'ADC_offset_average') to SD card (send/print +
line ending)
logfile.println(result_ADCoffset);
389 // [bit]
logfile.println(""); // [bit]
390 // write in file + line ending; add whitespace
391 // create headers for the columns
logfile.print("hh:mm:ss");
392
393 logfile.print(","); // write in file + line ending; units
394 logfile.print("[deg C]"); // write in file + line ending; separator
395 logfile.print(","); // write in file + line ending; units
396 logfile.print("[bit]"); // write in file + line ending; separator
397 logfile.print(","); // write in file + line ending; units
398 logfile.println("[m/s]"); // write in file + line ending; separator
399 logfile.print("Time"); // write in file + line ending; units
400 logfile.print(","); // write in file + line ending; header
401 // write in file + line ending; separator
402 // [bit]; send/print variable ('ADC_average')
logfile.print(",");
403 // send/print (delimiter)
logfile.println(result_u);
404 // [m/s]; send/print variable ('u_average') + line
ending
405 // close the file after writing to it
logfile.close();
406 // end of the writeResultsToFile function
407 //
-----
408 // start of dateTime function: call back for file timestamps (add the right date-time
to files); DO NOT! REMOVE THIS FUNCTION IN THE SECOND SCRIPT
409 void dateTime(uint16_t* date, uint16_t* time) {
410 // receive the current time on/from the RTC module
DateTime now = rtc.now();
411 // return the date, using the FAT_DATE macro, formatting date-field to be
compatible with FAT file systems (e.g., when using SD cards)
*date = FAT_DATE(now.year(), now.month(), now.day());
412 // return the time, using the FAT_TIME macro, formatting time-field to be
compatible with FAT file systems (e.g., when using SD cards)
*time = FAT_TIME(now.hour(), now.minute(), now.second());
413 // end of dateTime function
414 //
-----
415 // start of the printCurrentExperiment_lcd() function: prints current mode +
experiment number to the LCD screen
416 void printCurrentExperiment_lcd(const char* inputFile) {
417 // start and position of the 3-digit number in the current file/experiment
int start = 1;
418 // "EXP000.CSV"; digits start at index 3
int end = 4;
419 // "EXP000.CSV"; digits end at index 6
420 // start of for-loop: send/print 3-digit number of the current file to the LCD
screen
421 for (int i = start; i < end; i++) {
422 // send/print text to LCD screen: add the number of the current file/experiment
logfile.print(inputFile[i]);
423 }
424 // end of for-loop
425 // send/print extra spaces to whipe LCD screen clean (i.e., filling all 16
characters on a single line); omits lcd.clear()
logfile.print(" ");
426 // end of the printCurrentExperiment_lcd() function
427 //
-----
428 // start of the initialization of the main program, i.e., void setup()
429 //
-----
430 // start of the void setup() function: initialization of the program/routine; this

```

Figure 145

```

446 logfile.print(","); // [bit]; send/print variable ('ADC_average')
447 logfile.println(result_u); // send/print (delimiter)
448 // [m/s]; send/print variable ('u_average') + line
ending
449 // close the file after writing to it
logfile.close();
450 // end of the writeResultsToFile function
451 //
-----
452 // start of dateTime function: call back for file timestamps (add the right date-time
to files); DO NOT! REMOVE THIS FUNCTION IN THE SECOND SCRIPT
453 void dateTime(uint16_t* date, uint16_t* time) {
454 // receive the current time on/from the RTC module
DateTime now = rtc.now();
455 // return the date, using the FAT_DATE macro, formatting date-field to be
compatible with FAT file systems (e.g., when using SD cards)
*date = FAT_DATE(now.year(), now.month(), now.day());
456 // return the time, using the FAT_TIME macro, formatting time-field to be
compatible with FAT file systems (e.g., when using SD cards)
*time = FAT_TIME(now.hour(), now.minute(), now.second());
457 // end of dateTime function
458 //
-----
459 // start of the printCurrentExperiment_lcd() function: prints current mode +
experiment number to the LCD screen
460 void printCurrentExperiment_lcd(const char* inputFile) {
461 // start and position of the 3-digit number in the current file/experiment
int start = 1;
462 // "EXP000.CSV"; digits start at index 3
int end = 4;
463 // "EXP000.CSV"; digits end at index 6
464 // start of for-loop: send/print 3-digit number of the current file to the LCD
screen
465 for (int i = start; i < end; i++) {
466 // send/print text to LCD screen: add the number of the current file/experiment
logfile.print(inputFile[i]);
467 }
468 // end of for-loop
469 // send/print extra spaces to whipe LCD screen clean (i.e., filling all 16
characters on a single line); omits lcd.clear()
logfile.print(" ");
470 // end of the printCurrentExperiment_lcd() function
471 //
-----
472 // start of the initialization of the main program, i.e., void setup()
473 //
-----
474 // start of the void setup() function: initialization of the program/routine; this

```

Figure 147

```

part determines the average digital pressure sensor offset
490 void setup() {
491   // startup: rocket switch
492   pinMode(switchPin_2, INPUT_PULLUP);
493   2 and VCC (5V) // define switch pin 4 use internal resistor between digital pin
   pinMode(switchPin_3, INPUT_PULLUP);
494   2 and VCC (5V) // define switch pin 4 use internal resistor between digital pin
495   // startup: initialize various components
496   Wire.begin();
497   lcd.init(); // Wire (i.e., I2C/TWI) communication
498   rtc.begin(); // LCD (I2C) communication
499   // RTC (I2C) communication
500   // Remove forward slashes ('/') to check the time on the RTC
501   Serial.begin(9600); // Remove forward slashes ('/')
502   to check the time on the RTC
503   // turn on the backlight of the LCD screen
504   lcd.backlight();
505   // check RTC: checks/prints if the initialization was successful; if not, routine
506   stops here
507   checkRTC();
508   // RTC (I2C) communication;
509   // update the date & time on the RTC module, adding a 'driftTime' compensation for
510   compile-, upload- and MCU startup time
511   adjustRTC(driftTime);
512   // REMOVE LINE IN THE SECOND SCRIPT!
513   // check if the rocket switch is in the correct position (Standby: to note the
514   offset); if not, routine stops here
515   checkSwitchPosition();
516   // end of the void setup()
517   //
518   //-----
519   /*
520   start of the routine of the main program, i.e., void loop()
521   */
522   //-----
523   // start of the void loop() function: main part of the program/routine; this part
524   provides the test-, standby- and experiment mode of this program/routine
525   void loop() {
526     // start of the while-loop: experiment mode
527     while ((digitalRead(switchPin_2) == 0) && (digitalRead(switchPin_3) == 1)) {
528       // start of if-statement: communicate in which mode the rocket switch is
529       positioned
530       if (!experimentExecuted) {
531         // initialize communication with SD card module
532         SD.begin(csPin);
533         //
534         //-----
535         /*
536         start of the checkSD function: checks (and prints) if the SD card module is

```

Figure 148

```

537   in, to either true or false
538   updateSwitchBooleans(true, false, false);
539   // 'Test' mode is not executed; i.e., change to 'false'
540   // goto-statement: teleport code to label 'jumpToStandby'
541   goto jumpToStandby;
542   // break (free) from the loop and
543   continue
544   // end of the if-statement
545   // end of the while-loop
546   // end of if-statement
547   // if SD module communication is checked send/print text to LCD screen
548   lcd.setCursor(0, 1);
549   // go to start (left) of first line (upward)
550   lcd.print("SD Card Set ");
551   // send/print; added extra spaces to whipe LCD screen
552   clean; omits lcd.clear();
553   lcd.setCursor(0, 1);
554   // go to start (left) of second line
555   lcd.print(" ");
556   // send/print; added extra spaces to whipe LCD screen
557   clean; omits lcd.clear();
558   // end-delay of the SD Card check
559   delay(1000);
560   // 1000 [ms] or 1 [s]
561   //
562   /*
563   end of the checkSD function: a separate function was not made for this piece of
564   code, as the Goto statement becomes dysfunctional
565   */
566   // set the date & time of files using the callback function and the RTC module
567   SDFile:dateTimeCallback(dateTime);
568   // if SD card module is initialized create a file 'EXP000.CSV', or a newer one
569   with ascending number
570   currentFile = csvFileMaker();
571   // calculate pressure sensor offset: use 'ADC offset average_size' samples to
572   calculate an average offset ('ADC_offset_average')
573   ADC_offset_average = readAverageADC(pressureSensor, ADC_baseline, ADC_offset_average_size);
574   // [bit]
575   // write the result ('ADC_offset_average') to SD the card once in the
576   'EXP000.CSV' file, or a newer one with ascending number
577   writeOffsetToFile(ADC_offset_average, currentFile);
578   // send/print text to LCD screen: current run (experiment mode) + average
579   'offset' ('ADC_offset_average')
580   lcd.setCursor(0, 1);
581   // go to start (left) of first line (upward)
582   lcd.print("E R");
583   // send/print; added extra spaces to whipe
584   LCD screen clean; omits lcd.clear();
585   printCurrentExperiment_lcd(currentFile);
586   printAverageOffset_lcd(ADC_offset_average);
587   // change the boolean variables, that keep track in which mode you are in, to

```

Figure 150

```

ready or not (first this was a separate function called void checkSD(), but
then the goto-statement doesn't work)
*/
// send/print text to LCD screen: SD module communication check
532 lcd.setCursor(0, 1);
533 // go to start (left) of first line (upward)
534 lcd.print("Check SD Card ");
535 // send/print; added extra spaces to whipe LCD screen
536 clean; omits lcd.clear();
537 lcd.setCursor(0, 1);
538 // go to start (left) of second line
539 (downward)
540 lcd.print(" ");
541 // send/print; spaces to whipe LCD screen clean; omits
542 lcd.clear();
543 // start-delay of the SD Card check
544 delay(1000);
545 // 1000 [ms] or 1 [s]
546 // start of if-statement: see if the SD card is present and can be initialized
547 if (!SD.begin(csPin)) {
548   // send/print text to LCD screen
549   lcd.setCursor(0, 1);
550   // go to start (left) of second line
551   (downward)
552   lcd.print("SD Card Fail! ");
553   // send/print; added extra spaces to whipe LCD screen
554   clean; omits lcd.clear();
555   // pause-delay of the SD Card check
556   delay(1000);
557   // send/print text to LCD screen
558   lcd.setCursor(0, 1);
559   // go to start (left) of second line
560   (downward)
561   lcd.print("Flip to Standby!");
562   // send/print; added extra spaces to whipe LCD screen
563   clean; omits lcd.clear();
564   // start of while-loop: if the rocket switch is put into the Standby
565   position, then you may leave the while loop
566   while (1) {
567     // start of if-statement: if the rocket switch is put into the Standby
568     position, then you may leave the while loop
569     if (((digitalRead(switchPin_2) == 1) && (digitalRead(switchPin_3) == 1))) {
570       // send/print text to LCD screen
571       lcd.setCursor(0, 1);
572       // go to start (left) of second line
573       (downward)
574       lcd.print("Proceed ");
575       // send/print; added extra spaces to whipe LCD
576       screen clean; omits lcd.clear();
577       // end-delay of the switch check
578       delay(1000);
579       // 1000 [ms] or 1 [s]
580       // change the boolean variables, that keep track in which mode you are

```

Figure 149

```

581   either true or false
582   updateSwitchBooleans(true, false, false);
583   // order: 'Experiment-', 'Standby-' and 'Test' mode
584   // end of the if-statement
585   // retrieve time from the RTC module to create a timestamp
586   DateTime now = rtc.now();
587   // [hh:mm:ss]; get current time from the RTC module
588   sprintf(timestamp_rtc, "%02d:%02d:%02d", now.hour(), now.minute(), now.second());
589   timestamp string // [hh:mm:ss]; format the
590   // retrieve temperature from the RTC module
591   float T_rtc = 0.0;
592   // [°C]; initialize variable ('T_rtc')
593   T_rtc = rtc.getTemperature();
594   // [°C]; read variable ('T_rtc')
595   // use 'ADC_average_size' ADC readings from the pressure sensor to calculate an
596   average ADC reading
597   float ADC_average = 0.0;
598   // [bit]; initialize variable ('ADC_average')
599   ADC_average = readAverageADC(pressureSensor, ADC_baseline, ADC_average_size,
600   ADC_offset_average); // [bit]; read
601   variable ('ADC_average')
602   // use 'ADC_average' to calculate an average airspeed
603   float u_average = 0.0;
604   // [m/s]; initialize variable ('u_average')
605   u_average = calculateAverageAirspeed(ADC_average, ADC_baseline, zero_span, rho_a);
606   // [m/s]; calculate
607   variable ('u_average')
608   // write the result ('ADC_offset_average') to SD the card once in the
609   'EXP000.CSV' file, or a newer one with ascending number
610   writeResultsToFile(timestamp_rtc, T_rtc, ADC_average, u_average, currentFile);
611   //
612   /*
613   Between the block notes (this one and the next) there is the code to send/print a
614   formatted 'u_average' (so that the LCD screen displays without staggering) at
615   lower frequency than the measurements
616   */
617   // format the result ('u_average') enabling sending/printing to the LCD screen
618   without staggering
619   char* u_average_formatted = formatForLCD(u_average);
620   // [m/s]
621   // define temporary variable: unsigned long value (positive with no decimals) to
622   store the current millis() from starting up the Arduino circuit board
623   unsigned long currentMillis_lcd = millis();
624   // [ms]
625   // start of if-statement: if the interval between 'previousMillis_lcd' and
626   'currentMillis_lcd' exceeds the desired send/print interval, i.e.,
627   'minPrintInterval_lcd' then we send/print it to the LCD screen
628   if (currentMillis_lcd - previousMillis_lcd >= minPrintInterval_lcd) {
629     // store current millis() relative to the startup of the Arduino circuit board
630     in 'previousMillis_lcd' to be used in the next iteration
631     previousMillis_lcd = currentMillis_lcd;
632     // [ms] save currentMillis as previousMillis for the next
633     iteration

```

Figure 151



```

649 // send/print formatted 'speed' (i.e., 'formattedSpeed') to LCD screen at lower
    // frequency than the measurements (the 3 statements contain 16 characters in
    // total)
650 lcd.setCursor(0, 1);

    (downward)
    // go to start (left) of second line
651 lcd.print("u ");

    // send/print
652 lcd.print(u_average_formatted);

    // [m/s]; send/print variable (formatted 'u_average')
653 lcd.print(" ");

    // send/print
    // end of if-statement
654 }
655 /*
656 A separate function was not made for this piece of code, since
657 'previousMillis_lcd' should be a global variable
658 */
659 // delay for stability purposes
660 delay(10);

    // 10 [ms] or 0.01 [s]
661 }
662 // end of the while-loop
663 //
-----
664 // start of the while-loop: standby mode
665 while ((digitalRead(switchPin_2) == 1) && (digitalRead(switchPin_3) == 0)) {
666 // goto label: code is teleported towards this label 'jumpToStandby'
667 jumpToStandby:
668 // start of if-statement: communicate in which mode the rocket switch is
    // positioned
669 if (!testExecuted) {
670 // send/print text to LCD screen: communicate in which mode the rocket switch
    // is positioned
671 lcd.setCursor(0, 0);

672 // go to start (left) of first line (upward)
673 lcd.print("S ");

    // send/print; added extra spaces to whipe LCD screen
674 clean; omits lcd.clear()
    lcd.setCursor(0, 1);

    // go to start (left) of second line
675 (downward)
    lcd.print(" ");

    // send/print; added extra spaces to whipe LCD screen
676 clean; omits lcd.clear()

677 // change the boolean variables, that keep track in which mode you are in, to
    // either true or false
678 updateSwitchBooleans(false, true, false);

    // order: 'Experiment-', 'Standby-' and 'Test' mode
679 }
680 // end of the if-statement
681 // retrieve time from the RTC module to create a timestamp
682 DateTime now = rtc.now();

683 // [hh:mm:ss]; get current time from the RTC module
684 sprintf(timestamp_rtc, "%02d:%02d:%02d", now.hour(), now.minute(), now.second());

685 // [°C]; read variable ('temperature')

```

Figure 152

```

timestamp string // [hh:mm:ss]; format the
687 // Remove forward slashes ('/') to check the time on the RTC
688 //
689 Serial.println(timestamp_rtc);
    // Remove forward slashes
690 ('/') to check the time on the RTC
691 // send/print text to LCD screen: current time ('timestamp')
692 lcd.setCursor(0, 1);

693 // go to start (left) of second line (downward)
694 lcd.print(timestamp_rtc);

    // send/print
695 lcd.print(" ");

    // send/print
    // send/print; added extra spaces to whipe LCD
696 }
697 // end of the while-loop
698 //
-----
699 // start of the while-loop: test mode
700 while ((digitalRead(switchPin_2) == 1) && (digitalRead(switchPin_3) == 0)) {
701 // start of if-statement: communicate in which mode the rocket switch is
    // positioned
702 if (!testExecuted) {
703 // calculate pressure sensor offset: use 'ADC_offset_average_size' samples to
    // calculate an average offset ('ADC_offset_average')
704 ADC_offset_average = readAverageOffset(pressureSensor, ADC_baseline,
    ADC_offset_average_size); // [bit]
705 // send/print text to LCD screen: current mode + average 'offset'
    ('ADC_offset_average')
706 lcd.setCursor(0, 1);

    // go to start (left) of first line (upward)
707 lcd.print("T ");

    // send/print; added extra spaces to
708 whipe LCD screen clean; omits lcd.clear()
    printAverageOffset_lcd(ADC_offset_average);

709 // change the boolean variables, that keep track in which mode you are in, to
    // either true or false
710 updateSwitchBooleans(false, false, true);

    // order: 'Experiment-', 'Standby-' and 'Test' mode
711 }
712 // end of the if-statement
713 // retrieve time from the RTC module to create a timestamp
714 DateTime now = rtc.now();

715 // [hh:mm:ss]; get current time from the RTC module
716 sprintf(timestamp_rtc, "%02d:%02d:%02d", now.hour(), now.minute(), now.second());

717 // [hh:mm:ss]; format the
    timestamp string
718 // retrieve temperature from the RTC module
719 float T_rtc = 0.0;

720 // [°C]; initialize variable ('temperature')
721 T_rtc = rtc.getTemperature();

722 // [°C]; read variable ('temperature')

```

Figure 153

```

723 // use 'ADC_average_size' ADC readings from the pressure sensor to calculate an
    // average ADC reading
724 float ADC_average = 0.0;

725 // [bit]; initialize variable ('ADC_average')
726 ADC_average = readAverageADC(pressureSensor, ADC_baseline, ADC_average_size,
    ADC_offset_average); // [bit]; read
    variable ('ADC_average')
727 // use 'ADC_average' to calculate an average airspeed
728 float u_average = 0.0;

729 // [m/s]; initialize variable ('u_average')
730 u_average = calculateAverageAirspeed(ADC_average, ADC_baseline, zero_span, rho_a);
    // [m/s]; calculate
    variable ('u_average')
731 //
732 /*
733 Between the block notes (this one and the next) there is the code to send/print a
    // formatted 'u_average' (so that the LCD screen displays without staggering) at
    // lower frequency than the measurements
734 */
735 // format the result ('u_average') enabling sending/printing to the LCD screen
    // without staggering
736 char* u_average_formatted = formatForLCD(u_average);

737 // [m/s]
738 // define temporary variable: unsigned long value (positive with no decimals) to
    // store the current millis() from starting up the Arduino circuit board
739 unsigned long currentMillis_lcd = millis();

    // [ms]
740 // start of if-statement: if the interval between 'previousMillis_lcd' and
    // 'currentMillis_lcd' exceeds the desired send/print interval, i.e.,
    // 'minPrintInterval_lcd' then we send/print it to the LCD screen
741 if (currentMillis_lcd - previousMillis_lcd >= minPrintInterval_lcd) {
742 // store current millis() relative to the startup of the Arduino circuit board
    // in 'previousMillis_lcd' to be used in the next iteration
743 previousMillis_lcd = currentMillis_lcd;

    // [ms]; save currentMillis as previousMillis for the next
    // iteration
744 // send/print formatted 'speed' (i.e., 'formattedSpeed') to LCD screen at lower
    // frequency than the measurements (the 3 statements contain 16 characters in
    // total)
745 lcd.setCursor(0, 1);

    // go to start (left) of second line
746 (downward)
    lcd.print("u ");

    // send/print
747 lcd.print(u_average_formatted);

    // [m/s]; send/print variable (formatted 'u_average')
748 lcd.print(" ");

    // send/print
    // end of if-statement
749 }
750 // end of the if-statement
751 /*
752 A separate function was not made for this piece of code, since
753 'previousMillis_lcd' must be a global variable
754 */
755 // delay for stability purposes
756 delay(10);

```

Figure 154

```

761 // 10 [ms] or 0.01 [s]
762 // end of the while-loop
763 //
-----
764 // end of the void loop() - to be repeated infinitely (when powered)
765 //
-----
766 // end of the sketch

```

Figure 155

### C.2.3 Programming logic (summary of the Arduino sketch)

The scheme below shows the program logic that summarizes the Arduino sketch. The scheme highlights one of the RTC-module commands, which must be removed in the second script.

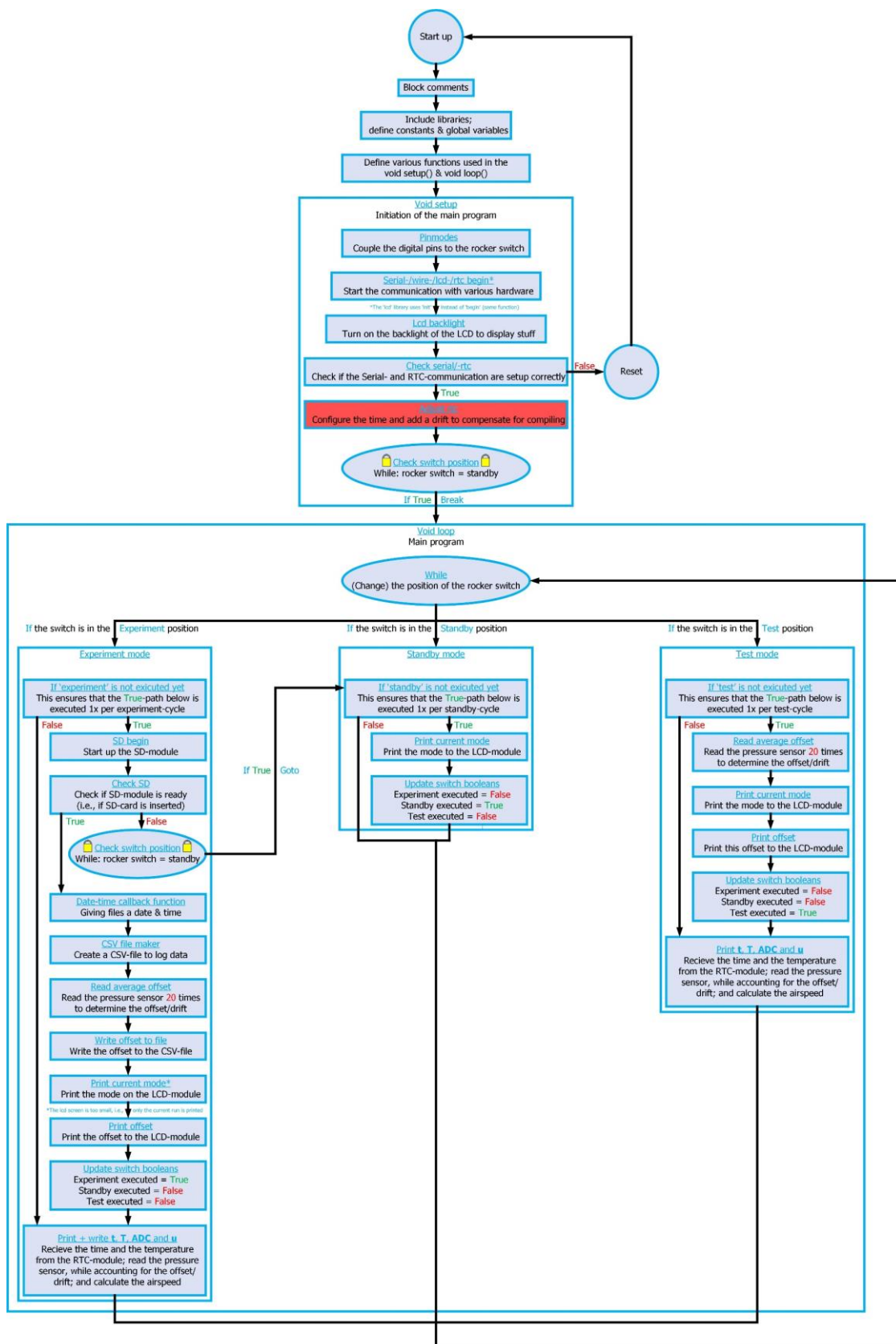


Figure 156 - Programming logic of the Arduino sketch



## C.2.4 The adapted pitot tube formula

### C.2.4.1 The differential pitot tube formula

Pitot tube formula (Çengel & Cimbala, 2014)

$$85) \quad u = \sqrt{\frac{2\Delta p}{\rho_a}}$$

Where:

- $u$  [m/s] is the wind speed.
- $\Delta p$  [Pa] is the differential pressure.
- $\rho_a$  [kg/m<sup>3</sup>] is the air density.

### C.2.4.2 The differential pressure sensor relation

Transfer function (calibration) of the pressure sensor (NXP, 2021)

$$86) \quad V_{out} = V_{system} \left( \frac{1}{5} \Delta p + \frac{1}{2} \right)$$

Where:

- $V_{out}$  [V] is the output voltage of the pressure sensor.
- $V_{system}$  [V] (i.e., abbreviated to  $V_s$  [V]) is the system voltage of the Arduino.

The formula is in [kPa], i.e., it needs to be converted to [Pa].

Plug in the information and re-arrange

$$87) \quad \Delta p = 5,000 \left( \frac{V_{out}}{V_s} - \frac{1}{2} \right)$$

### C.2.4.3 The Analogue-to-Digital-Converter (ADC) relation

The Analogue-to-Digital Converter relation (Elektor, 2022)

$$88) \quad \frac{ADC_{resolution}}{V_{system}} = \frac{ADC_{out}}{V_{measured}}$$

Where:

- $ADC_{resolution}$  [–] is the resolution of the ADC.
- $ADC_{out}$  [–] is the output value of the ADC.
- $V_{measured}$  [V] is the measured voltage.
- $V_{system}$  [V] (i.e., abbreviated to  $V_s$  [V]) is the system voltage of the Arduino.

The resolution ( $ADC_{resolution}$ ) of a 10-bit ADC is  $2^{10} = 1024$  [–], running from 0 [–] up until and including 1,023 [–]. Next, the measured voltage ( $V_{measured}$ ) is equal to the output voltage of the sensor (i.e.,  $V_{measured} = V_{out}$  [V]).

Plug in the information and re-arrange

$$89) \quad V_{out} = \frac{ADC_{out} V_s}{1024}$$

#### C.2.4.4 Combining all relations

Pitot tube formula

$$90) \quad u = \sqrt{\frac{2\Delta p}{\rho_a}}$$

Plug in transfer function


$$91) \quad u = \sqrt{\frac{10,000 \left( \frac{V_{out}}{V_s} - \frac{1}{2} \right)}{\rho_a}}$$

Plug in ADC relation (Hrisko, 2019)

$$92) \quad u = \sqrt{\frac{10,000 \left( \frac{ADC_{out}}{1,024} - \frac{1}{2} \right)}{\rho_a}}$$

## C.3 Power supply

The datasheet from the manufacturer is added below.



### 12,8 V & 25,6 V Lithium SuperPack batteries

[www.victronenergy.com](http://www.victronenergy.com)

**Integrated BMS and safety switch**  
 The SuperPack batteries are extremely easy to install, needing no additional components. The internal switch will disconnect the battery in case of over discharge, over charge, low or high temperature.

**Abuse proof**  
 A lead-acid battery will fail prematurely due to sulfation:

- If it operates in deficit mode during long periods of time (i.e. if the battery is rarely, or never at all, fully charged).
- If it is left partially charged or worse, fully discharged.

A Lithium-Ion battery does not need to be fully charged. Service life even slightly improves in case of partial charge instead of a full charge. This is a major advantage of Li-ion compared to lead-acid.


The SuperPack batteries will cut-off the charge or discharge current when the maximum ratings are exceeded.

**Efficient**  
 In several applications (especially off-grid solar), energy efficiency can be of crucial importance. The round-trip energy efficiency (discharge from 100 % to 0 % and back to 100 % charged) of the average lead-acid battery is 80 %. The round-trip energy efficiency of a Li-ion battery is 92 %.

The charge process of lead-acid batteries becomes particularly inefficient when the 80 % state of charge has been reached, resulting in efficiencies of 50 % or even less in solar systems where several days of reserve energy are required (battery operating in 70 % to 100 % charged state).

In contrast, a Li-ion battery will still achieve 90 % efficiency even under shallow discharge conditions.

**Can be connected in parallel**  
 The batteries can be connected in parallel. Series connection is not allowed. Use in upright position only.



Lithium SuperPack	12,8/20	12,8/60	12,8/100	12,8/100 High current	12,8/200	25,6/50
Chemistry	LiFePO4					
Nominal voltage	12,8 V					25,6 V
Nominal capacity @ 25 °C	20 Ah	60 Ah	100 Ah		200 Ah	50 Ah
Nominal capacity @ 0 °C	16 Ah	48 Ah	80 Ah		160 Ah	40 Ah
Nominal energy @ 25 °C	256 Wh	768 Wh	1280 Wh		2560 Wh	1280 Wh
Cycle life @ 80 % DoD and 25 °C	2500 cycles					
<b>CHARGE and DISCHARGE</b>						
Max. cont. discharge current <sup>(1)</sup>	30 A	30 A	50 A	100 A	70 A	50 A
Peak discharge current (10 sec)	80 A	80 A	100 A	150 A	100 A	100 A
End of discharge voltage	10 V					20 V
Charge voltage, absorption <sup>(2)</sup>	14,2 V – 14,4 V					28,4 V – 28,8 V
Charge voltage, float	13,5 V					27 V
Max. cont. charge current	15 A	30 A	50 A	100 A	70 A	50 A
<b>OPERATING CONDITIONS</b>						
Parallel configuration	Yes, unlimited					
Series configuration	No					
Operating temperature	Discharge: -20 °C to +50 °C    Charge: +0 °C to +45 °C <sup>(3)</sup>					
Storage temperature	-40 °C to +65 °C					
Max. storage time when fully charged	1 year ≤ 25 °C    3 months ≤ 40 °C					
Humidity (non-condensing)	Max. 95 %					
Protection class	IP 43					
<b>OTHER</b>						
Power connection (threaded inserts)	M5	M6	M8		M8	M8
Dimensions (h x w x d) mm	167 x 181 x 77	213 x 229 x 138	220 x 330 x 172		208 x 520 x 269	220 x 330 x 172
Weight	3,5 kg	9,5 kg	14 kg		21 kg	14 kg

1. The battery may disconnect when a load with a high input capacitance is connected, such as an inverter. The battery will however retry and connect after approximately 10 seconds.

2. The absorption period should preferably not exceed 4 hrs. A longer absorption period may slightly reduce service life.

3. Serial number HQ2040 and newer: charge is automatically blocked when the cell temperature decreases below 0±3 °C. It will accept charging again when increased above 3±3 °C. Discharge is automatically blocked when cell temperature decreases below -20±3 °C. This protection resets when temperature above -15±3 °C.

Figure 157 – Datasheet for the used power supply

The power capacity can be calculated according to the following equation.

93)

$$P_c = V \cdot I_c$$

Where:

- $P_c$  is the power capacity in Watt-hours [Wh].
- $V$  is the electrical energy (or voltage) in volts [V]
- $I_c$  is the electrical capacity in ampere-hour [Ah].

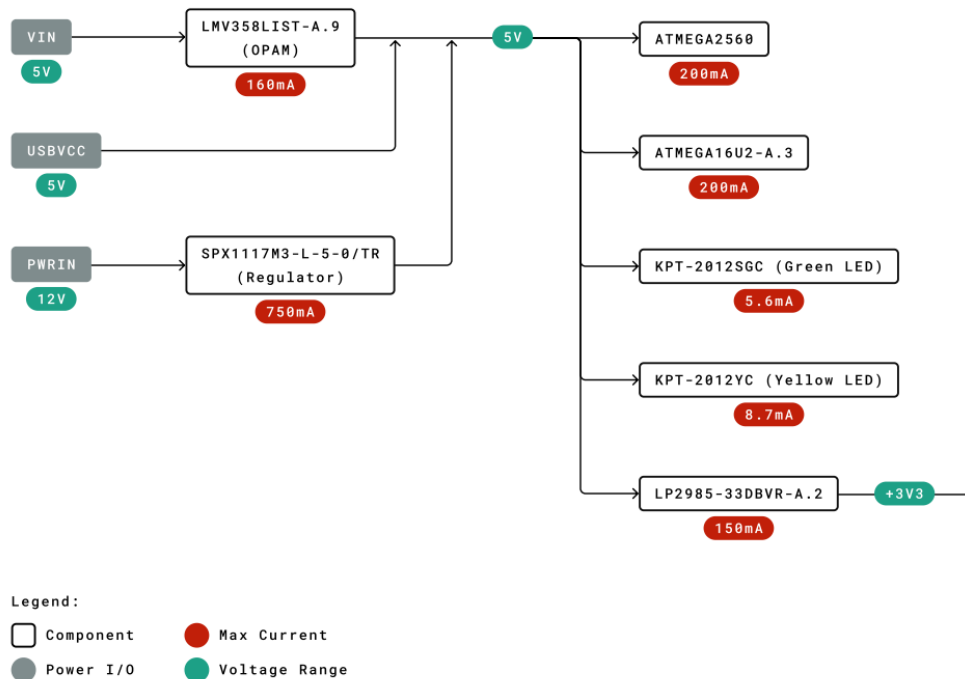
The used power supply has an electrical voltage ( $V$  [V]) equal to 12.8 [V]; and it has an electrical current capacity ( $I_c$  [Ah]) of 60 [Ah]. The power capacity in Watt-hours then becomes 768 [Wh].

Table 40 - Calculation box

$P_c = V \cdot I_c$
$P_c = 12.8 \cdot 60 = 768$ [Wh]

The power (consumption) tree of the Arduino microcontroller is provided below.

### 3.4 Power Tree



Power Tree

Figure 158 - Power tree of an Arduino (Arduino SRL, 2024)

The power supply is connected to the Arduino through the power-jack. The power-jack corresponds to the 12 [V] PWRIN entry in the power tree above. However, an electrical voltage of 12.8 [V] must be used, as a 12.8 [V] power supply is used. Just after the power jack, a regulator is present. This regulator scales down the incoming electrical voltage, through heat losses, towards the operating voltage of the Arduino; i.e., 12.8 [V]  $\rightarrow$  5 [V]. The regulator draws a maximum electrical current ( $I$  [A]) of 750 [mA] from the 12.8 [V] input. The consumed power can be calculated according to the formula below.

94)

$$P = V \cdot I$$

Where:

- $P$  is the electrical power in Watts [W].
- $V$  is the electrical energy (voltage) in volts [V].
- $I$  is the electrical current (amperage) in ampere (amps) [A].

It is assumed that the Arduino consumes the maximum electrical current; which is a safe approach as these conditions are usually not reached.

Table 41 - Calculation box

$P = V \cdot I$
$P_{max} [W] = V [V] \cdot I_{max} [A] = 12.8 [V] \cdot \frac{750 [mA]}{1000} = 9.6 [W]$

The fan is powered by the same 12.8 [V] power supply. Below there is another datasheet of the used fan. To be clear, this is the same fan as in [appendix C.1.1](#). This datasheet is however obtained from the seller where the fan was purchased. This seller still offers the fan to this day. The fan draws a maximum electrical current of 17.1 [A] (i.e., when the speed controller is fully opened).

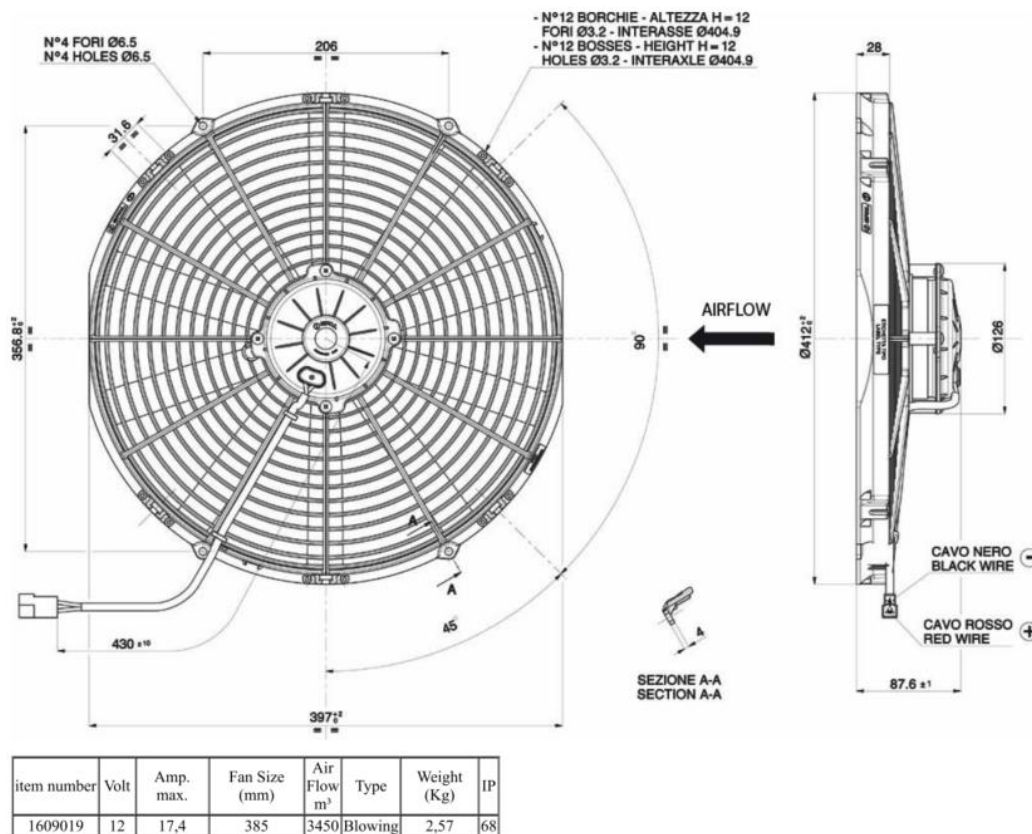


Figure 159 - VA18-AP70/LL-86S datasheet (Venus, 2024)

The maximum electrical power (i.e., drawn by the fan) can now be calculated.

Table 42 - Calculation box

$P = V \cdot I$
$P_{max} [W] = V [V] \cdot I_{max} [A] = 12.8 [V] \cdot 17.1 [A] = 218.88 [W]$



The Arduino consumes about 9.6 [W] and the fan consumes about 218.88 [W]; so, in comparison:

- Relative power consumption → Arduino vs. total

Table 43 - Calculation box

$\frac{P_{Arduino} [W]}{P_{fan} [W] + P_{Arduino} [W]} \cdot 100 [\%]$
$\frac{9.6 [W]}{218.88 [W] + 9.6 [W]} \cdot 100 [\%] = 4.201 \dots \approx 4.20 [\%]$

- Relative power consumption → fan vs. total

Table 44 - Calculation box

$\frac{P_{fan} [W]}{P_{fan} [W] + P_{Arduino} [W]} \cdot 100 [\%]$
$\frac{218.88 [W]}{218.88 [W] + 9.6 [W]} \cdot 100 [\%] = 95.798 \dots \approx 95.80 [\%]$

If the fan consumes about 218.88 [W] and the Arduino consumes about 9.6 [W]; then one can calculate the lifetime of one (battery) discharging-cycle with this setup.

Table 45 - Calculation box

$t [h] = \frac{P_c [Wh]}{P [W]}$
$\frac{768 [Wh]}{228.48 [W]} = 3.361 \dots \approx 3.36 [h]$

This is equal to 3 [h], 21 [min] and a rounded 40.8 [s].

## D Pipe flow analysis

The equations to conduct a pipe flow analysis are provided below (Çengel & Cimbala, 2014).

Table 46 - Pipe flow analysis equations

Minor loss	Major loss
$\Delta p_{minor} = -K_l \frac{\rho u^2}{2}$	$\Delta p_{major} = -f \frac{L}{D_h} \frac{\rho_a u^2}{2}$

The pipe flow analysis will contain loss terms for the honeycomb, the ducts and the outflow. However, the contraction will not contain a term, as it has negligible energy losses.

- $\Delta p_{honeycomb} = -K_l \frac{\rho u^2}{2}$
- $\Delta p_{duct} = -f \frac{L}{D_h} \frac{\rho_a u^2}{2}$
- $\Delta p_{outflow} = -\frac{\rho u^2}{2}$  (i.e.,  $K_l = 1.0$  [-]).

To estimate the friction factor the Moody-Diagram must be used (Engineers Edge, 2024).

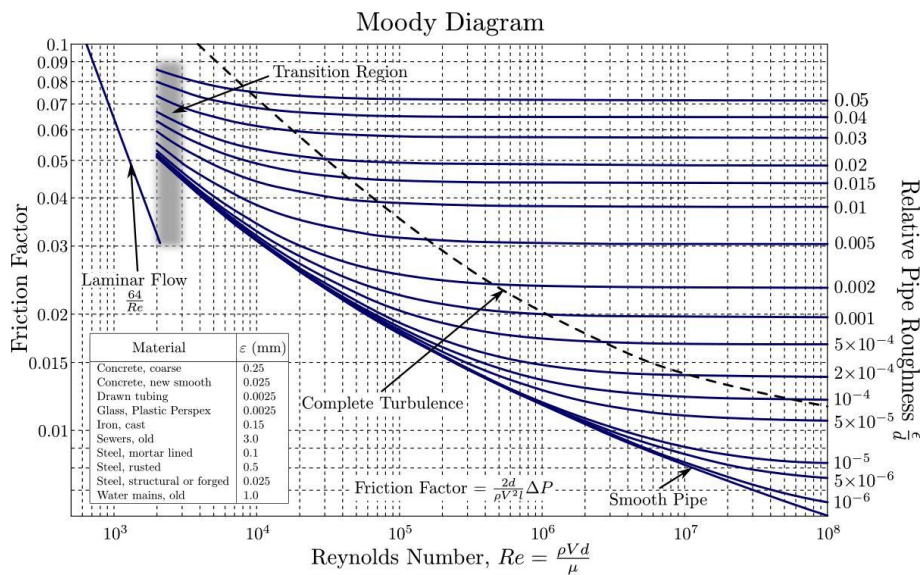


Figure 160 – Moody diagram (Engineers Edge, 2024)

Next, an energy balance must be constructed to perform a pipe flow analysis; where the mentioned terms should be plugged in.

95)

$$p_1 + \frac{\rho_a u_1^2}{2} = p_2 + \frac{\rho_a u_2^2}{2} + \sum \Delta p$$

Solving the pipe flow analyses is done iteratively; and provides an estimate of the pressure losses. This pressure loss can be used in combination with the pressure-discharge relation of the fan (next page; or [appendix C.1.1](#)). In turn, this allows finding the discharge that can still be produced by the fan, according to the pressure losses.

The datasheet of the fan ([appendix C.1.1](#)) contains the fan discharge ( $Q$  [ $m^3/s$ ]) according to the pressure buildup ( $p$  [ $mmH_2O$ ]). [Equation 96](#) is used to convert the units of the pressure from [ $mmH_2O$ ] into [ $Pa$ ]. The mentioned formula calculates (hydrostatic) pressure ( $p$  [ $Pa$ ]), from the density of the fluid ( $\rho$  [ $kg/m^3$ ]), the gravitational acceleration ( $g$  [ $m/s^2$ ]); and the height of the fluid-column ( $h$  [ $m$ ]). The density of fresh water is used ( $\rho_w = 1,000$  [ $kg/m^3$ ]).

96)

$$p = \rho gh$$

Next, the discharge-pressure relation is plotted. The plot also includes curves for two fans in series and in parallel connection ([Rotron, N.d.](#)). This was done in advance of buying an extra fan. Two fans in series, causes having twice the pressure capacity ( $2p$  [ $Pa$ ]), for an equal air flow ( $Q$  [ $m^3/s$ ]). Two fans in parallel, causes having twice the air flow ( $2Q$  [ $m^3/s$ ]), for an equal pressure capacity ( $p$  [ $Pa$ ]). If two fans are connected in series, some spacing is required ([Noctua, N.d.](#)).

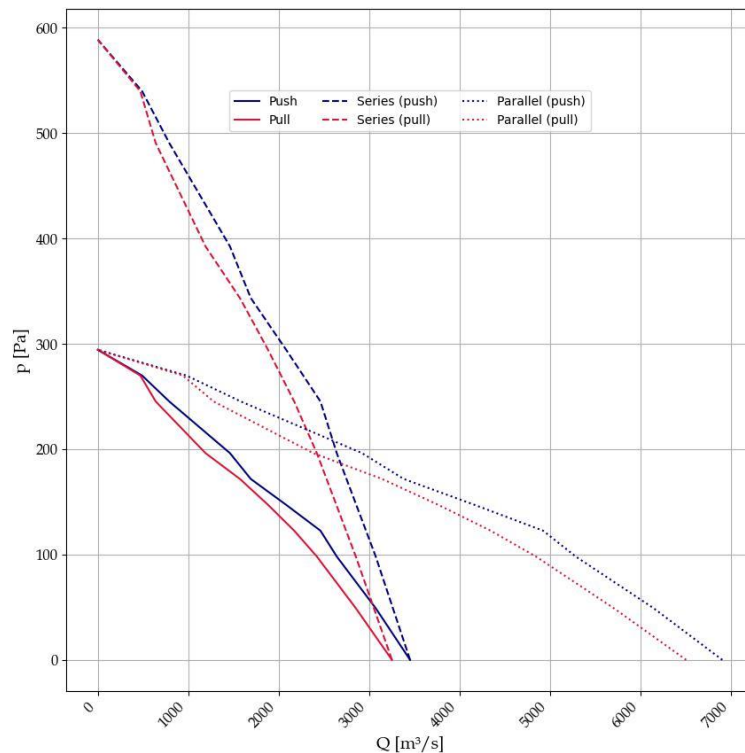


Figure 161 – Va18-ap70ll-86s discharge ( $Q$  [ $m^3/s$ ]) pressure ( $p$  [ $Pa$ ]) relation

## E Handling the pitot tubes

The pitot tube is situated along the horizontal centreline of the duct and can solely be repositioned along the vertical. The pitot tube is embedded in a 3D-printed holder (see the left picture). This holder can be attached in a 3D-printed hatch that is located in the roof of the erosion zone (upper right picture). Additionally, there is a 3D-printed cap as well (see the lower right picture). This cap can be used to seal of the hatch (i.e., mitigating energy losses); when the pitot tube is not in use.



Figure 162

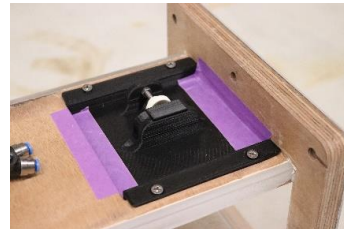


Figure 163

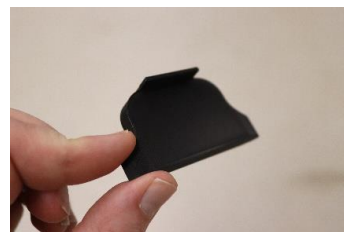


Figure 164

### E.1.1 Levelling the pitot tube

The air within Mobi-Gust 2 flows longitudinally, from the upwind- to the downwind boundary. It is thus safe to assume that the streamlines within Mobi-Gust 2 run parallel to the boundaries of the duct system. It is namely quite straightforward to mount the pitot tubes roughly parallel to the boundaries of the system. To this end, the pitot tube must be positioned against the roof (see the left picture below). In this position the pitot tube is oriented roughly parallel to the boundaries of Mobi-Gust 2; and thus also roughly parallel to the streamlines within Mobi-Gust 2. While the pitot tube still touches the roof, a mini-level must be attached to the pitot tube holder (see the right picture below). Make sure this mini-level shows a levelled (i.e., a flat) reading; even if Mobi-Gust 2 is mounted on a sloping surface. The levelled state of the mini-level then indicates that the pitot tube is mounted parallel to the streamlines within Mobi-Gust 2.

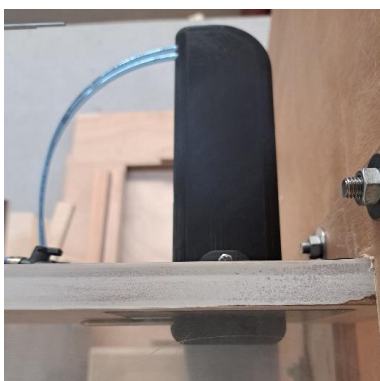


Figure 165



Figure 166

## E.1.2 Repositioning the pitot tube

The holder sticks out of the roof of the erosion zone; which can be used to infer the vertical position of the pitot tube within the duct. This is schematically shown in the sketch below.

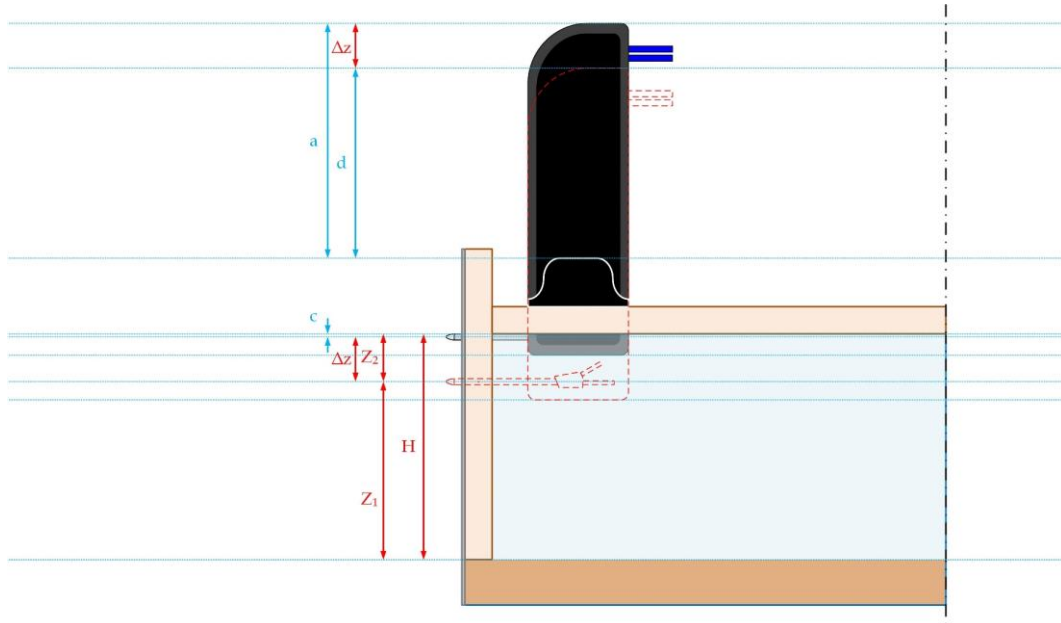


Figure 167 – Visualized distances to deduce relations to reposition the pitot tube

To this end, the pitot tube is positioned against the roof of the duct. The distance between the top of the holder; and the raised plate (i.e., where sealing-cap rests if the pitot tube is not in use) is called the **reference-distance**  $a$ . Next, the cross-section of the pitot tube is circular. Consequently, the stagnation entrance is exactly one radius below the roof of the duct. The radius of the pitot tube is called the **radius-distance**  $c$ . After positioning the pitot tube at the desired height (i.e., which is still an unknown distance), the distance between the top of the holder and the raised plate is called the **position-distance**  $d$ .

Now the pitot tube is lowered into the duct. The stagnation entrance of the pitot tube is lowered over an arbitrary **lowering-distance**  $\Delta z$ . The pitot tube and the holder are part of the same rigid body. Consequently, if the stagnation entrance is lowered a certain **lowering-distance**  $\Delta z$ , then the entire holder has also lowered a certain **lowering-distance**  $\Delta z$ . Next, the difference between the **reference-distance**  $a$ ; and the **position-distance**  $d$  is equal to the **lowering-distance**  $\Delta z$ .

Next, some extra definitions are required to finalize. The height of the duct is called the **duct-height**  $H$ ; the distance between the stagnation entrance and the bottom is called the **bottom-distance**  $Z_1$ ; and the distance between the stagnation entrance and the roof is called the **roof-distance**  $Z_2$ . The **duct-height**  $H$  is equal to the sum of the **bottom-distance**  $Z_1$  and the **roof-distance**  $Z_2$ . Finally, the **roof-distance**  $Z_2$  is equal to the sum of the **radius-distance**  $c$  and the **lowering-distance**  $\Delta z$ . Now that all definitions and relations are clarified, two equalities can be written down.

Distance from the bottom		Distance from the roof	
$\Delta z = Z_2 - c$	$a = \Delta z + d$	$\Delta z = H - Z_1 - c$	$a = \Delta z + d$
$a = \Delta z + d$		$a = \Delta z + d$	
$a = (Z_2 - c) + d$		$a = (H - Z_1 - c) + d$	
$a - (Z_2 - c) = d$		$a - (H - Z_1 - c) = d$	
$d = a - Z_2 + c$		$d = a - H + Z_1 + c$	

After selecting a certain **bottom-distance**  $Z_1$  or **roof-distance**  $Z_2$ , the only unknown is the **position-distance**  $d$ . All the other distances can be determined; i.e., with a calliper. The use of a calliper and the measured distances are shown following sections.



### E.1.3 Using a calliper

The pitot tubes are vertically adjustable. To adjust the pitot tube in elevation an analogue calliper was used. A calliper can measure inside and outside distances; but it can also measure depths. The used calliper had a precision of  $0.02\text{ [mm]}$ . A calliper has a special vernier scale. The Vernier scale is the smaller scale that is located on the slider of the calliper (shown in the picture below). The zero of the vernier scale provides the amount of  $\text{[mm]}$  measured. If the 0 falls in between two values, such as  $20\text{ [mm]}$  and  $21\text{ [mm]}$ , then the value before the comma is equal to the smallest value (i.e.,  $20\text{ [mm]}$ ). The next stripe on the Vernier scale that is collapsing on one of the stripes of the normal scale provides the digits behind the comma; which should be read from the Vernier scale instead of the normal scale. In the picture below a calliper is shown with  $0.05\text{ [mm]}$  precision. The stripe falls exactly on the  $0.7\text{ [mm]}$ ; so the length measured is  $20.70\text{ [mm]}$ . If the second stripe of the vernier scale would have been between  $0.7\text{ [mm]}$  and  $0.8\text{ [mm]}$  then the total measured length would have been  $20.75\text{ [mm]}$ . If the zero of the Vernier scale exactly collapses on a stripe of the normal scale, then the measured length has no digits behind the comma.

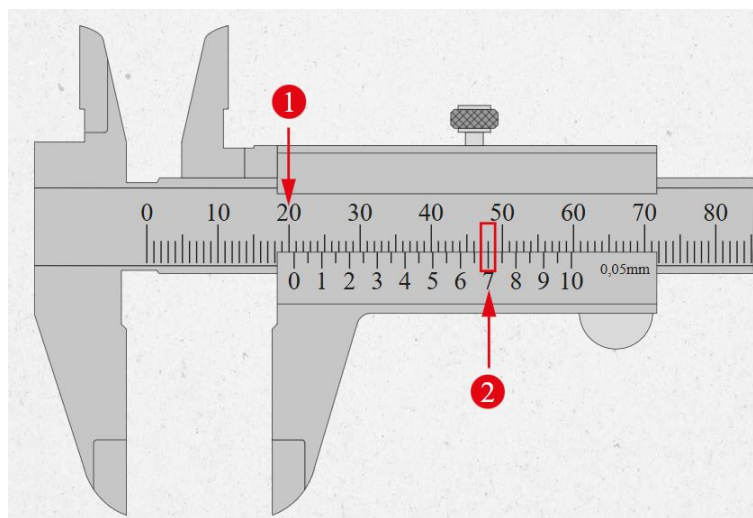


Figure 168 - How to read a calliper (Duursma, N.d.)

### E.1.3.1 Reference height

Upwind pitot tube:  $a = 172.96$  [mm].



Figure 169

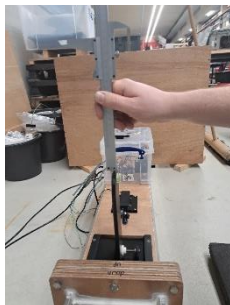


Figure 171

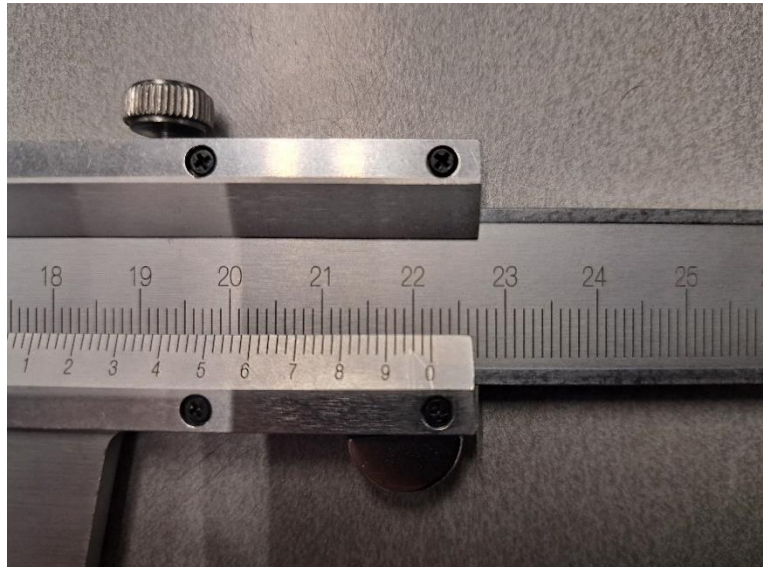


Figure 170

Downwind pitot tube:  $a = 172.56$  [mm].



Figure 172



Figure 174

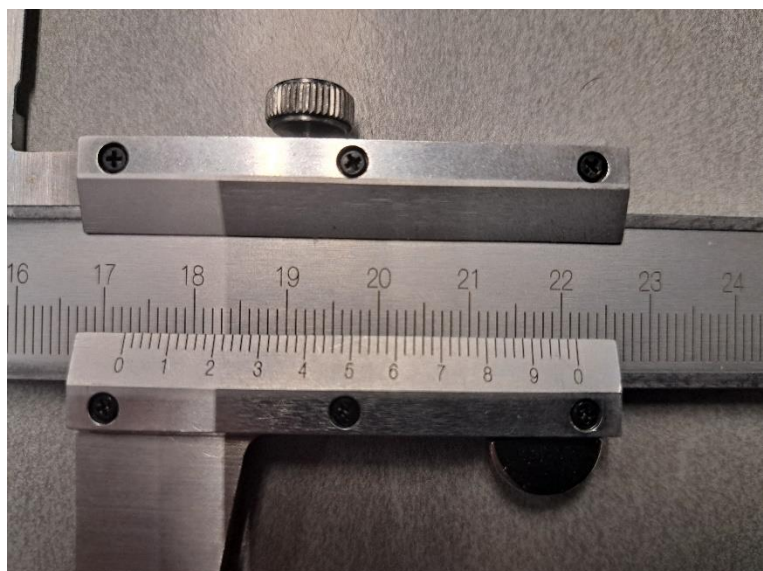


Figure 173

### E.1.3.2 Duct heights

Upwind erosion zone:

- $H_{erosion}^{upwind} = 148.00 \text{ [mm]}$
- Height 'c' is half the pitot tube diameter:  $\frac{1}{2}d_{pitot} = r_{pitot} = 2 \text{ [mm]}$ .
- Centreline height  $\rightarrow d = a - H_{erosion}^{upwind} + c = 172.96 - \left(\frac{148.00}{2}\right) + 2 = 100.96 \text{ [mm]}$ .



Figure 175



Figure 177

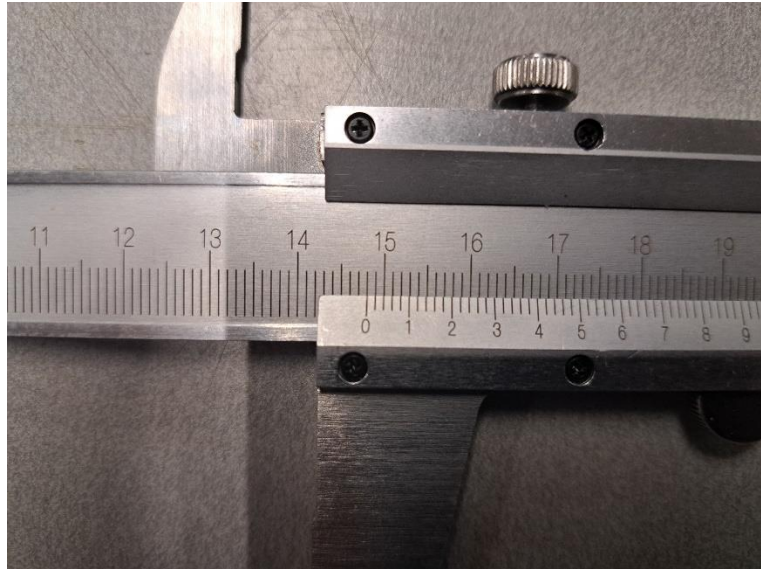


Figure 176

Downwind erosion zone:

- $H_{erosion}^{downwind} = 148.04 \text{ [mm]}$
- Height 'c' is half the pitot tube diameter:  $\frac{1}{2}d_{pitot} = r_{pitot} = 2 \text{ [mm]}$ .
- Centreline height  $\rightarrow d = a - H_{erosion}^{downwind} + c = 172.56 - \left(\frac{148.04}{2}\right) + 2 = 100.54 \text{ [mm]}$ .

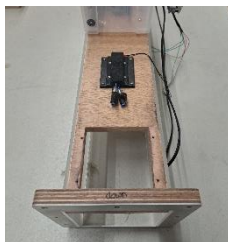


Figure 178



Figure 180

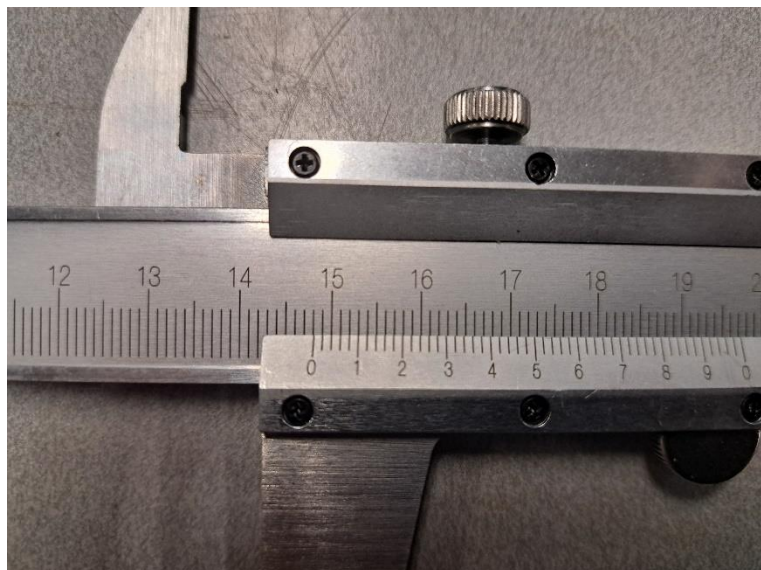


Figure 179



## F Anemometer

All pictures below are taken from (Amazon, N.d.).



Figure 181

Battery Type	CR2032 3.0V
Temperature measurement	NTC thermometer
Relative temperature	-10°C~45°C (14°F~113°F)
Resolution	≤90%RH
Temperature Range	-40°C~60°C (-40°F~140°F)
Current	About 3mA
Weight	53g(with battery land yard)

### SPECIFICATION

Unit	Range	wind speed range		Accuracy
		Resolution	Threshold	
M/s	0-30	0.1	0.1	±5%
ft/min	0-5860	19	39	
Knots	0-55	0.2	0.1	
Km/hr	0-90	0.3	0.3	
Mph	0-65	0.2	0.2	



Figure 182

### YF-816B BASIC FUNCTIONS

- Wind speed measurement
- Temperature measurement
- With a backlight
- Manual/Automatic power-off function
- 5 kinds of wind speed unit selection



Figure 183

### BATTERY REPLACEMENT OPERATION



Figure 184

## G Fieldwork management

### G.1 Preparation plan

#### G.1.1 Date selection

To select a measurement, check the weather frequently. Conditions that are not favourable for measuring with Mobi-Gust 2 are listed below (i.e., learned from experience; [appendix H](#)).

- **Rain.** During or just after a rainy period the sand bed is hard to mobilize; i.e., moisture contents from 2 to 10 [%] might be enough to prevent aeolian erosion.
- **Frost.** It is hard to invoke aeolian erosion during a frost period, as the sand bed might be hard and dry (especially when the frost period follows after a rainy one).
- **Wind.** Wind forces of 5 [*bft*] or higher, complicate the measurements; as they become unpleasant, unpractical and unreliable; and most importantly it might become unsafe.
  - The safety plan treated this; yet during the field expedition of 02-02-2024 winds of > 6 [*bft*] were experienced by accident; i.e., caused by optimistic forecasting and incorrect real-time weather updates (i.e., 4 [*bft*]).

#### G.1.2 Packing list

Table 47

What	Category	Purpose
Intake shield walls	Mobi-Gust 2	Shield the mobile wind tunnel entrance
Fan	Mobi-Gust 2	Propel the air through the mobile wind tunnel
Vertical contraction	Mobi-Gust 2	Accelerate the airflow
Horizontal contraction	Mobi-Gust 2	Accelerate the airflow
Honeycomb screen	Mobi-Gust 2	Minimize the spiral flow produced by the fan
Transition duct (2x); one has the saltation hopper mounted on it	Mobi-Gust 2	Facilitate flow development; add an upwind supply of sand
Erosion duct; it has the wind gauge box* mounted on it	Mobi-Gust 2	Provide the test section for aeolian erosion; measure the wind speed
Sand trap	Mobi-Gust 2	Catch the eroded sediment
Sand trap tray	Mobi-Gust 2	Retrieve the eroded sediment
LiFePO <sub>4</sub> battery and its housing	Mobi-Gust 2	Power Mobi-Gust 2 (i.e., the mobile wind tunnel + the wind gauge system)
Wire mesh cylinder	Mobi-Gust 2	Breaking the (jet) outflow from the erosion zone
(Back-up) Nuts, washers and bolts	Mobi-Gust 2	Connect the parts of Mobi-Gust 2
Batting wood (2x)	Mobi-Gust 2	Place the erosion duct
SD card	Mobi-Gust 2	Log the windspeed data
Box wagon	Transportation	Transport Mobi-Gust 2 and additional gear
Carrying plate	Transportation	Transport Mobi-Gust 2 and additional gear
Lashing strips	Transportation	Secure Mobi-Gust 2 and additional gear
Rubber hammer	Tools	Drive the erosion zone walls into the sand bed
Pliers	Tools	Remove the lids from the saltation hopper
Brush	Tools	Clean equipment
Crosshead screwdriver (2x 100 [mm])	Tools	Open the erosion hatches
Flat screwdriver (3.0 [mm])	Tools	Open the pressure sensor covers
Flat screwdriver (2.5 [mm])	Tools	Adjust the contrast of the LCD-module
Stanley knife	Tools	Cut stuff (e.g., tape)
Combination spanner 13	Tools	(Un)Tighten the connections of Mobi-Gust 2
Ratchet spanner 13	Tools	(Un)Tighten the connections of Mobi-Gust 2
Protection gloves	Safety	Protection while mounting
Stopwatch	Time	Keep track of time
Parking license	Utility	Park at the Schelpenpad

\*The wind gauge box consists of the wind gauge system, i.e., the differential pitot tube; the differential pressure sensor; the Arduino Mega 2650 Rev3 microcontroller; the RTC-, LCD-, SD-modules; tumbler switches (3x); and the speed controller of the fan.



Table 48

What	Category	Purpose
USB cable	Electrical tools	Update or repair the Arduino;
Beach laptop	Electrical tools	Update or repair the Arduino; check the SD card
Multi-meter	Electrical tools	Check the Arduino hardware
Anemometer	Electrical tools	Check the windspeed
Sand scraper	Sediment	Excavate the sand bed in layers
Shovel	Sediment	Excavate the sand bed
Buckets	Sediment	Store the sand
Weighing scale	Sediment	Weigh the sand samples
Zip bags	Sediment	Confine the sand samples
Pre-weighted sandbags	Sediment	Conduct the saltation experiment
Markers	Sediment/notes	Label the sand samples; write notes
GNSS suitcase; this includes a GNSS unit, tablet, batteries (2x) and chargers (2x)	GNSS	Make beach elevation profiles
GNSS pole	GNSS	Make beach elevation profiles
GNSS holder	GNSS	Make beach elevation profiles
TU Delft jacket	Clothing	To be recognizable
Safety jacket	Clothing	To be recognizable
Duct tape	Tape	Repair stuff
Painters tape	Tape	Sealing off gaps
Double sided tape	Tape	Mount levels on the pitot tube; mount electrical hardware of the wind sensing system
Level	Slopes	Level the ducts and other parts
Small levels	Slopes	Level the pitot tubes
Folding ruler	Distances	Measure distances
Roller tape	Distances	Measure distances
Paper	Notes	Write notes
Pen	Notes	Write notes
Pocket calculator	Notes	Make or check (quick) calculations
Mobile phone	Pictures/timekeeping/safety	Take pictures; keep track of time; make emergency calls
Photo camera	Pictures	Take pictures
Differential pitot tube	Arduino backup	Sense differential pressure
Differential pressure sensor	Arduino backup	Sense differential pressure + convert that into voltage output
Arduino Mega 2650 Rev3 microcontroller	Arduino backup	Control the wind gauge system + computations
RTC-module	Arduino backup	Keep track of time
LCD-module	Arduino backup	Display real-time information
SD-module	Arduino backup	Datalogging
Tumbler switch	Arduino backup	Configure the modes of the wind gauge system
Jumper cables	Arduino backup	Provide the electrical connections between the electrical hardware of the wind gauge system
Food and water	Food and drinks	Measurements last the entire day; i.e., you need enough energy
Coffee	Food and drinks	Measurements last the entire day; i.e., you need enough energy
Folding chairs	Comfort	Resting in between experiments

\* The sand scraper includes two steel components; a rubber hammer, a batting wood, a plastic carrying device, a small garden shovel and sandbags.

### G.1.3 Charging the electrical components

Empty the SD-card and charge the following electronics:

- The LiFePO<sub>4</sub> battery.
- The Global Navigation Satellite System (GNSS) batteries (2x) and the tablet.
- The camera.
- The beach laptop.



Figure 185



Figure 186



Figure 187

Print the following documents:

- The Global Navigation Satellite System (GNSS) manual.
- The measurement plan (including the manuals for the wind tunnel system)
- The safety plan.

## G.2 Measurement plan

### G.2.1 Mobility

#### G.2.1.1 Route

##### G.2.1.1.1 TU Delft ↔ Sand Engine

There are three parking lots available (see [appendix A](#)), i.e., *P1* ([Google, 2023](#)), *P2* ([Google, 2023](#)) and *P3* ([Google, 2023](#)). The average distance between Delft University of Technology and the three parking concerns roughly  $21.5 \pm 1$  [km] spread over 3 main routes. The average duration involved is checked around 9AM and 5AM (i.e., rush hours). At 9AM the mean duration concerns about  $33.5 \pm 1.5$  [min]. But the mentioned duration at 9AM can be as low as  $24.5 \pm 1.5$  [min] or as high as  $42.0 \pm 2$  [min]; depending on traffic. At 5PM the mean duration concerns about  $36.5 \pm 2.0$  [min]. But the mentioned duration at 5PM can be as low as  $25.5 \pm 2.0$  [min] or as high as  $48.0 \pm 1.5$  [min]; again depending on traffic. The main choice to park concerns the specialized parking along the Schelpenpad, Monster (location B on the next page). The second car can be parked along the Haagweg (location A on the next page). Parking the second car at location A minimizes interference from the public; and the parking along the Haagweg is free of charge.

The coordinates and addresses are listed below.

- 52°02'34.9"N 4°11'05.0"E; Schelpenpad, Monster.
- 52°02'20.9"N 4°11'26.8"E; Haagweg, 2681 PB Monster.



Figure 188 - Haagweg & parking Schelpenpad (Google, 2022)

#### G.2.1.1.2 Sand Engine ↔ Measurement location

After unloading the car at location B the measurement location (i.e., location C) must be reached. Experience showed that the walk to the measurement location lasts quite long. Amongst others, that is because the box wagon is quite heavy when fully loaded. The walk lasts approximately 30 [min] with a field crew of three people in total.



Figure 189 - Measurement location (Google, 2022)

Measurement will take place at location C because of the following main reasons.

- The relevant parts of the beach concern the supratidal- and the intertidal beach; those areas namely contribute to dune growth.
- Conditions at the beach are expected to be relatively wet everywhere, since it is winter-time in The Netherlands (i.e., low evaporation and moist conditions). So, a somewhat higher elevation is preferred, to have the highest probability for relatively dry conditions.
- The locations just seaward of the embryo dunes contain relatively few shells, pebbles and other non-erodible materials; which is beneficial, as the focus is shifted towards aeolian erosion in relation to the moisture and an upwind supplies of sand.

## G.2.1.2 Transport

### G.2.1.2.1 Packing the car

Table 49




<p>Place the sand trap.</p>	 <p>Figure 190</p>
<p>Fill the box-wagon with a variety of gear (in this case some bags, a laptop, the honeycomb, a GNSS unit and some shovels).</p>	 <p>Figure 191</p>
<p>Load the box wagon, by lifting the sand trap and placing the box wagon underneath it. Next, apply lashing straps to secure everything.</p>	 <p>Figure 192</p>



Table 50

Put the sand tray within the sand trap. By twisting the ropes, extra space is created below the sand trap tray, for the gear that was stored in the previous step. On top of the sand tray some additional equipment can be stored that is preferably not too heavy (i.e., to not damage the aluminium plate).



Figure 193

Put the intake (i.e., the fan and the contractions) besides the box wagon in a tilted manner.



Figure 194

Add the ducts against the box wagon. Next, add the sand trap lid at the side. Then, add the carrying plate; also at the side.



Figure 195

The leftover space can now be filled with the additional gear.



Figure 196



### G.2.1.2.2 Packing the box wagon

Table 51


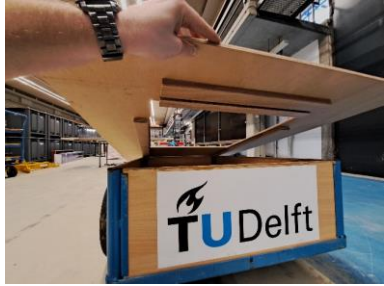

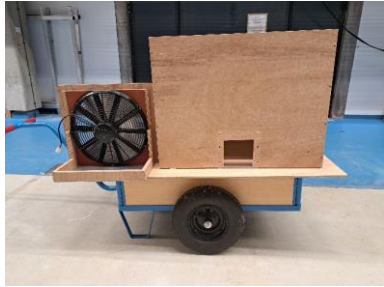
<p>Position the box wagon.</p>	 <p>Figure 197</p>
<p>Place the carrying plate on top of the box wagon. Grooves are carved into the carrying plate, to fit the walls of the box wagon.</p>	 <p>Figure 198</p>
<p>Place the intake (i.e., the fan and the contractions) on the carrying plate. A raised edge is added to the carrying plate, between which the intake fits.</p>	 <p>Figure 199</p> <p>Figure 200</p>
<p>Place the sand trap on the carrying plate, gently against the intake.</p>	 <p>Figure 201</p>

Table 52

Place power supply in the sand trap. The power supply is quite heavy, i.e., use it to balance the box wagon. Next, add other stuff in the sand trap as well.



Figure 202

Place the sand tray in the sand trap. Next, rotate the ropes to elevate the sand tray. This action creates extra space, so that the power supply actually fits below it.



Figure 203



Figure 204

Place the ducts (3x) on the sand trap. Preferably the flanges touch each other.



Figure 205

Use lashing strips to secure the sand trap and ducts to each other.



Figure 206

There is also a lid for the sand trap, which was not included in the pictures. Yet, this sand trap lid can easily be placed on the sand trap like shown below.



*Figure 207*

## G.3 (Dis)Mount Mobi-Gust 2

It is important to correctly setup and use Mobi-Gust 2. The setup of Mobi-Gust 2 consists of (dis)mounting the mobile wind tunnel system; and configuring the wind gauging system.

### G.3.1 Prepare the mobile wind tunnel

First some general remarks. In the manual below, the parts are placed levelled. However, one can also mount the components on a sloping surface. In that case, make sure that every component is equally tilted. To level of components, sand can be added or removed below them (i.e., of course except for the erosion zone). Also, preferably only walk along one side of the mobile wind tunnel system; to enable taking neat pictures from the other side. Before one tightens the components, it is important that contact surfaces (e.g., the flanges) touch completely. For example, check whether there is sand in between (i.e., if so remove it).

#### G.3.1.1 Step 1 – Place the erosion duct

- The erosion duct is a duct without bottom and has hatches in its roof (i.e., these hatches are designed to hold the removable pitot tubes).

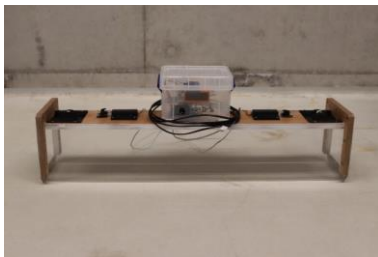


Figure 208

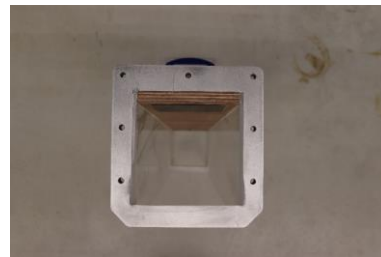


Figure 209

- Place the duct gently on the undisturbed sand surface (i.e., do not yet drive the erosion duct walls into the sand bed).



Figure 210

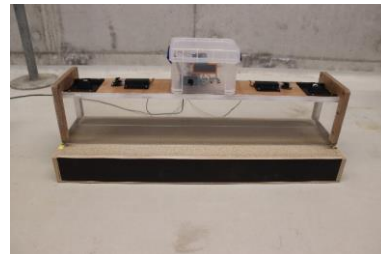


Figure 211



Figure 212

- Place the batting wood on one end of the erosion zone roof; and place a hand on the other end of the erosion duct roof. The hand stabilizes the duct when driving the erosion zone walls into the sand bed (next bullet).



Figure 213

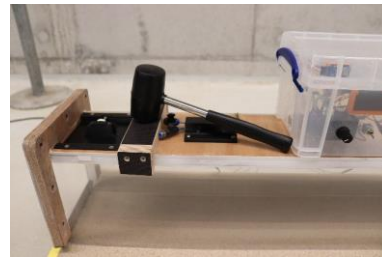


Figure 214

- Drive the erosion duct walls into the sand bed. To do so, use a rubber hammer and strike repeatedly on the batting wood; the stabilizing hand on the other end of the roof helps mitigating lateral displacements of the duct. It is important to swap the batting wood and the stabilising hand regularly; so that the walls subside steadily and evenly into the sand bed; and on top it minimizes the formation of loose sand along the erosion zone walls.

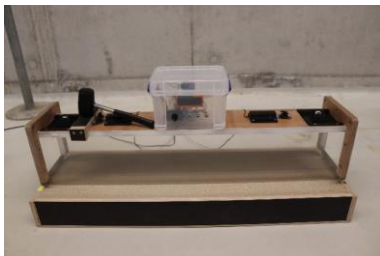


Figure 215

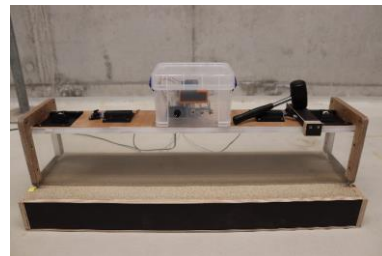


Figure 216

- Stop hammering when the top of the iron strips, that are located on each end of the erosion duct, are levelled with the undisturbed sand bed. In that case the bottom of the sand trap will be levelled with the undisturbed sand bed in the erosion duct. From now on, it is important to not disrupt the sand bed within the erosion duct anymore.

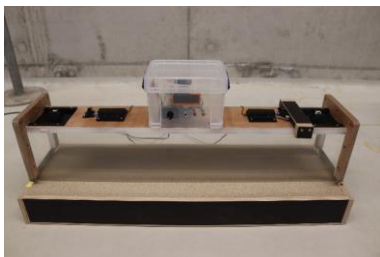


Figure 217



Figure 218

- Make sure the erosion duct is levelled (or as equally tilted as the other parts).



Figure 219

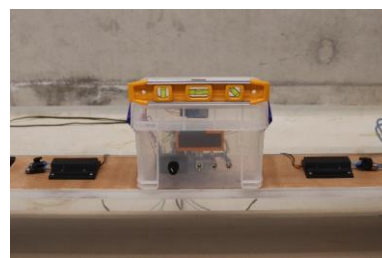


Figure 220



- Carefully excavate a trench at both ends of the erosion duct (i.e., just outside the erosion duct). These trenches help mitigating disturbances to the sand bed within the erosion duct, while mounting the other components.



Figure 221

- Tape the hatches in the roof of the erosion duct to prevent sand- and energy losses.

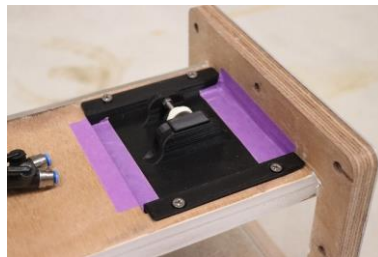


Figure 222

- Check and/or place the lids in the hatches in the roof of the erosion duct (i.e., if applicable) to prevent sand- and energy losses.

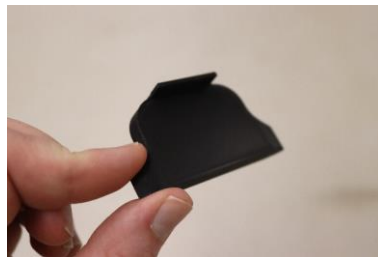


Figure 223



Figure 224

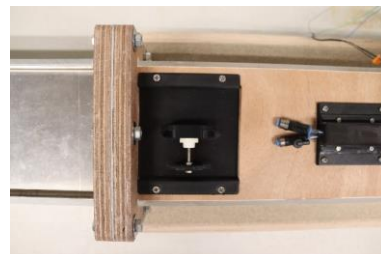


Figure 225

### G.3.1.2 Step 2 – Place the downwind transition duct

- The transition duct is a duct with bottom.



Figure 226

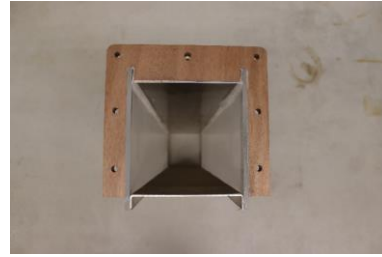


Figure 227

- Construct Mobi-Gust 2 in outward direction. So, place the transition duct gently against the erosion duct; and be careful to not disturb the sand bed within the erosion duct.

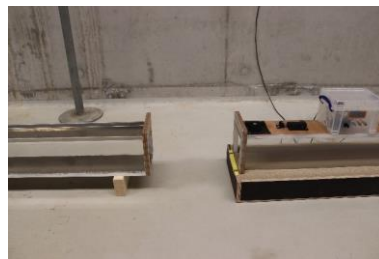


Figure 228

- As said, if the components do not connect well, e.g., due to an uneven beach surface, remove or add sand below the component. If the transition duct needs to be driven a bit into the bed use the batting wood as well. Be careful to not disturb the sand bed within the erosion duct; and try to avoid sand falling into the transition duct. On top, make sure that the contact surfaces between the flanges completely touch (e.g., without sand grains in between); this assists the mounting process and reduces the stress on the flanges.
- Make sure the transition duct is levelled (or as equally tilted as the other parts); and connect the flanges by tightening the hexagon bolts, nuts and washers.



Figure 229



Figure 230



Figure 231

### G.3.1.3 Step 3 – Place the upwind transition duct

- Again, the transition duct is a duct with bottom. Additionally, this upwind transition duct contains the saltation hopper.

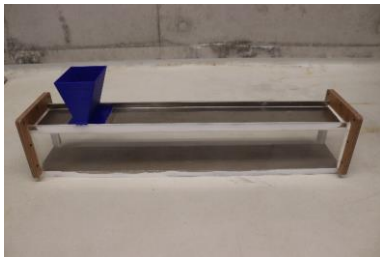


Figure 232

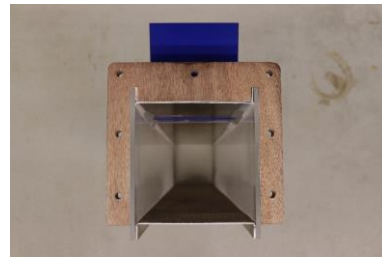


Figure 233

- Place the upwind transition duct against the downwind transition duct; and then follow the same procedure as in the previous step (i.e., placing the downwind transition duct).



Figure 234

- Place a lid in the saltation hopper:
  - Place a lid without gap when the saltation hopper will not be used; to prevent energy losses.
  - Place a lid with gap when the saltation hopper will be used; there are lids with different gap sizes available.



Figure 235



Figure 236



Figure 237

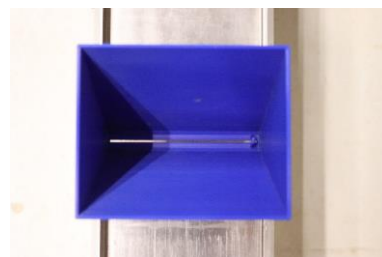


Figure 238

- The lids can be removed in two ways. First of all, a pliers can be used. Second of all, a chord can be attached to the lids, so that it can pulled out later.



Figure 239



Figure 240

#### G.3.1.4 Step 4 – Place the honeycomb screen

- The honeycomb is a 3D printed cross-section divider with squared openings.



Figure 241

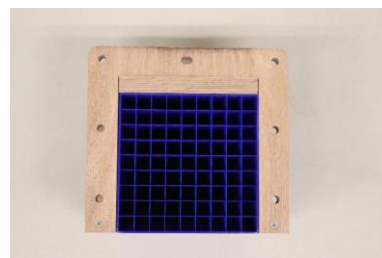


Figure 242

- Place the honeycomb gently against the transition duct.

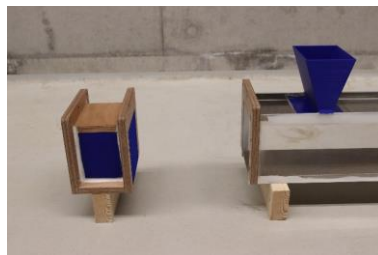


Figure 243

- In repetition, if the components do not connect well, e.g., due to an uneven beach surface, remove or add sand below the component. Next, try to avoid sand falling into the components. Also, make sure that the contact surfaces between the flanges completely touch (e.g., without sand grains in between); this assists the mounting process and reduces the stress on the flanges.
- Make sure the honeycomb is levelled (or as equally tilted as the other parts); and connect the flanges by tightening the hexagon bolts, nuts and washers.



Figure 244



Figure 245

### G.3.1.5 Step 5 – Place the intake (fan and horizontal-/vertical contraction)

- This is the intake, consisting of a fan, a vertical- and a horizontal contraction. These components are tightened 'always' as it is hard to neatly connect them when in the field.



Figure 246

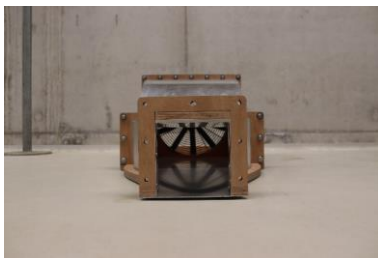


Figure 247



Figure 248

- Place the intake gently against the honeycomb.

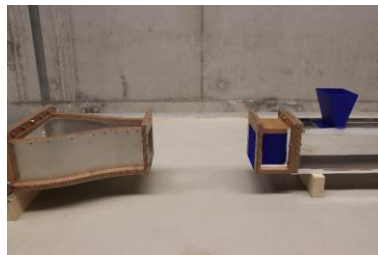


Figure 249

- In repetition, if the components do not connect well, e.g., due to an uneven beach surface, remove or add sand below the component. Next, try to avoid sand falling into the components. Also, make sure that the contact surfaces between the flanges completely touch (e.g., without sand grains in between); this assists the mounting process and reduces the stress on the flanges.
- Make sure the intake is levelled (or as equally tilted as the other parts); and connect the flanges by tightening the hexagon bolts, nuts and washers.



Figure 250



Figure 251



#### G.3.1.6 Step 6 – Place the fan shield (if there is surrounding aeolian transport)

- This is the fan shield; i.e., removable wooden walls. These walls can be used to (partly) shield the intake from the sand-laden ambient winds. Preferably, this part is not in use.

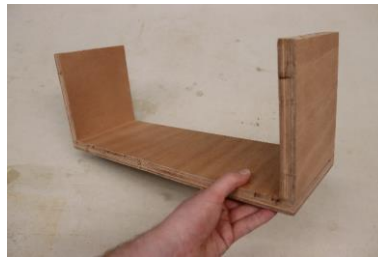


Figure 252

- Place the fan shield against the intake; if required.



Figure 253



Figure 254

#### G.3.1.7 Step 7 – Place the sand trap

- This is the sand trap; i.e., a large hollow crate.



Figure 255



Figure 256

- Place the sand trap gently against the erosion duct.



Figure 257

- In repetition, be careful to not disturb the sand bed within the erosion duct. Also, make sure that the contact surfaces (i.e., between the flange of the erosion duct and the wall of the sand trap) completely touch (e.g., without sand grains in between); this assists the mounting process and reduces the stress on the flange.

- Make sure the sand trap is levelled (or as equally tilted as the other parts); and connect the flanges by tightening the lock bolts, nuts and washers. To facilitate the levelling process, the sand trap lid can be temporarily placed.



Figure 258



Figure 259



Figure 260



Figure 261

- Place the sand trap tray within the sand trap. After placing the sand trap tray, sometimes the bottom of the erosion duct does not connect neatly to the bottom of the sand trap tray (e.g., due to an unlevelled sand surface). Fix this by excavating a shallow pit (i.e., a few [mm] to [cm]) inside the sand trap. In this way, the sand trap tray will always be levelled with the sand bed within the erosion duct, as it is suspended inside the sand trap by steel plates. Again, be careful to not disturb the sand bed within the erosion duct.

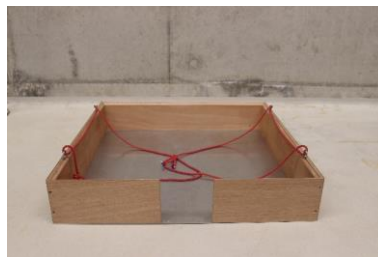


Figure 262



Figure 263



Figure 264

- Tape the transition between the erosion duct and the sand trap to prevent sand losses.



Figure 265

- Tape the edges of the sand tray inside the sand trap to prevent sand losses.



Figure 266



Figure 267

- Place the wire mesh cylinder that breaks the jet flow exiting the erosion duct; ultimately, to prevent sand losses. Be careful to not place it too close to the exit of the erosion duct, as this affects the achievable wind speeds within Mobi-Gust 2 due to (partial) blockage.



Figure 268



Figure 269

- Place the sand trap lid. This sand trap lid is only placed temporarily, in order to determine the zero offset and -drift of the wind gauging system. The ropes of the sand trap tray can be temporarily stored within the sand trap; so that the sand trap lid fits neatly on the sand trap.



Figure 270



Figure 271

### G.3.1.8 Step 8 – Place the $\text{LiFePO}_4$ battery

- This is the  $\text{LiFePO}_4$  battery, with its wooden protection box. The battery must always be kept in this box, e.g., to mitigate battery corrosion; i.e., which is important for battery performance, as well as safety.



Figure 272



Figure 273

- Place the  $\text{LiFePO}_4$  battery in the vicinity of the wind gauging system and the fan.



Figure 274

- Connect the  $\text{LiFePO}_4$  battery to the wind gauging system. The required plug is situated at the backside of the plastic box of the wind gauging system, located on the erosion duct.



Figure 275

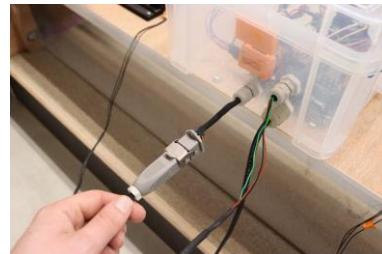


Figure 276

- Connect the  $\text{LiFePO}_4$  battery to the fan. The required plug is attached to the fan.



Figure 277



Figure 278

## G.3.2 Prepare the wind gauge system

### G.3.2.1 Step 1 – Place the pitot tube

- Unscrew the hatch in the roof of the erosion duct; and remove them (see [appendix E](#)).
- Place a pitot tube in the removed hatch; and do not place the hatch back just yet.
- Connect the PVC-tubing between the pitot tube and the pressure sensor, by means of a coupler (see [appendix E](#)).
- Check if the PVC-tubing is connected correctly. The check involves switching on the wind gauging system; and waiting for the offset determination to finish. Next, blow into the pitot tube; and check the received values (i.e., on the LCD-module).
  - When the returned values are positive, the system is configured correctly.
  - When the returned values are negative, the system is configured incorrectly. In that case disconnect the PVC-tubing and swap them.
- Place back the hatch in the roof of the erosion duct (see [appendix E](#)).
- Position the pitot tube at the correct elevation (see [appendix E](#)).
- Make sure the pitot tube is levelled (or as equally tilted as the other components), by checking the mini level attached to it (see [appendix E](#)).

### G.3.2.2 Step 2 – Place the SD-card

- Place the SD-card in the SD-module. This SD-module is located within the plastic box of the wind gauging system, located on the erosion duct.

### G.3.2.3 Step 3 – Configure the mode and determine the pressure sensor offset

- It is repeated to place the sand trap lid. This sand trap lid is only placed temporarily, in order to determine the zero offset and -drift of the wind gauging system. The ropes of the sand trap tray can be temporarily stored within the sand trap; so that the sand trap lid fits neatly on the sand trap.
- Configure the wind gauging system into the desired mode and wait for the offset to be determined automatically ([appendix C.2.3](#)).
- The experiment may now start. Mind removing the sand trap lid.



## G.4 Experimental setup

### G.4.1 Favourable conditions

The figures within this section show a sandy shoreline with a dune row. This coastal profile is not universal (!); but common for The Netherlands. The erodibility near the waterline and near the dunes will be different. The approach assumes similar erodibility for measurements carried out close to each other; and dissimilar erodibility for measurements carried out further away from each other. From a general point of view (e.g., regarding the distribution of salt, moisture, grain sizes, armouring patterns, benthos or vegetation) this might be justified. Yet, there is of course always natural variability present; and the site of interest (i.e., the Sand Engine) is also not a conventional shoreline. Some additional procedures are carried out to quantify the erodibility; i.e., quantifying [moisture content](#) (i.e., by weighing wet and dry sand samples), [grain size distributions](#) (i.e., by sieving sand samples) and exploring other [environmental](#)- and [bed characteristics](#) (i.e., by taking notes and pictures). On top, the test site around Mobi-Gust 2 can be shielded from [solar radiation](#) or [winds](#), respectively by parasols or wind shields.

#### G.4.1.1 Experiment one

This experiment involves multiple locations along a transect (see figure below). This experiment might reveal (possible) gradients in the erosion flux along the cross-shore. On top, this experiment provides an idea of what to expect later on.

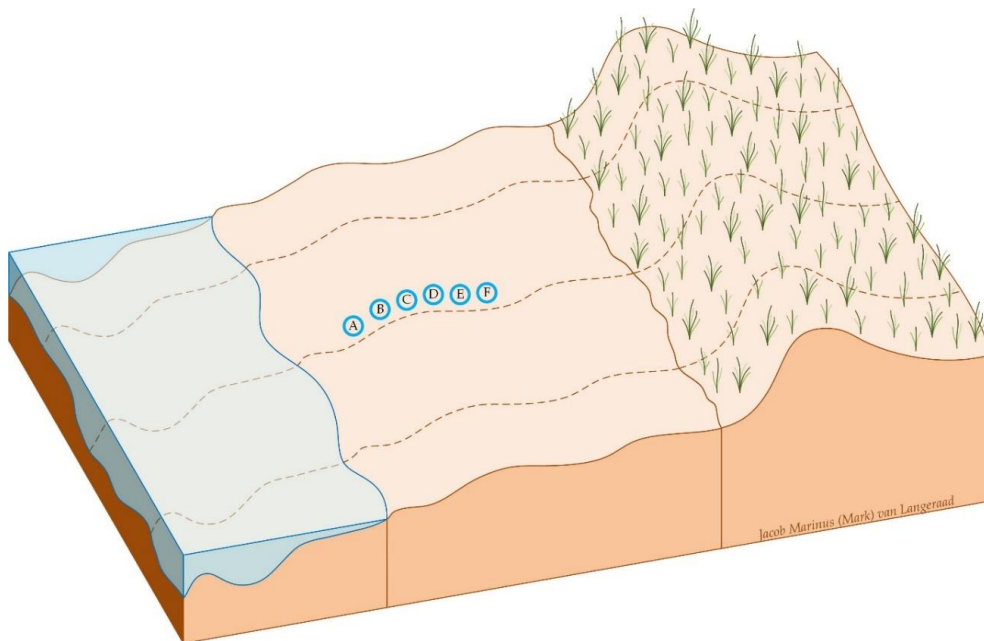


Figure 279 – Experiment one

#### G.4.1.2 Experiment two

This experiment targets to measure the erodibility. To do so, the erosion flux ( $E$ ) is used to measure this erodibility ( $e$ ); as the wind speed ( $u$ ) is controlled (i.e., kept as constant as possible). In its most elementary form there are two general experimental types.

1. Type 1 consists of two experiments performed at two nearby sites in the cross-shore. The two sand beds of (supposedly) similar erodibility ( $e_1 \cong e_2$ ) are mobilised with dissimilar wind speeds ( $u_1 \neq u_2$ ). E.g., perform tests at site A vs. B or C vs. D (next page).
2. Type 2 consists of two tests conducted at two distant sites in the cross-shore. The two sand beds of (supposedly) dissimilar erodibility ( $e_1 \neq e_2$ ) are mobilised with similar wind speeds ( $u_1 \cong u_2$ ). E.g., perform tests at site A vs. C or B vs. D (next page).

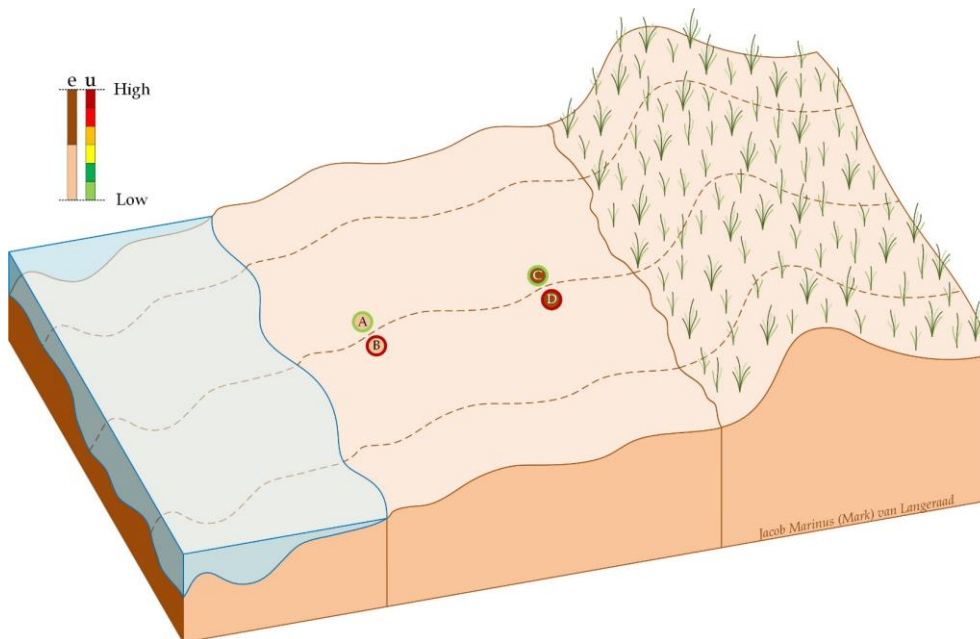


Figure 280 – Experiment two

If the erodibility ( $e$ ) really controls the erosion flux ( $E$ ) along a sandy shores; i.e., rather than the wind speed ( $u$ ); experimental type 1 should result in comparable erosion fluxes ( $E_1 \cong E_2$ ); while experimental type 2 should result in incomparable erosion fluxes ( $E_1 \neq E_2$ ).

Table 53

Type	Strength	Force	Outcome
1	$e_1 \approx e_2$	$u_1 \neq u_2$	$E_1 \approx E_2$
2	$e_1 \neq e_2$	$u_1 \approx u_2$	$E_1 \neq E_2$

#### G.4.1.3 Experiment three

If the experiments are successful; carry out as many experiments as possible (see below).

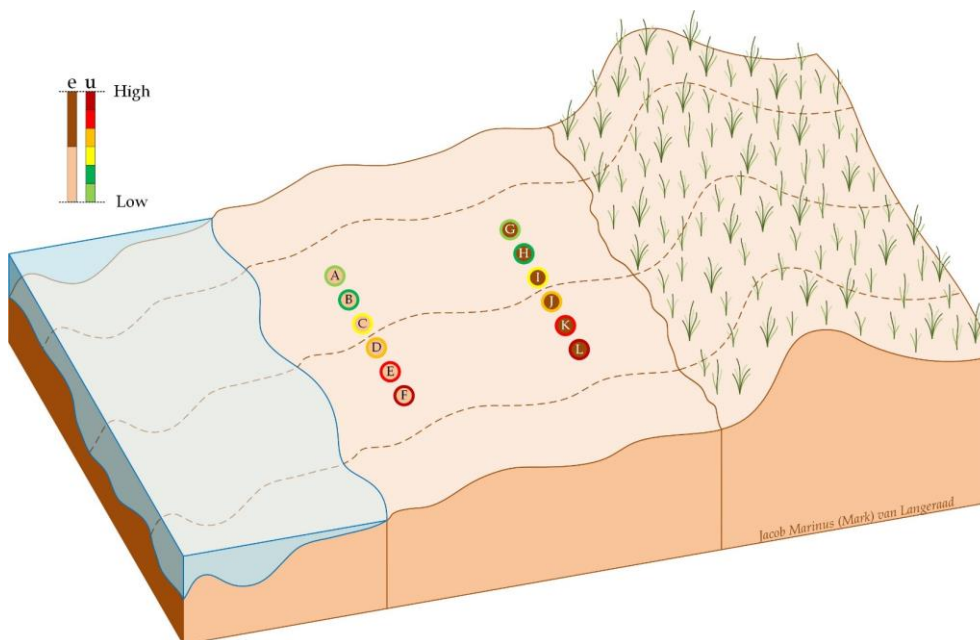


Figure 281– Experiment three

As the measurements contain time intervals, timeseries of the erosion flux are obtained. The different measurements can thus be statistically compared in order to form conclusions.

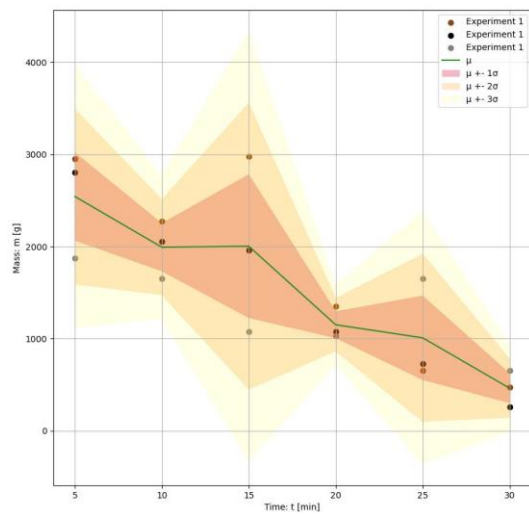


Figure 282 – Timeseries of the erosion mass + statistics

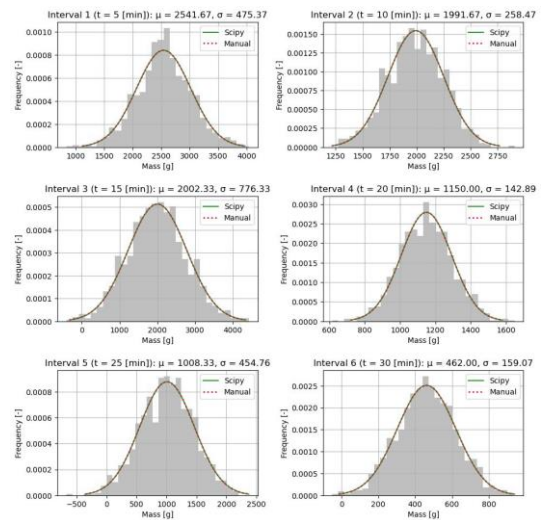


Figure 283 – Statistics of the erosion mass

## G.4.2 Hampering conditions

The table below shows the tests to be conducted during the field expedition and the measurement location is shown below the table.

Table 54 - Tests to be conducted

Experiment [–]	Saltation sand	Wet surface	Excavation	Duration [min]	Intervals [min]
Field I	No	Yes	Yes	10	0
Field II	No	Yes	No	10	0
Field III	Yes	Yes	No	10	0



Figure 284 - Measurement locations (Google, 2022)

When arrived at location I, perform Field I.

Table 55 – Measurement schedule

Step	1	2	3
Action	Choose a location for the erosion duct and place it on the sand surface; do not start mounting Mobi-Gust 2 just yet.	Use the GNSS-unit according to the <b>manual</b> to log the measurement location.	Mark a 1 by 1 [m] space (e.g., using folding rulers) on the sand surface and take a picture of the sand bed.
Time	5 [min]	10 [min]	5 [min]
Step	4	5	6
Action	Take a moisture content sample, i.e., by digging a small hole in the sand surface; and collect the sand in a sample bag.	Mount Mobi-Gust 2 (i.e., the mobile wind tunnel + the wind gauging system) according to the <b>manuals</b> .	Start Field I (or Field II); and mind the timekeeping.
Time	5 [min]	40 [min]	10 [min]
Step	7	8	9
Action	After 10 [min] stop the experiment; and collect the sand from the sand trap in a sample bag.	Dismount Mobi-Gust 2 (i.e., the mobile wind tunnel + wind gauging system)	If Field I is performed, then excavate the sand bed afterwards; and make use of the sand scraper! Sand pit volume: $V = L \cdot B \cdot H$ $V = 1.10 \cdot 0.30 \cdot 0.10 [m^3]$
Time	5 [min]	30 [min]	10 [min]

Following experiment Field I a lunch break can be held. On top, use the Global Navigation Satellite System (GNSS) unit (i.e., create a beach elevation profile, by walking a beach transect). If the time goes faster than expected, then move the lunchbreak behind the following activities. When arrived at location II, perform experiment Field II (see the previous table; except for action 8 and 9); and then perform experiment Field III (see the next table).

Table 56 – Measurement schedule

Step	1	2	3
Action	Leave Mobi-Gust 2 where it was mounted during Field II; i.e., do not reposition it!	Start Field III; mind the timekeeping; and inject sand into Mobi-Gust 2 through the saltation hopper (i.e., 15 sample bags of 1 [kg] sand for a test of 10 [min])	After 10 [min] stop the experiment; and collect the sand from the sand trap in a sample bag.
Time	5 [min]	10 [min]	5 [min]
Step	4	-	-
Action	Dismount Mobi-Gust 2 (i.e., the mobile wind tunnel + wind gauging system)	-	-
Time	30 [min]	-	-

Go measuring at location III or go home:

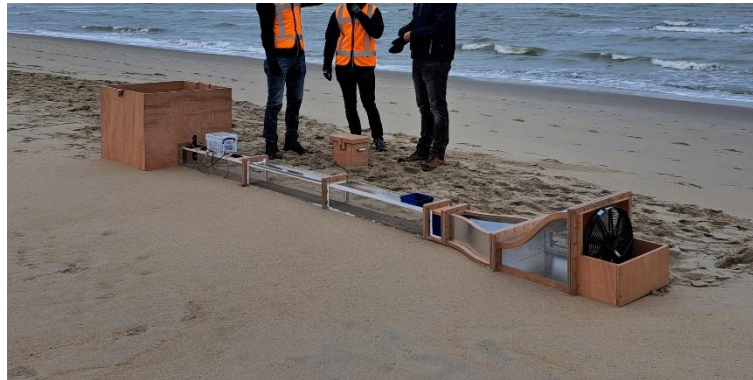
- After the experiments above it is desired to measure for 30 [min] straight and add time intervals to these tests. Yet, it might also be time to go home; as the desired tests are quite lengthy, while the other activities are also quite lengthy: i.e., transporting the gear to the car (~30 [min]); unpacking the box wagon and loading the car (~ 30 [min]); and driving towards home (~ 1 [h]); tidying and cleaning equipment (~ 30 [min]).
- But if there is some time left, then start extra tests at Location III. The plan is virtually the same as at locations I and II; only now the tests last 30 [min] with 5 [min] intervals.



## H Conducted field trips

### H.1 Field trip 12-12-2023

On the 12<sup>th</sup> of December Mobi-Gust 2 left the laboratory for the very first time. This field expedition mainly focussed on learning how to use Mobi-Gust 2 in-situ. The sand surface was in general wet and compact; following a relatively rainy period. Mobi-Gust 2 could not generate aeolian erosion on this sand surface. The deployment of Mobi-Gust 2 is visible below. The outdated saltation hopper is also visible. This hopper was redesigned following this very expedition, since it was too low (i.e., too little sand fits in it), too wide (i.e., you only need a small gap to discharge the sand); while the horizontally sliding hatch easily jams due to sand grains.



*Figure 285 – Test deployment of Mobi-Gust 2 on 15-12-23*

### H.2 Field trip 12-1-2024

A second attempt was initiated a month later; on the 12<sup>th</sup> of January. This expedition was initiated following a brief period of relatively calm and dry weather; after weeks of rain. It was hoped that the few calm and dry days initiated some sand surface drying. While the sand surface was still generally wet and compact; an immobile sand bed was coated by a very thin, relatively dry and loose top layer. Mobi-Gust 2 was able to partly mobilize this top layer; within the first few seconds of a faulty experiment. Unfortunately, the data was flawed, as it began to rain. While the electrical hardware is protected in a splash-waterproof box; the expedition got cancelled. On top, rain is also not accommodating the aeolian field measurements themselves.



*Figure 286 – Deployment of Mobi-Gust 2 on 12-1-24*

### H.3 Field trip 2-2-2024

The third field expedition was conducted on the 2<sup>nd</sup> of February. This attempt was conducted in the calmest and driest period; compared to the other attempts. However, also this expedition got aborted. The expedition was cancelled due to strong ambient winds; which resulted in unpractical and dangerous situations; as well as unreliable results. Preceding the expedition, winds around 4 [bft] were forecasted. However, once on the beach the ambient winds already felt quite strong. On top, there was ambient aeolian transport occurring on the beach. At its peak, a saltation layer of several centimetres was visible. The decision was however made to continue the expedition. This decision was fuelled by reassuring weather updates (i.e., 4 [bft]) and the hunger to produce valid measurements. The sand surface within Mobi-Gust 2 was moved a bit in the first experiment. Yet, shielding entrance of Mobi-Gust 2 from the ambient sand-laden winds proved to be virtually impossible. Also, the fan seemed to be affected by these ambient winds (i.e., later on it was found that loose battery connections were also responsible for this observation). As Mobi-Gust 2 got buried increasingly, the call was made to cancel the expedition. The gathered results were in the end unusable as well. As said, the influx of sand from outside was close to unmitigable, affecting the erosion experiments. In hindsight, ambient winds exceeded 6 [bft] during the expedition.



Figure 287 – Deployment of Mobi-Gust 2 on 2-2-24

### H.4 Field trip 14-2-2024

The beach was visited once again on the 17<sup>th</sup> of February. This was the final attempt to gain usable and reliable field data. This expedition proved to be a success. During this expedition, the beach surface was initially wet and compact. However, as the day progressed, temperatures rose, while the sun began to shine every now and then. These weather conditions made sure the sand bed partially dried during the day. Mobi-Gust 2 was able to mobilise the sand surface just a little bit on its own. Yet, the involved quantities were so small, that they were virtually meaningless. However, when the saltation hopper was used, relatively strong erosion was generated.



Figure 288 – Deployment of Mobi-Gust 2 on 17-2-24

# I Results

## I.1 Measuring frequency (Arduino)

```
void setup() {
    // Setup serial communication (speed):
    Serial.begin(9600);
}

void loop() {
    // determine the start-time and print result:
    long int t_start = millis();
    Serial.print("t (start) = "); Serial.print(t_start); Serial.println("
[ms]");

    // add whatever task, whose time needs to be measured:
    Serial.println("Hello World!");
    delay(10);

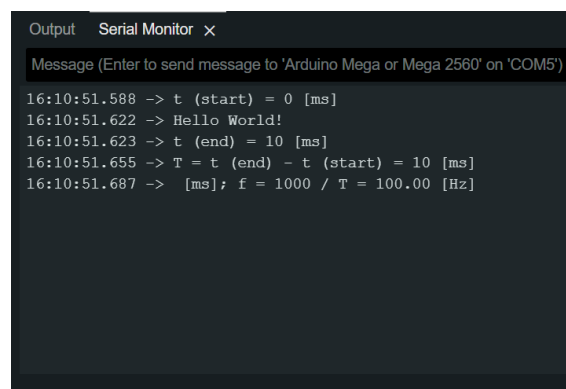
    // determine the end-time and print result:
    long int t_end = millis();
    Serial.print("t (end) = "); Serial.print(t_end); Serial.println(" [ms]");

    // determine the period and print result:
    long int T_task = t_end - t_start;
    Serial.print("T = t (end) - t (start) = "); Serial.print(T_task);
    Serial.println(" [ms]");

    // determine the frequency and print result:
    float f_task = 1000 / T_task;
    Serial.print(" [ms]; f = 1000 / T = "); Serial.print(f_task);
    Serial.println(" [Hz]");

    // add a while loop to trap the code (handy for debugging):
    while(1) {

    }
}
```



The screenshot shows the Serial Monitor window with the following output:

```
16:10:51.588 -> t (start) = 0 [ms]
16:10:51.622 -> Hello World!
16:10:51.623 -> t (end) = 10 [ms]
16:10:51.655 -> T = t (end) - t (start) = 10 [ms]
16:10:51.687 -> [ms]; f = 1000 / T = 100.00 [Hz]
```

Figure 289 – Output in the Serial Monitor of the Arduino IDE software

## I.2 Wind speed data

### I.2.1 Power supply and wind gauging system

The raw datasets of the entire experiments are shown below. The first test that was conducted is shown in figure 290 and the second one is shown in figure 291.

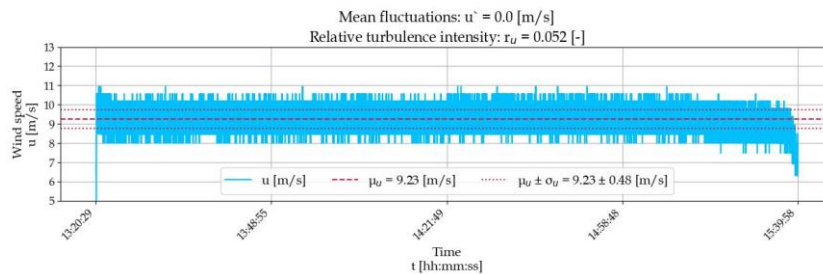


Figure 290 – First durability experiment

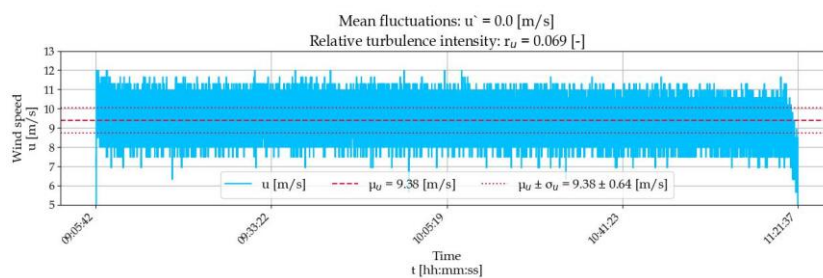


Figure 291 – Second durability experiment

The datasets were trimmed (i.e., between the first and last time the mean wind speed was exceeded); resulting in figure 292 and figure 293.

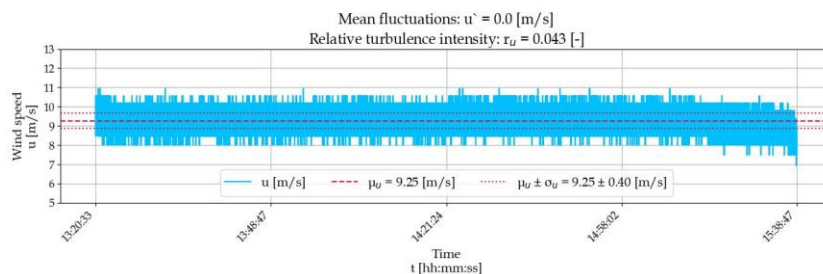


Figure 292 – First durability experiment trimmed

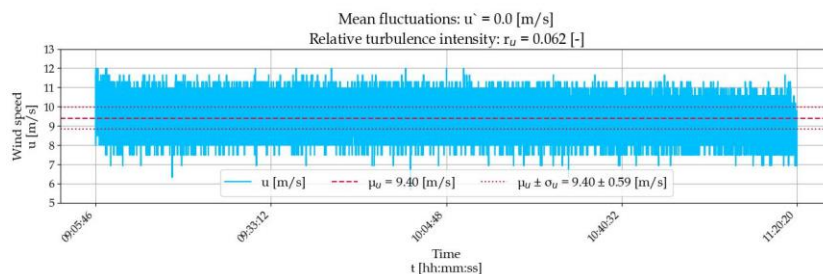


Figure 293 – Second durability experiment trimmed

Moving averages over one-second periods are shown in [figure 294](#) and [figure 295](#).

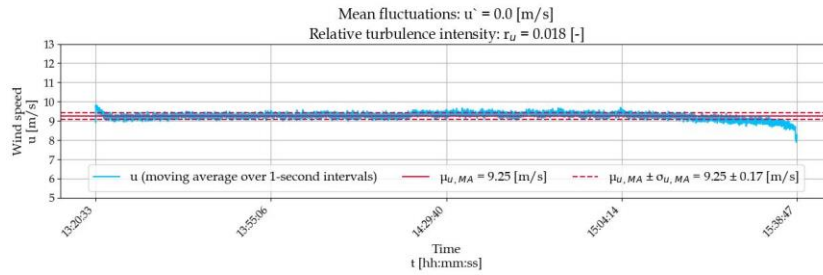


Figure 294 – Moving average of the first durability experiment

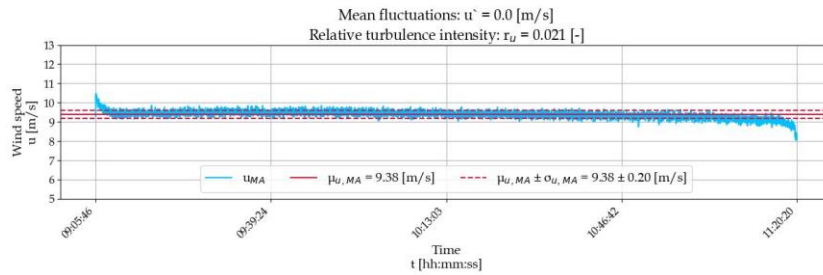


Figure 295 – Moving average of the second durability experiment

The isolated periods originate from the second test ([figure 291](#)). The first test was namely compromised by loose connections (i.e., between the power supply and the electrical systems).

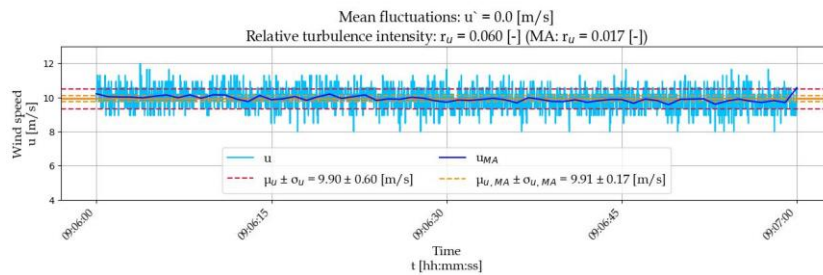


Figure 296 – Isolated timeframe around the start of the second experiment and its moving average (figure 293)

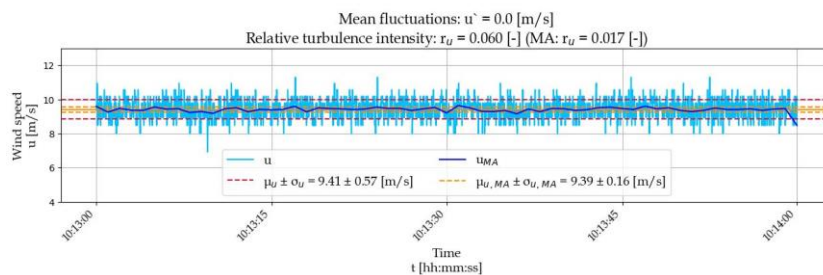


Figure 297 – Isolated timeframe around the centre of the second experiment and its moving average (figure 293)

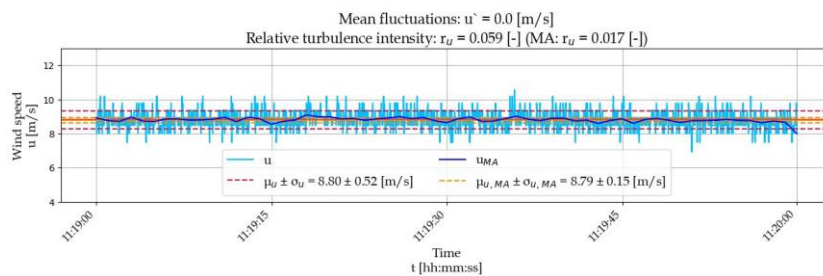


Figure 298 – Isolated timeframe around the end of the second experiment and its moving average (figure 293)



## 1.2.2 Wind speed vs. modular design

The raw datasets of all experiments are provided in [figure 299](#).

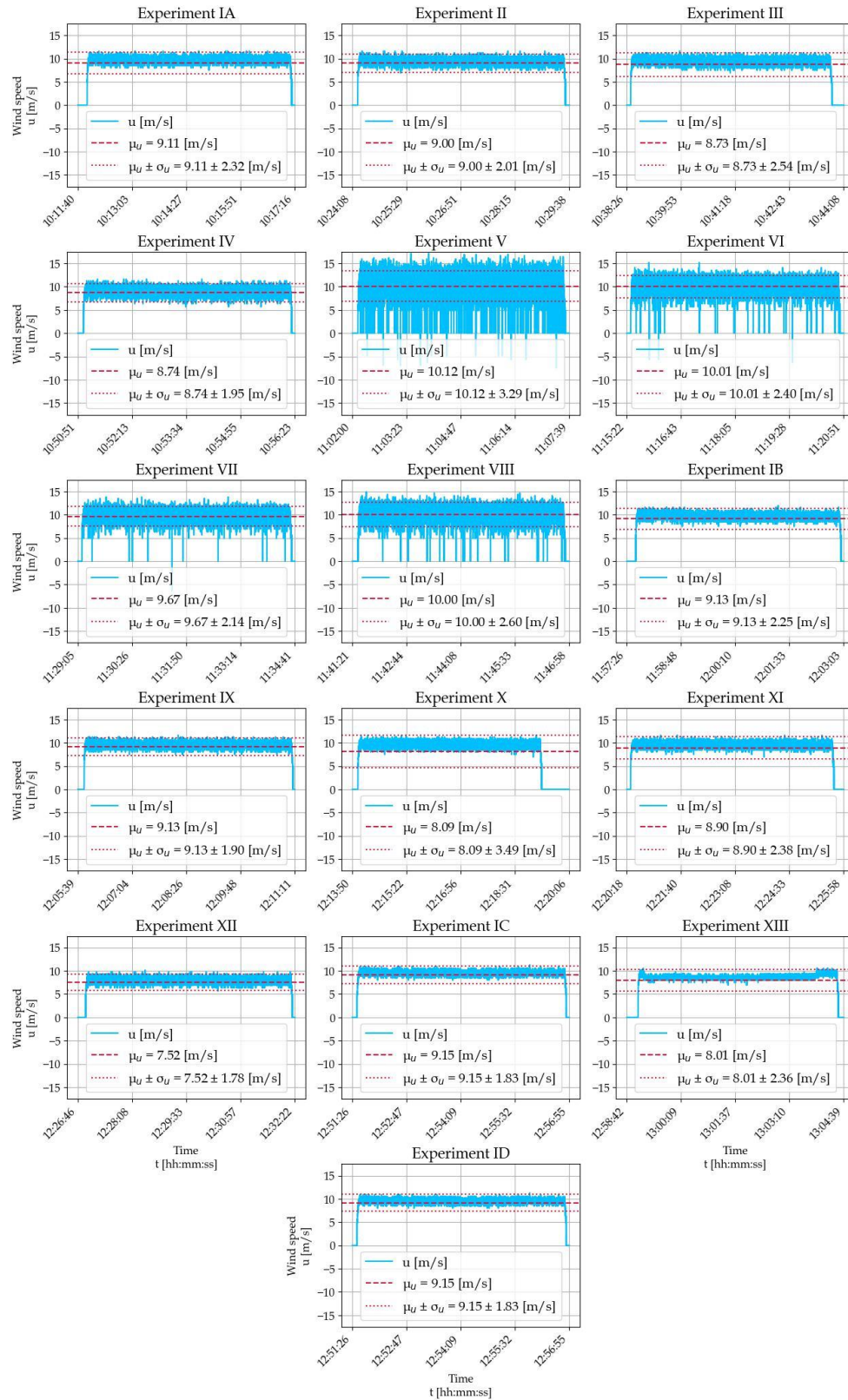


Figure 299 – Raw wind speed data as used in the speed-component test

After selecting appropriate periods, with a duration of 1 [min], the datasets were trimmed; and subsequently moving averages were determined over one-second periods. This results in the graphs provided in figure 300. The statistics of the moving averages are not added for clarity purposes; but these can be found in the main report (e.g., §2.3.5).

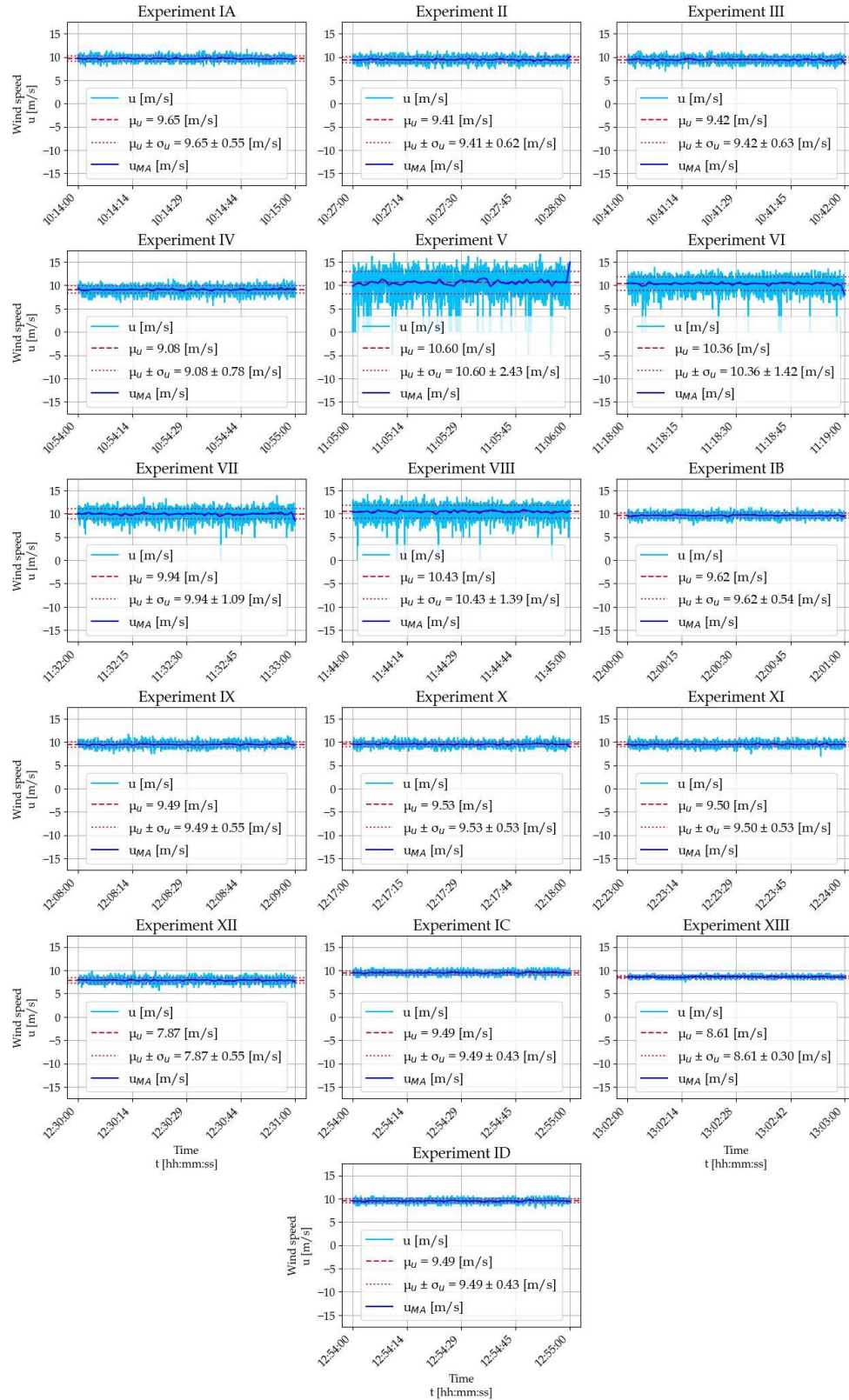


Figure 300 – Isolated and averaged wind speed data as used in the speed-component test

### 1.2.3 Velocity profiles

The raw and averaged datasets, with which the velocity profiles are constructed, are shown below.

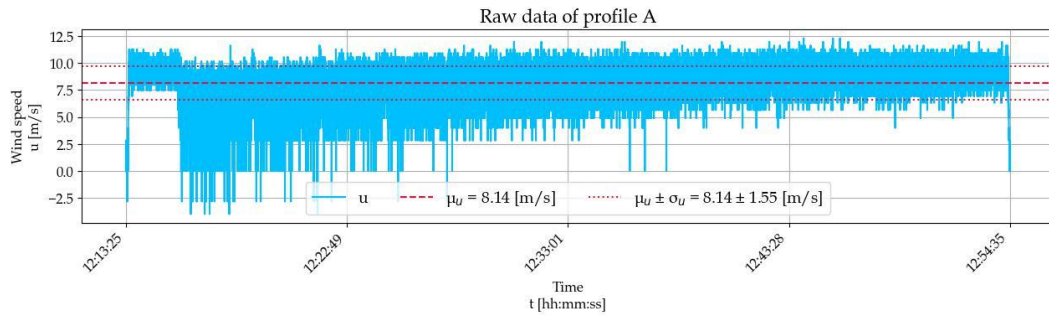


Figure 301 – Raw velocity data for profile A

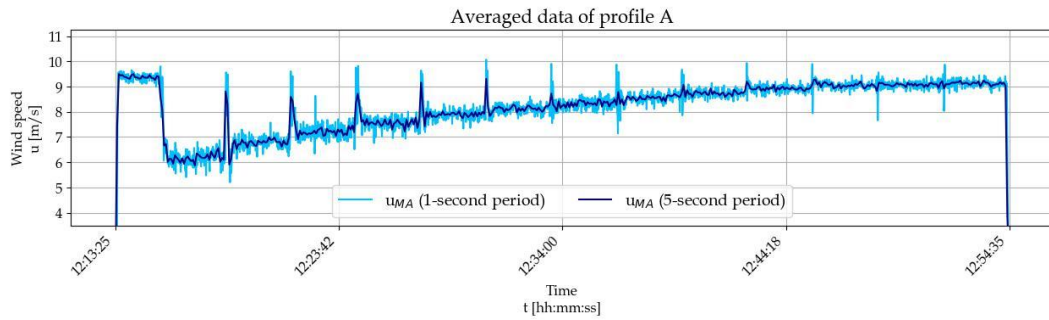


Figure 302 – Averaged velocity data for profile A

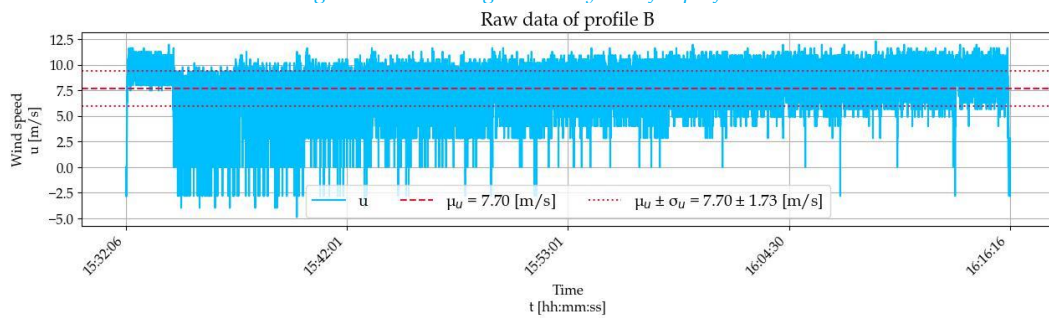


Figure 303 – Raw velocity data for profile B

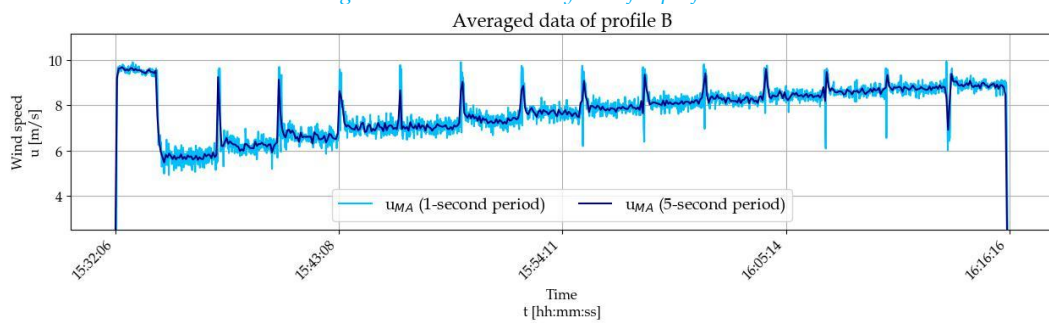


Figure 304 – Averaged velocity data for profile B

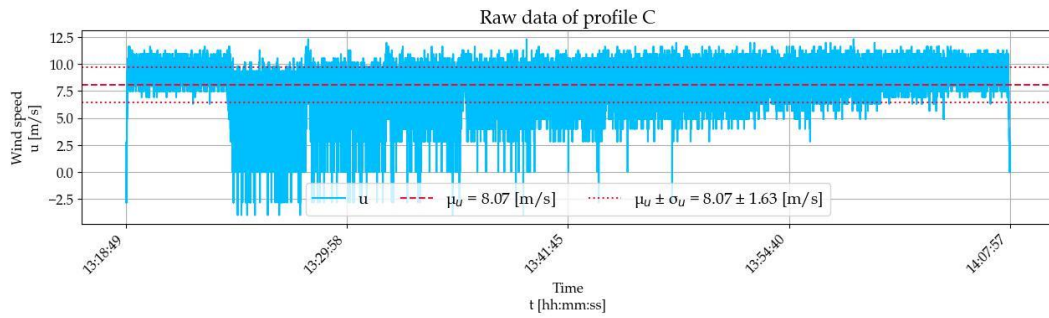


Figure 305 – Raw velocity data for profile C

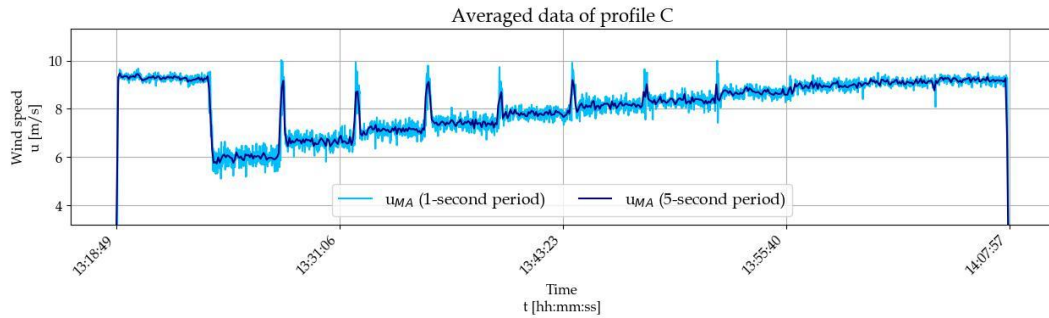


Figure 306 – Averaged velocity data for profile C

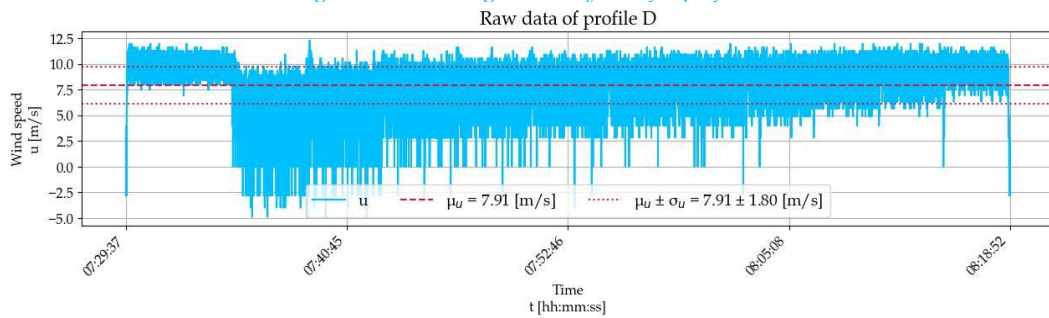


Figure 307 – Raw velocity data for profile D

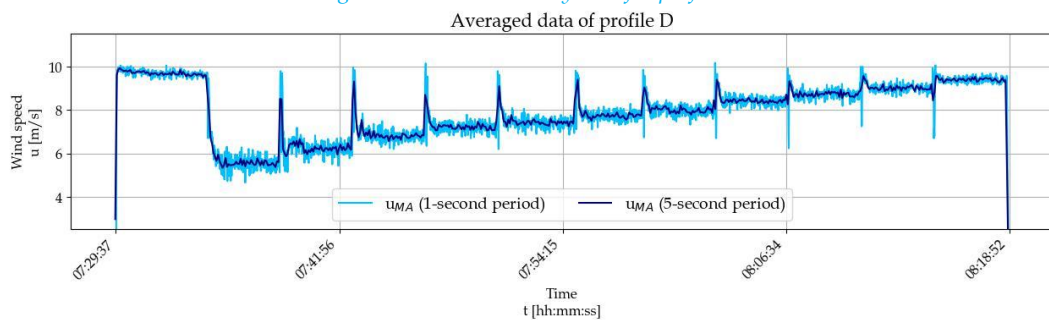


Figure 308 – Averaged velocity data for profile D



Periods of one minute were isolated per elevation; and averaged. This results in measured velocity profiles, as shown below.

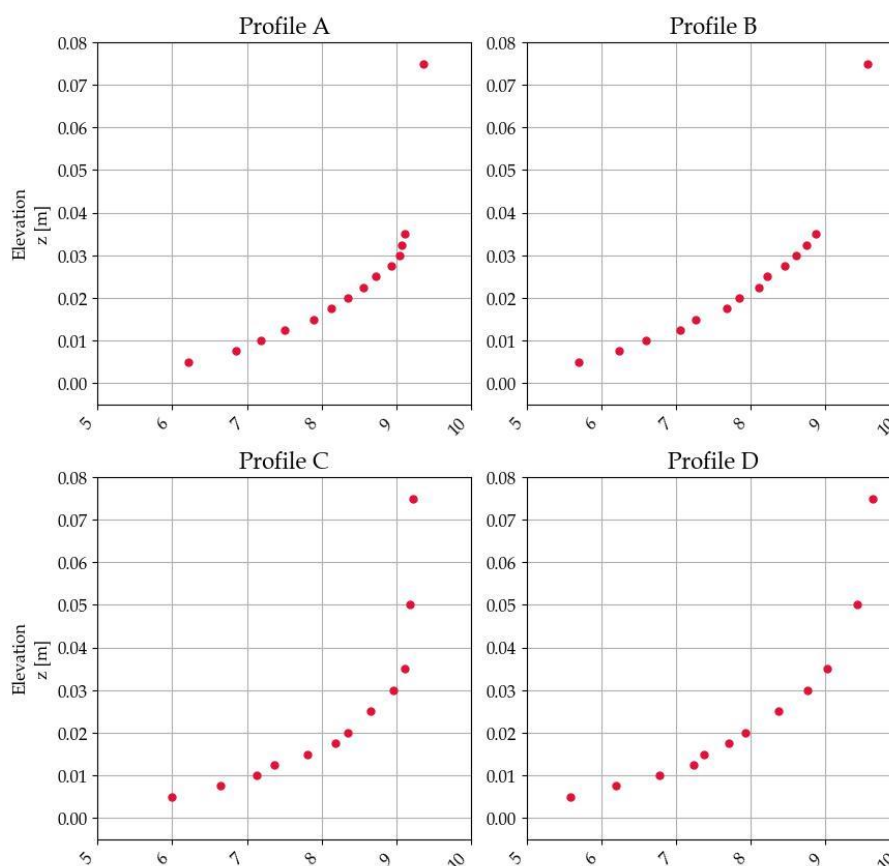


Figure 309 – Measured vertical velocity profiles

The involved data is listed in the table below.

Table 57 - Measured velocity profiles (values)

Profile A		Profile B		Profile C		Profile D	
$z$ [m]	$u$ [m]	$z$ [m]	$u$ [m]	$z$ [m]	$u$ [m]	$z$ [m]	$u$ [m]
0.0050	6.21	0.0050	5.69	0.0050	6.00	0.0050	5.58
0.0075	6.85	0.0075	6.24	0.0075	6.64	0.0075	6.19
0.0100	7.18	0.0100	6.6	0.0100	7.13	0.0100	6.77
0.0125	7.51	0.0125	7.06	0.0125	7.37	0.0125	7.23
0.0150	7.89	0.0150	7.26	0.0150	7.81	0.0150	7.38
0.0175	8.13	0.0175	7.68	0.0175	8.18	0.0175	7.71
0.0200	8.35	0.0200	7.85	0.0200	8.35	0.0200	7.93
0.0225	8.56	0.0225	8.11	0.0250	8.66	0.0250	8.37
0.0250	8.72	0.0250	8.22	0.0300	8.96	0.0300	8.76
0.0275	8.93	0.0275	8.45	0.0350	9.11	0.0350	9.02
0.0300	9.05	0.0300	8.61	0.0500	9.19	0.0500	9.42
0.0325	9.07	0.0325	8.74	0.0750	9.22	0.0750	9.64
0.0350	9.12	0.0350	8.87				
0.0750	9.37	0.0750	9.57				



## I.2.4 Wind speed data of the applied research

The raw data of the experiments are provided below.

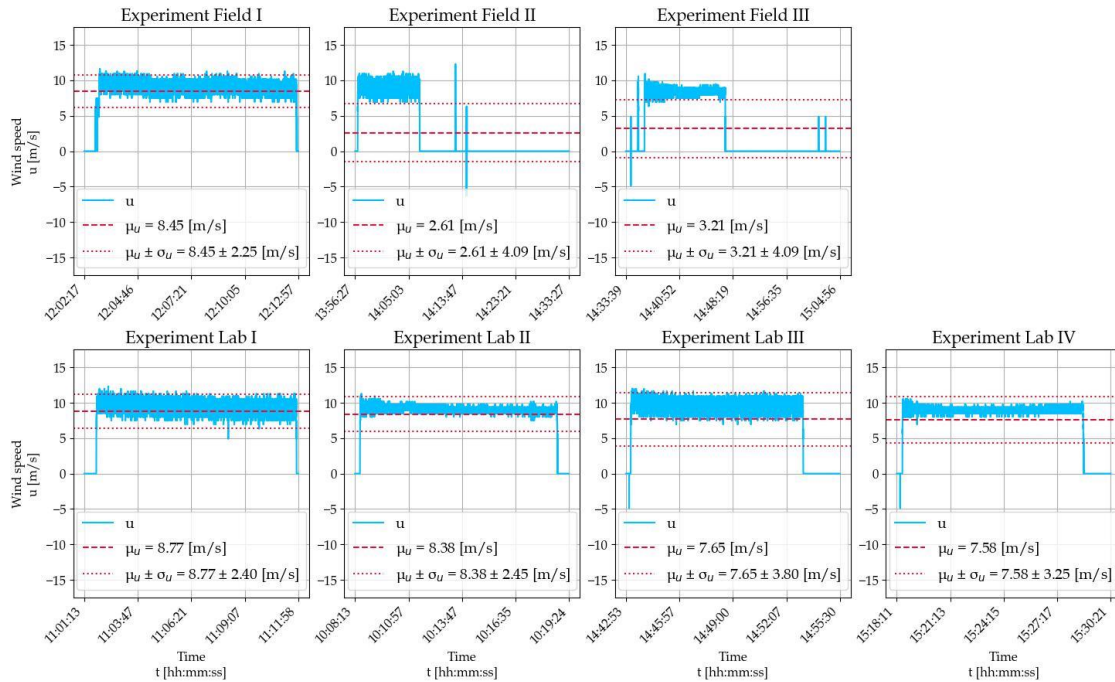


Figure 310 – Raw wind speed data of the field- and laboratory experiments

The isolated data of the experiments is provided below.

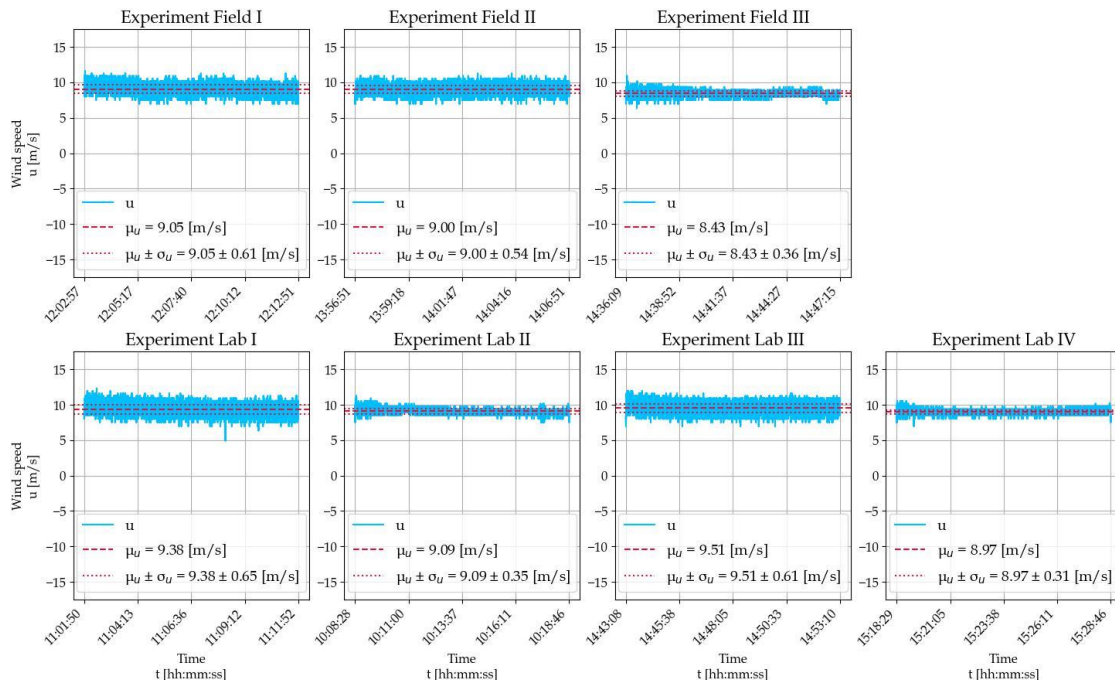


Figure 311–Isolated wind speed data of the field- and laboratory experiments

The moving averages of the data (i.e., over one-second periods) are provided below.

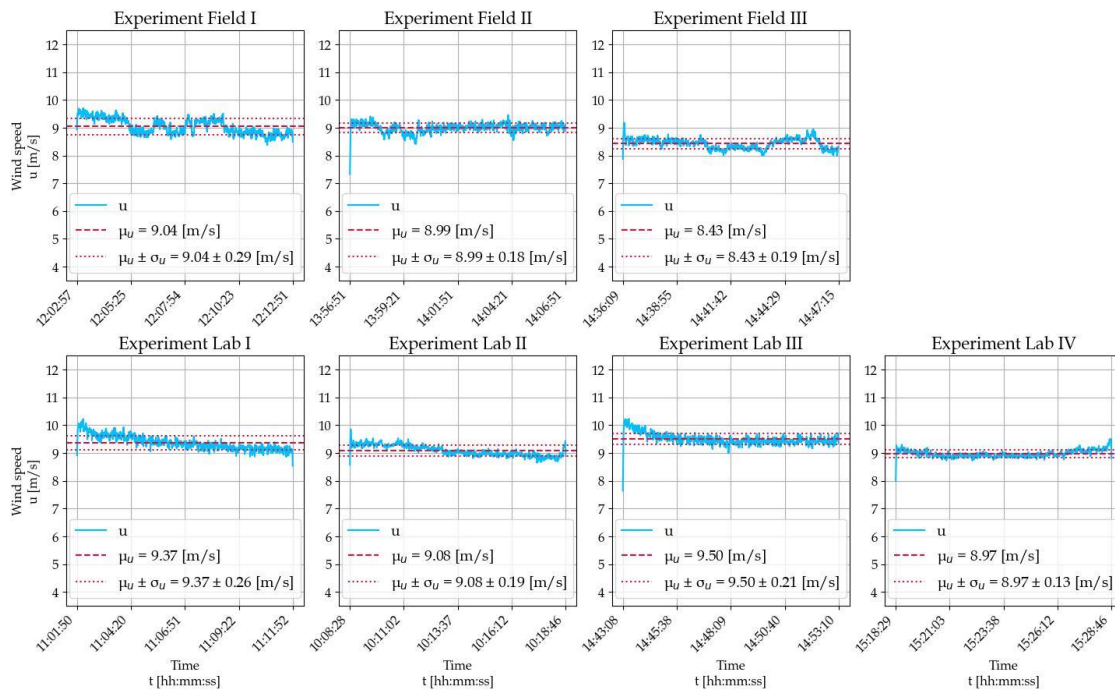


Figure 312– Averaged wind speed data of the field- and laboratory experiments

## I.3 Erosion results

The weighing process was generally performed three times per sand sample. The involved standard deviations are rather small; at maximum  $O(2)$  [g] of 1,000 [g] samples (i.e., the standard deviation is 0.2 [%] of the sample weight). Some weighing's were not performed three times; yet it is safe to say that weighing was done appropriately.

### I.3.1 Field I

After finishing Field I the sand trap was virtually empty. The sand trap contained only a very small quantity of sand (figure 313). The granular material was still retrieved; and weighted in the laboratory (figure 314 and figure 315).



Figure 313 – A virtually empty sand trap following Field I



Figure 314 – Eroded sand of Field I



Figure 315 – Weighing the eroded sand of Field I

This amount is virtually negligible. When comparing this erosion quantity to the erosion quantity from a dry bed (e.g., lab I); then it becomes clear that Field I showed a negligible erosion quantity (i.e.,  $\sim 1$  [g] erosion is 0.1 [%] of 1,000 [g] erosion). This negligible amount may have also resulted from driving the erosion zone walls into the sand bed; i.e., loosening some sand along the sides.

### I.3.2 Field II

Field II is a repetition of Field I; conducted about 1-2 hours later in time and just a few meters apart in space. The outcomes of Field II greatly resemble the outcomes of Field I. When Field II was finished, the sand trap was (again) virtually empty. On top (and again), a very small quantity of sand was visible within the sand trap (figure 316). The granular material was still retrieved; and weighted in the laboratory (figure 317 and figure 318).



Figure 316 – A virtually empty sand trap following Field II



Figure 317 – Eroded sand of Field II



Figure 318 – Weighing the eroded sand of Field II

The amount of erosion is very comparable to Field I, i.e., a negligible amount of erosion. However, Field II showed a little more erosion than Field I ([figure 315](#) vs. [figure 318](#); and [figure 319](#)). While the result remains unusable, one might say that this discrepancy indicates a little bit of surface drying (as Field II is conducted 1-2 hours later than Field I).



*Figure 319 – Visual comparison between the erosion fluxes of Field I and II*

### I.3.3 Field III

Sand-laden sample bags of known mass were prepared before this field expedition. This was done to slightly ease the workload during the field experiments. Additionally, experience learned that weighing the sand within the field can be difficult as ambient winds may exert pressure on the weighing plate (i.e., influencing the measurements). In the end six bags were emptied into the saltation hopper ([figure 320](#)); of which the weights are shown in and [figure 321](#) through [figure 326](#) (more sample bags were prepared, but of course only the used ones are shown). The plastic bowl was tarred in the weighing process; and is thus not part in the mass determination.



*Figure 320 – The emptied sandbags into the saltation hopper during Field III*

*Table 58 – Mass of the added sand through the saltation hopper*

Batch	1	2	3	4	5	6	Total
Mass	2,001	2,005	2,002	2,002	2,020	2,019	12,049



*Figure 321 – Field III added batch 1*



*Figure 322 – Field III added batch 2*



*Figure 323 – Field III added batch 3*





Figure 324 – Field III added batch 4



Figure 325 – Field III added batch 5



Figure 326 – Field III added batch 6

Following Field III the sand trap appeared as shown in figure 327 and figure 328. The sand trap contains the added sand mass from using the saltation hopper; and an erosion mass from the erosion zone. The shown sand mass in figure 327 and figure 328 was collected and put into sample bags. The sand was taken to the laboratory, where it was weighted (table 59). This was done three times. The determined mass includes the bags, like shown in figure 329 through figure 343.



Figure 327 – The sand trap and its wire mesh cylinder after Field III



Figure 328 – The sand trap after Field III

Table 59 – The masses of the eroded sand from Field III  
W1 = weighing 1 and B1 = bag 1 (and so on)

	B1 [–]	B2 [–]	B3 [–]	B4 [–]	B5 [–]	Total (incl. bag)	Total (excl. bag)
W1 [g]	3,012	3,029	3,023	3,013	3,172	15,249	15,220
W2 [g]	3,012	3,031	3,023	3,016	3,176	15,258	15,228
W3 [g]	3,011	3,024	3,017	3,009	3,171	15,232	15,204
$\mu$ [g]	3,011.67	3,028.00	3,021.00	3,012.67	3,173.00	15,246.33	15,217.33
$\sigma$ [g]	0.44	2.67	2.67	2.44	2.00	9.56	8.89



Figure 329 – W1; B1



Figure 330 – W1; B2



Figure 331 – W1; B3



Figure 332 – W1; B4



Figure 333 – W1; B5



Figure 334 – W2; B1



Figure 335 – W2; B2



Figure 336 – W2; B3



Figure 337 – W2; B4



Figure 338 – W2; B5





Figure 339 – W3; B1



Figure 340 – W3; B2



Figure 341 – W3; B3



Figure 342 – W3; B4



Figure 343 – W3; B5

As can be seen [table 59](#) is corrected for the mass of the empty bags ([table 60](#)). Weighing the empty sample bags was done exactly the same as shown [figure 329](#) through [figure 343](#). It is visible in [figure 320](#) that sample bag 1, 2 and 3 differ from sample bag 4 and 5. In the end, sample bag 1, 2 and 3 were slightly lighter than sample bag 4 and 5. Sample bag 1, 2, and 3 have a mass of roughly 5.5 [g] and bag 4 and 5 have a mass of roughly 6.5 [g].

Table 60  
W1 = weighing 1 and B1 = bag 1 (and so on)

	B1 [–]	B2 [–]	B3 [–]	B4 [–]	B5 [–]	Total (incl. bag)
W1 [g]	5	5	6	7	6	29
W2 [g]	5	6	6	7	6	30
W3 [g]	6	5	5	6	6	28
$\mu$ [g]	5.33	5.33	5.67	6.67	6.00	29.00
$\sigma$ [g]	0.44	0.44	0.44	0.44	0.00	0.67

Other tests (see Lab II) demonstrated that the saltation hopper does not always fully drain. This can be mitigated by gently hammering the saltation hopper during drainage. Yet this was not done within the field- and laboratory experiments. On top, it was unfortunately not documented how much residue mass was left on the lid of the saltation hopper. Lab II showed a residue mass in the order of 11.4 [g]. This residue mass has to be subtracted from the added sand mass; as the residue mass was not used to enhance erosion. Other unrecorded tests showed similar residue masses.

$$\begin{aligned} \text{Erosion sand mass} &= \text{collected sand mass} - \text{injected sand mass} \\ \text{Erosion sand mass} &= \text{collected sand mass} - (\text{added sand mass} - \text{saltation hopper residue}) \\ m_e &= m_c - (m_a - m_r) \\ m_e &= 15,217 - (12,049 - 11.4) = 3,179.4 \text{ [g]} \end{aligned}$$

Other experiments (e.g., Lab II) showed that there might be some reliability issues. In Field III those issues, appeared not to be very influential. The erosion zone walls were namely not undermined ([figure 344](#), [figure 345](#) and [figure 346](#)). Next, the saltation hopper appeared to work properly, but was maybe partly clogged ([figure 347](#)). Finally, taping the edges of the sand trap proved to crucial ([figure 348](#)).



Figure 344 – Erosion duct  
(upwind)



Figure 345 – Erosion duct  
(centre)



Figure 346 – Erosion duct  
(downwind)



Figure 347 – View of the saltation hopper working



Figure 348) The sand tray edges with sand grains on them

### I.3.4 Lab I

This experiment is the counterpart of Field I. After excavating the sand bed, it was brought to the laboratory. After drying the sand, it was put in the tailored sand pit of Mobi-Gust 2. Then, an erosion test was conducted. After the test, the sand trap contained eroded sand. The eroded sand was poured into an aluminium container, which was then weighted. The aluminium containers was tarred; and is thus not part in the mass determination.



Figure 349

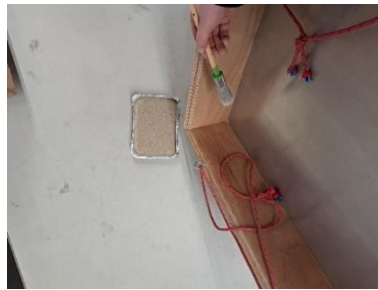


Figure 350



Figure 351

Table 61  
W1 = weighing 1 (and so on)

W1 [g]	W2 [g]	W3 [g]	$\mu$ [g]	$\sigma$ [g]
1,068.6	1,068.4	1,068.6	1,068.53	0.09



Figure 352



Figure 353



Figure 354

### I.3.5 Lab II

The sand masses that were added through the saltation hopper are shown in the table below.

Table 62

Batch	Mass [g]
1	931.6
2	1,046.8
3	1,026.2
4	1,038.2
5	1,156.0
6	1,322.4
7	1,205.2
8	1,203.4
9	1,227.6
10	1,196.0
11	1,164.0
Total	12,517.4

Pictures of the weighing process are provided below. The steel bowl was tarred; and is thus not part in the mass determination.



Figure 355



Figure 356



Figure 357



Figure 358



Figure 359



Figure 360





Figure 361



Figure 362



Figure 363



Figure 364



Figure 365

After the experiment, the sand trap appeared as follows.



Figure 366

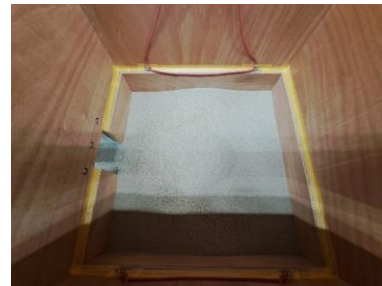


Figure 367

The sand was then collected from the sand trap and weighted; as shown in the table below.

Table 63  
W1 = weighing 1 (and so on)

W1 [g]	W2 [g]	W3 [g]	$\mu$ [g]	$\sigma$ [g]
18,239.6	18,239.8	18,239.4	18,239.6	0.13

The pictures of the weighing process are added below. The bucket was tarred; and is thus not part in the mass determination.



Figure 368



Figure 369



Figure 370

Between the weighing's the bucket was emptied in another one; to provide fair weighing's.



Figure 371

There is some residue sand mass left in the saltation hopper. To this end, the residue mass was retrieved and weighted.



Figure 372



Figure 373

Table 64

W1 = weighing 1 (and so on)

W1 [g]	W2 [g]	W3 [g]	$\mu$ [g]	$\sigma$ [g]
11.2	11.4	11.6	11.4	0.13

Pictures of the weighing process are provided below. The aluminium containers was tarred; and is thus not part in the mass determination.





Figure 374



Figure 375



Figure 376

$$\begin{aligned} \text{Erosion sand mass} &= \text{collected sand mass} - \text{injected sand mass} \\ \text{Erosion sand mass} &= \text{collected sand mass} - (\text{added sand mass} - \text{saltation hopper residue}) \\ m_e &= m_c - (m_a - m_r) \\ m_e &= 18,239.6 - (12,517.4 - 11.4) = 5,733.6 [g] \end{aligned}$$

The experiment was however unreliable due to undermining. The experiment was thus redone two times. However, reconducting the test showed similar outcomes. On top, the saltation hopper appeared to clog partly.



Figure 377



Figure 378

### I.3.6 Lab III

This experiment is virtually the same as other laboratory experiments. However, the sand surface was sprayed wet (see [appendix I.4](#)). The spraying was done systematically.

- 4 rows over the length; of 20 shots per row (2x).
- 15 rows over the width; of 5 shots per row (1x).

After the experiment, the sand trap was virtually empty. This amount is negligible due to the same reasons provided by the experiments Field I and Field II.



Figure 379



Figure 380



Figure 381

### I.3.7 Lab IV

This test was virtually the same as Lab III. For example, the sand pit was left untouched (i.e., the sand surface was also not rewetted). The sand bed might have dried a bit, because of the winds in the previous test; but other than that the sand surface was confined from the outside world. The added sand mass through the saltation hopper is shown in the table below.

Table 65

Batch	Mass [g]
1	1053.6
2	1211.2
3	1069.8
4	1205.2
5	1045.8
6	1225.4
7	1336.8
8	1155.4
9	1431.4
10	1104.6
11	709.0
12	563.2
13	207.2
Total	13,318.6

The pictures of the weighing process appear as follows. The bowl was tarred; and not included in the mass determination.



Figure 382



Figure 383



Figure 384



Figure 385



Figure 386



Figure 387



Figure 388



Figure 389



Figure 390



Figure 391



Figure 392



Figure 393



Figure 394

After the experiment, the sand was collected from the sand trap.



Figure 395



Figure 396

The involved sand mass is provided in the table on the next page.



Table 66  
W1 = weighing 1 (and so on)

W1 [g]	W2 [g]	W3 [g]	$\mu$ [g]	$\sigma$ [g]
15,100.4	15,100.0	15,100.2	15,100.2	0.13

The weighing process appears as shown in the pictures below. The bucket was tarred; and not included in the mass determination.



Figure 397



Figure 398



Figure 399

Again, between the weighing's the bucket was emptied in another one; to provide fair weighing's.



Figure 400

$$\begin{aligned} \text{Erosion sand mass} &= \text{collected sand mass} - \text{injected sand mass} \\ \text{Erosion sand mass} &= \text{collected sand mass} - (\text{added sand mass} - \text{saltation hopper residue}) \\ m_e &= m_c - (m_a - m_r) \\ m_e &= 15,100.2 - (13,318.6 - 11.4) = 1,793.0 \text{ [g]} \end{aligned}$$

In other tests (e.g., Lab II) some reliability issues were spotted. This time, the erosion walls were not undermined; and the saltation hopper was partially clogged at some spots.

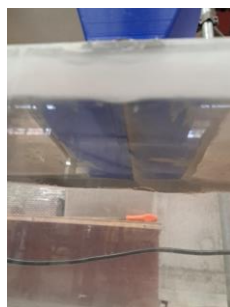


Figure 401



Figure 402

## I.4 Spray can calibration (used in lab III and IV)

The characteristics of the used spray can were determined as follows (i.e., facilitating repeatability).

- Filling the spray can with tap water.
- Squeeze the spray mechanism a few times to get rid of the air.
- Use the desired spray mode (i.e., the level of mistiness).
- Spray in a measuring cup; while pressing the spray mechanism completely and also releasing it completely after spraying; and count the number of sprays to reach 100 [ml].

Table 67

Test	1	2	3	$\mu$ [-]	$\sigma$ [-]
Shots	153	155	158	155.33	1.78



Figure 403



Figure 404

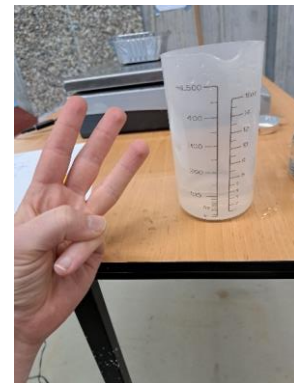


Figure 405

The amount of water per spray is approximately calculated as follows.

$$\bullet \quad \frac{100 \text{ [ml]}}{155.33 \text{ [shots]}} \approx 0.64 \left[ \frac{\text{ml}}{\text{shot}} \right]$$

The sand bed is then sprayed according to specific rules (i.e., facilitating repeatability).

- Do not change the spray mode (i.e., the level of mistiness).
- Use the spray container to spray 1 row at a time:
  - Note the number of shots per row.
  - Note the number of rows to fill the entire sand pit.
  - Note when the lanes are doubled, tripled, etc.
- Spray ~5 [cm] above the surface.

The following sketch is just an example of how the process appears. The sketch shows 6 lanes; and every layer is applied 3 times (i.e., 6 layers, each 3 thick).



Figure 406

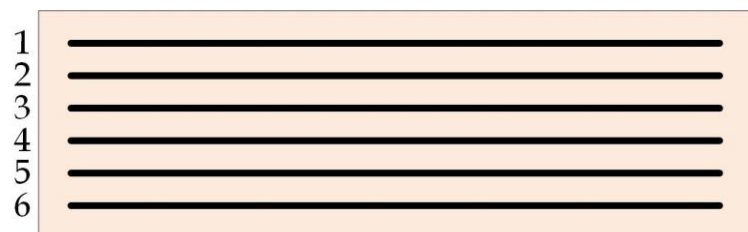


Figure 407



## I.5 Grain Size Distribution (GSD) analysis

This section shows how the Grain Size Distribution (GSD) analyses were conducted. The steps/rules were written down, because there is no European or global standard available; consequently, the steps/rules safeguard the consistency throughout this report.

### I.5.1 Dry sieve analysis guideline

1. Dry the sand sample; or sand grains might stick to the sieves. Use a sand sample of  $\sim 300$  [g]. Next, dry the sand for roughly 2 [h] with an oven temperature of  $110 \pm 5$  [°C].
2. Weigh the total sand sample. The total sand mass provides a useful check. To clarify, after the shaking process each sieve will contain a sand fraction. Summing all sand fractions should roughly provide the mentioned total sand mass. This approach might reveal (possible) sand losses during the analysis.
3. Select the sieves. The used sieve tower can hold up to 12 sieves. The size-bounds for sand are: 2.000 [mm] (pebbles), 1.000 [mm] (very coarse sand), 0.500 [mm] (coarse sand), 0.250 [mm] (medium sand), 0.125 [mm] (fine sand), 0.063 [mm] (very fine sand). Mesh sizes are selected, based on these bounds. Next, this research encountered grain sizes in the order of 0.350 [mm] to 0.450 [mm]. Based on that extra information, the following mesh sizes were selected: 2.000 [mm], 1.000 [mm], 0.800 [mm], 0.600 [mm], 0.560 [mm], 0.500 [mm], 0.400 [mm], 0.300 [mm], 0.250 [mm], 0.125 [mm], 0.090 [mm], 0.063 [mm]. Note the 0.090 [mm] mesh size; i.e., about equal to the sand dust bound, as defined by R.A. Bagnold. Next, sieves might have circular or squared openings; and only squared openings will be used. Choosing between the mentioned shapes would not matter much if sand grains were perfectly spherical. Yet as sand has irregular (and sometimes elongated) shapes, the circular openings are slightly more accurate. Most importantly, one must document the opening-shape that is used. On top, one must not use openings of different shapes in a single analysis. Next, also only use sieves that fit well. For example, sieves that are too loose, might cause sand losses during the shaking-process. On top, sieves that clamp too much, might cause sand losses while separating the sieves from each other; after the analysis. Next, preferably also only use sieves from the same manufacturer. Those sieves namely involve similar tolerances. The sieves that are used in this analysis are generally manufactured by a company called 'Interlab'; and some sieves are manufactured by a company called 'Fritsch'. 'Interlab' only uses the term 'opening [mm]' to define the mesh size; while 'Fritsch' uses 'Maschenweite,  $w$  [mm]' to define the mesh size. The sieves from 'Fritsch' also include a ' $d$  [mm]' that refers to the wire thickness of the sieves. Finally, a rubber must be added to every sieve; as this helps to disconnect the sieves from one another.
4. Clean the sieves before analysis starts. Do not use a (paint) brush or something similar; as this might damage the sieves. Instead, clean the sieves by gently tapping it against an arbitrary object (e.g., a table).
5. Weigh the empty sieves before the analysis. Preferably, take pictures of the mass-determination; i.e., to check the process later on. Do not remove or add heavy objects around the weighing plate; as this might influence the mass-determination. On top, also not tare the scale in between weighing subsequent sieves; for fair (relative) weighing's. Next, the smallest (i.e., 0.063 [mm]) and largest (i.e., 2.000 [mm]) mesh sizes normally contains no sand; and thus, these sieves can be used to check whether the weighing scale was set correctly.
6. Prepare the sieve tower. The mesh sizes should decrease from top to bottom.
7. Add the total sand sample in the top sieve and switch on the sieve tower. Make sure the sieve tower shakes with maximum force for about half an hour. After the shaking is finished, carefully disconnecting the sieves from each other (i.e., to prevent sand losses). If only one or two sieves contain almost the entire sand sample, swap some of the empty sieves, for mesh sizes around the sand-laden sieves.

8. Weighing the fractal sand samples. Weighing can be done using a 'normal' scale, which has a resolution and precision of 0.2 [g]. This normal scale allows weighing the sand-laden sieves. The difference between the empty- and laden sieve then provides the retained mass on that particular sieve. However, a 'precision' scale can also be used. Unfortunately, this precision scale has two negative side effects. First of all, the precision scale determines masses up to 205 [g]. So, the total sample mass cannot be determined using this precision scale (i.e., when samples of  $\sim 300$  [g]). Second of all, the precision scale is quite small in size. In elaboration, the sand-laden sieves do not fit on this scale (i.e., both in terms of their size, as well as their mass). That means that the sand fractions have to be separated from the sieves; to weigh them in smaller (aluminium) containers. In other words, the approach can be associated with sand losses. Comparing both analysis (i.e., the normal scale vs. the precision scale) provides comparable results, as shown below. So, it was decided to use the normal scale in view of time efficiency.

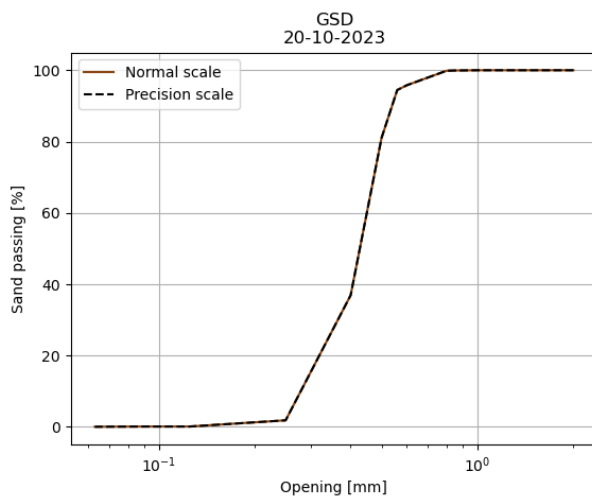


Figure 408



Figure 409

9. As a last optional step, sometimes there is some sand that passes all the sieves. This fraction, smaller than sand, can also be weighted.

Some additional gear is required.

- Oven gloves or pliers [*emptying the oven*].
- Aluminium container [*weighing-oven container*].
- Spoon [*scooping and stirring*].
- Hopper [*pouring*].
- Brush [*emptying/cleaning the containers (not the sieves!)*].

## I.5.2 An example of a sieve analysis

The total mass of the sand sample (weighted upfront) is 300.2 [g].

Table 68


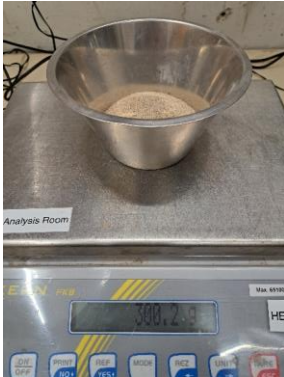












Sand sample	Weighing	Sieve tower
		

Table 69

Sieve	Opening [mm]	Empty sieve [g]	Laden sieve [g]	Sand retained [g]	Sand retained [%]	Sand cumulatively retained [%]	Sand cumulatively passed [%]
		A	B	C	D	E	F
		Weigh and fill in	Weigh and fill in	$C_i = B_i - A_i$	$\frac{D_i}{M_t} * 100$	$E_i = D_i + E_{i-1}$	$F_i = 100 - E_i$
1	2.000	376.2	376.2	0.0	0.00	0.00	100.00
2	1.000	429.2	429.4	0.2	0.07	0.07	99.93
3	0.800	358.4	361.8	3.4	1.13	1.20	98.80
4	0.600	321.0	343.4	22.4	7.46	8.66	91.34
5	0.560	387.6	391.2	3.6	1.20	9.86	90.14
6	0.500	300.2	327.4	27.2	9.06	18.92	81.08
7	0.400	349.0	428.2	79.2	26.38	45.30	54.70
8	0.300	282.4	380.8	98.4	32.78	78.08	21.92
9	0.250	271.6	308.8	37.2	12.39	90.47	9.53
10	0.125	261.6	290.0	28.4	9.46	99.93	0.07
11	0.090	253.4	253.6	0.2	0.07	100.00	0.00
12	0.063	251.0	251.0	0.0	0.00	100.00	0.00
			Total mass	300.2	100.00		

### I.5.2.1 Empty sieves













Table 70

0.063 [mm]	0.090 [mm]	0.125 [mm]
		
0.250 [mm]	0.300 [mm]	0.400 [mm]
		
0.500 [mm]	0.560 [mm]	0.600 [mm]
		
0.800 [mm]	1.000 [mm]	2.000 [mm]
		



## I.5.2.2 Laden sieves

Table 71

0.063 [mm]	0.090 [mm]	0.125 [mm]
		
0.250 [mm]	0.300 [mm]	0.400 [mm]
		
0.500 [mm]	0.560 [mm]	0.600 [mm]
		
0.800 [mm]	1.000 [mm]	2.000 [mm]
		



## I.6 Moisture content

This section shows the moisture-content analysis for several tests. Yet the analyses in this section generally show minor variation. The field samples were namely taken too deep. Consequently, minor variation is measured in the moisture content. The interface between the beach surface and the atmosphere is namely most important. That region, i.e., the top layer of the sand bed, namely contains most variability (e.g., surface drying). On top, aeolian processes focus exactly within that region as well. Shallower samples must thus be taken in the future. Yet it must also be noted that minimum masses are required for two reasons. First of all, the Grain Size Distribution analysis requires a minimum mass of  $\sim 300$  [g] ([appendix I.5](#)). On top, the moisture content analysis itself requires a weighing scale with a precision of about 0.1 [%] with respect to the sand sample; meaning that a sand sample of 300 [g] requires a scale having a precision of at least 0.3 [g].



Figure 410

### I.6.1 Field I, II and III

The moisture content is calculated as the ratio of water mass to the sand mass.

$$97) \quad MC = \frac{m_w}{m_s} \cdot 100 [\%]$$

The moisture content can also be calculated as the ratio of water mass to the total mass.

$$98) \quad MC = \frac{m_w}{m_t} \cdot 100 [\%]$$

Determining the moisture content is straightforward; and consists of five steps. First, a sand sample is taken. Secondly, the (wet) sand sample is weighted. Thirdly, the sand sample is dried in an oven. Fourthly, once dry the sand sample is weighted again. Finally, the explained equations are used to calculate the moisture content.

Rules [Method of Test for Moisture Content of Soils and Aggregates by Oven Drying \(ca.gov\)](#).

- The oven temperature:  $110 [^{\circ}\text{C}] \pm 5 [^{\circ}\text{C}]$ .
- The oven time:  $\sim 16$  [h] (e.g. during the night).
- The minimum sand mass should be at least: 100 [g].

The moisture content determination is shown in the tables below. The analysis contains samples that were taken throughout the day. The weighing process was conducted three times; i.e., there is also a mean table. All rows are obtained by weighing, except for row *D*, *F*, *H*, *I* and *J*; the associated relations are provided in the table.

Table 72 – Definitions

Time [hh:mm]	A	The time was recorded when the sample was taken
Dry laden bag [g]	B	The laden sample bag was weighted after drying
Empty bag [g]	C	The empty sediment bag was weighted
Dry sand only [g]	D	$D = B - C$
Check dry sand only [g]	E	The sand was weighted after drying without sample bag
Error [g]	F	$F =  D - E $
Wet laden bag [g]	G	The sample weight before drying
Wet sand only [g]	H	$H = G - C$
Moisture content ( $MC_1$ ) [%]	I	$I(= MC_1) = \frac{m_w}{m_s} \cdot 100 [\%] = \frac{m_{wet} - m_{dry}}{m_{dry}} \cdot 100 [\%]$
Moisture content ( $MC_2$ ) [%]	J	$J(= MC_2) = \frac{m_w}{m_t} \cdot 100 [\%] = \frac{m_{wet} - m_{dry}}{m_{wet}} \cdot 100 [\%]$

Below there is the table of the first weighing round.

Table 73 – First analysis

Time [hh:mm]	A	13:39	12:00	13:47	14:25	15:20
Dry laden bag [g]	B	1320.00	1665.00	1495.00	1419.00	1454.00
Empty bag [g]	C	5.00	5.00	6.00	5.00	6.00
Dry sand only [g]	D	1315.00	1660.00	1489.00	1414.00	1448.00
Check dry sand only [g]	E	1313.00	1658.00	1489.00	1414.00	1448.00
Error [g]	F	2.00	2.00	0.00	0.00	0.00
Wet laden bag [g]	G	1363.00	1734.00	1547.00	1464.00	1501.00
Wet sand only [g]	H	1358.00	1729.00	1541.00	1459.00	1495.00
Moisture content ( $MC_1$ ) [%]	I	3.27	4.16	3.49	3.18	3.25
Moisture content ( $MC_2$ ) [%]	J	3.17	3.99	3.37	3.08	3.14

Below there is the table of the second weighing round.

Table 74 – Second analysis

Time [hh:mm]	A	13:39	12:00	13:47	14:25	15:20
Dry laden bag [g]	B	1321.00	1664.00	1493.00	1419.00	1455.00
Empty bag [g]	C	6.00	5.00	5.00	6.00	5.00
Dry sand only [g]	D	1315.00	1659.00	1488.00	1413.00	1450.00
Check dry sand only [g]	E	1313.00	1657.00	1488.00	1412.00	1448.00
Error [g]	F	2.00	2.00	0.00	1.00	2.00
Wet laden bag [g]	G	1365.00	1733.00	1550.00	1466.00	1503.00
Wet sand only [g]	H	1359.00	1728.00	1545.00	1460.00	1498.00
Moisture content ( $MC_1$ ) [%]	I	3.35	4.16	3.83	3.33	3.31
Moisture content ( $MC_2$ ) [%]	J	3.24	3.99	3.69	3.22	3.20

Below there is the table of the third weighing round.

Table 75 – Third analysis

Time [hh:mm]	A	13:39	12:00	13:47	14:25	15:20
Dry laden bag [g]	B	1320.00	1663.00	1495.00	1418.00	1455.00
Empty bag [g]	C	5.00	5.00	5.00	5.00	5.00
Dry sand only [g]	D	1315.00	1658.00	1490.00	1413.00	1450.00
Check dry sand only [g]	E	1315.00	1657.00	1489.00	1412.00	1448.00
Error [g]	F	0.00	1.00	1.00	1.00	2.00
Wet laden bag [g]	G	1363.00	1735.00	1549.00	1465.00	1503.00
Wet sand only [g]	H	1358.00	1730.00	1544.00	1460.00	1498.00
Moisture content ( $MC_1$ ) [%]	I	3.27	4.34	3.62	3.33	3.31
Moisture content ( $MC_2$ ) [%]	J	3.17	4.16	3.50	3.22	3.20

Below there is the table that provides the mean values of the three weighing rounds.

Table 76 – Mean values

Time [hh:mm]	A	13:39	12:00	13:47	14:25	15:20
Dry laden bag [g]	B	1320.33	1664.00	1494.33	1418.67	1454.67
Empty bag [g]	C	5.33	5.00	5.33	5.33	5.33
Dry sand only [g]	D	1315.00	1659.00	1489.00	1413.33	1449.33
Check dry sand only [g]	E	1313.67	1657.33	1488.67	1412.67	1448.00
Error [g]	F	1.33	1.67	0.33	0.67	1.33
Wet laden bag [g]	G	1363.67	1734.00	1548.67	1465.00	1502.33
Wet sand only [g]	H	1358.33	1729.00	1543.33	1459.67	1497.00
Moisture content ( $MC_1$ ) [%]	I	3.30	4.22	3.65	3.28	3.29
Moisture content ( $MC_2$ ) [%]	J	3.19	4.05	3.52	3.17	3.18

## I.6.2 Lab III and IV

The same rule, as provided in the previous section, apply to this section.

- The wet sand sample mass is provided in the table below.

Table 77  
W1 = weighing 1 (and so on)

W1 [g]	W2 [g]	W3 [g]	$\mu$ [g]	$\sigma$ [g]
305.8	305.8	305.6	305.73	0.09



Figure 411



Figure 412



Figure 413

- The dry sand sample mass is provided in the table below.

Table 78  
W1 = weighing 1 (and so on)

W1 [g]	W2 [g]	W3 [g]	$\mu$ [g]	$\sigma$ [g]
290.6	290.2	290.4	290.40	0.13

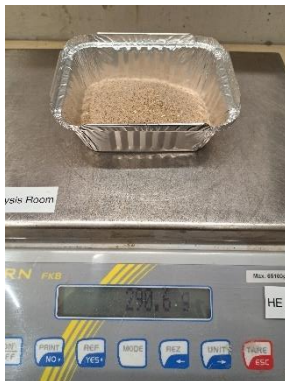


Figure 414



Figure 415



Figure 416

The moisture content is calculated as follows.

- $MC_1 = \frac{m_w}{m_s} = \frac{m_{wet} - m_{dry}}{m_{dry}} = \frac{305.73 - 290.40}{290.40} \approx 0.053 [-] (5.3 [\%])$
- $MC_2 = \frac{m_w}{m_t} = \frac{m_{wet} - m_{dry}}{m_{wet}} = \frac{305.73 - 290.40}{305.73} \approx 0.050 [-] (5.0 [\%])$